

# The first double Dalitz plane analysis of $B^0 \rightarrow DK^+\pi^-$ decays at LHCb

by

Aidan Richard Wiederhold

A thesis submitted in partial fulfilment of the requirements for the degree  
of

Doctor of Philosophy in Physics

University of Warwick, Department of Physics

November 2024







# Contents

List of tables	i
List of figures	iii
Acknowledgements	ix
Declaration	xiii
Abstract	xv
1 Introduction	1
2 Theory	3
2.1 The electroweak interaction and $CP$ violation	3
2.1.1 Types of $CP$ violation	4
2.1.2 CKM and the origin of $CP$ violation in the SM	5
2.2 The CKM angles	8
2.3 Multi-body decay kinematics	10
2.4 Electroweak penguin decays	12
2.5 Summary	14
3 Data acquisition and processing at LHCb	17
3.1 The Large Hadron Collider	17
3.2 The LHCb detector	20
3.2.1 Tracking	20
3.2.2 Particle identification	25
3.2.3 Detector performance	28
3.3 Triggering	30
3.4 Offline processing	32
3.5 Summary	33

<b>4</b>	<b>The double Dalitz method</b>	<b>35</b>
4.1	Single Dalitz analysis of $B^+ \rightarrow Dh^+$ decays	35
4.1.1	Binned signal population expectation	37
4.1.2	$B^+ \rightarrow D\pi^+$ decays	40
4.1.3	Charm factory inputs	41
4.1.4	Recursive parameterisation	41
4.1.5	Analysis result	42
4.2	The double Dalitz analysis	43
4.2.1	Deriving the expectation equation for the general double Dalitz binned signal population	45
4.2.2	Re-parameterising the normalisation parameters	47
4.2.3	The Cartesian parameterisation	47
4.2.4	Binned amplitude ratios	48
4.2.5	The expectation equation for all $D$ final states of interest	49
4.2.6	Full observables and parameters list	50
4.3	External inputs	52
4.3.1	Phase conventions	54
4.4	Binning schemes	54
4.4.1	Binning definitions and optimisation	55
4.5	Background decays	55
4.6	Extracting $\gamma$	56
4.6.1	The $CP$ fit	56
4.6.2	Interpreting the result	57
4.6.3	Evaluating uncertainties	57
4.7	Summary	58
<b>5</b>	<b>Selection</b>	<b>61</b>
5.1	Basic selection	61
5.2	Selection	66
5.2.1	PID cuts on $B$ companion particles	66
5.2.2	Boosted decision tree	66
5.2.3	PID cut on $D$ children	70
5.2.4	Double misidentification	70
5.2.5	$D^*(2010)^-$ veto	70
5.2.6	$D^-$ , $D^0$ , and $D_s^+$ veto	71
5.2.7	Double $D^0$ veto	74
5.2.8	$B^+$ veto	74
5.2.9	Charmless suppression	75

5.3	Selection results	77
5.3.1	Multiple candidates	77
5.3.2	The $D$ Dalitz efficiency profiles	78
5.4	Summary	83
<b>6</b>	<b>Reweighting of backgrounds</b>	<b>85</b>
6.1	Background fractions	85
6.2	Kinematic reweighting	86
6.2.1	Laura++	86
6.2.2	Signal projected measurements	88
6.2.3	Background polluted Dalitz distributions	88
6.2.4	Model reweighting results	90
6.2.5	Combinatorial background modelling	95
6.3	Helicity weighting	95
6.3.1	$B_s^0 \rightarrow D_{s1}^-(\rightarrow \bar{D}^{*0} K^-)\pi^+$	97
6.3.2	$B^0 \rightarrow D_1^-(\rightarrow \bar{D}^{*0}\pi^-)K^+$	98
6.3.3	$B_s^0 \rightarrow \bar{D}^{*0} \bar{K}^{*0}(\rightarrow K^-\pi^+)$ , $B^0 \rightarrow \bar{D}^{*0} K^{*0}(\rightarrow K^+\pi^-)$	98
6.3.4	Reweighting procedure	98
6.3.5	Rewighted helicity angle distributions	99
6.3.6	Rewighted mass distributions	102
6.4	Summary	105
<b>7</b>	<b>Invariant mass fits</b>	<b>107</b>
7.1	Strategy	107
7.1.1	Components of the fit	107
7.2	Determining the PDF shapes	109
7.2.1	$B^0 \rightarrow DK^+\pi^-$ and $B_s^0 \rightarrow DK^-\pi^+$	109
7.2.2	$B^0 \rightarrow D^*K^+\pi^-$ and $B_s^0 \rightarrow D^*K^-\pi^+$	110
7.2.3	Partially reconstructed background with $DK_{(1,2)}^{(*)}(\rightarrow K^\pm\pi^\mp\pi^0)$	110
7.2.4	$B^0 \rightarrow D\pi^+\pi^-$	111
7.2.5	$B^0 \rightarrow D^*\pi^+\pi^-$	111
7.2.6	$B^+ \rightarrow DK^+\pi^+\pi^-$	111
7.2.7	$B^+ \rightarrow D\pi^+\pi^+\pi^-$	111
7.2.8	Other peaking backgrounds	112
7.3	Fit to data	112
7.4	Pseudo-experiment studies	126
7.5	Summary	126

<b>8</b>	<b><i>CP</i> fit and interpretation</b>	<b>129</b>
8.1	<i>CP</i> fit	129
8.1.1	Choice of parameterisation	129
8.1.2	Ambiguities	130
8.1.3	Parameter constraints	132
8.1.4	Fitter verifications	133
8.1.5	Fit configuration	139
8.1.6	Data <i>CP</i> fit results	139
8.1.7	Pseudo-experiment studies	147
8.2	Interpretation results	149
8.2.1	Pseudo-experiment studies	149
8.2.2	Data <i>CP</i> fit interpretation results (currently blinded)	149
8.2.3	Sensitivity to $\gamma$	150
8.3	Summary	152
<b>9</b>	<b>Systematic uncertainties</b>	<b>155</b>
9.1	Systematic methodologies	156
9.1.1	External inputs	156
9.1.2	Efficiency variations across the Dalitz space	157
9.1.3	Background yield uncertainty	157
9.1.4	Background source binned distribution	158
9.1.5	Factorisation of <i>B</i> plane and <i>D</i> plane	158
9.1.6	PID correction	158
9.1.7	Mass fit parameterisation	158
9.1.8	Charmless contributions	159
9.1.9	<i>CP</i> violation in background decays	159
9.1.10	Production and detection asymmetries	159
9.1.11	Bin migration	159
9.2	Results	160
<b>10</b>	<b>Rare decays at the FCC-ee</b>	<b>163</b>
10.1	Current status, prospects and limitations of $b \rightarrow s\nu\bar{\nu}$ measurements	163
10.2	The Future Circular Collider	164
10.2.1	FCC-ee	164
10.2.2	The IDEA detector and simulation production	165
10.3	Prospects for $b \rightarrow s\nu\bar{\nu}$ measurements at the FCC-ee	167
10.3.1	Basic sensitivity studies in an ideal detector	167
10.3.2	Detector performance requirements	174

10.4 Implications of the FCC-ee prospects . . . . .	176
10.4.1 SM implications . . . . .	176
10.4.2 NP implications . . . . .	178
10.5 Summary . . . . .	178
<b>11 Conclusions</b>	<b>181</b>
11.1 Double Dalitz . . . . .	181
11.2 The FCC-ee . . . . .	182
11.2.1 $b \rightarrow s\nu\bar{\nu}$ at the FCC-ee . . . . .	182
11.2.2 FCC-ee flavour physics . . . . .	182
<b>A Double Dalitz BDT</b>	<b>185</b>
<b>B <math>CP</math> fit correlations</b>	<b>191</b>
<b>C FCC-ee BDT inputs</b>	<b>193</b>
<b>References</b>	<b>201</b>

# List of tables

2.1 CKM angles from direct measurements.	9
2.2 SM prediction for integrated decay rates of $b \rightarrow s\nu\bar{\nu}$ decays summed over the three neutrino flavors.	14
4.1 Number of observables and parameters per decay mode in the double Dalitz analysis.	51
4.2 External input parameters and values.	54
5.1 Preselection cuts.	63
5.2 Preselection efficiency on signal MC samples	65
5.3 Summary of the variables used for BDT training.	68
5.4 Optimal BDT cut values.	68
5.5 All particle candidate combinations that are vetoed for certain $D$ final states.	71
5.6 Sideband definitions for the various signal final states.	75
5.7 Multiple candidate rate in data after the full selection.	78
6.1 Type of model used for each background and their source.	86
7.1 Summary of background components in the invariant mass fits.	109
7.2 Fitted invariant mass PDF parameters for the two-body decays.	113
7.3 Fitted invariant mass PDF parameters for the three-body decays.	114
7.4 Fitted invariant mass PDF parameters for the four-body decays	114
7.5 Mass fit yields per $B$ flavour within $\mu \pm 3\sigma$ for $D \rightarrow K^+K^-$	115
7.6 Mass fit yields per $B$ flavour within $\mu \pm 3\sigma$ for $D \rightarrow \pi^+\pi^-$	116
7.7 Mass fit yields per $B$ flavour within $\mu \pm 3\sigma$ for $D \rightarrow K^\pm\pi^\mp$	117
7.8 Mass fit yields per $B$ flavour within $\mu \pm 3\sigma$ for $D \rightarrow \pi^\pm K^\mp$	118
7.9 Mass fit yields per $B$ flavour within $\mu \pm 3\sigma$ for $D \rightarrow K_S^0\pi^+\pi^-$ LL	119
7.10 Mass fit yields per $B$ flavour within $\mu \pm 3\sigma$ for $D \rightarrow K_S^0\pi^+\pi^-$ DD	120
7.11 Mass fit yields per $B$ flavour within $\mu \pm 3\sigma$ for $D \rightarrow K_S^0K^+K^-$ LL	121
7.12 Mass fit yields per $B$ flavour within $\mu \pm 3\sigma$ for $D \rightarrow K_S^0K^+K^-$ DD	122
7.13 Mass fit yields per $B$ flavour within $\mu \pm 3\sigma$ for $D \rightarrow \pi^+\pi^-\pi^+\pi^-$	123

7.14	Mass fit yields per $B$ flavour within $\mu \pm 3\sigma$ for $D \rightarrow K^\pm \pi^\mp \pi^+ \pi^-$	124
7.15	Mass fit yields per $B$ flavour within $\mu \pm 3\sigma$ for $D \rightarrow \pi^\pm K^\mp \pi^+ \pi^-$	125
8.1	Binned signal populations observed in the $B^+ \rightarrow Dh^+$ analysis for $B^+ \rightarrow DK^+, D \rightarrow K_S^0 \pi^+ \pi^-$ decays.	134
8.2	Binned signal populations observed in the $B^+ \rightarrow Dh^+$ analysis for $B^+ \rightarrow DK^+, D \rightarrow K_S^0 K^+ K^-$ decays.	134
8.3	Comparison between the $B^+ \rightarrow Dh^+$ analysis values of parameters of interest and the values obtained by the double Dalitz fitter with only the $B^+ \rightarrow DK^+$ decay.	135
8.4	Binned signal populations observed in the $B^+ \rightarrow Dh^+$ analysis for $B^+ \rightarrow D\pi^+, D \rightarrow K_S^0 \pi^+ \pi^-$ decays.	136
8.5	Binned signal populations observed in the $B^+ \rightarrow Dh^+$ analysis for $B^+ \rightarrow D\pi^+, D \rightarrow K_S^0 \pi^+ \pi^-$ decays.	136
8.6	Comparison between the $B^+ \rightarrow Dh^+$ analysis values of parameters of interest and the values obtained by the double Dalitz fitter.	138
8.7	Results of the double Dalitz $CP$ fit to data.	146
8.8	Results of the interpretation of double Dalitz fit result to data.	151
8.9	Model values and experimentally determined values of the $\bar{\kappa}_\alpha, r_\alpha$ and $T_\alpha$ hadronic parameters.	152
9.1	Results of systematic uncertainty studies.	161
10.1	Advantages of Belle II, the LHC and the FCC-ee.	165
10.2	Children PID and candidate mass requirements.	168
10.3	Signal and background population expectations at the FCC-ee for $B^0 \rightarrow K^{*0} \nu \bar{\nu}$ and $B_s^0 \rightarrow \phi \nu \bar{\nu}$ decays.	173
11.1	Estimated relative branching fraction uncertainty for measurements of $b \rightarrow s \nu \bar{\nu}$ decays at the FCC-ee.	182
B.1	Statistical correlation matrix for the $CP$ fit to data.	191
B.2	Statistical correlation matrix for the nominal $CP$ fit.	192
C.1	Feature importance for the input variables in the stage 1 BDT for the $B^0 \rightarrow K^{*0} \nu \bar{\nu}$ decay.	193
C.2	Feature importance for the input variables in the stage 2 BDT for the $B^0 \rightarrow K^{*0} \nu \bar{\nu}$ decay.	197

# List of figures

2.1 The rescaled “db” unitarity triangle.	7
2.2 Fit of the “db” unitarity triangle to CKM measurements.	8
2.3 The LHCb $\gamma$ combination.	9
2.4 Sketch of a Dalitz plane definition.	10
2.5 Example of a $B_s^0 \rightarrow DK^- \pi^+$ model Dalitz distribution.	12
2.6 The simplest Feynman diagrams for a $b \rightarrow s \nu \bar{\nu}$ decay.	13
3.1 Schematic of the LHC layout	18
3.2 Cross section of an LHC cryodipole.	19
3.3 Beam spot pattern on the LHC dump block.	19
3.4 The angular distribution of the production cross-section of $b\bar{b}$ pairs.	20
3.5 Side view of the LHCb detector.	21
3.6 Sketch of the LHCb tracking systems.	21
3.7 Sketch of the VELO sub-detector.	22
3.8 Schematic of the third tracking layer of the tracker turicensis.	23
3.9 Schematic of a single tracking layer of the inner tracker.	24
3.10 Configuration of the outer tracker modules and the cross section of single tracking layer.	25
3.11 The relation between the Cherenkov angle and particle momentum for different species and radiator mediums.	27
3.12 Sketch of the RICH 1 sub-detector.	27
3.13 Quarter cross section of the lateral segmentation of the SPD, PS and ECAL and the HCAL.	28
3.14 Schematic of the muon sub-detector.	29
3.15 Relative momentum resolution as a function of momentum for long tracks in LHCb data.	30
3.16 Primary vertex and impact parameter resolution in LHCb data.	30
3.17 PID efficiency and mis-identification as a function of momentum in LHCb data for charged particle species.	31



3.18 Overview of the Run 2 LHCb trigger system. . . . .	31
4.1 Feynman diagrams for the suppressed and favoured $B^+ \rightarrow DK^+$ decays. . . . .	36
4.2 Optimal binning schemes for $D \rightarrow K_S^0 \pi^+ \pi^-$ & $D \rightarrow K_S^0 K^+ K^-$ Dalitz planes. . . . .	37
4.3 Dalitz distribution of $D \rightarrow K_S^0 \pi^+ \pi^-$ and $D \rightarrow K_S^0 K^+ K^-$ decays. . . . .	38
4.4 Contour plot of the single Dalitz $B^+ \rightarrow Dh^+$ analysis result. . . . .	42
4.5 Feynman diagrams for the suppressed and favoured $B^0 \rightarrow DK^+ \pi^-$ decays. . . . .	43
4.6 Signal-only optimal binning scheme (left) for the Dalitz plane of $B^0 \rightarrow$ $DK^+ \pi^-$ decays and (right) the distribution of such decays in fully selected Run 1 and 2 LHCb data. . . . .	44
5.1 BDT response distributions for the $D \rightarrow K_S^0 h^+ h^-$ DD topology. . . . .	69
5.2 BDT optimisation plots for $D \rightarrow K_S^0 h^+ h^-$ DD, $D \rightarrow K^\pm \pi^\mp$ & $D \rightarrow$ $K^\pm \pi^\mp \pi^+ \pi^-$ decays. . . . .	69
5.3 Distributions of mis-reconstructed masses for $D \rightarrow \pi^+ \pi^-$ , $D \rightarrow K_S^0 \pi^+ \pi^-$ & $D \rightarrow K_S^0 K^+ K^-$ decays. . . . .	72
5.4 Distributions of mis-reconstructed masses for $D \rightarrow \pi^+ \pi^- \pi^+ \pi^-$ & $D \rightarrow$ $K^\pm \pi^\mp \pi^+ \pi^-$ decays. . . . .	73
5.5 $B_{(s)}^0 \rightarrow D^0 \bar{D}^0$ mass veto. . . . .	74
5.6 $B^+ \rightarrow DK^+$ ( $B^+ \rightarrow D\pi^+$ ) mass veto. . . . .	75
5.7 $B/S$ as a function of $\text{FDS}_D$ for $D \rightarrow K_S^0 \pi^+ \pi^-$ , $D \rightarrow K_S^0 K^+ K^-$ , and $D \rightarrow K^\pm \pi^\mp$ . . . . .	76
5.8 $B/S$ as a function of $\text{FDS}_D$ for $D \rightarrow \pi^+ \pi^-$ and $D \rightarrow K^+ K^-$ , $D \rightarrow$ $K^\pm \pi^\mp \pi^+ \pi^-$ , and $D \rightarrow \pi^+ \pi^- \pi^+ \pi^-$ . . . . .	77
5.9 Flat $D$ Dalitz plane distributions for $B^+ \rightarrow D\pi^+$ , $D \rightarrow K_S^0 \pi^+ \pi^-$ DD and $B^0 \rightarrow DK^+ \pi^-$ , $D \rightarrow K_S^0 \pi^+ \pi^-$ DD decays. . . . .	79
5.10 Flat $D$ Dalitz plane distributions for $B^+ \rightarrow D\pi^+$ , $D \rightarrow K_S^0 K^+ K^-$ DD and $B^0 \rightarrow DK^+ \pi^-$ , $D \rightarrow K_S^0 K^+ K^-$ DD decays. . . . .	79
5.11 Dalitz plane ratios between $B^+ \rightarrow D\pi^+$ and $B^0 \rightarrow DK^+ \pi^-$ decays . . . . .	79
5.12 $D$ Dalitz bin population fractions for $B^+ \rightarrow D\pi^+$ and $B^0 \rightarrow DK^+ \pi^-$ decays for $D \rightarrow K_S^0 \pi^+ \pi^-$ DD. . . . .	80
5.13 $D$ Dalitz bin population fractions for $B^+ \rightarrow D\pi^+$ and $B^0 \rightarrow DK^+ \pi^-$ decays for $D \rightarrow K_S^0 K^+ K^-$ DD. . . . .	80
5.14 1D $D$ Dalitz distributions per $B$ Dalitz bin. . . . .	81
5.15 1D $D$ Dalitz distributions per $B$ Dalitz bin. . . . .	82
5.16 1D $D$ Dalitz distributions per $B$ Dalitz bin. . . . .	82
6.1 Model square Dalitz distributions . . . . .	87
6.2 $A_b^0 \rightarrow Dp\pi^-$ square Dalitz distribution and adaptive binning. . . . .	89

6.3	$\bar{A}_b^0 \rightarrow DK^+\bar{p}$ square Dalitz distribution and adaptive binning.	89
6.4	$\bar{B}_s^0 \rightarrow DK^+\pi^-$ & $B^0 \rightarrow D\pi^+\pi^-$ Dalitz reweighting result.	91
6.5	$B^0 \rightarrow D^*K^+\pi^-$ , $\bar{B}_s^0 \rightarrow D^*K^+\pi^-$ & $B^0 \rightarrow D^*\pi^+\pi^-$ Dalitz reweighting result.	92
6.6	$\Lambda_b^0 \rightarrow Dp\pi^-$ & $\Lambda_b^0 \rightarrow D^*p\pi^-$ Dalitz reweighting result.	93
6.7	$\Lambda_b^0 \rightarrow DpK^-$ & $\Lambda_b^0 \rightarrow D^*pK^-$ Dalitz reweighting result.	94
6.8	Sideband definition for $D \rightarrow K_S^0\pi^+\pi^-$ DD.	96
6.9	$B$ Dalitz plane combinatorial extrapolation for $D \rightarrow K_S^0\pi^+\pi^-$ DD.	96
6.10	$D$ Dalitz plane combinatorial extrapolation for $D \rightarrow K_S^0\pi^+\pi^-$ DD.	97
6.11	$B_s^0 \rightarrow D_{s1}^-(\rightarrow \bar{D}^{*0}K^-)\pi^+$ helicity following helicity reweighting.	99
6.12	$B^0 \rightarrow D_1^-(\rightarrow \bar{D}^{*0}\pi^-)K^+$ helicity following helicity reweighting.	99
6.13	$B_s^0 \rightarrow \bar{D}^{*0}\bar{K}^{*0}(0,0)$ helicity following helicity reweighting.	100
6.14	$B_s^0 \rightarrow \bar{D}^{*0}\bar{K}^{*0}(1,1)$ helicity following helicity reweighting.	100
6.15	$B^0 \rightarrow \bar{D}^{*0}K^{*0}(0,0)$ helicity following helicity reweighting.	100
6.16	$B^0 \rightarrow \bar{D}^{*0}K^{*0}(1,1)$ helicity following helicity reweighting.	101
6.17	$B_s^0 \rightarrow D_{s1}^-(\rightarrow \bar{D}^{*0}K^-)\pi^+$ $B^0$ mass distribution following helicity reweighting.	102
6.18	$B_s^0 \rightarrow \bar{D}^{*0}\bar{K}^{*0}(0,0)$ $B^0$ mass distribution following helicity reweighting.	102
6.19	$B_s^0 \rightarrow \bar{D}^{*0}\bar{K}^{*0}(1,1)$ $B^0$ mass distribution following helicity reweighting.	103
6.20	$B^0 \rightarrow D_1^-(\rightarrow \bar{D}^{*0}\pi^-)K^+$ $B^0$ mass distribution following helicity reweighting.	103
6.21	$B^0 \rightarrow \bar{D}^{*0}K^{*0}(0,0)$ $B^0$ mass distribution following helicity reweighting.	103
6.22	$B^0 \rightarrow \bar{D}^{*0}K^{*0}(1,1)$ $B^0$ mass distribution following helicity reweighting.	104
6.23	$B_s^0 \rightarrow \bar{D}^{*0}K^-\pi^+$ $B^0$ mass distribution following helicity reweighting.	104
6.24	$B^0 \rightarrow D^*K^+\pi^-$ $B^0$ mass distribution following helicity reweighting.	104
7.1	$D \rightarrow K^+K^-$ mass fit	115
7.2	$D \rightarrow \pi^+\pi^-$ mass fit	116
7.3	$D \rightarrow K^\pm\pi^\mp$ mass fit	117
7.4	$D \rightarrow \pi^\pm K^\mp$ mass fit	118
7.5	$D \rightarrow K_S^0\pi^+\pi^-$ LL mass fit	119
7.6	$D \rightarrow K_S^0\pi^+\pi^-$ DD mass fit	120
7.7	$D \rightarrow K_S^0K^+K^-$ LL mass fit	121
7.8	$D \rightarrow K_S^0K^+K^-$ DD mass fit	122
7.9	$D \rightarrow \pi^+\pi^-\pi^+\pi^-$ mass fit	123
7.10	$D \rightarrow K^\pm\pi^\mp\pi^+\pi^-$ mass fit	124
7.11	$D \rightarrow \pi^\pm K^\mp\pi^+\pi^-$ mass fit	125
7.12	Mass fit pseudo-experiment pull distributions (1 of 2).	127
7.13	Mass fit pseudo-experiment pull distributions (2 of 2).	128
8.1	Bands of degenerate fit solutions due to $\langle\bar{\kappa}\rangle_\alpha$ ambiguities in the double Dalitz expectation equations.	132

8.2	$CP$ fit results of the reproduction of the $B^+ \rightarrow Dh^+$ analysis with only the $B^+ \rightarrow DK^+$ decay.	135
8.3	$CP$ fit results of the reproduction of the $B^+ \rightarrow Dh^+$ analysis.	137
8.4	Cartesian parameters obtained in the $CP$ fit to data.	140
8.5	$D \rightarrow K_S^0 \pi^+ \pi^-$ double Dalitz fit to data.	141
8.6	$D \rightarrow K_S^0 K^+ K^-$ double Dalitz fit to data.	142
8.7	Favoured and suppressed $D \rightarrow K^\pm \pi^\mp$ double Dalitz fit to data.	143
8.8	$D \rightarrow \pi^+ \pi^-$ and $D \rightarrow K^+ K^-$ double Dalitz fit to data.	144
8.9	Favoured and suppressed $D \rightarrow K^\pm \pi^\mp \pi^+ \pi^-$ , and $D \rightarrow \pi^+ \pi^- \pi^+ \pi^-$ double Dalitz fit to data.	145
8.10	Pull results for the double Dalitz fit using pseudo-experiments.	148
8.11	Pull results of the interpretation of the double Dalitz fit results using pseudo-experiments.	150
8.12	Comparison between the $CP$ fit with and without backgrounds present, and between the model and the hadronic parameters obtained in this analysis.	153
10.1	Cross-section of the IDEA detector concept.	166
10.2	A sketch of a $B^0 \rightarrow K^{*0} \nu \bar{\nu}$ decay.	168
10.3	First stage BDT response distributions for signal and background simulations.	170
10.4	First stage BDT response efficiencies for signal and background simulations.	170
10.5	Distributions of hemispherical energy differences in signal and background simulations.	171
10.6	Second stage BDT response distributions for signal and background simulations.	171
10.7	Sensitivity of BF measurements of $B^0 \rightarrow K^{*0} \nu \bar{\nu}$ and $B_s^0 \rightarrow \phi \nu \bar{\nu}$ decays at the FCC-ee.	173
10.8	Sensitivity of BF measurements of $B^0 \rightarrow K_S^0 \nu \bar{\nu}$ and $\Lambda_b^0 \rightarrow \Lambda \nu \bar{\nu}$ decays at the FCC-ee.	174
10.9	PID performance dependence of $B^0 \rightarrow K^{*0} \nu \bar{\nu}$ and $B_s^0 \rightarrow \phi \nu \bar{\nu}$ decay BF measurements at the FCC-ee.	175
10.10	Vertexing performance dependence of $B^0 \rightarrow K^{*0} \nu \bar{\nu}$ and $B_s^0 \rightarrow \phi \nu \bar{\nu}$ decay BF measurements at the FCC-ee.	175
10.11	Sensitivity of CKM factor extractions from $b \rightarrow s \nu \bar{\nu}$ BF measurements at the FCC-ee.	177
10.12	Sensitivity of Wilson coefficient extractions from $b \rightarrow s \nu \bar{\nu}$ BF measurements at the FCC-ee.	178
A.1	Comparison between the signal and background distributions for the BDT input variables used in the $D \rightarrow K_S^0 \pi^+ \pi^-$ DD topology for Run 1.	186

A.2	Comparison between the signal and background distributions for the BDT	
	input variables used in the $D \rightarrow K_S^0 \pi^+ \pi^-$ DD topology for Run 1.	187
A.3	Comparison between the signal and background distributions for the BDT	
	input variables used in the $D \rightarrow K_S^0 \pi^+ \pi^-$ DD topology for Run 2.	188
A.4	Comparison between the signal and background distributions for the BDT	
	input variables used in the $D \rightarrow K_S^0 \pi^+ \pi^-$ DD topology for Run 2.	189
A.5	Feature importance for the input variables to the BDT for the $D \rightarrow K_S^0 \pi^+ \pi^-$	
	DD decay.	190
C.1	Distributions of the input variables for the stage 1 BDT in signal and	
	inclusive background simulated data for the $B^0 \rightarrow K^{*0} \nu \bar{\nu}$ decay, in order	
	of feature importance. Figure one of three.	194
C.2	Distributions of the input variables for the stage 1 BDT in signal and	
	inclusive background simulated data for the $B^0 \rightarrow K^{*0} \nu \bar{\nu}$ decay, in order	
	of feature importance. Figure two of three.	195
C.3	Distributions of the input variables for the stage 1 BDT in signal and	
	inclusive background simulated data for the $B^0 \rightarrow K^{*0} \nu \bar{\nu}$ decay, in order	
	of feature importance. Figure three of three.	196
C.4	Distributions of the input variables for the stage 2 BDT in signal and	
	inclusive background simulated data for the $B^0 \rightarrow K^{*0} \nu \bar{\nu}$ decay, in order	
	of feature importance. Figure three of three.	198
C.5	Distributions of the input variables for the stage 2 BDT in signal and	
	inclusive background simulated data for the $B^0 \rightarrow K^{*0} \nu \bar{\nu}$ decay, in order	
	of feature importance. Figure three of three.	199
C.6	Distributions of the input variables for the stage 2 BDT in signal and	
	inclusive background simulated data for the $B^0 \rightarrow K^{*0} \nu \bar{\nu}$ decay, in order	
	of feature importance. Figure three of three.	200



# Acknowledgements

I have been incredibly lucky throughout my life to have had many people support me.

First I should thank my teachers at Churchdown Academy who did the best with what we had. To Phil Hayman and Jo Bagworth for pushing to start a further maths course and fighting to keep it going beyond the first year. To Stephen Bayliss and Juliet Jeffrey for being willing to teach it to just George and I. To Sam Rooksby and Jo Paxton for supporting the students against sub-standard teaching. To Julian Boon, and Richard Cooper especially, for pushing me to consider my potential as a physicist.

Thanks to my undergraduate tutor Erwin for his support and advice to *“fake it ’til you make it”*. To my summer supervisors Paul and Bora for giving me my first tastes of research. Many thanks to my Masters and PhD supervisor Matt for taking me on and his free rein approach to my supervision while providing constant support and opportunities. I know this could have been a far less enjoyable time without you. Thanks also to Tim for being an endless source of knowledge and excellent group leader. Without my analysis partner Yuya this analysis would have been an immense drag and an insurmountable amount of work. Thanks for saving me from fighting the mass fits. And to his supervisor Frédéric, and Luismi for all of their help and guidance with the analysis. Tom Latham deserves an honourable mention for all of his amplitude model knowledge and putting up with every Warwick LHCb students’ non-stop computing problems.

To all of my LHCb colleagues I’ve encountered over the years, many thanks for being such a welcoming and knowledgeable group. Particularly those in the B2OC working group for all their help and comments during the analysis, especially Sneha, Resmi, Jordy, Andy, Arnau, Innes, and Alex. Thanks to Chris and Eduardo for all I’ve learned about software from working with you, and to all the shift leaders that went out of their way to show me how to look after the detector.

To Yasmine, thanks for letting me join in on the FCC work and all your enthusiastic support, and MÉRIL and Olcyr for their theory discussions I could never quite follow. Thanks also to Stéphane for all his support with workshop and conference talks.

Thanks to all the friends I’ve made during the PhD for keeping the humanity in the physics. To Alex, Dan and Niall for all the lunches and beers. To Anja, Lorenzo, Matthew and Emir for the *interesting* conversations and office distractions. To the LTA lot for all

the late nights. To my friends at Warwick: Matthew, Eva, Roxanne, and the others for their friendship over these years. To Ryan, Jason, Becca, Freya, Meg, Molly, Haider and Alex for the many years of friendship.

Finally to my family. My brothers, Alex and Dylan, and sister Izzie for their love and pride. To Kaia who I can't wait to meet. To Grandpa for all your encouragement. To the rest of my family around the world for all their support. And to my parents without whom this would never have been possible, no thanks could be long enough.

*To Justin, Joe, Oma, Opa and Granny.*

*Hamba kahle.*





# Declaration

The work presented herein is a description of the first double Dalitz plane analysis of  $B^0 \rightarrow DK^+\pi^-$  decays at LHCb and the first feasibility study of  $b \rightarrow s\nu\bar{\nu}$  decays at the FCC-ee. My work can not be given the proper context without discussing the work of others. Parts of this thesis therefore explain work that is not entirely my own, but the product of close collaboration with others or the product of others entirely; this will be highlighted where relevant. This thesis has not been submitted in any form to this or any other university for another qualification. This work was supervised by Dr Matt Kenzie and Prof. Tim Gershon.

– Aidan Wiederhold



# Abstract

This thesis presents the first double Dalitz plane analysis of  $B^0 \rightarrow DK^+\pi^-$  decays at LHCb, utilising data collected by the LHCb experiment in Runs 1 and 2 of the LHC, corresponding to an integrated luminosity of  $9\text{ fb}^{-1}$ . This is the first ever use of this novel analysis method. In this analysis  $D$  refers to an admixture of the states  $D^0$  and  $\bar{D}^0$ , reconstructed in the final states  $D \rightarrow K_S^0 h^+ h^-$ ,  $D \rightarrow h^+ h^-$ , and  $D \rightarrow h^+ h^- h^+ h^-$ , where  $h$  is either a kaon or pion. The primary goal of this analysis is to measure the CKM angle  $\gamma$ , the central value of which is currently blinded. The statistical uncertainty is determined to be  $\sigma_\gamma = 6.8^\circ$  and the total systematic uncertainty is yet to be determined.

The penultimate chapter of this thesis presents the first feasibility study of measurements of the branching fractions of  $b \rightarrow s\nu\bar{\nu}$  decays at the FCC running electron-positron collisions at the  $Z$  pole center of mass energy. This study shows that for  $B^0 \rightarrow K^{*0}\nu\bar{\nu}$  and  $B_s^0 \rightarrow \phi\nu\bar{\nu}$  decays the branching fractions could be measured with a relative uncertainty of  $\mathcal{O}(1\%)$ , and  $\mathcal{O}(3\%)$  and  $\mathcal{O}(10\%)$  for  $B^0 \rightarrow K_S^0\nu\bar{\nu}$  and  $\Lambda_b^0 \rightarrow \Lambda\nu\bar{\nu}$  decays, respectively.

**Word count:** 28620



# 1 Introduction

*“The Big Bang created the Universe in one mad explosion  
... and it was so long ago now it’s probably best not to keep dredging it up.”*

---

Philomena Cunk

The observation of the Higgs boson in 2012 [1,2] marked the end of decades of work to observe all fundamental particles in what had become known as the Standard Model (SM) of particle physics. The SM has time and again proven itself as the most successful theory of the fundamental behaviour of the Universe but it is incomplete, to quite a significant degree. One issue is that the observed matter-antimatter asymmetry within the Universe is several orders of magnitude greater than that predicted by the SM [3]. This poses a question – how is it that we exist in a universe that is vastly dominated by matter?

There must be some as-yet-unknown additional source of asymmetry, physics beyond the SM (BSM), that allowed the Universe to evolve to its current state. Discovering the nature of this physics is a central goal of modern particle physics, and it is fraught with difficulty. To date the SM is consistent with all measurements of the fundamental behaviour of the Universe, some potential anomalies have been seen but are yet to convincingly exceed the typical  $5\sigma$  threshold for discovery. One can approach the search for new physics in two ways, direct and indirect measurements. For example one can search for evidence of dark matter candidates or supersymmetric particles produced at collider experiments, this is limited by the maximum collision energy one can achieve. Indirect measurements however allow one to probe for these and other BSM phenomena across a vast range of energies thanks to their virtual contributions to high order calculations. Precision measurements can be compared to SM predictions or other measurements to search for deviations caused by new physics.

The Large Hadron Collider (LHC) [4] has allowed for a vast array of direct and indirect searches, however it has known limitations and will eventually be decommissioned by CERN. Ideally a new collider at CERN would allow for precision measurements orders of magnitude more sensitive than is possible with current experiments and serve as a Higgs factory to allow for a thorough exploitation of this unique particle. One such candidate is

the Future Circular Collider (FCC) which is proposed to first run as an electron-positron collider (FCC-ee) and subsequently a hadron collider (FCC-hh) [5].

The remainder of this thesis presents the results of a precision flavour measurement at the Large Hadron Collider beauty (LHCb) experiment, the first double Dalitz plane analysis of  $B^0 \rightarrow DK^+\pi^-$  decays, and the first feasibility study of  $b \rightarrow s\nu\bar{\nu}$  decays at the FCC-ee. It is organised as follows. A short introduction to the theoretical physics on which this work relies is given in Chapter 2. This introduces the SM parameter  $\gamma$ , a measurement of which is the primary goal of the LHCb analysis. The value of  $\gamma$  measured is currently blinded as the analysis is not yet complete. The origin of the data used in this analysis is presented in Chapter 3. Chapters 4 to 9 explain the LHCb analysis in detail starting with Chapter 4 which explains the overall methodology of the analysis. Chapter 5 explains the full selection applied to the data to obtain a high-purity data sample. Chapter 6 explains the methods used to reweight simulated data to model the distribution of background sources in LHCb data. Chapter 7 describes the invariant mass fits which are used to estimate the total presence of backgrounds within the fully selected data sample obtained in Chapter 5, using the results of Chapter 6. Chapter 8 then explains how all of the work presented in Chapters 5 to 7 is combined to allow for an extraction of  $\gamma$ . Chapter 9 completes the explanation of this analysis with a description of the methods required to determine the systematic uncertainties associated with the obtained measurements. Chapter 10 discusses the current status of measurements of  $b \rightarrow s\nu\bar{\nu}$  decays, the motivation for their measurement at the FCC-ee and the expected sensitivity one could obtain under the proposed nominal conditions. Chapter 11 concludes with a discussion of the significance of the work presented and the future developments it motivates.

## 2 Theory

*“Physicist and professional tongue model Albert Einstein came up with his theory of relativity,  $E$  equals  $Mc^2$ , which to this day nobody understands. I’m only mentioning it because it turns out to be important later.”*

---

Philomena Cunk

This chapter presents the theoretical background necessary to put the experimental contributions of this thesis into their proper context. It features a concise explanation of the weak mixing of quarks, introduces the Cabibbo-Kobayashi-Maskawa (CKM) matrix and summarises the current status of measurements of CKM parameters. The definition of Dalitz planes is given and finally the basics of weak effective field theories are presented to introduce the topic of “electroweak penguin” decays.

### 2.1 The electroweak interaction and $CP$ violation

Symmetries are fundamental to our understanding of particle physics and the phenomena we study. For a given symmetry the predictions one can make about a system are invariant under the operation of that symmetry. Noether’s theorem states that any symmetry of a continuous Lagrangian of a system corresponds to a conservation law, for example a system with translational symmetry conserves linear momentum [6]. Three fundamental discrete symmetry operations of the Universe are charge conjugation ( $C$ ), parity ( $P$ ) and time reversal ( $T$ ). The  $C$  and  $P$  symmetries are preserved by the strong interaction however the electroweak interaction exhibits a maximal violation of them. For example  $W$  bosons couple only to left-handed matter and right-handed antimatter [7]. One can also consider the symmetries corresponding to a simultaneous application of these such as simultaneous time and parity reversal. The combination of all three,  $CPT$ , is required to be conserved by any Lorentz invariant field theory [8]. The electroweak interaction violates the symmetry of the simultaneous combination  $CP$ , this is known as  $CP$  violation. Under  $CP$  a particle is transformed to its antiparticle state, *i.e.* the electroweak interactions of matter and antimatter exhibit slightly different physics.  $CP$  violation was first observed



in 1964 in the decay of neutral kaons and has been studied by a variety of experiments ever since [9].

### 2.1.1 Types of $CP$ violation

$CP$  violation can be classified into three different categories with the following definitions [7].

#### $CP$ violation in decay

For the decays of a hadron  $\bar{H}$  to a final state  $f$  with amplitude  $\bar{A}_f$  and  $H$  to a final state  $\bar{f}$  with amplitude  $A_{\bar{f}}$ ,  $CP$  violation is present if  $|\bar{A}_f/A_f| \neq 1$ . The asymmetry can be quantified as

$$\mathcal{A}_{(\bar{f})} = \frac{\Gamma(\bar{H} \rightarrow \bar{f}) - \Gamma(H \rightarrow f)}{\Gamma(\bar{H} \rightarrow \bar{f}) + \Gamma(H \rightarrow f)} = \frac{|\bar{A}_f/A_f|^2 - 1}{|\bar{A}_f/A_f|^2 + 1}. \quad (2.1)$$

If one writes

$$A_f = |a_1|e^{i(\delta_1+\phi_1)} + |a_2|e^{i(\delta_2+\phi_2)}, \quad (2.2)$$

where the amplitude  $A_f$  has two contributions with the amplitudes  $a_i$ , strong phases  $\delta_i$  and weak phases  $\phi_i$ . It can be shown that

$$\mathcal{A}_f \sim |a_1 a_2| \sin(\delta_2 - \delta_1) \sin(\phi_2 - \phi_1), \quad (2.3)$$

*i.e.* the observation of a  $CP$  asymmetry requires both a non-zero strong phase and weak phase difference between the contributing amplitudes. This is the kind of  $CP$  violation that is exhibited by the  $B^0 \rightarrow DK^+\pi^-$  decay, where  $D$  is an admixture of  $D^0$  and  $\bar{D}^0$ , and is further discussed in Chapter 4.

#### $CP$ violation in mixing

This occurs when the probability per unit time of oscillation between a matter and antimatter state is greater in a given “direction”, *i.e.*  $P(H \rightarrow \bar{H}) \neq P(\bar{H} \rightarrow H)$ .

This requires that  $|q/p| \neq 1$ , where  $q$  and  $p$  are the proportions with which the flavour eigenstates contribute to the mass eigenstates.

#### $CP$ violation in interference between a decay with and without mixing

This occurs when a final state is commonly accessible by corresponding matter and antimatter states such that the amplitude depends both on the direct decay,  $H \rightarrow f$ , and the indirect decay,  $H \rightarrow \bar{H} \rightarrow f$ .

This requires that

$$\arg(\lambda_f) + \arg(\lambda_{\bar{f}}) \neq 0, \quad \text{where} \quad \lambda_f \equiv \frac{q}{p} \frac{\bar{A}_f}{A_f}. \quad (2.4)$$

### 2.1.2 CKM and the origin of CP violation in the SM

The Lagrangian of the charged-current weak interaction can be written as

$$\mathcal{L}_q = -\frac{g}{\sqrt{2}} W_\mu^- \bar{u}_L^j \gamma^\mu d_L^j - \frac{g}{\sqrt{2}} W_\mu^+ \bar{d}_L^j \gamma^\mu u_L^j, \quad (2.5)$$

where  $u_L^j$  ( $d_L^j$ ) are the flavour eigenstates of the up-type (down-type) quarks,  $g$  is a coupling constant and  $W_\mu^\pm$  represents the charged  $W$  boson.

To write this in terms of the quark masses one must transform Eq. (2.5) from the flavour basis to the mass basis. This is achieved by the unitary transformations

$$u_L^j \mapsto u_L^{j'} = U_L u_L^j, \quad (2.6)$$

$$d_L^j \mapsto d_L^{j'} = D_L d_L^j. \quad (2.7)$$

It therefore follows that

$$\mathcal{L}_q = -\frac{g}{\sqrt{2}} W_\mu^- \bar{u}_L^{j'} U_L \gamma^\mu D_L^\dagger d_L^{j'} - \frac{g}{\sqrt{2}} W_\mu^+ \bar{d}_L^{j'} D_L \gamma^\mu U_L^\dagger u_L^{j'}, \quad (2.8)$$

from which one can infer that the strength of the weak-interaction of quarks is proportional to  $U_L D_L^\dagger$  ( $D_L U_L^\dagger$ ) in the case of  $d \rightarrow W^- u$  ( $u \rightarrow W^+ d$ ), where  $u$  and  $d$  refer to all generations of the up and down type quarks respectively. This is referred to as the CKM matrix [10, 11]

$$V_{\text{CKM}} \equiv \begin{pmatrix} V_{ud} & V_{us} & V_{ub} \\ V_{cd} & V_{cs} & V_{cb} \\ V_{td} & V_{ts} & V_{tb} \end{pmatrix} = U_L D_L^\dagger = (D_L U_L^\dagger)^\dagger. \quad (2.9)$$

In general a complex  $3 \times 3$  matrix has 18 degrees of freedom. Unitarity reduces this to nine since  $V_{\text{CKM}}^\dagger V_{\text{CKM}} = 1$  yields nine relations of the form

$$V_{i\alpha} V_{j\alpha}^* + V_{i\beta} V_{j\beta}^* + V_{i\gamma} V_{j\gamma}^* = \delta_{ij}. \quad (2.10)$$

Of these remaining degrees of freedom, five can be absorbed by arbitrary rephasing of the quark fields. Therefore the CKM matrix can be represented by four real independent parameters. One standard choice of parameterisation is in terms of three mixing angles,

$\theta_{ij}$  and one complex phase,  $\delta_{CP}$  [12]. This can be written as

$$V_{\text{CKM}} = \begin{pmatrix} 1 & 0 & 0 \\ 0 & c_{23} & s_{23} \\ 0 & -s_{23} & c_{23} \end{pmatrix} \begin{pmatrix} c_{13} & 0 & s_{13}e^{-i\delta_{CP}} \\ 0 & 1 & 0 \\ -s_{13}e^{i\delta_{CP}} & 0 & c_{13} \end{pmatrix} \begin{pmatrix} c_{12} & s_{12} & 0 \\ -s_{12} & c_{12} & 0 \\ 0 & 0 & 1 \end{pmatrix}, \quad (2.11)$$

where  $s_{ij} \equiv \sin(\theta_{ij})$  and  $c_{ij} \equiv \cos(\theta_{ij})$ . This clearly illustrates the presence of  $CP$  violation in weak mixing since if one considers Eq. (2.8), if this complex phase,  $\delta_{CP}$ , enters a decay amplitude as  $A = |A|e^{i(\delta+\delta_{CP})}$  then it enters the  $CP$  conjugate decay amplitude as  $A = |A|e^{i(\delta-\delta_{CP})}$ , where  $\delta$  is a  $CP$  conserving phase arising from other SM effects, which is typically referred to as a strong-phase [7]. Another useful parameterisation is the Wolfenstein parameterisation [13]

$$V_{\text{CKM}} = \begin{pmatrix} 1 - \lambda^2/2 & \lambda & A\lambda^3(\rho - i\eta) \\ -\lambda & 1 - \lambda^2/2 & A\lambda^2 \\ A\lambda^3(1 - \rho - i\eta) & -A\lambda^2 & 1 \end{pmatrix} + \mathcal{O}(\lambda^4), \quad (2.12)$$

where  $A, \lambda, \rho, \eta$  are real valued parameters whose values according to experiment are  $A \sim 0.810$ ,  $\lambda \sim 0.22548$ ,  $\rho \sim 0.149$ ,  $\eta \sim 0.352$  [14]. Given that  $\mathcal{O}(A) = 1$  and  $\rho$  and  $\eta$  appear only in the off-diagonal corner elements one can consider the structure of the matrix in orders of  $\lambda$  from which a striking pattern can be observed. Why the CKM matrix takes this exact form is one of the many puzzles of modern flavour physics which it is hoped that measurements at the LHC, and perhaps the FCC, will help to answer. Equation (2.10) reveals six relations in which the sum of three complex numbers is 0, *i.e.* the relations can be represented by triangles in the complex plane. These are known as unitarity triangles, one of the most famous of which is the “db” triangle defined by

$$V_{ud}V_{ub}^* + V_{cd}V_{cb}^* + V_{td}V_{tb}^* = 0 \quad (2.13)$$

and shown in Fig. 2.1. Note that the sides of the triangle are not each term of Eq. (2.13) but are scaled by  $1/(V_{cd}V_{cb}^*)$  such that the vertices are exactly  $(0,0)$ ,  $(1,0)$  and  $(\bar{\rho}, \bar{\eta})$ . A measurement of its angle  $\gamma$  is the central focus of this thesis.

The parameters  $\bar{\rho}$  and  $\bar{\eta}$  are defined according to

$$A\lambda^3(\rho + i\eta) = \frac{A\lambda^3(\bar{\rho} + i\bar{\eta})\sqrt{1 - A^2\lambda^4}}{\sqrt{1 - \lambda^2}[1 - A^2\lambda^4(\bar{\rho} + i\bar{\eta})]}, \quad (2.14)$$

such that  $(\bar{\rho} + i\bar{\eta}) = -(V_{ud}V_{ub}^*)/(V_{cd}V_{cb}^*)$  regardless of the chosen phase convention and so that the CKM matrix is unitary in all orders of  $\lambda$  if written in terms of  $\bar{\rho}, \bar{\eta}$  [7].

The non-zero area of these triangles is another consequence of the complex phase of the

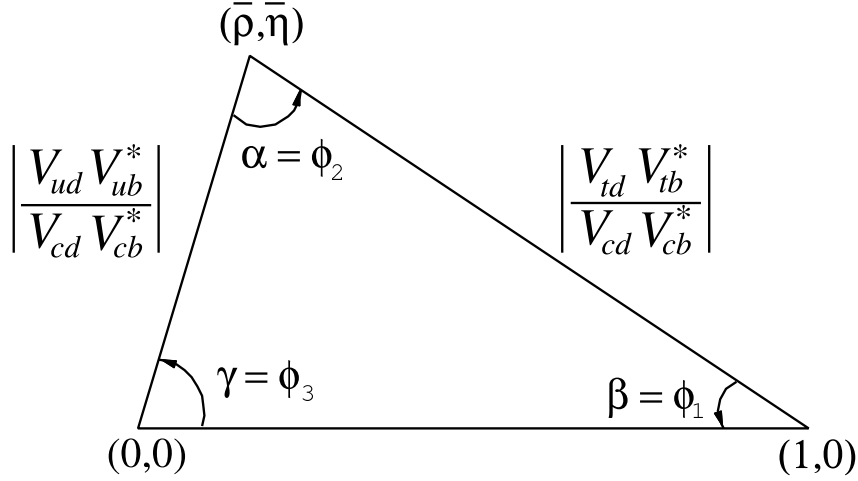


Figure 2.1: The rescaled “db” unitarity triangle which is commonly used in measurements of  $CP$  violation in  $B$  hadron decays. From Ref. [7].

CKM matrix and is proportional to the total  $CP$  violation in the quark sector predicted by the SM. All of the unitarity triangles, when not rescaled, have the same area,  $J/2$ , where  $J$  is the Jarlskog invariant [15]. This is a phase-convention-independent measure of  $CP$  violation defined as

$$\text{Im} [V_{ij} V_{kl} V_{il}^* V_{kj}^*] = J \sum_{m,n} \epsilon_{ikm} \epsilon_{jln}. \quad (2.15)$$

where  $\epsilon_{ijk}$  is the Levi-Civita symbol. Predictions for the matter-antimatter symmetry based on the experimentally observed value of this quantity compared to cosmological observations show that the  $CP$  violation in the SM is several orders of magnitude too small to account for the observed matter-antimatter asymmetry in the Universe [3]. This is one of many sources of evidence that motivate the search for BSM physics.

Since the CKM elements are fundamental parameters of the SM there is no prediction of the exact dimensions of the unitarity triangles and therefore one goal of modern flavour physics is to perform as many measurements related to them as possible to overconstrain their determination. This allows for comparisons between the various angles and side lengths via direct and indirect determinations of each to search for any inconsistencies which may point to signs of BSM physics. For example, measurements resulting in an open unitarity triangle could suggest the existence of a fourth generation of quarks. An example of such a comparison performed by the CKMFitter group is shown in Fig. 2.2.

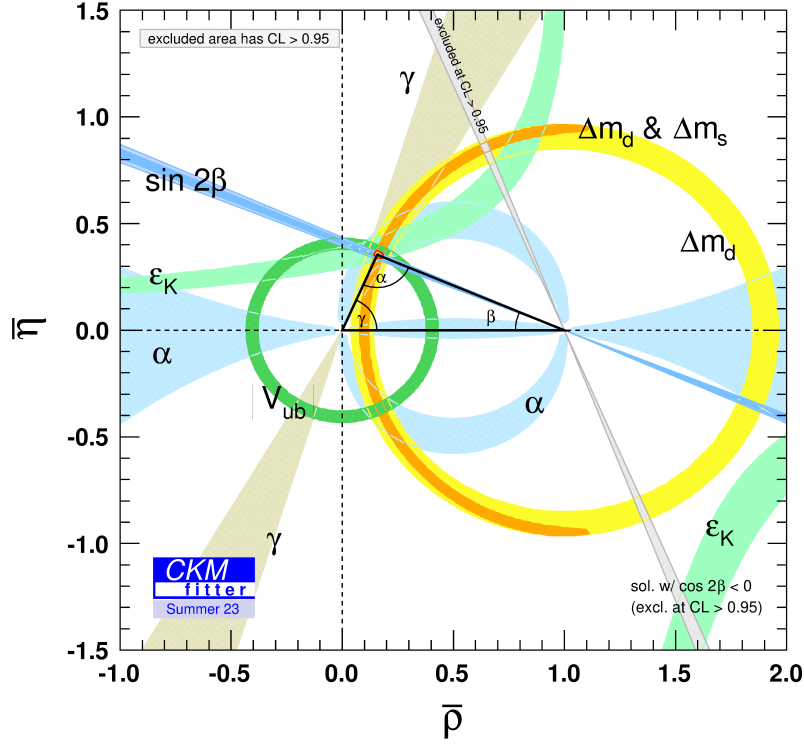


Figure 2.2: Fit of the “db” unitarity triangle to CKM measurements. From Ref. [14]

## 2.2 The CKM angles

The analysis described in this thesis, the first double Dalitz plane analysis of  $B^0 \rightarrow DK^+\pi^-$  decays at LHCb, is a novel analysis which provides a direct measurement of the CKM angle  $\gamma$ . Amongst the other CKM angles of the “db” triangle,  $\alpha$  and  $\beta$ ,  $\gamma$  is unique in that it is accessible via tree-level only decays. The consequence of this is that direct measurements are associated with relatively small theoretical uncertainties [16] making  $\gamma$  an ideal SM benchmark parameter against which other parameters can be compared to search for BSM effects. Measurements of the other angles rely on higher order processes for which BSM effects could enter the loop processes and break unitarity under the SM hypothesis. Until recently  $\gamma$  was the least precisely measured of these angles; the uncertainty has fallen below that of  $\alpha$  but is yet to reach sub-degree uncertainty like  $\beta$ . If one compares the value of  $\gamma$  in world averages obtained indirectly by fitting together other CKM parameters,  $\gamma = (66.3^{+0.7}_{-1.9})^\circ$ , and from world averages of direct measurements,  $\gamma = (65.9^{+3.3}_{-3.5})^\circ$ , the current sensitivity is not sufficient to reveal possible discrepancies [14]. In general the significance with which fits such as that of Fig. 2.2 can constrain contributions from BSM is limited by the direct measurements of the CKM angles. It is therefore a priority of LHCb to perform as many precise measurements of CKM parameters as possible. In

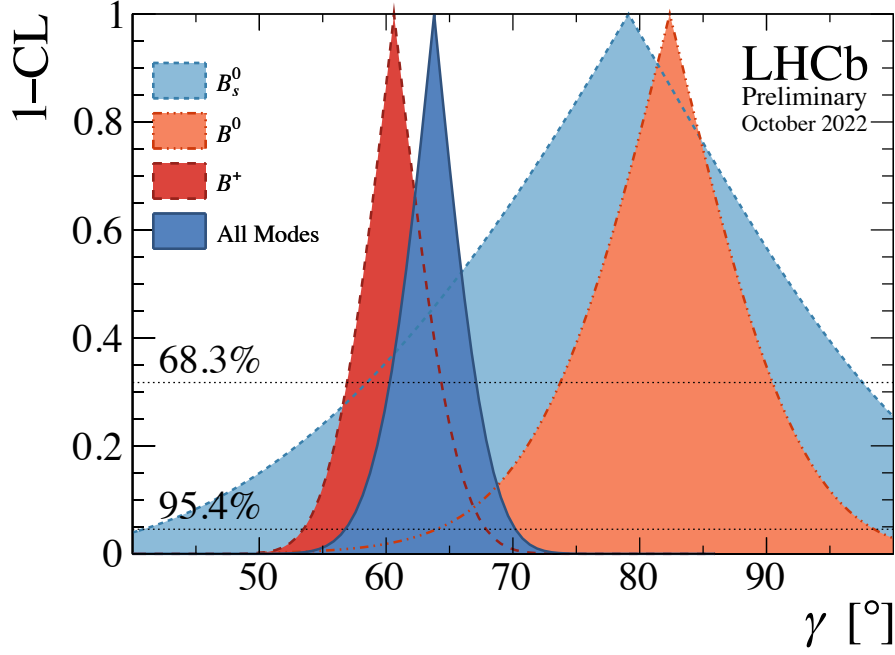


Figure 2.3: One dimensional profile likelihood scans of the  $1 - \text{CL}$  (confidence level) for  $\gamma$  obtained by LHCb in the simultaneous combination of beauty and charm measurements for all beauty measurements and per- $B$  species. From Ref. [17].

the case of  $\gamma$ , such measurements are all combined together to obtain a single LHCb determination of  $\gamma$ . The latest combination from LHCb, performed in 2022, obtained a value of  $\gamma = (63.8^{+3.5}_{-3.7})^\circ$  [17]. The  $1 - \text{CL}$  for  $\gamma$  is shown in Fig. 2.3. Currently the measurements from  $B^+$  mesons lead the sensitivity to  $\gamma$  and have a small tension with those from neutral  $B$  mesons. However given recent measurements at LHCb since this combination it is expected that the measurements from  $B^0$  mesons will become more competitive with that of  $B^+$  mesons and with a reduced tension between them in future combinations [18, 19].

The values of the CKM angles from world averages of direct measurements are shown in Table 2.1, the sum of which is  $(175 \pm 5)^\circ$  and is consistent with the expectation of  $180^\circ$  in the SM.

CKM angle	Value
$\alpha$	$(86.2^{+3.9}_{-3.5})^\circ$
$\beta$	$(22.5^{+0.5}_{-0.4})^\circ$
$\gamma$	$(65.9^{+3.3}_{-3.5})^\circ$

Table 2.1: Values of the CKM angles from world averages of direct measurements [14].

## 2.3 Multi-body decay kinematics

The decay of a particle to a multi-body final state can in general occur via a number of different intermediate resonances, each of which can be associated with its own amplitude dependent on the phase space of the decay. To consider the dynamics of these decays and their resonant amplitudes it is required to first introduce the Dalitz plane [20]. The “Dalitz coordinate” of a pair of particles  $i, j$ , *i.e.* the pairwise invariant mass squared of two particles, is defined as

$$m_{ij}^2 \equiv (p_i^\mu + p_j^\mu)(p_{\mu,i} + p_{\mu,j}). \quad (2.16)$$

From energy and momentum conservation one can then write for a decay  $P \rightarrow c_1 c_2 c_3$

$$m_P^2 + m_1^2 + m_2^2 + m_3^2 = m_{12}^2 + m_{13}^2 + m_{23}^2, \quad (2.17)$$

where  $m_i$  ( $m_P$ ) is the mass of  $c_i$  ( $P$ ). Given the masses of these particles are known, Eq. (2.17) defines the kinematic phase space of the decay with two degrees of freedom. That is to say that if one considers two Dalitz coordinates, for which the common convention is to use  $m_{13}^2$  and  $m_{23}^2$ , there is a finite physically allowed plane of  $(m_{13}^2, m_{23}^2)$  values that this decay can result in. An example in terms of arbitrary particles is shown in Fig. 2.4, which illustrates how the boundary of the plane depends on the relations between the various particle masses. In particular it is useful to note that  $(m_{ij}^2)_{\max} = (M - m_k)^2$  and  $(m_{ij}^2)_{\min} = (m_i + m_j)^2$  where  $i, j, k$  index each child uniquely.

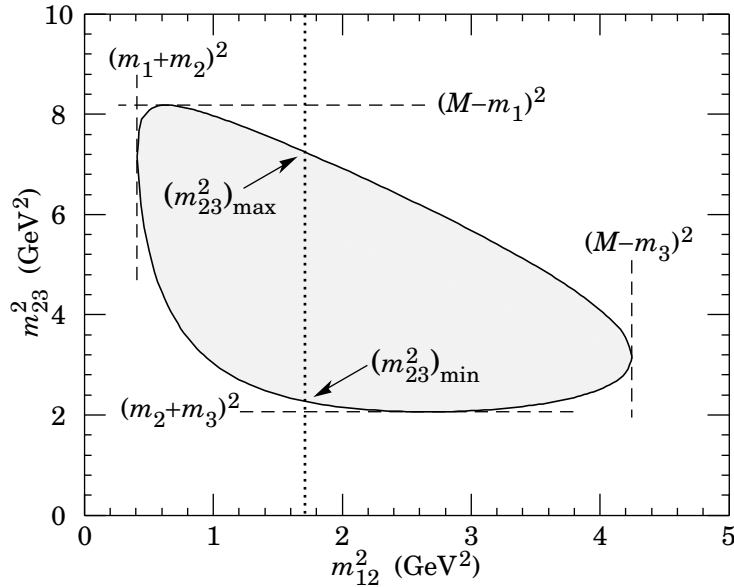


Figure 2.4: A Dalitz plane associated with a decay  $P \rightarrow c_1 c_2 c_3$  where  $M$  is the mass of  $P$  and  $m_i$  is the mass of  $c_i$  [7].

The differential decay rate is

$$d\Gamma = \frac{1}{(2\pi)^3} \frac{1}{32m_P^3} |\mathcal{A}|^2 dm_{13}^2 dm_{23}^2, \quad (2.18)$$

where  $\mathcal{A}$  is the total decay amplitude [21]. If  $\mathcal{A}$  is independent of the Dalitz coordinates then the distribution of decays across the Dalitz plane will be uniform. However, in general this is not the case due to the presence of intermediate resonances and their interference in 3-body decays. Interference effects between the amplitudes of each resonance can be observed in regions of phase space where resonances coincide. For example one could consider a decay  $B_s^0 \rightarrow \bar{D}^0 \bar{K}^*(892)^0, \bar{K}^*(892)^0 \rightarrow K^-\pi^+$ . The invariant mass of the combined kaon and pion 4-momenta would be consistent with that of the  $\bar{K}^*(892)^0$  resonance, therefore repeated measurement of such a decay would not result in a uniform distribution across the  $B_s^0 \rightarrow DK^-\pi^+$  Dalitz plane but rather a band of points across the Dalitz plane. In the case of non-spin-0 resonances the amplitude density of the resonance would vary as a function of the helicity angle between the corresponding decay children [21]. This variation is described by functions of the form of Legendre polynomials of the cosine of the helicity angle,  $P_L(\cos(\theta))$ , this results in nodes/gaps in the resonance lineshape. Figure 2.5 shows the lineshapes of a spin-1 resonance (yellow) and two spin-2 resonances (red, blue) in a mock  $B_s^0 \rightarrow DK^-\pi^+$  decay model.

The total amplitude of a decay can be modelled in terms of its resonances using the isobar model formalism [22–24]. The amplitude at a given Dalitz coordinate can therefore be defined as

$$\mathcal{A}(m_{13}^2, m_{23}^2) = \sum_{j=1}^N c_j F_j(m_{13}^2, m_{23}^2), \quad (2.19)$$

where  $j$  is an index associated with each resonance,  $c_j$  is a complex coefficient and  $F_j$  describes the resonance dynamics. Although this is not a complete analytical representation of the decay amplitude it is a useful way to think about the resonant structure of a decay. The analysis presented in this thesis is model-independent, however in Section 6.2.1 the isobar formalism is used to model the Dalitz distribution backgrounds in LHCb data. These models are created with the **Laura++** software package which is developed for the modelling of spin-0 3-body decays [21].

While it is often useful to envision multi-body kinematics in terms of the conventional Dalitz plane there are often times when another description is more practical. For instance for a generalised definition of a multi-body phase space it is convenient to be able to map any conventional Dalitz plane into a unit square. The resulting Dalitz plane is referred to as a “square Dalitz plane”. Given a decay  $P \rightarrow c_1 c_2 c_3$  the square Dalitz plane coordinates,



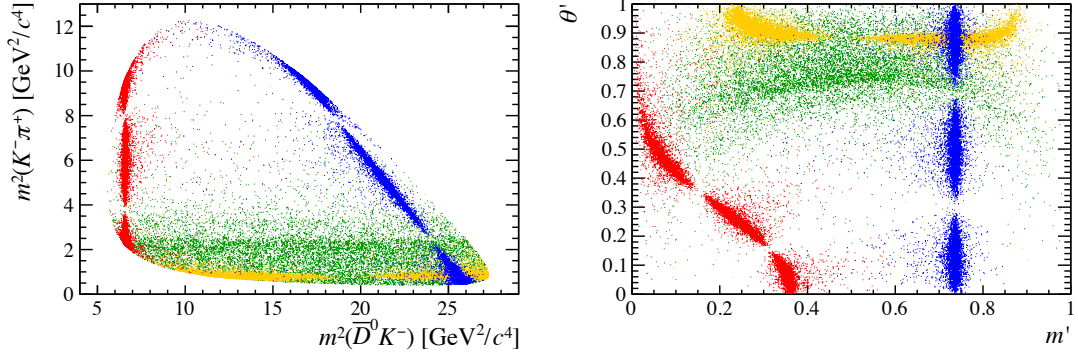


Figure 2.5: A simple example of a model for a  $B_s^0 \rightarrow DK^- \pi^+$  decay in both the conventional (left) and square (right) Dalitz plane parameterisations. This shows a  $D_{s2}^*(2573)^-$  resonance (red), a  $\bar{K}^*(892)^0$  resonance (yellow), a  $D_2^*(2460)^+$  resonance (blue) and an S-wave contribution (green). From Ref. [21].

$(m', \theta')$ , are defined as

$$m' = \frac{1}{\pi} \arccos \left( 2 \frac{m_{12} - m_{12}^{\min}}{m_{12}^{\max} - m_{12}^{\min}} - 1 \right) \quad \text{and} \quad \theta' = \frac{1}{\pi} \theta_{12}, \quad (2.20)$$

where  $\theta_{12}$  is the angle between the momenta of  $c_1$  and  $c_3$  in the rest frame of  $c_1 c_2$  [21]. This parameterisation is particularly useful when generating simulations, or using discretised mappings of the phase space as is seen in Sections 6.2.2 and 6.2.3. Figure 2.5 illustrates how resonances in a conventional Dalitz plot map to a square Dalitz parameterisation.

## 2.4 Electroweak penguin decays

The topics covered in the previous sections of this chapter are sufficient to understand the double Dalitz plane analysis which is the topic of the majority of this thesis, however Chapter 10 discusses a study performed to estimate the feasibility of measurements of  $b \rightarrow s \nu \bar{\nu}$  decays at the FCC-ee which requires some additional theoretical context. These decays belong to a class of decays known colloquially as “electroweak penguin decays”, which are flavour changing neutral current (FCNC) decays [25]. FCNCs are forbidden at tree-level in the SM since the only known mechanism that can change flavour at tree-level is the charged electroweak interaction. Therefore the simplest Feynman diagrams for a  $b \rightarrow s \nu \bar{\nu}$  decay are those shown in Fig. 2.6. The requirement of loops for the decay suppresses the probability of such a decay due to the additional EW factors, such as the dependence on the CKM elements, that enter the amplitude. The GIM mechanism further suppresses these decays [26], *i.e.* the existence of multiple up-type quarks with differing masses results in amplitudes that contribute to the total amplitude of the decay with opposite signs resulting in a lower amplitude. The small branching fractions of

these decays is a double-edged sword. Due to the small expected values of the branching fractions (BFs), detailed study of these decays can be a powerful way to probe for signs of BSM physics as any unexpected contributions to their amplitudes could result in relatively large deviations from the SM BFs. However, the rarer a decay is the harder it is for experiments to produce significant datasets with which to measure the BFs and other observables of interest.

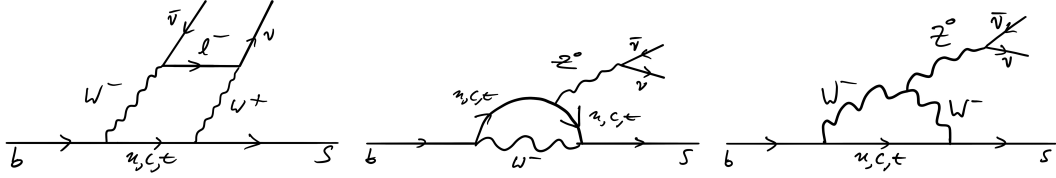


Figure 2.6: The simplest Feynman diagrams for a  $b \rightarrow s\nu\bar{\nu}$  decay.

In the study of such decays a weak effective field theory (WEFT) approach is used to factorise out the short-distance and long-distance phenomena. The short-distance phenomena are the electroweak interactions within the decay and the long-distance phenomena are the quantum chromodynamic (QCD) interactions between the initial and final state hadrons. The use of WEFTs therefore allows theorists to handle the calculations of these phenomena separately, which greatly simplifies their methods of prediction. The electroweak parts can be handled with perturbative methods and the QCD parts can be handled with lattice QCD methods.

In the case of  $b \rightarrow s\nu\bar{\nu}$  decays the WEFT Hamiltonian, which accounts for the short-distance processes, can be written as

$$\mathcal{H}_{\text{eff}} = -\frac{4G_F}{\sqrt{2}}\lambda_t \sum_i \mathcal{C}_i \mathcal{O}_i + \text{h.c.}, \quad (2.21)$$

where  $G_F$  is the Fermi constant,  $\lambda_t = V_{tb}V_{ts}^*$  is a CKM factor [27].  $\mathcal{O}_i$  is a WEFT operator, each of which correspond to a different physics process that contributes to the  $b \rightarrow s\nu\bar{\nu}$  decay.  $\mathcal{C}_i$  is the Wilson coefficient associated with  $\mathcal{O}_i$ , this encodes how much the process defined by  $\mathcal{O}_i$  contributes to the total Hamiltonian.

In the SM the only non-zero Wilson coefficient for Eq. (2.21),  $\mathcal{C}_L$ , corresponds to

$$\mathcal{O}_L = \frac{e^2}{16\pi^2} (\bar{s}\gamma_\mu P_L b) (\bar{\nu}\gamma^\mu (1 - \gamma_5) \nu), \quad (2.22)$$

With next to leading order (NLO) QCD and next to next leading order (NNLO) electroweak contributions accounted for  $\mathcal{C}_L$  can be determined to be  $\mathcal{C}_L = -6.32 \pm 0.07$  [27].

The study in Section 10.3 focuses on  $B^0 \rightarrow K_S^0 \nu\bar{\nu}$ ,  $B^0 \rightarrow K^{*0} \nu\bar{\nu}$ ,  $B_s^0 \rightarrow \phi \nu\bar{\nu}$  and  $\Lambda_b^0 \rightarrow \Lambda \nu\bar{\nu}$  decays, the decay rates of which can be written in the SM as [28, 29]

$$\frac{d\mathcal{B}(B^0 \rightarrow K_S^0 \nu \bar{\nu})_{\text{SM}}}{dq^2} = 3 \tau_{B^0} |N_{B^0}|^2 |C_L^{\text{SM}}|^2 |\lambda_t|^2 \rho_+^{K_S^0}, \quad (2.23)$$

$$\frac{d\mathcal{B}(B^0 \rightarrow K^{*0} \nu \bar{\nu})_{\text{SM}}}{dq^2} = 3 \tau_{B^0} |N_{B^0}|^2 |C_L^{\text{SM}}|^2 |\lambda_t|^2 (\rho_{A_1}^{K^{*0}} + \rho_{A_{12}}^{K^{*0}} + \rho_V^{K^{*0}}), \quad (2.24)$$

$$\frac{d\mathcal{B}(B_s^0 \rightarrow \phi \nu \bar{\nu})_{\text{SM}}}{dq^2} = 3 \tau_{B_s^0} |N_{B_s^0}|^2 |C_L^{\text{SM}}|^2 |\lambda_t|^2 (\rho_{A_1}^\phi + \rho_{A_{12}}^\phi + \rho_V^\phi), \quad (2.25)$$

$$\frac{d\mathcal{B}(\Lambda_b^0 \rightarrow \Lambda \nu \bar{\nu})_{\text{SM}}}{dq^2} = 3 \tau_{\Lambda_b^0} |N_{\Lambda_b^0}|^2 |C_L^{\text{SM}}|^2 |\lambda_t|^2 (\rho_{f_\perp^A}^\Lambda + \rho_{f_\perp^A}^\Lambda + \rho_{f_0^A}^\Lambda + \rho_{f_0^A}^\Lambda), \quad (2.26)$$

where

$$N_{B_q} = \frac{G_F \alpha_{\text{em}}}{16\pi^2} \sqrt{\frac{m_{B_q}}{3\pi}}. \quad (2.27)$$

and  $\rho_i \equiv \rho_i(q^2)$  are functions of the hadronic form factors, which account for the long-distance processes. Further details of these, namely their leading uncertainties, and  $b \rightarrow s \nu \bar{\nu}$  phenomenology can be found in Ref. [27]. Table 2.2 shows the current SM values of the BF's for the decays of interest which are used as inputs to the feasibility study in Section 10.3. The two main sources of uncertainty in the prediction of the BF's are the CKM factor and the hadronic form factors.

Decay mode	$\mathcal{B}/ \lambda_t ^2 [10^{-3}]$	$\mathcal{B} [10^{-6}]$	Source
$B^0 \rightarrow K_S^0 \nu \bar{\nu}$	$1.33 \pm 0.04$	$2.02 \pm 0.12$	Ref. [30, 31]
$B^0 \rightarrow K^{*0} \nu \bar{\nu}$	$5.13 \pm 0.51$	$7.93 \pm 0.89$	Ref. [30]
$B_s^0 \rightarrow \phi \nu \bar{\nu}$	$6.31 \pm 0.67$	$9.74 \pm 1.15$	Ref. [30]
$\Lambda_b^0 \rightarrow \Lambda \nu \bar{\nu}$	$5.55 \pm 0.56$	$8.57 \pm 0.97$	Ref. [32]

Table 2.2: Current SM prediction for integrated decay rates summed over the three neutrino flavors. In the second column the exclusive determination of  $|V_{cb}| = (40.0 \pm 1.0) \times 10^{-3}$  is used, which yields  $|\lambda_t| = (39.3 \pm 1.0) \times 10^{-3}$ , as described in Ref. [27].

## 2.5 Summary

In order to understand the importance of the analysis presented in this thesis it is necessary to derive the CKM matrix from the EW Lagrangian and explain the origin of  $CP$  violation within the SM. This led to a discussion of the Wolfenstein parameterisation of the CKM matrix, the definition of unitarity triangles and the CKM angle  $\gamma$ . The current status of CKM angle measurements and the motivation for further developments was discussed.

Finally the basics of multi-body kinematics and Dalitz planes are summarised. To prepare for the discussion of the FCC-ee feasibility study detailed in Chapter [10](#) it was necessary to explain the basics of electroweak penguins.



# 3 Data acquisition and processing at LHCb

*“Can you explain how they work without resorting to science?  
... I think they run on belief.”*

---

Philomena Cunk

The analysis presented in this thesis was performed using data collected by the LHC beauty (LHCb) experiment, which receives proton-proton collisions from the LHC, at CERN. This data was collected during the first two data taking periods of the LHC, Runs 1 and 2, which occurred during the years 2011–2012 and 2015–2018. Since my work in LHCb can be described entirely in the context of the LHC and LHCb as they were configured during Runs 1 and 2 I will not make reference to the upgrades made to LHCb for Runs 3 and 4 of the LHC.

## 3.1 The Large Hadron Collider

The LHC is a circular collider with a circumference of 26.7km [4]. It is located in a tunnel  $\sim 100\text{m}$  underground in which the Large Electron Positron (LEP) collider was originally located. A schematic of the LHC is shown in Fig. 3.1. Proton-proton collisions are delivered to four collision points located around the ring, at one of which the LHCb experiment is located. The collisions are achieved by accelerating two counter-rotating beams in separate rings that intersect at each collision point. The protons for the beams are obtained from ionised hydrogen and first accelerated in the LINAC2 linear accelerator. They then proceed through a number of stages of acceleration in circular accelerators of increasing size until they are at a sufficient energy, 450 GeV, for injection into the LHC. They are then accelerated to their nominal collision energy of 3.5 TeV, 4 TeV and 6.5 TeV per beam, where the different energies correspond to the years 2011, 2012 and 2015–2018, respectively. The period of time for which the LHC has beams present is known as a “fill”, and in nominal conditions can last for several hours. The radio frequency (RF) system

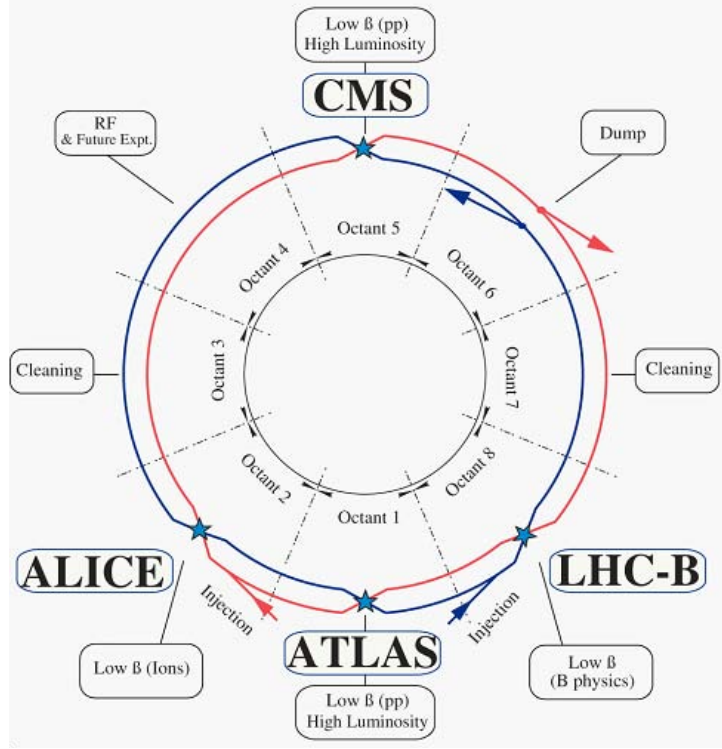


Figure 3.1: Schematic of the LHC layout, from Ref. [4].

located in the 4th octant of the LHC is used to accelerate the beams, and magnets located around the LHC control the paths of the beams. As shown in Fig. 3.2 the two beam pipes are encased in a single cold mass. This results in a complicated magnet structure but allows for a lower overall cost for the magnets and a smaller machine design to fit within the limited space in the LHC tunnel.

The beams are arranged not as a continuous stream of protons but in discrete bunches of  $\mathcal{O}(10^{11})$  protons separated by 25 ns allowing a maximum collision frequency of 40 MHz. Due to the presence of empty bunches in the LHC fill scheme the actual collision rate is  $\sim 30$  MHz. The instantaneous luminosity delivered to LHCb was  $10^{32}\text{cm}^{-2}\text{s}^{-1}$ , 1% of what is possible at the LHC. This is because the LHCb detector [33] is designed for performing precision measurements of beauty, and charm, hadron decays and therefore requires low pileup, *i.e.* few interactions happening per unit time, in order to be able to accurately resolve primary vertices (PVs). This instantaneous luminosity results in  $\sim 1$  interaction per collision which is compatible with the expected performance of the LHCb detector. Over the duration of a fill the maximum instantaneous luminosity that the LHC can deliver to any given collision point decreases. Since LHCb only requires 1% of the nominal LHC instantaneous luminosity, luminosity levelling can be used to deliver a constant instantaneous luminosity to the detector. This is achieved by varying the beam-beam overlap as the luminosity decreases. This constant luminosity allows LHCb to have a constant trigger configuration throughout a fill, and a uniform detector

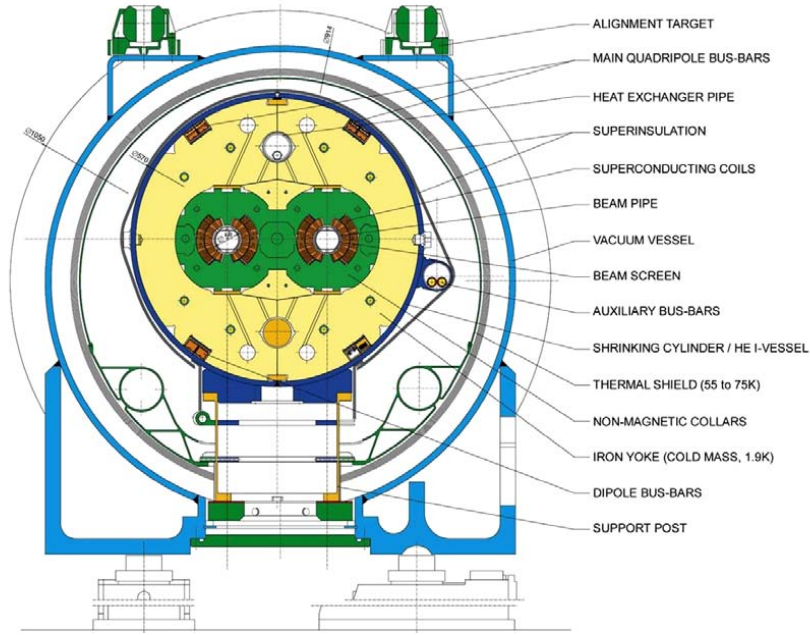


Figure 3.2: Cross section of an LHC cryodipole, from Ref. [4].

configuration. This simplifies both data acquisition and simulated data generation.

When the instantaneous luminosity decreases to a level such that it is no longer worth providing collisions to the experimental points the beams are safely disposed of, “dumped”, at point 6. They are diluted by kicker magnets by sweeping the beam in an “e” shape as shown in Fig. 3.3 and directing them into a carbon target. The beams are also dumped in cases where they can not be controlled safely due to faults in the LHC or the experiments.

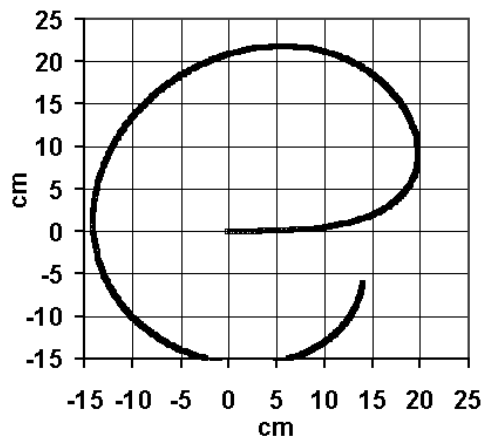


Figure 3.3: Beam spot pattern on the LHC dump block, from Ref. [4].



## 3.2 The LHCb detector

The relatively low luminosity requirement of the LHCb detector is not the only consequence of it being designed for precision measurements of beauty and charm hadrons. As shown in Fig. 3.4 the vast majority of beauty hadrons at the LHC are produced in the forward region, *i.e.* along the beamline, therefore one can save on material costs by designing the detector as a single-arm forward spectrometer whose acceptance encloses the angular distribution of one of the peaks in the  $b\bar{b}$  angular distribution. This results in  $\sim 1/4$  of  $b\bar{b}$  pairs produced being within the LHCb acceptance [34]. The detector, as shown in Fig. 3.5, consists of a number of sub-detector modules which work together to provide a dataset of precise measurements suitable for world leading flavour physics measurements. The detector is shown in the  $(z, y)$  plane, the  $x$  axis points into the page.

### 3.2.1 Tracking

The LHCb detector utilises three tracking detectors and a magnet to determine the kinematics of the charged particles produced by the proton-proton collisions and their

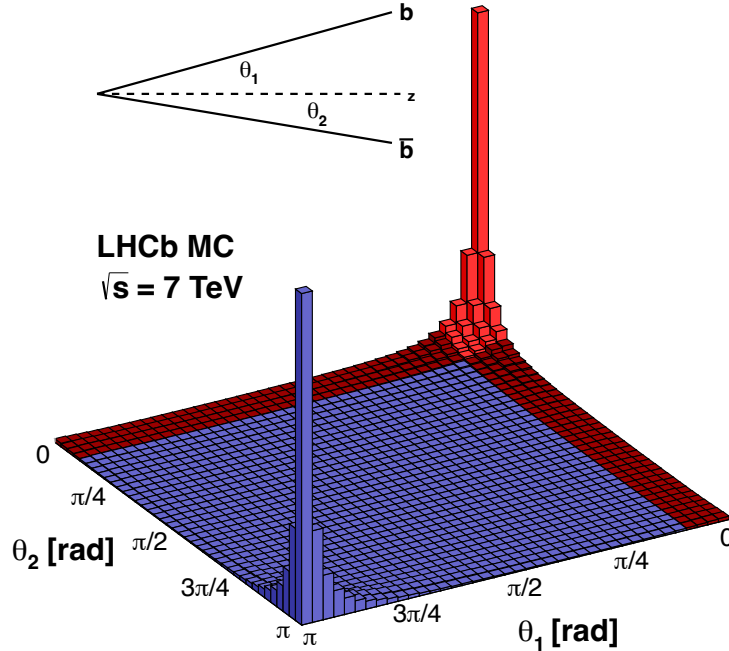


Figure 3.4: The angular distribution of the production cross-section of  $b\bar{b}$  pairs from proton-proton collisions in the LHC, and the LHCb acceptance (red). The distribution is similar for all center of mass energies. Taken from Ref. [34].

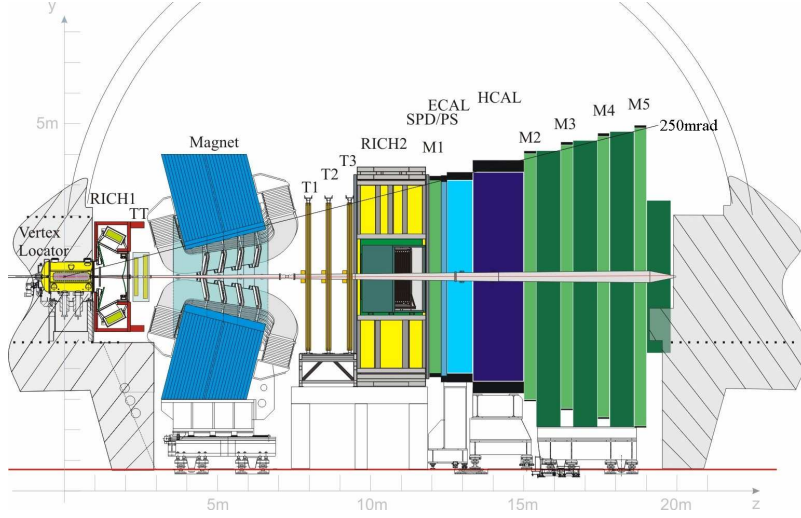


Figure 3.5: Side view of the LHCb detector, from Ref. [33].

decay products. The tracking systems are called the Vertex Locator (VELO), Tracker Turicensis (TT) and the T1, T2, and T3 (T) trackers [35–37]. Figure 3.6 shows a sketch of the LHCb tracking system and the five track types. VELO tracks only have hits in the VELO, upstream tracks only have hits in the VELO and TT, T tracks only have hits in the T trackers, downstream tracks only have hits in the TT and T trackers and long tracks have hits in all trackers. VELO tracks, T tracks and upstream tracks are not used in the analysis discussed in this thesis as they do not contain momentum information. Each event in data involving a  $K_S^0$  meson is categorised according to whether the subsequent pion tracks are long (LL) or downstream (DD).

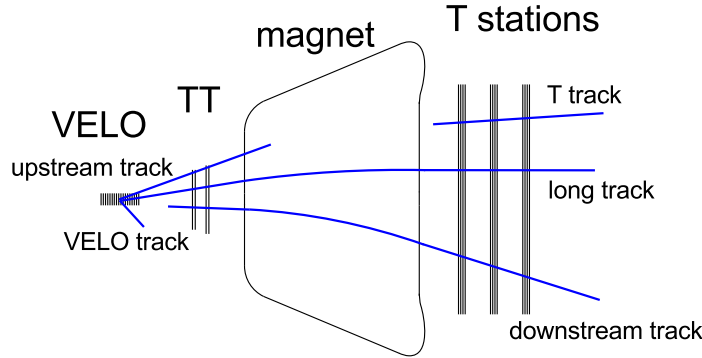


Figure 3.6: Sketch of the LHCb tracking systems and the track type definitions, from Ref. [38]

### Vertex locator

As shown in Fig. 3.7 the VELO consists of two sets of 21 semi-circle silicon tracker modules. Before the beams are declared stable the sensors are separated by several centimetres

and then moved into position in the presence of the stable beams such that they are a mere 8.2 mm from the beams. This enclosure of the collision point allows for a precise determination of the initial tracks of the collision products and the primary and secondary vertices. As shown in Fig. 3.7 each VELO sensor features both an  $r$ -sensor and a  $\phi$ -sensor, the ordering of which alternates between each VELO sensor. An  $r$ -sensor consists of concentric semi-circular silicon strips which allow it to measure the position of hits in terms of the radial distance from the  $z$ -axis. A  $\phi$ -sensor instead consists of silicon strips positioned perpendicularly to the  $z$ -axis such that a hit in the sensor translates to a position in the azimuthal axis of the sensor.

The VELO sensors are positioned such that any particle within the LHCb acceptance will deposit hits in at least four of the sensors. The first 16 VELO sensors on a given half of the VELO are positioned with a separation in the  $z$  direction of 3.5cm, the sensors further downstream have a greater separation to increase coverage for particles whose momenta are close to parallel with the  $z$ -axis. When the VELO is closed the two halves from each side have a separation in the  $z$  direction of 1.5cm, this allows for a slight overlap between the two sides in the  $(x, y)$  plane to ensure particles with zero momentum along the  $x$ -axis can be detected.

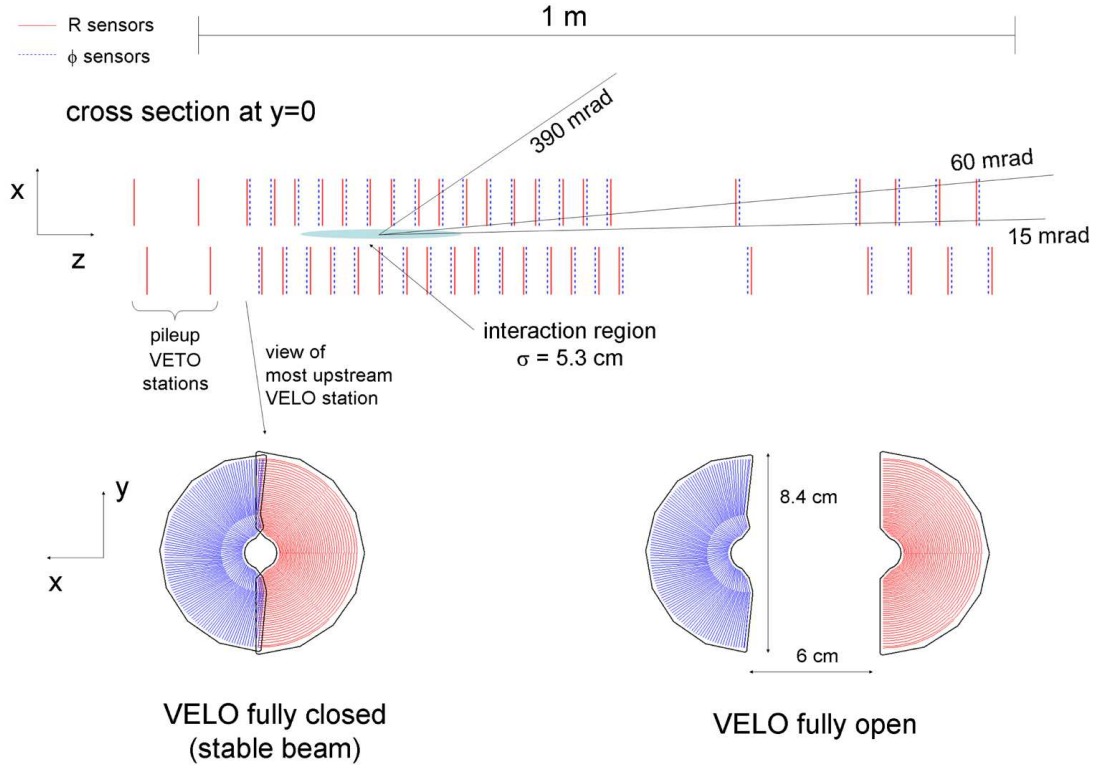


Figure 3.7: Sketch of the VELO sub-detector in the  $(z, x)$  plane (top), and the  $(x, y)$  plane when open (bottom right) and closed (bottom left). This also illustrates the  $r$  (red) and  $\phi$  (blue) sensors. From Ref. [33].

### The silicon tracker

The TT and inner trackers of the T trackers were designed simultaneously and together form the silicon tracker (ST) of the LHCb detector.

As shown in Fig. 3.5 the TT is located in between the RICH 1 sub-detector and the magnet. This is essential for the measurement of decays of long lived particles such as  $\Lambda_b^0$  baryons and  $K_S^0$  mesons, in particular the momentum resolution of the DD  $K_S^0$  dataset used in this analysis would be severely reduced without it. The TT consists of four layers of silicon strip tracking detectors aligned with the  $(x, y)$ -plane. A schematic of the third layer is shown in Fig. 3.8. The two inner layers are placed with a  $\pm 5^\circ$  offset about the  $z$ -axis to improve the spatial resolution in the  $(x, y)$  plane. The first (latter) two layers consist of 14 (16) half modules as the columns of the layer, with an additional two in the middle with a separation to leave space for the beams.

The T tracker modules, as shown in Fig. 3.9 are located between the magnet and the RICH 2 sub-detector and consist of an inner (IT) and an outer tracker (OT). Each inner tracker module, shown in Fig. 3.9, similar to the TT features four layers of silicon trackers with a  $\pm 5^\circ$  offset about the  $z$ -axis for the inner layers relative to the outer layers. The IT however does not cover the full LHCb acceptance like the TT does as the cost would be too great given that it is located much further from the collision point. The T stations were therefore designed to have a high sensitivity tracker close to the beam, the area of highest occupancy, and a lower sensitivity tracker to cover the remainder of the LHCb acceptance.

The OT, shown in Fig. 3.10 in the T tracker modules, is a gas straw-tube design drift time chamber. Similar to the TT and IT, each module of the OT features four tracking layers with the middle layers offset by  $\pm 5^\circ$  about the  $z$ -axis. Each layer of an OT module

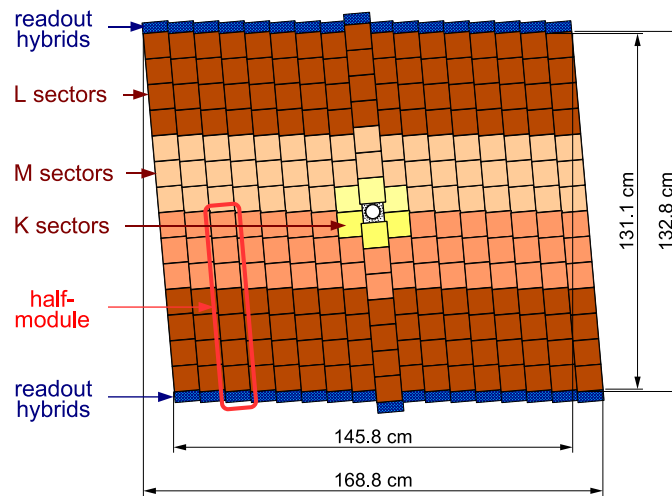


Figure 3.8: Schematic of the third tracking layer of the TT, from Ref. [33]

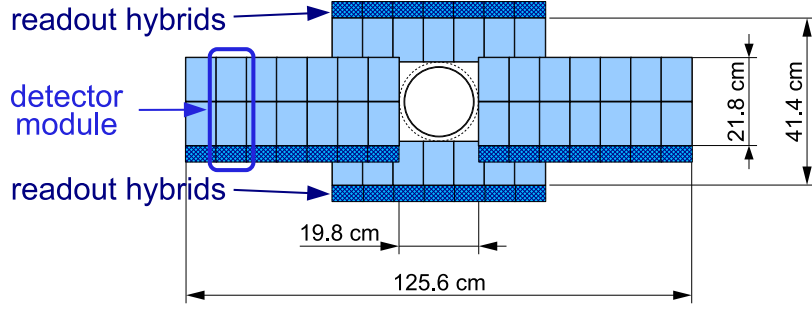


Figure 3.9: Schematic of a single tracking layer of the IT, from Ref. [33]

features two layers of drift-tubes filled with a mixture of Argon and  $\text{CO}_2$ , chosen to allow for a fast drift time. A potential difference is applied to each tube and its central wire to induce the drift of the gases when they ionise in the presence of the incoming charged particles.

### LHCb magnet

As shown in Fig. 3.5, the LHCb magnet [40] is located in the middle of the ST. This is crucial for measuring the momenta of charged particles. If one considers a long track, as a charged particle traverses the detector it will deposit hits in the VELO and TT, then experience an acceleration proportional to its charge, velocity and the field strength of the magnet, and then deposit hits in the T tracker. The hits in the VELO and TT, and the T tracker allows one to determine the path of the particle through the detector to a high precision from which one can infer the curvature of the particle path induced by traversing the magnetic field. By combining this with a detailed knowledge of the magnetic field, for which a map was obtained to a relative precision of  $4 \times 10^{-4}$  via the use of Hall probes, one can determine the momentum of the particle.

The LHCb magnet is a warm dipole magnet with saddle-shaped coils in a window-frame yoke. The maximum magnetic field strength is  $\sim 1\text{T}$ , parallel to the  $y$ -axis. The photodetectors in the RICH sub-detectors are incredibly sensitive to magnetic fields so the magnet was required to have a field strength of less than 2 mT in the region of the RICH sub-detectors while having as high a field strength as possible between the VELO and the TT, the photodetectors are further protected by iron cases to reduce the risk of malfunction. The polarity of the magnet can be swapped between “Up” and “Down”, during each year of data taking the roughly equivalent datasets are taken with each polarity. This can be used to reduce systematic effects from asymmetries in the experiment.

### 3.2.2 Particle identification

Several different kinds of final state particles are produced in the decays studied with the LHCb detector. For the analysis presented in this thesis it is imperative that one can distinguish between pions and kaons with a high level of confidence to construct each dataset correctly. It is also necessary to identify any decays that contain final state particles besides pions and kaons in order to veto them. Therefore a number of sub-detectors are required to identify each type of particle with a high level of confidence. These are shown in Fig. 3.5. Charged hadrons are identified by the Ring Imaging Cherenkov (RICH) sub-detectors, muons are identified by the muon sub-detector (M1–5), and electrons and photons are identified using the electromagnetic (ECAL) and hadronic (HCAL)

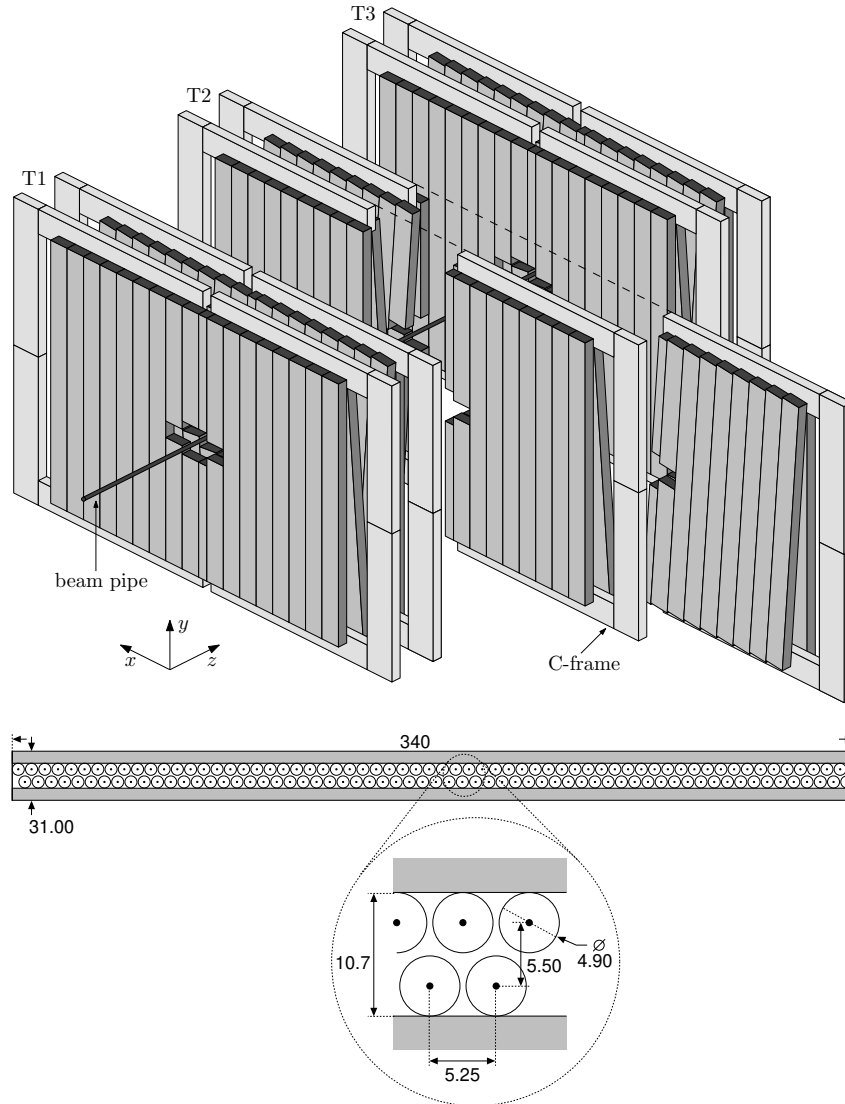


Figure 3.10: Configuration of the OT tracker modules (top) and the cross section of a tracking layer (bottom) with distances shown in mm, from Ref. [39]. T2 is shown open as if during maintenance, the gaps around the beam pipe correspond to where the IT is located.

calorimeters.

### The RICH detectors

RICH 1 is located in between the VELO and the TT, and RICH 2 is located in between the T tracker and the first muon station [41]. Together they perform particle identification (PID) for charged particles in the momentum range of  $\sim 1 - 100 \text{ GeV}/c$ . The detectors work by measuring the angle of Cherenkov radiation emitted as the charged particles pass through a medium, also known as the radiator, at a speed greater than the speed of light in the medium. The angle of the emitted light cone,  $\theta$ , depends on the refractive index of the medium,  $n$ , and the velocity of the charged particle,  $v$ , according to

$$\cos(\theta) = \frac{c}{nv}. \quad (3.1)$$

The relation between the Cherenkov angle and particle velocity is shown in Fig. 3.11 and shows that for the different radiators used in the RICH sub-detectors by simultaneously measuring the Cherenkov angle and the momentum of a charged particle one can achieve a clear separation between each species over a substantial momentum range, assuming a precise knowledge of the refractive index of the radiator material. The RICH 1 used aerogel (in Run 1 only) and  $\text{C}_4\text{F}_{10}$  radiators to cover the momentum range of  $\sim 1 - 60 \text{ GeV}/c$  and RICH 2 uses a  $\text{CF}_4$  radiator to cover the high momentum range  $\sim 15 - 100 \text{ GeV}/c$ .

As shown in the schematic of the RICH 1 in Fig. 3.12 in each RICH sub-detector the Cherenkov radiation is focused and reflected by spherical and flat mirrors into Hybrid Photon Detectors (HPDs) located outside of the LHCb acceptance to reduce material cost.

From Fig. 3.11 one can infer that although the RICH sub-detectors are powerful PID detectors for charged hadrons, across the  $\sim 1 - 100 \text{ GeV}/c$  momentum range, additional detectors, namely the calorimeters and muon system, are required to ensure high performance PID for the other charged particle species.

### The calorimeters

The LHCb calorimeter system consists of four sub-detectors, the Scintillating Pad Detector (SPD), the Pre-Shower (PS) detector, the ECAL and HCAL [43].

Each of the sub-detectors are designed around the same principle. An organic scintillator emits light which is then transmitted to a Photo-Multiplier (PMT) by wavelength-shifting (WLS) fibres. The basic design of the calorimeters is to have alternating layers of scintillator, doped polystyrene, and lead absorber layers. Each detection layer has concentric sections of varying sizes, as shown in Fig. 3.13, such that each section has

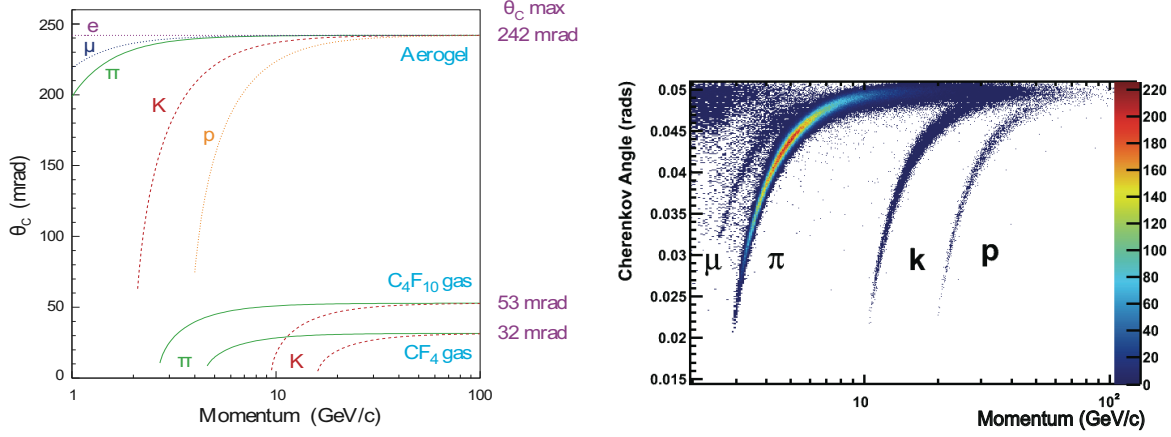


Figure 3.11: Left: Plot of the relation between the Cherenkov angle and the momentum of different species of charged particles for different radiator mediums, from Ref. [33]. Right: Reconstructed Cherenkov angle and track momentum in the  $C_4F_{10}$  radiator in Run 1, from Ref. [42].

similar hit densities.

The SPD is used to select for charged particles which allows for separation between electrons and photons or neutral pions. The large number of charged pions produced are a significant background which is mitigated by the PS as it allows for longitudinal segmentation of the electromagnetic shower. The energies of electrons and photons is measured by the ECAL alone, whereas both the ECAL and HCAL measure the energies

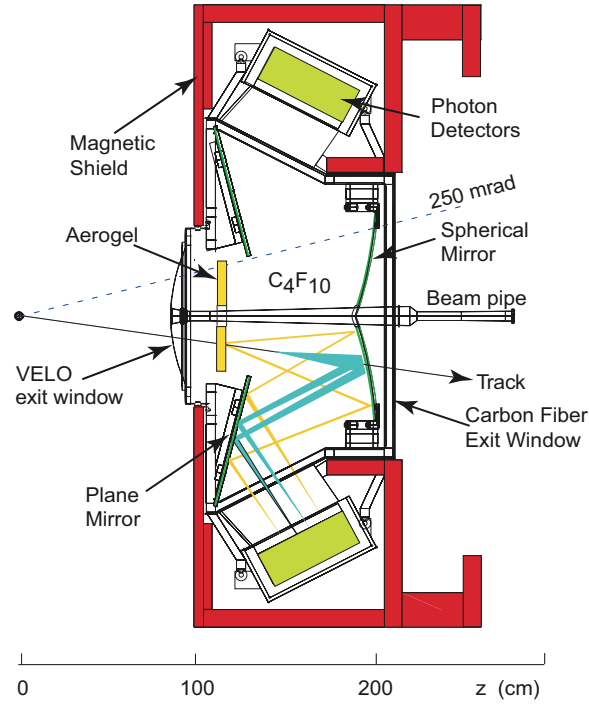


Figure 3.12: Sketch of the RICH 1 sub-detector, from Ref. [33].



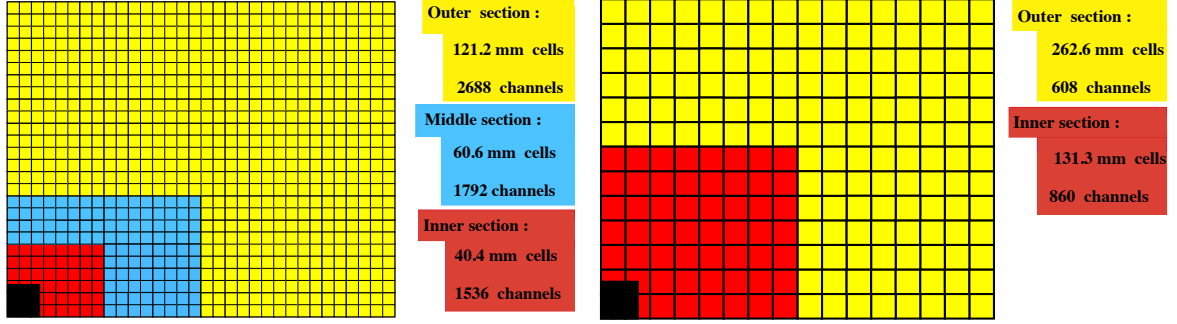


Figure 3.13: Quarter cross section of the lateral segmentation of the SPD, PS and ECAL (left) and the HCAL (right). The cell dimensions on the left are only for the ECAL. From Ref. [33].

of hadrons.

### The muon system

A muon has  $\sim 200$  times the mass of an electron and does not interact strongly, therefore it can typically penetrate material much further than the other final state particles studied at LHCb. As shown by Fig. 3.11 the RICH sub-detectors are not sufficient to distinguish muons from pions. The final PID sub-detector is therefore designed specifically to identify muons and features five stations, one located between RICH 2 and the calorimeters with the rest positioned at the end of the detector volume [44]. In between each of the last four muon stations are muon filters, as shown in Fig. 3.14. Muon filters are 80cm thick sheets of iron so it is highly unlikely that any charged particle besides a muon would penetrate them, therefore the further a charged particle traverses the muon stations the greater the likelihood it is that it is a muon. The muon stations are partitioned into four concentric rectangles such that each section has the same hit density. Each section consists of multi-wire proportion chambers (MWPCs), besides the inner most section of M1 which uses triple gas electron multiplier (GEM) detectors due to the expected particle rate of this region exceeding safety limits for detector ageing [45]. Stations M1-M3 have a high spatial resolution along the  $x$ -axis in order to determine the transverse momentum of muons with a resolution of  $\sim 20\%$ . The latter stations have a worse resolution as they are required only to verify the existence of tracks.

### 3.2.3 Detector performance

Track reconstruction is performed by first determining initial track candidates, seeds, in the VELO and T stations with low magnetic field. The trajectories are then fitted with a Kalman filter which accounts for multiple scattering and energy loss. For a long track particle with momentum greater than  $10 \text{ GeV}/c$  the reconstruction efficiency is  $\sim 94\%$

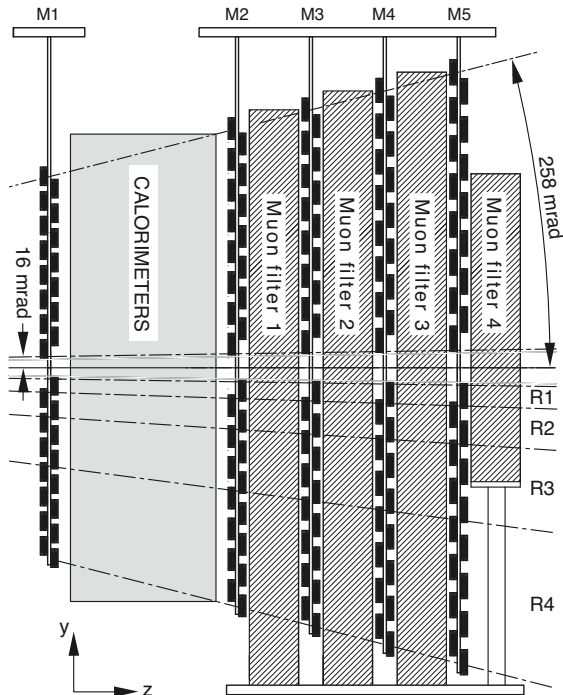


Figure 3.14: Schematic of the muon sub-detector. The  $R_i$  divisions delineate the vertical limits of the partitions in each muon station, from Ref. [33].

and downstream tracks have an efficiency of  $\sim 80\%$  for a particle with momentum greater than  $5 \text{ GeV}/c$ .

Measurements of the RICH, calorimeters and muon system are combined for each charged particle track to determine a log-likelihood that a particle of species  $X$  is not mis-identified as a pion. This is then maximised by varying the hypothesis for each track in turn between electron, muon, pion, kaon and proton. The PID performance in LHCb is illustrated by Fig. 3.17, one can see that for low momenta high efficiency is achieved in all cases. However, as one would expect from Fig. 3.11 low efficiency is observed for kaon to pion mis-identification at high momenta.

The nominal LHCb detector performance was first determined during Run 1 of the LHC [46,47]. For long tracks the relative momentum resolution is  $< 0.8\%$  for  $p < 100 \text{ GeV}/c$ , and reaches  $\sim 1.1\%$  for  $p > 200 \text{ GeV}/c$ , this is shown in Fig. 3.15. The  $B$  mass resolution is  $\sim 20 \text{ MeV}/c^2$  which allows for good separation of  $B^0$  and  $B_s^0$  mesons with a mass difference of  $87 \text{ MeV}/c^2$  [7]. The primary vertex and impact parameter resolutions are shown in Fig. 3.16.

For particles below  $20 \text{ GeV}/c$  the

It was found that in Run 2 the detector achieved similar performance, however thanks to improvements in reconstruction and the removal of the aerogel from the RICH detectors the PID efficiency for kaons was found to be a few percent higher [48].

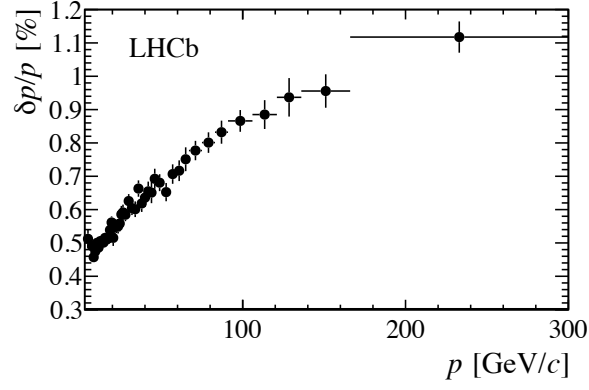


Figure 3.15: Relative momentum resolution as a function of momentum for long tracks in LHCb data. From [46].

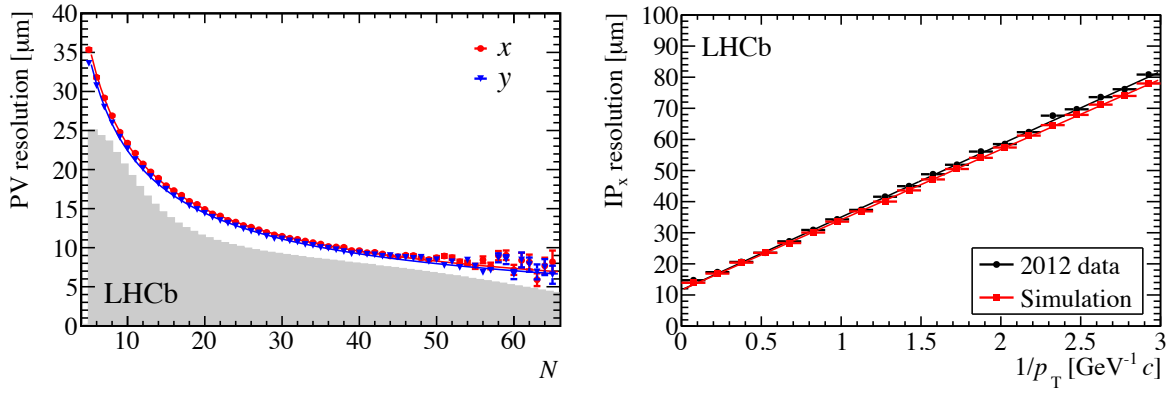


Figure 3.16: Primary vertex (left) and impact parameter (right) resolution in LHCb data. From [46].

### 3.3 Triggering

The data collected from a single event at LHCb corresponded to  $\mathcal{O}(10)$  kB, given a collision rate of 30 MHz this corresponds to  $\mathcal{O}(300)$  TB/s. However the majority of collisions at the LHC result in inelastic collisions with no value for physics measurements. Therefore a trigger system was required to ensure that the majority of recorded events are of value to the experiment to allow for efficient and responsible use of our data storage and computing capacity.

As shown in Fig. 3.18 the LHCb trigger [51] had three levels, one hardware trigger (L0) and two software high level triggers (HLT1 and HLT2) which is run on a server farm near the detector. The maximum readout speed of the LHCb detector was 1.1 MHz, far less than the collision frequency of the LHC of 30 MHz so the hardware trigger system needed to reduce this rate by a factor of at least 30 by vetoing any events which did not feature physics of interest. However this was still far too high for efficient use of data storage so further reductions are required. The L0 trigger first reduced the rate to 1 MHz,

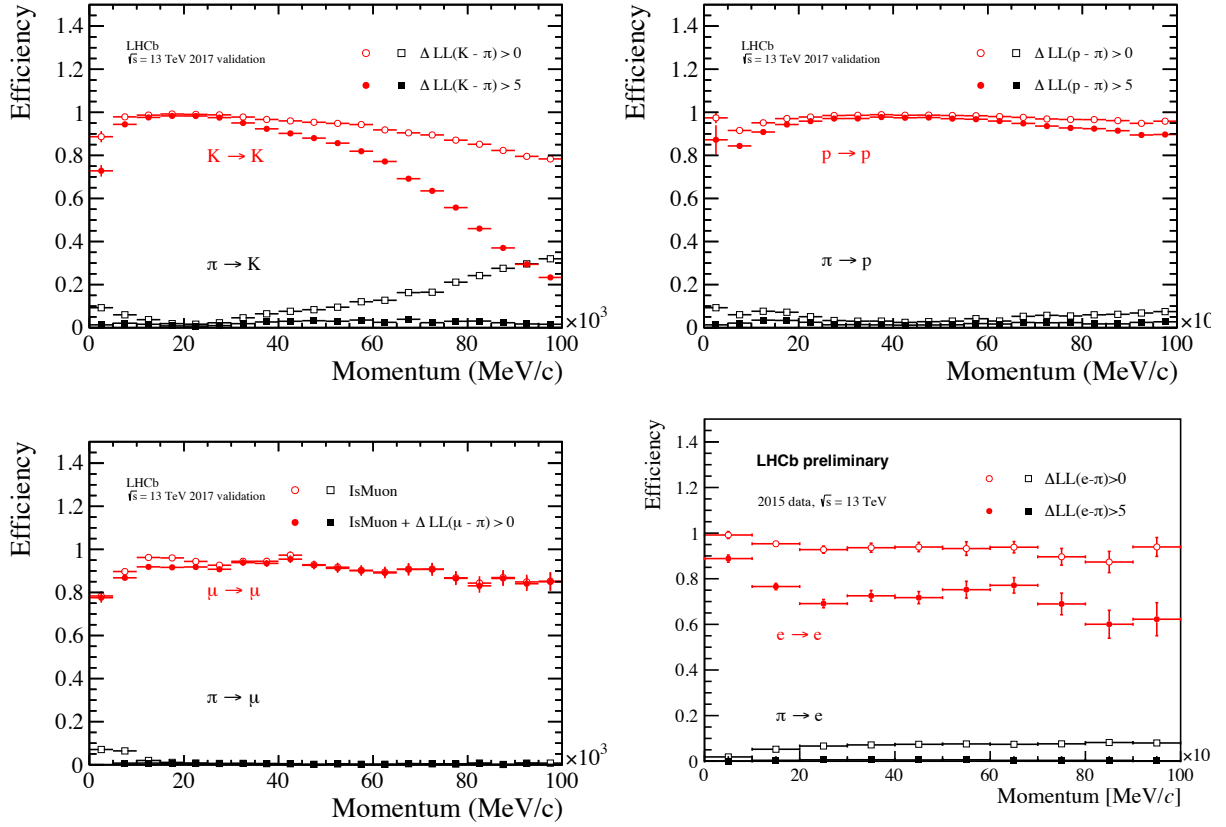


Figure 3.17: PID efficiency and mis-identification as a function of momentum in LHCb data for charged particle species, from Ref. [49].

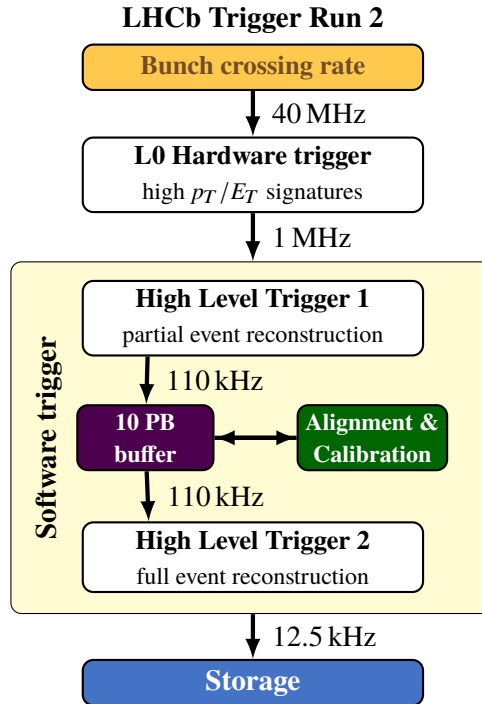


Figure 3.18: Overview of the Run 2 LHCb trigger system, from Ref. [50]

HLT1 would further reduce this to 110 kHz and finally HLT2 reduced it to 12.5 kHz. In Run 2 thanks to improvements in the reconstruction software and the computing farm the alignment and calibration step was performed in real time as shown by Fig. 3.18 and the nominal HLT2 trigger rate was more than doubled [52].

The L0 had a fixed latency of 4  $\mu$ s and used information from the ECAL, HCAL and muon stations to perform the first basic vetoing to remove the majority of uninteresting events. The HLT1 then performed an inclusive selection of events based on one- or two-track signatures, muon tracks displaced from PVs or dimuon combinations in the event. These events were then buffered to disk storage in order to allow for alignment of the detector before running the events through the HLT2. The HLT2 performed a full reconstruction to allow for triggering on inclusive and exclusive final states.

### 3.4 Offline processing

After the initial data taking the recorded data is stored in files across the Worldwide LHC Computing Grid (WLCG). For any given analysis the decays of interest will be extremely diluted amongst the entire LHCb dataset so it is processed into different streams of data based on the kind of decay observed in the event. This is referred to as “stripping”. The stream definitions are broad, *e.g.* Bhadron refers to any event from a B hadron decay, so will still require one final level of processing before the data is ready for analysis. For each stream a number of stripping lines are defined with varying levels of inclusivity. For example a stripping line used in the analysis described in this thesis is named `StrippingB02D0KPiD2HHBeauty2CharmLine` which corresponds to simultaneously building candidates for a  $B^0 \rightarrow DK^+\pi^-$  decay followed by a  $D \rightarrow \pi^+\pi^-$ ,  $D \rightarrow K^+K^-$  or  $D \rightarrow K^\pm\pi^\mp$  decay. During stripping the decays are fully reconstructed and candidates are built according to these stripping lines. Selection is applied to the data using loose cuts that are known to remove the majority of data whilst maintaining a high efficiency for the decays of interest.

Following stripping the next step is to use the DaVinci software [53] to select events for specific decays that were reconstructed under a given stripping line to be saved for analysis. Despite the relatively small size of the output files of this final step it is still not insignificant. Indeed when summed over all of the data and simulation used in even a single large analysis, such as the analysis discussed herein, the storage requirements can become  $\mathcal{O}(10)$  TB. Across all LHCb analyses therefore the “analysis ready” datasets can correspond to PBs of storage space. This will increase at an accelerated rate as the LHC progresses with future runs. The non-centralisation of this final data processing step therefore poses an issue – it requires all analysts to archive or delete all tuples that are not required for analysis to ensure that LHCb utilises storage capacity efficiently and responsibly. Another

issue is that the processing itself is inherently computing intensive and time consuming, particularly when transient errors occur that require manual intervention on the part of the analyst. To mitigate these issues, the LHCb collaboration developed the Analysis Productions (AP) software [54].

AP is a framework for analysts to configure tupling jobs such that they can easily be submitted to the DIRAC transformation system [55]. AP provides a simple method of job configuration and testing prior to full scale processing, this simplifies the preparation of productions and prevents users from running problematic productions. Submissions are reviewed by experts for each LHCb sub-group to facilitate knowledge transfer and to prevent faults that can not be identified by automated testing, and productions are run by experts to allow for efficient use of person power. The AP framework also preserves all output in a centralised location to enable easy preservation, reproduceability and data sharing. Therefore the success of this framework relies on a large body of code, documentation and training to which I contributed in many ways.

## 3.5 Summary

This chapter has summarised the origin of data and the entire workflow of its processing from collisions to analysis in the LHCb experiment. Section [3.1] described the LHC and how it delivers collisions to the LHCb experiment and Section [3.2] introduced the design goals of the LHCb detector. Section [3.2.1] summarised each of the components of the LHCb tracking system and Section [3.2.2] summarised the components responsible for PID at LHCb. Section [3.2.3] presented the performance of the LHCb detector and Section [3.3] explained how the detector information is used to determine which collision events to record. Finally Section [3.4] explained the offline data processing to convert the full LHCb dataset into smaller datasets ready for physics analysis.



## 4 The double Dalitz method

*“When you’re having a big idea, is it best to break it up into lots of little thoughts, about the size of peas, and squeeze them through in quick succession, or just bite the bullet and force it through your mind pipe in one huge clod, like gritting your teeth and thinking for dear life?”*

---

Philomena Cunk

Before detailing each analysis step in Chapters 5 to 9 this chapter describes the overall method, and the motivation and general methodology for each step. The double Dalitz plane analysis is a generalisation of a single Dalitz plane analysis. This can be seen by considering a decay for which the two children of the initial decay that do not produce a 3/4-body decay can be considered as a single state. For example,  $B^0 \rightarrow DK^{*0}, D \rightarrow K_S^0 h^+ h^-$  is a single Dalitz decay but if the  $K^{*0}$  is replaced with  $K^+ \pi^-$  such that the decay is now  $B^0 \rightarrow DK^+ \pi^-, D \rightarrow K_S^0 h^+ h^-$  then this can be treated as a double Dalitz decay whose phase space contains the  $B^0 \rightarrow DK^{*0}, D \rightarrow K_S^0 h^+ h^-$  phase space.

The LHCb collaboration has performed several measurements of  $\gamma$  using Dalitz plane analyses, most notably the model-independent single Dalitz analysis of  $B^+ \rightarrow Dh^+$  decays, where  $h$  is either a kaon or pion, which is the most sensitive single measurement of  $\gamma$  [56]. Charge conjugation is implied throughout, unless discussing asymmetries or otherwise stated, and the difference between model-independent and model-dependent analyses is explained in the following section. The  $B^+ \rightarrow Dh^+$  and  $B^0 \rightarrow DK^+ \pi^-$  analyses both study the Dalitz distributions of  $D \rightarrow K_S^0 h^+ h^-$  decays using very similar methodologies, therefore it is beneficial to first discuss the  $B^+ \rightarrow Dh^+$  methodology and then extend the discussion to a double Dalitz plane formalism.

### 4.1 Single Dalitz analysis of $B^+ \rightarrow Dh^+$ decays

This is a model-independent measurement of  $\gamma$  using a single Dalitz analysis of  $B^+ \rightarrow DK^+, D \rightarrow K_S^0 h^+ h^-$  decays where  $h$  is either a kaon or a pion [57–61].



The Feynman diagrams for  $B^+ \rightarrow DK^+$  decays are shown in Fig. 4.1. This shows that the  $\bar{D}^0$  decay amplitude is proportional to  $V_{cb}$  and the  $D^0$  amplitude is proportional to  $V_{ub}$ , therefore the ratio of these amplitudes have a weak-phase difference equal to  $\gamma$ , up to a very good approximation. Since the final state is accessible via either a  $B^+ \rightarrow \bar{D}^0 K^+$  decay or a  $B^+ \rightarrow D^0 K^+$  decay there is no way to know the flavour of the  $D$  that took part in the decay. Therefore in measuring the  $B^+ \rightarrow DK^+$ ,  $D \rightarrow K_S^0 h^+ h^-$  decay one must consider the sum of the  $D^0$  and  $\bar{D}^0$  decay amplitudes. If one considers the Dalitz plane defined by the pairwise invariant masses

$$s_{\pm} = m_{K_S^0 h^{\pm}}^2, \quad (4.1)$$

one can then write the  $B^+$  decay amplitude as

$$A \propto \bar{A}_{B^+} |A_{\bar{D}^0}(s_-, s_+)| + e^{i\gamma} A_{B^+} |A_{D^0}(s_-, s_+)| e^{i\Delta\delta_D(s_-, s_+)}, \quad (4.2)$$

where

- $A_{B^+}$  is the  $B^+ \rightarrow D^0 K^+$  amplitude
- $A_{D^0}(s_-, s_+)$  is the amplitude of the  $D^0 \rightarrow K_S^0 h^+ h^-$  decay at point  $(s_-, s_+)$  in the Dalitz plane,
- $\Delta\delta_D(s_-, s_+)$  is the strong-phase difference between the  $D^0$  and  $\bar{D}^0$  decays at point  $(s_-, s_+)$  in the Dalitz plane.

One can not directly measure the amplitude of a decay, only the square of its magnitude.

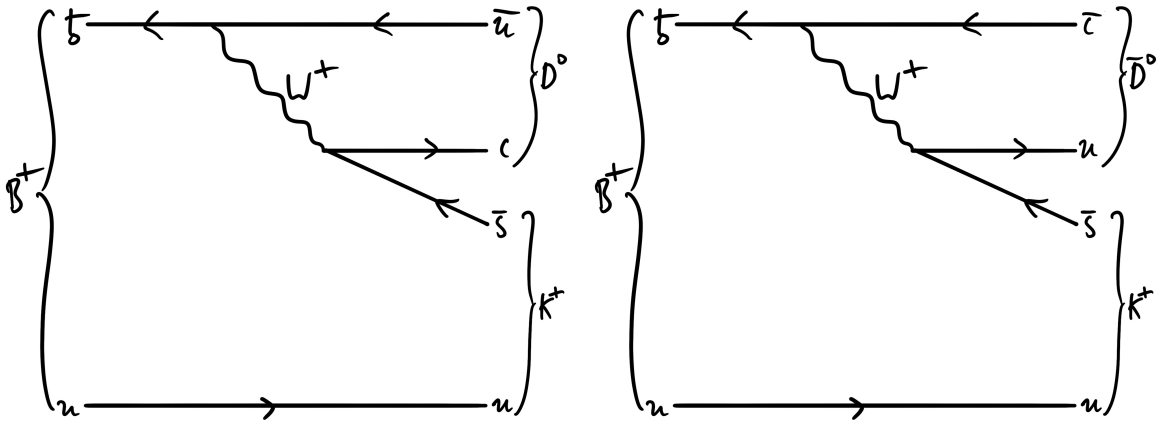


Figure 4.1: Feynman diagrams for the suppressed (left) and favoured (right)  $B^+ \rightarrow DK^+$  decays.

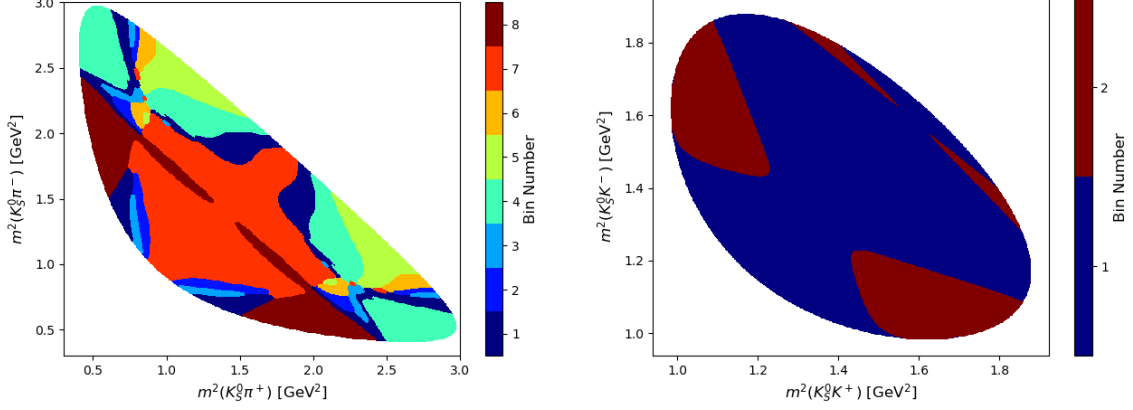


Figure 4.2: Optimal binning schemes for the Dalitz planes of (left)  $D \rightarrow K_S^0 \pi^+ \pi^-$  and (right)  $D \rightarrow K_S^0 K^+ K^-$  decays [62].

Three terms appear in the equation for  $|A|^2$ , two of which are simply the square of the favoured and suppressed amplitudes and the third is an interference term which depends on  $\gamma$ . Therefore  $\gamma$  can be measured by studying how the amplitude-squared density varies across the Dalitz plane in data, both  $B$  flavours are required to access the weak phase independently of the strong phase since the interference phase of the amplitude squared for a  $B^\pm \rightarrow DK^\pm$  decay is of the form  $\Delta\delta \pm \gamma$ , where  $\Delta\delta$  is the total strong-phase difference between the  $B^\pm \rightarrow \bar{D}^0 K^\pm$  and  $B^\pm \rightarrow D^0 K^\pm$  decays. This can be achieved by a number of methods, the two most common are amplitude fits and binned analyses. Currently, binned methods are the primary way that Dalitz plane  $\gamma$  measurements are performed. The benefits of a binned method over an amplitude fit method are discussed in Section 4.4 along with how the choice of binning is made. The binnings of the  $D \rightarrow K_S^0 \pi^+ \pi^-$  and  $D \rightarrow K_S^0 K^+ K^-$  Dalitz planes are shown in Fig. 4.2 [62]. The distribution of these decays in LHCb data is shown in Fig. 4.3. Due to the symmetry of the final state the Dalitz plane is symmetric along the  $s_+ = s_-$  line, one can take advantage of this by splitting the binnings across the line, where the indices are defined such that  $\pm i$  bins are in the  $s_\mp > s_\pm$  region. Under the assumption that there is no direct  $CP$  violation in the  $D$  decay, *i.e.*  $|A_D(s_-, s_+)| = |A_{\bar{D}}(s_+, s_-)|$ , this doubles the number of observables without increasing the number of free parameters. This is assumed since the effect of direct  $CP$  violation in the  $D$  decay is expected to be small in the SM [63]. Once a binning has been defined Eq. (4.2) can be squared and integrated over each bin to obtain a per-bin population expectation equation.

#### 4.1.1 Binned signal population expectation

Since it can be trivially obtained from the double Dalitz plane binned signal population derivation in Section 4.2.1, the derivation for the single Dalitz plane is omitted for brevity

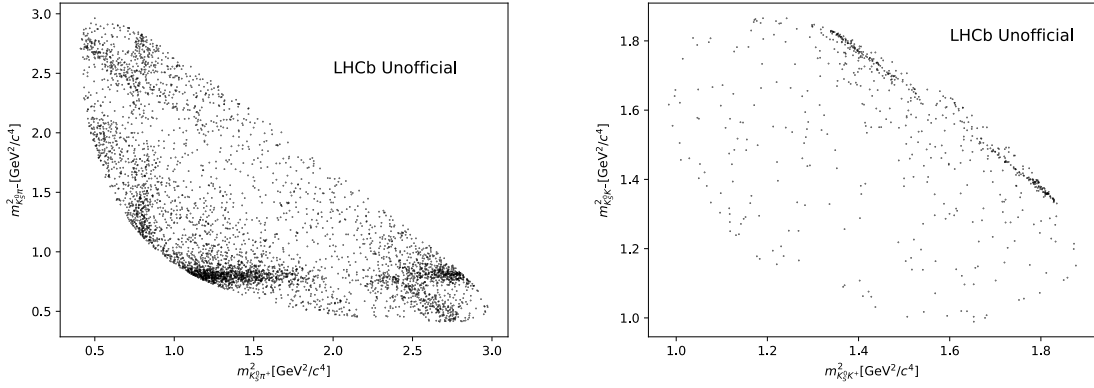


Figure 4.3: Dalitz distribution of  $D \rightarrow K_S^0 \pi^+ \pi^-$  and  $D \rightarrow K_S^0 K^+ K^-$  decays in fully selected Run 1 and 2 data, with  $K_S^0$  in the DD category.

and the result is simply stated here. For  $B^+ \rightarrow DK^+$ ,  $D \rightarrow K_S^0 h^+ h^-$  the number of signal decays expected in bin  $i$  of the  $D$  Dalitz plane is

$$N_i^\pm = h_{DK,D}^\pm [F_{\mp i} + (x_{DK}^\pm)^2 + (y_{DK}^\pm)^2] F_{\pm i} + 2\sqrt{F_{+i}F_{-i}}(c_i x_{DK}^\pm \mp s_i y_{DK}^\pm), \quad (4.3)$$

where the  $\pm$  corresponds to the  $B$  flavour, with Cartesian parameters

$$x_{DK}^\pm = r_{B,DK} \cos(\Delta\delta_{B,DK} \pm \gamma), \quad y_{DK}^\pm = r_{B,DK} \sin(\Delta\delta_{B,DK} \pm \gamma), \quad (4.4)$$

where the parameters can be interpreted as

- $h_{DK,D}^\pm$  are normalisation parameters, the total number of  $B^\pm \rightarrow DK^\pm$  decays to the chosen  $D$  final state,
- $F_{\pm i}$  is the fraction of pure  $D^0$  decays in bin  $\pm i$ ,
- $c_i$  ( $s_i$ ) is the amplitude-weighted cosine (sine) of the average strong-phase difference between the  $D^0$  and  $\bar{D}^0$  decays in bin  $i$ ,
- $r_{B,DK}$  is the magnitude of the ratio between the suppressed and favoured  $B$  decay amplitudes,
- $\Delta\delta_{B,DK}$  is the strong-phase difference between the suppressed and favoured  $B$  decay amplitudes.

The formal definitions are

$$F_{\pm i} = \frac{1}{N_D} \int_{\pm i} \eta_D(s_-, s_+) |A_{D^0}(s_-, s_+)|^2 ds^2, \quad (4.5)$$

$$c_i = \frac{\int_i |A_{D^0}(s_-, s_+)| |A_{\bar{D}^0}(s_-, s_+)| \cos \Delta\delta_D(s_-, s_+) ds^2}{\sqrt{\int_i |A_{D^0}(s_-, s_+)|^2 ds^2 \int_i |A_{\bar{D}^0}(s_-, s_+)|^2 ds^2}}, \quad (4.6)$$

$$s_i = \frac{\int_i |A_{D^0}(s_-, s_+)| |A_{\bar{D}^0}(s_-, s_+)| \sin \Delta\delta_D(s_-, s_+) ds^2}{\sqrt{\int_i |A_{D^0}(s_-, s_+)|^2 ds^2 \int_i |A_{\bar{D}^0}(s_-, s_+)|^2 ds^2}}, \quad (4.7)$$

$$r_{B,DK} e^{i(\Delta\delta_{B,DK} + \gamma)} = \frac{A(B^+ \rightarrow D^0 K^+)}{A(B^+ \rightarrow \bar{D}^0 K^+)} \quad (4.8)$$

where

$$N_D = \int_{\mathcal{D}} \eta_D(s_-, s_+) |A_{D^0}(s_-, s_+)|^2 ds^2, \quad (4.9)$$

$\eta_D$  is the experimental acceptance as a function of the  $D$  Dalitz plane variables and  $\int ds^2 \equiv \int ds_- ds_+$  *i.e.* the integral over the Dalitz plane as a whole,  $\mathcal{D}$ , or bin  $i$  of the Dalitz plane.

The basic setup of the model-independent single Dalitz  $B^+ \rightarrow Dh^+$  analysis is that Eq. (4.3) is fitted to fully selected data, this is referred to as “the  $CP$  fit”. The values of  $x_{DK}^\pm$ ,  $y_{DK}^\pm$  are then used to extract  $\gamma$ , this is referred to as “the interpretation”. The same language is used in describing the double Dalitz analysis, although the  $CP$  fits have a fundamental difference which is explained in Section 4.5.

Given the binnings in Fig. 4.2 and the above parameter definitions one can count the number of observables and parameters present in the fit.

The observables are:

- 32 binned  $D \rightarrow K_S^0 \pi^+ \pi^-$  populations, since there are 16 bins per  $B$ -flavour.
- Eight binned  $D \rightarrow K_S^0 K^+ K^-$  populations, since there are four bins per  $B$ -flavour.

The parameters are

- 20  $F_{\pm i}$  parameters (16  $D \rightarrow K_S^0 \pi^+ \pi^-$ , 4  $D \rightarrow K_S^0 K^+ K^-$ ). Again, assuming there is no  $CP$  violation in the  $D$  decay  $A_D(s_-, s_+) = A_{\bar{D}}(s_+, s_-)$  means there is only one  $F_{\pm i}$  parameter per  $D$  bin,
- 20  $c_i$ ,  $s_i$  parameters (16  $D \rightarrow K_S^0 \pi^+ \pi^-$ , 4  $D \rightarrow K_S^0 K^+ K^-$ ), similar to above since the strong-phase is invariant under  $CP$  transformation.
- Four Cartesian  $x_{DK}^\pm$ ,  $y_{DK}^\pm$  parameters,

- Four normalisation parameters  $h_{DK,D}^{\pm}$ .

Therefore there are 40 observables and 48 parameters to be measured, the  $B^+ \rightarrow DK^+$ ,  $D \rightarrow K_S^0 h^+ h^-$  decays alone are not sufficient to constrain all of these parameters. Two additional sources of information are used. The first, discussed in Section 4.1.2, is the introduction of  $B^+ \rightarrow D\pi^+$ ,  $D \rightarrow K_S^0 h^+ h^-$  decays which are high-statistics control modes with little expected  $CP$  violation and the second is measurements of the strong-phase  $c_i$ ,  $s_i$  parameters from the CLEO-c and BES-III charm factories discussed in Section 4.1.3. By fixing, or constraining, the  $c_i$ ,  $s_i$  parameters to the measured values and incorporating the  $B^+ \rightarrow D\pi^+$  data the number of observables can be increased to 64 and the number of free parameters simultaneously decreased to 34 to overconstrain the system, where external inputs are not counted as observables but their corresponding parameter is no longer counted as a free parameter. The system has gained four normalisation parameters and two Cartesian nuisance parameters associated with the  $B^+ \rightarrow D\pi^+$  decay which are defined in the following discussion.

#### 4.1.2 $B^+ \rightarrow D\pi^+$ decays

$B^+ \rightarrow D\pi^+$ ,  $D \rightarrow K_S^0 h^+ h^-$  decays have very little sensitivity to  $\gamma$  since the ratio between the favoured and suppressed  $B^+$  decay amplitudes is  $r_{B,D\pi} = 0.0049_{-0.0005}^{+0.0006}$  [17] resulting in a small interference term relative to the favoured amplitude squared term. For contrast the value of the corresponding parameter for  $B^+ \rightarrow DK^+$  decays is  $r_{B,DK} = 0.097 \pm 0.002$ . However, the value of these decays is not their direct sensitivity to  $\gamma$  but rather their relatively high branching fraction. The branching fraction  $\mathcal{B}(B^+ \rightarrow \bar{D}^0 \pi^+) = (4.6 \pm 0.1) \times 10^{-3}$  is  $\sim 13$  times greater than  $\mathcal{B}(B^+ \rightarrow \bar{D}^0 K^+) \sim (3.6 \pm 0.2) \times 10^{-4}$  [7]. This results in a larger dataset for  $B^+ \rightarrow D\pi^+$  than for  $B^+ \rightarrow DK^+$  which makes it an excellent control mode to determine the values of the  $F_{\pm i}$  parameters. Therefore both datasets are fitted simultaneously to their corresponding expectation equations with the  $F_{\pm i}$  parameters being shared between the decays.

For  $B^+ \rightarrow D\pi^+$ ,  $D \rightarrow K_S^0 h^+ h^-$  the expectation equation is

$$N_i^{\pm} = h_{D\pi,D}^{\pm} [F_{\mp i} + (x_{D\pi}^{\pm 2} + y_{D\pi}^{\pm 2}) F_{\pm i} + 2\sqrt{F_{+i} F_{-i}} (c_i x_{D\pi}^{\pm} \mp s_i y_{D\pi}^{\pm})], \quad (4.10)$$

where

$$x_{D\pi}^{\pm} = x_{D\pi}^{\xi} x_{DK}^{\pm} - y_{D\pi}^{\xi} y_{DK}^{\pm}, \quad (4.11)$$

$$y_{D\pi}^{\pm} = x_{D\pi}^{\xi} y_{DK}^{\pm} + y_{D\pi}^{\xi} x_{DK}^{\pm}. \quad (4.12)$$

Note that the  $x_{D\pi}^{\pm}$ ,  $y_{D\pi}^{\pm}$  parameters are not defined in exactly the same way as their  $B^+ \rightarrow DK^+$  counterparts but are instead parameterised in terms of the  $B^+ \rightarrow DK^+$

parameters. This parameterisation is used as it improves fit stability for low values of  $r_{B,D\pi}$  and is possible since the  $CP$  parameters for the  $B^+ \rightarrow DK^+$  and  $B^+ \rightarrow D\pi^+$  decays are not independent [64]. The definitions for all other parameters are the same as for  $B^+ \rightarrow DK^+$  besides trivial differences due to mapping  $DK \mapsto D\pi$ .

### 4.1.3 Charm factory inputs

Using quantum correlated pairs of  $D^0$  and  $\bar{D}^0$  decays the CLEO and BES-III collaborations have measured the values of the  $c_i$  and  $s_i$  parameters in  $D \rightarrow K_S^0 \pi^+ \pi^-$  and  $D \rightarrow K_S^0 K^+ K^-$  decays [62, 65, 66]. In the latest BES-III papers these measurements are combined to yield the most precise constraints of these parameters, performed with the same Dalitz binning schemes as is used in LHCb measurements. Therefore in LHCb fits these parameters can be fixed to the measured values and their uncertainty treated as a source of systematic uncertainty in the  $CP$  fit. As in the measurement of  $\gamma$  using  $B^0 \rightarrow DK^{*0}$ ,  $D \rightarrow K_S^0 h^+ h^-$  decays an additional systematic will be to determine the effect of the non-flat efficiency profile across the  $D$  Dalitz plane in this analysis [67].

### 4.1.4 Recursive parameterisation

Since the  $F_{\pm i}$  parameters are the fraction of decays that populate each bin they must satisfy

$$\sum_{-\mathcal{N} \leq i \leq \mathcal{N}, i \neq 0} F_{\pm i} = 1, \quad (4.13)$$

where  $\mathcal{N}$  is the number of positively indexed  $D$  Dalitz bins for the given  $D$  final state. It was found that in the  $B^+ \rightarrow Dh^+$  analysis constraining the sum of these parameters results in instability in the fits, so an alternate parameterisation was devised

$$R_i = \begin{cases} F_i & \text{for } i = -\mathcal{N}, \\ F_i / \left( \sum_{j \geq i} F_j \right) & \text{for } -\mathcal{N} < i < \mathcal{N}, \end{cases} \quad (4.14)$$

with the inverse relations given by

$$F_i = \begin{cases} R_i & \text{for } i = -\mathcal{N}, \\ R_i \prod_{j < i} (1 - R_j) & \text{for } -\mathcal{N} < i < \mathcal{N}, \\ Z \prod_{j < i} (1 - R_j) & \text{for } i = \mathcal{N}. \end{cases} \quad (4.15)$$

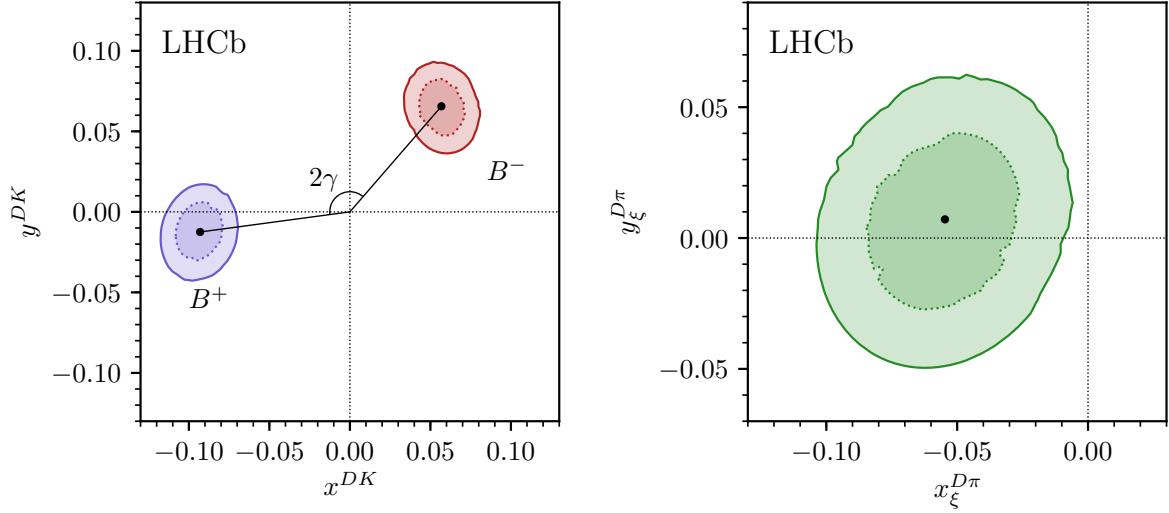


Figure 4.4: Contour plot of the single Dalitz  $B^+ \rightarrow Dh^+$  analysis result for the  $x_{DK}^{\pm}$ ,  $y_{DK}^{\pm}$ ,  $x_{D\pi}^{\xi}$  &  $y_{D\pi}^{\xi}$  parameters. From Ref. [56].

In the  $CP$  fit the  $F_{\pm i}$  parameters are instead re-parameterised according to Eqs. (4.14) and (4.15) for input to Eq. (4.3).

#### 4.1.5 Analysis result

Using this method the LHCb collaboration has presented the results from an analysis of data corresponding to an integrated luminosity of  $9 \text{ fb}^{-1}$  collected from the LHC with the LHCb detector over the periods 2011-2012 and 2015-2018. Following data collection, selection and fits to determine invariant mass PDF shapes the angle  $\gamma$  is extracted from a two-step fit.

1. The  $CP$  fit: A global per-bin mass fit is performed simultaneously with the fit of Eq. (4.3) to the yield of the signal PDF within the signal window.
2. The interpretation: The Cartesian parameters  $x_{DK}^{\pm}$ ,  $y_{DK}^{\pm}$ ,  $x_{D\pi}^{\xi}$ ,  $y_{D\pi}^{\xi}$  are fitted together in a multivariate Gaussian fit to extract  $\gamma$ ,  $r_{B,DK}$ ,  $r_{B,D\pi}$ ,  $\delta_{B,DK}$  and  $\delta_{B,D\pi}$ .

This analysis has been performed a number of times with slight variations, particularly to the  $F_{\pm i}$  measurement method, by the LHCb collaboration [56, 68–70]. The most recent result is the most sensitive single measurement of  $\gamma$  and yields the result,  $\gamma = (68.7^{+5.2}_{-5.1})^\circ$ . The central values and 2D contours of the Cartesian parameters are shown in Fig. 4.4.

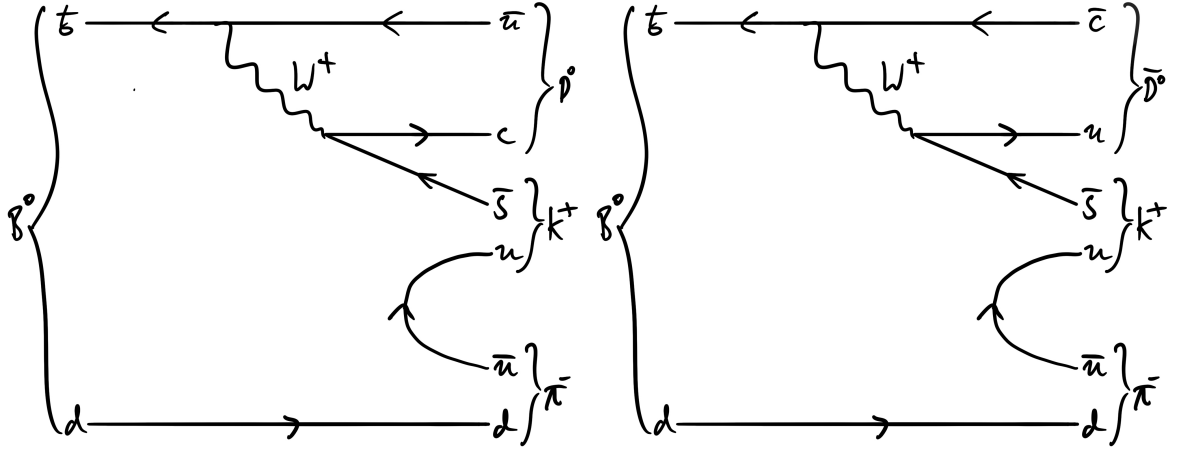


Figure 4.5: Feynman diagrams for the suppressed (left) and favoured (right)  $B^0 \rightarrow DK^+\pi^-$  decays.

## 4.2 The double Dalitz analysis

The double Dalitz plane method can be used to perform a model-independent measurement of  $\gamma$  using  $B^0 \rightarrow DK^+\pi^-$  decays, whose Feynman diagrams are shown in Fig. 4.5. This was first proposed in 2009 [71]. In 2016 the first study of  $CP$  violation with an amplitude analysis of  $B^0 \rightarrow DK^+\pi^-$  decays was performed, from which a model of the resonance structure was obtained [72]. A signal-only binning optimisation was then performed in 2018 [73], the resulting binning scheme is shown in Fig. 4.6. For comparison Fig. 4.6 also shows the Dalitz distribution of this decay in fully selected LHCb data. It was found during the analysis that because this binning is optimised considering only the signal decay Dalitz distribution, it is not optimal in the presence of backgrounds since the distribution of these can change the magnitude of the  $CP$  asymmetry of each bin relative to the total population of the bin. It was found that merging bins four and five is sufficient to obtain a stable fit. Therefore unless otherwise specified the binning with bins four and five merged is referred to as the  $B$  Dalitz plane binning and the binning shown in Fig. 4.6 is referred to as the signal-only optimal binning.

The heart of the analysis method lies in the consideration of  $B^0 \rightarrow DK^+\pi^-$ ,  $D \rightarrow K_S^0 h^+ h^-$  decays as a double Dalitz system. This means that the Dalitz planes are populated simultaneously by each decay, effectively coupling them together. In a binned analysis this results in  $2 \times \mathcal{M} \times 2\mathcal{N}$  observables per decay mode, where  $\mathcal{M}$  ( $\mathcal{N}$ ) is the number of positively indexed bins in the  $B$  ( $D$ ) Dalitz plane and the factors of two correspond to the two  $B^0$  flavours and the split bins in the  $D$  Dalitz plane. Furthermore this allows for a



larger dataset to be used than in a “quasi-two-body”  $B^0 \rightarrow DK^{*0}$ ,  $D \rightarrow K_S^0 h^+ h^-$  single Dalitz analysis since decays across the whole  $B^0 \rightarrow DK^+ \pi^-$  Dalitz plane can be used rather than just those within a cut around the  $K^*(892)$  resonance. This also allows one to take advantage of the full set of  $B^0 \rightarrow DK^+ \pi^-$  resonances which introduces additional sources of interference across the Dalitz plane. The  $B^0 \rightarrow DK^+ \pi^-$  decays themselves are also inherently more sensitive to  $\gamma$  than  $B^+ \rightarrow DK^+$  decays since sensitivity to  $\gamma$  is proportional to the magnitude of interference between the  $D^0$  and  $\bar{D}^0$  decays. This can be quantified by the ratio of the magnitudes of each decay amplitude, for  $B^0 \rightarrow DK^{*0}$  this is  $0.233 \pm 0.016$  [19] whereas for  $B^+ \rightarrow DK^+$  this is  $0.0904^{+0.0077}_{-0.0075}$  [56]. In the case of  $B^0 \rightarrow DK^+ \pi^-$  decays, both the favoured and suppressed decays are colour suppressed whereas for  $B^+ \rightarrow DK^+$  decays only one is colour suppressed which allows for this larger ratio. However the branching fraction of  $B^0 \rightarrow DK^+ \pi^-$ ,  $(8.8 \pm 1.7) \times 10^{-5}$ , is lower than that of  $B^+ \rightarrow DK^+$ ,  $(3.64 \pm 0.15) \times 10^{-4}$ , and has a greater number of final state particles to detect, so ignoring any further experimental effects this results in a considerably smaller  $B^0 \rightarrow DK^+ \pi^-$  dataset than  $B^+ \rightarrow DK^+$  [7]. One great benefit of this analysis method is the ability to utilise a vast number of additional decay modes. Given that the analysis revolves around both the  $B^0 \rightarrow DK^+ \pi^-$  and  $D \rightarrow K_S^0 h^+ h^-$  Dalitz planes single Dalitz decays related to either of the Dalitz planes can be incorporated, this analysis exclusively uses  $B^0 \rightarrow DK^+ \pi^-$  decays with varying  $D$  final states. This results in greater sensitivity to the hadronic parameters of each binned Dalitz plane and therefore greater sensitivity to  $\gamma$ . These decays in general also contribute their own direct sensitivity to  $\gamma$  depending on what particular final states are considered. Some of these additional decay modes are incorporated by studying their data directly, this is motivated in Section 4.2.5, whereas others are incorporated just by using previous measurements to provide external inputs which are explained in Section 4.3. First the binned signal expectation equation must be

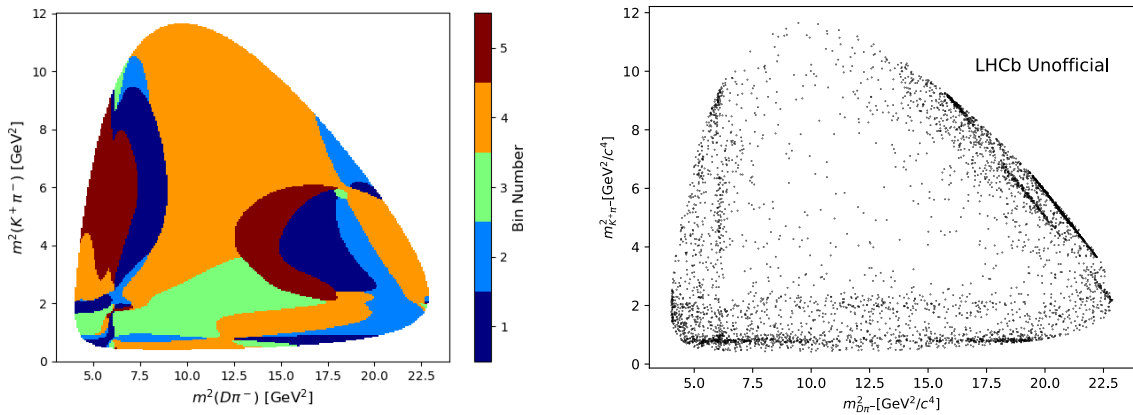


Figure 4.6: Signal-only optimal binning scheme (left) for the Dalitz plane of  $B^0 \rightarrow DK^+ \pi^-$  decays and (right) the distribution of such decays in fully selected Run 1 and 2 LHCb data.

derived.

### 4.2.1 Deriving the expectation equation for the general double Dalitz binned signal population

**Definitions** The amplitudes of each decay must first be defined. The favoured and suppressed  $B^0 \rightarrow DK^+\pi^-$  decays can be written with the strong-phases explicitly stated and the constant weak-phase difference  $\gamma$  assigned to the suppressed amplitude as

$$A_B(s_{D\pi}, s_{K\pi}) = A(B^0 \rightarrow D^0 K^+ \pi^-) \equiv e^{i\gamma} |A_B(s_{D\pi}, s_{K\pi})| e^{i\delta_B(s_{D\pi}, s_{K\pi})}, \quad (4.16)$$

$$\bar{A}_B(s_{D\pi}, s_{K\pi}) = A(B^0 \rightarrow \bar{D}^0 K^+ \pi^-) \equiv |\bar{A}_B(s_{D\pi}, s_{K\pi})| e^{i\delta_B(s_{D\pi}, s_{K\pi})}, \quad (4.17)$$

where  $s_{D\pi}$  ( $s_{K\pi}$ ) are the squared invariant masses of the  $D\pi$  ( $K\pi$ ) combinations, respectively. The equivalent definitions for a  $\bar{B}^0$  initial state are obtained by the transformation  $\gamma \mapsto -\gamma$ . In the case of a subsequent  $D$  decay to a 3-body final state, both the  $B$  and  $D$  decay modes have a corresponding Dalitz plane. The  $D^0 \rightarrow K_S^0 h^+ h^-$  and  $\bar{D}^0 \rightarrow K_S^0 h^+ h^-$  amplitudes are defined as

$$A_{D^0}(s_-, s_+) = A(D^0 \rightarrow K_S^0 h^+ h^-) \equiv |A_{D^0}(s_-, s_+)| e^{i\delta_{D^0}(s_-, s_+)}, \quad (4.18)$$

$$A_{\bar{D}^0}(s_-, s_+) = A(\bar{D}^0 \rightarrow K_S^0 h^+ h^-) \equiv |A_{\bar{D}^0}(s_-, s_+)| e^{i\delta_{\bar{D}^0}(s_-, s_+)}, \quad (4.19)$$

where  $s_{\pm}$  are the squared invariant masses of the  $Dh^{\pm}$  combinations, respectively.

**Derivation** In the following the  $(s_{D\pi}, s_{K\pi})$  notation is omitted and the  $(s_-, s_+)$  is replaced with  $\pm$  superscripts for ease of reading. Note the following assumptions and basic equalities. It is assumed that there is no direct  $CP$  violation in the  $D$  decay so one can write

$$A_D^{+-} = \bar{A}_D^{-+}, \quad (4.20)$$

and because strong-phases are invariant under  $CP$  conjugation

$$\Delta\delta_B \equiv \delta_{B^0} - \bar{\delta}_{B^0} = \delta_{\bar{B}^0} - \bar{\delta}_{\bar{B}^0}, \quad (4.21)$$

$$\Delta\delta_D \equiv \delta_{D^0}^{-+} - \delta_{\bar{D}^0}^{-+} = \delta_{D^0}^{+-} - \delta_{\bar{D}^0}^{+-}. \quad (4.22)$$

For  $B^0 \rightarrow DK^+\pi^-$ ,  $D \rightarrow K_S^0 h^+ h^-$  decays one can write the amplitude of the decay given

the admixture of the  $D$  flavour as

$$A = \bar{A}_{B^0} A_{\bar{D}^0}^{-+} e^{i\delta_{B^0}} e^{i\delta_{\bar{D}^0}^{++}} + e^{i\gamma} A_{B^0} A_{\bar{D}^0}^{-+} e^{i\delta_{B^0}} e^{i\delta_{\bar{D}^0}^{++}} \quad (4.23)$$

$$= \bar{A}_{B^0} A_{\bar{D}^0}^{-+} + e^{i\gamma} A_{B^0} A_{\bar{D}^0}^{-+} e^{i\Delta\delta_B} e^{i\Delta\delta_D}, \quad (4.24)$$

$$|A|^2 = \bar{A}_{B^0}^2 A_{\bar{D}^0}^{-+2} + A_{B^0}^2 A_{\bar{D}^0}^{-+2} + 2\sqrt{\bar{A}_{B^0} A_{\bar{D}^0}^{-+} A_{B^0} A_{\bar{D}^0}^{-+}} [\cos(\Delta\delta_D + (\Delta\delta_B + \gamma))] \quad (4.25)$$

$$\begin{aligned} &= \bar{A}_{B^0}^2 A_{\bar{D}^0}^{-+2} + A_{B^0}^2 A_{\bar{D}^0}^{-+2} + 2\sqrt{\bar{A}_{B^0} A_{\bar{D}^0}^{-+} A_{B^0} A_{\bar{D}^0}^{-+}} \\ &\quad \times [\cos(\Delta\delta_D)\cos(\Delta\delta_B + \gamma) - \sin(\Delta\delta_D)\sin(\Delta\delta_B + \gamma)] \\ &= \bar{A}_{B^0}^2 A_{\bar{D}^0}^{-+2} + A_{B^0}^2 A_{\bar{D}^0}^{-+2} + 2\sqrt{\bar{A}_{B^0} A_{\bar{D}^0}^{-+} A_{B^0} A_{\bar{D}^0}^{-+}} \\ &\quad \times [(\cos(\Delta\delta_D)\cos(\Delta\delta_B) - \sin(\Delta\delta_D)\sin(\Delta\delta_B))\cos(\gamma) \\ &\quad - (\sin(\Delta\delta_D)\cos(\Delta\delta_B) + \cos(\Delta\delta_D)\sin(\Delta\delta_B))\sin(\gamma)]. \end{aligned} \quad (4.26)$$

Performing a similar derivation for  $\bar{B}^0$  decays and integrating the result and Eq. (4.26) across each bin yields the expected population of  $\bar{B}^0 \rightarrow DK^\pm\pi^\mp$  decays in each bin  $(\alpha, i)$ , with the superscript  $+$  $(-)$  denoting a  $\bar{B}^0$  decay

$$\begin{aligned} N_{\alpha,i}^\pm &= h_D^\pm \{ \bar{\kappa}_\alpha F_{\mp i} + \kappa_\alpha F_{\pm i} + 2\sqrt{\kappa_\alpha F_{+i} \bar{\kappa}_\alpha F_{-i}} \\ &\quad \times [(\chi_\alpha c_i \mp \sigma_\alpha s_i)\cos(\gamma) \mp (\sigma_\alpha c_i \mp \chi_\alpha s_i)\sin(\gamma)] \}, \end{aligned} \quad (4.27)$$

where these parameters can be interpreted as

- $h_D^\pm$  is a normalisation parameter, the total number of  $B^0$  decays to the desired  $D$  final state.
- $(\bar{\kappa})_\alpha$  is the fraction of pure  $B^0 \rightarrow \bar{D}^0 K^+ \pi^-$  decays in bin  $\alpha$ .
- $\chi_\alpha$  ( $\sigma_\alpha$ ) is the amplitude-weighted cosine (sine) of the average strong-phase difference between the suppressed and favoured  $B$  decays in bin  $\alpha$ .

The formal definitions in analogy with Eqs. (4.5) to (4.8) are

$$(\bar{\kappa})_\alpha = \frac{1}{N_B} \int_\alpha \eta_B(s_{D\pi}, s_{K\pi}) |\bar{A}_B(s_{D\pi}, s_{K\pi})|^2 ds^2, \quad (4.28)$$

$$\chi_\alpha = \frac{\int_\alpha \eta_B(s_{D\pi}, s_{K\pi}) |A_B(s_{D\pi}, s_{K\pi})| |\bar{A}_B(s_{D\pi}, s_{K\pi})| \cos \Delta\delta_B(s_{D\pi}, s_{K\pi}) ds^2}{\sqrt{\int_\alpha |A_B(s_{D\pi}, s_{K\pi})|^2 ds^2 \int_\alpha |\bar{A}_B(s_{D\pi}, s_{K\pi})|^2 ds^2}}, \quad (4.29)$$

$$\sigma_\alpha = \frac{\int_\alpha \eta_B(s_{D\pi}, s_{K\pi}) |A_B(s_{D\pi}, s_{K\pi})| |\bar{A}_B(s_{D\pi}, s_{K\pi})| \sin \Delta\delta_B(s_{D\pi}, s_{K\pi}) ds^2}{\sqrt{\int_\alpha |A_B(s_{D\pi}, s_{K\pi})|^2 ds^2 \int_\alpha |\bar{A}_B(s_{D\pi}, s_{K\pi})|^2 ds^2}} \quad (4.30)$$

where

$$N_B = \int_{\mathcal{B}} \eta_B(s_{D\pi}, s_{K\pi}) (|A_B(s_{D\pi}, s_{K\pi})|^2 + |\bar{A}_B(s_{D\pi}, s_{K\pi})|^2) ds^2, \quad (4.31)$$

$\eta_B$  is the experimental acceptance as a function of the  $B$  Dalitz plane variables and  $\int ds^2 \equiv \int ds_{D\pi} ds_{K\pi}$  i.e. the integral over the Dalitz plane as a whole,  $\mathcal{B}$ , or bin  $\alpha$  of the Dalitz plane.

### 4.2.2 Re-parameterising the normalisation parameters

In the nominal fit configuration the total asymmetry between the two normalisation parameters is exploited such that for each  $D$  final states besides  $D \rightarrow K_S^0 h^+ h^-$  there is a single normalisation parameter  $h_D$  such that the per-flavour normalisations are written as

$$h_D^+ = h_D(1 + A), \quad (4.32)$$

$$h_D^- = h_D(1 - A), \quad (4.33)$$

where  $A$  quantifies the total production and detection asymmetry between  $B^0$  and  $\bar{B}^0$  decays. The value of  $A$  is fixed from external measurements and its uncertainty treated as a source of systematic uncertainty. Note that at the time of writing this has not yet been implemented into the  $CP$  fit, it will be added alongside the remaining systematics. The input values will be determined in the same way as in Ref. [19]. The effect of  $B^0$  mixing could also be incorporated though this is expected to have a negligible effect. For the  $D \rightarrow K_S^0 h^+ h^-$  decays however this shared normalisation would result in a bias to the values of the  $CP$  parameters due to the effect of  $CP$  violation and material interactions of the  $K_S^0$  [63] so the per-flavour normalisation parameters are instead written

$$h_D^+ = n_D^+(1 + A), \quad (4.34)$$

$$h_D^- = n_D^-(1 - A), \quad (4.35)$$

where  $n_D^\pm$  are the per-flavour normalisations in the absence of detector effects.

### 4.2.3 The Cartesian parameterisation

Equation (4.27) is written with  $\gamma$  appearing explicitly, however it is difficult to include explicit measurements of  $\gamma$  in a combination as the uncertainty distribution is typically non-Gaussian, therefore it is beneficial to use a Cartesian parameterisation instead [74, 75]. Therefore, as in Eq. (4.3), it is beneficial to choose a parameterisation where Cartesian  $CP$  parameters are fitted and then  $\gamma$  is extracted from them in a second fit.

Cartesian  $CP$  parameters can be defined as

$$x_{\alpha}^{\pm} = T_{\alpha} \cos(\Delta\delta_{\alpha} \pm \gamma), \quad y_{\alpha}^{\pm} = T_{\alpha} \sin(\Delta\delta_{\alpha} \pm \gamma), \quad (4.36)$$

where

- $T_{\alpha}$  is the coherence factor for bin  $\alpha$ ,
- $\Delta\delta_{\alpha}$  is the average strong-phase difference between the suppressed and favoured  $B$  decays in bin  $\alpha$ .

This is inspired by the quasi-two-body analyses of, *e.g.*  $B^0 \rightarrow DK^{*0}$  in Refs. [72, 76], where these parameters are formally according to

$$T_{\alpha} e^{i\Delta\delta_{\alpha}} = \frac{\int_{\alpha} |A_B(s_{D\pi}, s_{K\pi}) \bar{A}_B(s_{D\pi}, s_{K\pi})| \exp[i\Delta\delta_B(s_{D\pi}, s_{K\pi})] ds^2}{\sqrt{\int_{\alpha} |A_B(s_{D\pi}, s_{K\pi})|^2 ds^2 \int_{\alpha} |\bar{A}_B(s_{D\pi}, s_{K\pi})|^2 ds^2}}. \quad (4.37)$$

They can be identified with the  $B$  plane hadronic parameters in Eq. (4.27) by the relations

$$\tan \Delta\delta_{\alpha} = \sigma_{\alpha} / \chi_{\alpha}, \quad T_{\alpha}^2 = \chi_{\alpha}^2 + \sigma_{\alpha}^2. \quad (4.38)$$

Therefore one can now write

$$N_{\alpha,i}^{\pm} = h_D^{\pm} [\bar{\kappa}_{\alpha} F_{\mp i} + \kappa_{\alpha} F_{\pm i} + 2\sqrt{\bar{\kappa}_{\alpha} \kappa_{\alpha}} F_{-i} F_{+i} (c_i x_{\alpha}^{\pm} \mp s_i y_{\alpha}^{\pm})], \quad (4.39)$$

in close analogy to Eq. (4.27).

#### 4.2.4 Binned amplitude ratios

The sensitivity of various  $B$  decays to  $\gamma$  is often discussed in terms of the ratios of their favoured and suppressed amplitudes since this controls the magnitude of their interference within the chosen phase space. It is therefore instructive to measure the  $r_{\alpha}$  parameter for each  $B$  Dalitz bin. These are not measured directly in the analysis as this complicates the implementation of the fits, however they can be calculated after the fits using the relation

$$r_{\alpha} = \sqrt{\frac{\kappa_{\alpha}}{\bar{\kappa}_{\alpha}}}. \quad (4.40)$$

These are reported alongside the other measured parameters in the final result in Section 8.2.

### 4.2.5 The expectation equation for all $D$ final states of interest

Since this is a generalisation of a single Dalitz analysis, whether the Dalitz plane of interest is the  $B$  or  $D$  decay, one can use trivial mappings to obtain the expectation equations for all the  $D$  final states used in the analysis from Eq. (4.27). These decay modes are chosen either because they are known to have high sensitivity to  $\gamma$  itself or to certain hadronic parameters of the  $B$  Dalitz plane.

#### $D \rightarrow K^\pm \pi^\mp$ & $D \rightarrow K^\pm \pi^\mp \pi^+ \pi^-$

The first additional decay modes to consider are the doubly Cabibbo favoured  $D \rightarrow K^\pm \pi^\mp$  and  $D \rightarrow K^\pm \pi^\mp \pi^+ \pi^-$  decays. These decays serve a similar purpose to the  $B^+ \rightarrow D\pi^+$  decays in the single Dalitz  $B^+ \rightarrow Dh^+$  analysis since they have very little interference effects and high branching fractions so provide information about the hadronic  $\bar{\kappa}_\alpha$  parameters. To obtain the binned signal expectation for favoured  $B^0 \rightarrow DK^+\pi^-$ ,  $D \rightarrow K^\pm \pi^\mp$  decays the  $D$  decay Dalitz coordinate dependent amplitudes are substituted in Eq. (4.26) with  $A(\bar{D}^0 \rightarrow K^\pm \pi^\mp)$ . Given the definition

$$r_{D,K\pi} e^{i\delta_{D,K\pi}} \equiv \frac{A(D^0 \rightarrow K^\pm \pi^\mp)}{A(\bar{D}^0 \rightarrow K^\pm \pi^\mp)}, \quad (4.41)$$

one can write

$$N_\alpha^\pm = h_D^\pm [\bar{\kappa}_\alpha + r_{D,K\pi}^2 \kappa_\alpha + 2r_{D,K\pi} \kappa_{D,K\pi\pi\pi} \sqrt{\bar{\kappa}_\alpha \kappa_\alpha} \times (\cos(\Delta\delta_{D,K\pi}) x_\alpha^\pm \mp \sin(\Delta\delta_{D,K\pi}) y_\alpha^\pm)], \quad (4.42)$$

$$N_\alpha^\pm = h_D^\pm [\bar{\kappa}_\alpha + r_{D,K\pi\pi\pi}^2 \kappa_\alpha + 2r_{D,K\pi\pi\pi} \kappa_{D,K\pi\pi\pi} \sqrt{\bar{\kappa}_\alpha \kappa_\alpha} \times (\cos(\Delta\delta_{D,K\pi\pi\pi}) x_\alpha^\pm \mp \sin(\Delta\delta_{D,K\pi\pi\pi}) y_\alpha^\pm)], \quad (4.43)$$

for the favoured  $D \rightarrow K^\pm \pi^\mp$  and  $D \rightarrow K^\pm \pi^\mp \pi^+ \pi^-$  decays respectively.

The equivalent equation for the suppressed  $D \rightarrow K^\pm \pi^\mp$  and  $D \rightarrow K^\pm \pi^\mp \pi^+ \pi^-$  decays can be obtained by  $\kappa_\alpha \leftrightarrow \bar{\kappa}_\alpha$ . The values of  $r_{D,K\pi}$  and  $r_{D,K\pi\pi\pi}$  are  $\mathcal{O}(0.06)$  therefore one can infer from the above expressions that the favoured decays primarily provide sensitivity to the  $\bar{\kappa}_\alpha$  parameters since the  $\bar{\kappa}_\alpha$  term dominates the expectation of each bin [17, 77]. In contrast however the suppressed modes have larger interference terms relative to the squared amplitude terms, resulting in greater inherent sensitivity to  $\gamma$ . The associated datasets of these final states are, however, relatively small.

#### $D \rightarrow K^+ K^-$ & $D \rightarrow \pi^+ \pi^-$

These  $CP$ -even eigenstates are known to provide good sensitivity to  $\gamma$ , first motivated in Refs. [78, 79] and shown for example in a recent analysis Ref. [19], and have the signal

expectation

$$N_{\alpha}^{\pm} = h_{\text{D}}^{\pm} [\bar{\kappa}_{\alpha} + \kappa_{\alpha} + 2\sqrt{\bar{\kappa}_{\alpha}\kappa_{\alpha}}x_{\alpha}^{\pm}]. \quad (4.44)$$

$D \rightarrow \pi^{+}\pi^{-}\pi^{+}\pi^{-}$

This 4-body final state, if one ignores the multi-body dynamics, can be treated similarly to the 2-body  $CP$ -even eigenstates up to the addition of a  $CP$ -even fraction,  $F_{4\pi}^{+}$ , resulting in the signal expectation

$$N_{\alpha}^{\pm} = h_{\text{D}}^{\pm} [\bar{\kappa}_{\alpha} + \kappa_{\alpha} + (2F_{4\pi}^{+} - 1)\sqrt{\bar{\kappa}_{\alpha}\kappa_{\alpha}}x_{\alpha}^{\pm}]. \quad (4.45)$$

#### 4.2.6 Full observables and parameters list

Table 4.1 lists the number of observables and parameters associated with each decay mode. As explained in Section 3.2.1 data containing reconstructed  $K_{\text{S}}^0$  mesons is split between categories LL and DD. These different datasets therefore have slightly different efficiencies across the  $D$  Dalitz plane resulting in noticeably different  $F_{\pm i}$  values for the LL and DD categories, relative to their uncertainties. Therefore each category has its own independent set of  $F_{\pm i}$  parameters. The  $c_i$  and  $s_i$  parameters are not split between LL and DD and all subscript  $\alpha$  parameters are shared across all decay modes.

$D$ decay	$N_{\text{Obs}}$	$N_{\text{Par}}$	$N_{\text{Fixed}}$	$N_{\text{Free}}$	Parameters
$D \rightarrow K_S^0 \pi^+ \pi^-$ (LL)	128	58	32	26	$(h_{D \rightarrow K_S^0 \pi^+ \pi^-, \text{LL}}^\pm, \overline{\kappa}_\alpha^\pm, x_\alpha^\pm, y_\alpha^\pm, F_{\pm i}, C_i, s_i)$
$D \rightarrow K_S^0 \pi^+ \pi^-$ (DD)	128	58	32	26	$(h_{D \rightarrow K_S^0 \pi^+ \pi^-, \text{DD}}^\pm, \overline{\kappa}_\alpha^\pm, x_\alpha^\pm, y_\alpha^\pm, F_{\pm i}, C_i, s_i)$
$D \rightarrow K_S^0 K^+ K^-$ (LL)	32	34	8	26	$(h_{D \rightarrow K_S^0 K^+ K^-, \text{LL}}^\pm, \overline{\kappa}_\alpha^\pm, x_\alpha^\pm, y_\alpha^\pm, F_{\pm i}, C_i, s_i)$
$D \rightarrow K_S^0 K^+ K^-$ (DD)	32	34	8	26	$(h_{D \rightarrow K_S^0 K^+ K^-, \text{DD}}^\pm, \overline{\kappa}_\alpha^\pm, x_\alpha^\pm, y_\alpha^\pm, F_{\pm i}, C_i, s_i)$
$D \rightarrow K^\pm \pi^\mp$	8	27	2	25	$(h_{D \rightarrow K^\pm \pi^\mp}^\pm, \overline{\kappa}_\alpha^\pm, x_\alpha^\pm, y_\alpha^\pm, r_{D, K\pi}, \Delta\delta_{D, K\pi})$
$D \rightarrow \pi^\pm K^\mp$	8	27	2	25	$(h_{D \rightarrow \pi^\pm K^\mp}^\pm, \overline{\kappa}_\alpha^\pm, x_\alpha^\pm, y_\alpha^\pm, r_{D, K\pi}, \Delta\delta_{D, K\pi})$
$D \rightarrow K^+ K^-$	8	25	0	25	$(h_{D \rightarrow K^+ K^-}^\pm, \overline{\kappa}_\alpha^\pm, x_\alpha^\pm, y_\alpha^\pm)$
$D \rightarrow \pi^+ \pi^-$	8	25	0	25	$(h_{D \rightarrow \pi^+ \pi^-}^\pm, \overline{\kappa}_\alpha^\pm, x_\alpha^\pm, y_\alpha^\pm)$
$D \rightarrow K^\pm \pi^\mp \pi^+ \pi^-$	8	28	3	25	$(h_{D \rightarrow K^\pm \pi^\mp \pi^+ \pi^-}^\pm, \overline{\kappa}_\alpha^\pm, x_\alpha^\pm, y_\alpha^\pm, r_{D, K\pi\pi}, \Delta\delta_{D, K\pi\pi}, \kappa_{D, K\pi\pi})$
$D \rightarrow \pi^\pm K^\mp \pi^+ \pi^-$	8	28	3	25	$(h_{D \rightarrow \pi^\pm K^\mp \pi^+ \pi^-}^\pm, \overline{\kappa}_\alpha^\pm, x_\alpha^\pm, y_\alpha^\pm, r_{D, K\pi\pi}, \Delta\delta_{D, K\pi\pi}, \kappa_{D, K\pi\pi})$
$D \rightarrow \pi^+ \pi^- \pi^+ \pi^-$	8	26	1	25	$(h_{D \rightarrow \pi^+ \pi^- \pi^+ \pi^-}^\pm, \overline{\kappa}_\alpha^\pm, x_\alpha^\pm, y_\alpha^\pm, F_{4\pi}^+)$
<b>Total</b>	<b>376</b>	<b>85</b>	<b>46</b>	<b>39</b>	

Table 4.1: Modes included in the nominal fit with numbers of observables ( $N_{\text{Obs}}$ ) and parameters ( $N_{\text{Par}}$ ). The number of parameters is split into those which are fixed from external inputs ( $N_{\text{Fixed}}$ ) and those which have to be allowed to vary freely ( $N_{\text{Free}}$ ). The parameters column specifies the groups of parameters associated with each decay in the  $CP$  fit. This assumes four bins in the  $B$  decay plane, 16 bins in the  $D \rightarrow K_S^0 \pi^+ \pi^-$  decay plane and four bins in the  $D \rightarrow K_S^0 K^+ K^-$  decay plane.



### 4.3 External inputs

The introduction of additional decays introduces a number of new parameters. In principle, all of them could be measured in this analysis, however many of these parameters have already been measured by LHCb and/or CLEO-c & BES-III to greater precision than would be accessible in this analysis. Since there would be little to gain by complicating the  $CP$  fit by constraining these parameters according to these previous measurements, these are fixed to the measured values and their uncertainties are treated as a source of systematic uncertainty. All external parameters used in the analysis and their measured values are specified in Table 4.2.

$D$ decay	Parameter	Value $\pm$ Uncertainty	Source
$D \rightarrow K_S^0 \pi^+ \pi^-$	$c_1$	$-0.037 \pm 0.049$	Table 17 of Ref. [65]
	$c_2$	$0.837 \pm 0.067$	
	$c_3$	$0.147 \pm 0.067$	
	$c_4$	$-0.905 \pm 0.021$	
	$c_5$	$-0.291 \pm 0.041$	
	$c_6$	$0.272 \pm 0.082$	
	$c_7$	$0.918 \pm 0.017$	
	$c_8$	$0.773 \pm 0.033$	
	$s_1^*$	$0.829 \pm 0.097$	
	$s_2^*$	$0.286 \pm 0.152$	
	$s_3^*$	$0.786 \pm 0.154$	
	$s_4^*$	$0.079 \pm 0.059$	
	$s_5^*$	$-1.022 \pm 0.064$	
	$s_6^*$	$-0.977 \pm 0.176$	
	$s_7^*$	$-0.184 \pm 0.065$	
	$s_8^*$	$0.277 \pm 0.118$	
$D \rightarrow K_S^0 \pi^+ \pi^-$ LL	$R_{-8}$	$0.0243 \pm 0.0007$	[56], Table 51 of Ref. [80]
	$R_{-7}$	$0.1304 \pm 0.0014$	
	$R_{-6}$	$0.0734 \pm 0.0012$	
	$R_{-5}$	$0.0584 \pm 0.0011$	
	$R_{-4}$	$0.1281 \pm 0.0017$	
	$R_{-3}$	$0.2472 \pm 0.0024$	
	$R_{-2}$	$0.3147 \pm 0.0033$	
	$R_{-1}$	$0.2851 \pm 0.0033$	

	$R_1$	$0.0906 \pm 0.0024$	
	$R_2$	$0.0224 \pm 0.0015$	
	$R_3$	$0.0204 \pm 0.0013$	
	$R_4$	$0.2638 \pm 0.0039$	
	$R_5$	$0.1752 \pm 0.0039$	
	$R_6$	$0.0316 \pm 0.0021$	
	$R_7$	$0.4541 \pm 0.0062$	
$D \rightarrow K_S^0 \pi^+ \pi^-$ DD	$R_{-8}$	$0.0240 \pm 0.0004$	[56], Table 51 of Ref. [80]
	$R_{-7}$	$0.1362 \pm 0.0009$	
	$R_{-6}$	$0.0670 \pm 0.0008$	
	$R_{-5}$	$0.0537 \pm 0.0007$	
	$R_{-4}$	$0.1276 \pm 0.0011$	
	$R_{-3}$	$0.2470 \pm 0.0016$	
	$R_{-2}$	$0.3126 \pm 0.0021$	
	$R_{-1}$	$0.2879 \pm 0.0022$	
	$R_1$	$0.0842 \pm 0.0016$	
	$R_2$	$0.0229 \pm 0.0010$	
	$R_3$	$0.0179 \pm 0.0009$	
	$R_4$	$0.2649 \pm 0.0026$	
	$R_5$	$0.1452 \pm 0.0024$	
	$R_6$	$0.0238 \pm 0.0012$	
	$R_7$	$0.4402 \pm 0.0040$	
$D \rightarrow K_S^0 K^+ K^-$	$c_1$	$0.713 \pm 0.032$	Table 17 of Ref. [66]
	$c_2$	$-0.758 \pm 0.037$	
	$s_1^*$	$-0.107 \pm 0.132$	
	$s_2^*$	$-0.394 \pm 0.173$	
$D \rightarrow K_S^0 K^+ K^-$ LL	$R_{-2}$	$0.2068 \pm 0.0044$	[56], Table 52 of Ref. [80]
	$R_{-1}$	$0.2800 \pm 0.0054$	
	$R_1$	$0.5076 \pm 0.0070$	
$D \rightarrow K_S^0 K^+ K^-$ DD	$R_{-2}$	$0.2024 \pm 0.0029$	[56], Table 52 of Ref. [80]
	$R_{-1}$	$0.2885 \pm 0.0038$	
	$R_1$	$0.5218 \pm 0.0048$	
$D \rightarrow K^\pm \pi^\mp$	$\Delta\delta_{D,K\pi} * [^\circ]$	$-190.2^{+2.8}_{-2.8}$	Table 3 of Ref. [17]
$D \rightarrow \pi^\pm K^\mp$	$r_{D,K\pi}$	$0.05865^{+0.00014}_{-0.00015}$	
$D \rightarrow K^\pm \pi^\mp \pi^+ \pi^-$	$\kappa_{D,K\pi\pi\pi}$	$0.44^{+0.10}_{-0.09}$	Table 18 of Ref. [77]
$D \rightarrow \pi^\pm K^\mp \pi^+ \pi^-$	$\Delta\delta_{D,K\pi\pi\pi} * [^\circ]$	$-161^{+28}_{-18}$	
	$r_{D,K\pi\pi\pi}$	$0.0550 \pm 0.07$	

$D \rightarrow \pi^+ \pi^- \pi^+ \pi^-$	$F_{4\pi}^+$	$0.735 \pm 0.016$	Section 6 of Ref. [81]
---	--------------	-------------------	------------------------

Table 4.2: Externally measured parameters, their values and uncertainties, and their source. All uncertainties are the total uncertainties. Parameters marked with an asterisk have the opposite sign to their value in the source measurement due to this analysis using a different phase convention, see Section 4.3.1.

### 4.3.1 Phase conventions

There are many ways that one can define phases. The physics and outcome of the analysis is independent of the convention used as long as it is consistent between all measured parameters and any external inputs. How previously measured values need to be modified to be consistent with the choice of convention is summarised here. In this analysis the convention is that for some favoured  $D$  decay with amplitude  $A_{\text{fav.}}$  and suppressed decay with amplitude  $A_{\text{sup.}}$ , under the assumption of no direct  $CP$  violation between them, the ratio and strong-phase difference is always defined as

$$re^{i\Delta\delta} = \frac{A_{\text{sup.}}}{A_{\text{fav.}}} \quad (4.46)$$

In the BES-III measurement of binned strong-phase parameters for  $D \rightarrow K_S^0 \pi^+ \pi^-$  decays the convention used is  $\Delta\delta_D \equiv \delta_D(m_+^2, m_-^2) - \delta_D(m_-^2, m_+^2)$  [65]. This is equal to  $\delta_{\bar{D}}(m_-^2, m_+^2) - \delta_D(m_-^2, m_+^2)$  and therefore their phase convention is  $\delta_{\text{fav.}} - \delta_{\text{sup.}}$  so for the binned strong-phase parameters  $s_i$  their sign is flipped when inputting them into the  $CP$  fit. The same is true for all other BES-III measurements used as input for  $D \rightarrow K_S^0 K^+ K^-$  [66],  $D \rightarrow K^\pm \pi^\mp$  [17, 82] and  $D \rightarrow K^\pm \pi^\mp \pi^+ \pi^-$  [77].

## 4.4 Binning schemes

Sensitivity to  $\gamma$  depends on bin size since the sensitivity depends on the  $CP$  asymmetry in each bin. The amplitude densities of the decays vary across the Dalitz plane so the larger a bin is the more likely it is that opposite asymmetries cancel out. Therefore the binning must be defined such that the bins are small enough to maintain sizeable asymmetries. However given the present size of the LHCb dataset one must consider the effect of low populations in each bin. A balance must therefore be found between having many small bins that maximise the per-bin asymmetry whilst ensuring that they do not cause fit instabilities.

As mentioned previously, one could also use an amplitude model to measure  $\gamma$ , avoiding binning altogether. For a single Dalitz system one could construct an amplitude model

for the favoured and suppressed modes. As described in Section 2.3 this can be achieved using the isobar model formalism. These models can then be fitted according to Eq. (4.27) to extract  $\gamma$  from the data. However the issue with this method is that the use of a model assumes all resonances and other features of the decay have been correctly incorporated into the model. This results in a hard to evaluate, and typically large, systematic uncertainty. Furthermore many models violate unitarity and analyticity, breaking the link between the amplitude magnitudes and phases resulting in another source of uncertainty [83].

Consequently as available datasets grow the model-dependent method is limited by the systematic uncertainty associated to the choice of model. The advantage of a binned Dalitz analysis is that assumptions are not made about the resonances present across the Dalitz plane or what their particular shapes, amplitudes or weak/strong-phases are. So, even though a binned method induces a greater statistical uncertainty due to the binning this can “simply” be resolved by acquiring more data or by picking a binning that results in as little associated statistical uncertainty as possible.

#### 4.4.1 Binning definitions and optimisation

Thus far the binning of the Dalitz planes has been referred to but it has not yet been explained how this is determined. For all Dalitz planes used in the double Dalitz analysis the optimisation is performed by maximising a binning quality factor [62, 73]

$$Q^2 = \frac{\sum_{\alpha} (\chi_{\alpha}^2 + \sigma_{\alpha}^2) N_{\alpha}}{\sum_{\alpha} N_{\alpha}}, \quad (4.47)$$

where  $N_{\alpha}$  is the number of decays in bin  $\alpha$  assuming  $r_B$  is 0. *i.e.* assuming the suppressed mode is non-existent. This is written in terms of the  $B$  Dalitz plane but the equivalent expression for the  $D$  planes is obtained from  $\alpha \mapsto i, \chi_{\alpha} \mapsto c_i, \sigma_{\alpha} \mapsto s_i$ . This is derived in Ref. [60] as the ratio of the statistical sensitivity between the binning and the unbinned method. Therefore maximising this quantity corresponds to finding the binning scheme for a given number of bins that achieves statistical sensitivity as close to an unbinned method as possible.

## 4.5 Background decays

Following the data acquisition described in Chapter 3 there are still a considerable number of background decays in the resulting dataset. Various methods are employed to obtain a high signal purity data sample, full details are in Chapter 5. A short summary is that PID cuts are applied to remove misidentified backgrounds, boosted decision trees (BDT) are trained to remove combinatorial background and kinematic vetoes are determined to

remove specific backgrounds by searching for peaks in the invariant mass spectra of various combinations of final state particles. It is practically impossible to develop a selection method that would result in a  $\sim 100\%$  pure sample of  $B^0 \rightarrow DK^+\pi^-$  decays, or at least not without a tiny signal efficiency. Therefore one cannot simply compare Eq. (4.39) directly to the data to extract the  $CP$  parameters. The background that remains within the data sample must be accounted for. To do this one can consider a total expectation equation as the sum of the signal expectation and the background expectation. The background expectation, for a background source  $b$ , is constructed as the product of the total amount of that background that infiltrates the signal window,  $y^b$ , with the fraction of that background that is expected to be present in bin  $(\alpha, i)$ ,  $f_{\alpha,i}^b$ . The total expectation is therefore

$$N_{\alpha,i}^{\pm} = h_D^{\pm} [\bar{\kappa}_{\alpha} F_{\mp i} + \kappa_{\alpha} F_{\pm i} + 2\sqrt{\bar{\kappa}_{\alpha}\kappa_{\alpha} F_{-i} F_{+i}} (c_i x_{\alpha}^{\pm} \pm s_i y_{\alpha}^{\pm})] + \sum_{b \in \mathcal{B}} y^b f_{\alpha,i}^b, \quad (4.48)$$

where  $\mathcal{B}$  is the set of all backgrounds that infiltrate the signal window.

Per-flavour invariant mass fits are performed for each  $D$  decay, from which  $y^b$  is determined as the yield of a given background PDF within the signal window. The definition of which, along with the full methodology of the mass fits, is detailed in Chapter 7. To determine  $f_{\alpha,i}^b$  the fraction of fully selected data in each Dalitz bin is found separately for the  $B$  and  $D$  planes and multiplied together. Full details of the models and the methods used to obtain the fractions are given in Chapter 6.

This handling of the background decays is a fundamental difference between the latest single Dalitz  $B^+ \rightarrow Dh^+$  analysis and double Dalitz analyses, in the  $B^+ \rightarrow Dh^+$  analysis the  $CP$  fit is performed simultaneously with a per-bin mass fit from which the per-bin background contributions are determined. On the other hand in the double Dalitz analysis these contributions are determined prior to performing the  $CP$  fit motivated by the large number of bins in the double Dalitz binning resulting in such sparsely populated Dalitz bins that it is not practical to perform per-bin mass fits.

## 4.6 Extracting $\gamma$

### 4.6.1 The $CP$ fit

Now that it has been established that Eq. (4.48) gives the expectation for the number of decays in each bin  $(\alpha, i)$  for each  $D$  decay this equation can be fitted to the fully selected data. This is achieved by performing a binned likelihood fit to all decay modes simultaneously. Every parameter with an external input value is fixed to that value and all other parameters are allowed to float freely. The only constraint applied to any parameters

is that the sum of all the  $\langle \bar{\kappa} \rangle_\alpha$  must equal 1. This is enforced by multiplying the likelihood by a Gaussian of mean  $(1 - \sum_\alpha \langle \bar{\kappa} \rangle_\alpha)$  and width 0.001. One could also float all but one of these parameters and calculate the value of the unfloat parameter as the difference of the sum of the others from unity, but including the Gaussian term was simpler and there is negligible difference expected between the methods. The total likelihood is therefore given by

$$\mathcal{L} = \underbrace{\left( \prod_{\text{Decay}} \prod_{\alpha, i} \frac{N_{\alpha, i}^{\text{Exp.}} N_{\alpha, i}^{\text{Obs.}} e^{-N_{\alpha, i}^{\text{Exp.}}}}{N_{\alpha, i}^{\text{Obs.}}!} \right)}_{\text{Poisson term comparing the observation to the total expectation per bin}} \underbrace{\left( \prod_p e^{\frac{-(1 - \sum_\alpha \langle \bar{\kappa} \rangle_\alpha)^2}{2 \times 0.001^2}} \right)}_{\text{Gaussian constraint term}}, \quad (4.49)$$

where  $N_{\alpha, i}^{\text{Obs.}}$  are the observed number of decays in bin  $(\alpha, i)$  and  $N_{\alpha, i}^{\text{Exp.}}$  is the expectation of the binned population from Eq. (4.48).

This likelihood can then be maximised using the **MIGRAD** algorithm implemented in **iMinuit** [84, 85] to obtain values for all floating parameters.

## 4.6.2 Interpreting the result

The result of the  $CP$  fit is central values and covariance matrices for the  $x_\alpha^\pm, y_\alpha^\pm$  parameters. In a subsequent step these values can be interpreted in terms of the physical parameters,  $T_\alpha, \delta_\alpha$  and  $\gamma$ . A likelihood can be constructed for a multivariate Gaussian

$$f(\mathbf{x}) = \frac{1}{\sqrt{(2\pi)^k \det(\Sigma)}} \exp \left( -\frac{1}{2} (\mathbf{x} - \boldsymbol{\mu})^T \Sigma^{-1} (\mathbf{x} - \boldsymbol{\mu}) \right), \quad (4.50)$$

where  $\mathbf{x}$  are the values of the Cartesian parameters  $x_\alpha^\pm, y_\alpha^\pm$  according to Eq. (4.36),  $\boldsymbol{\mu}$  are their central values determined in the  $CP$  fit and  $\Sigma$  is the covariance matrix.

## 4.6.3 Evaluating uncertainties

For the majority of parameters the statistical uncertainty is simply obtained as the diagonal of the inverse of the Hesse matrix of the likelihood. There is potential for the fits to have an inherent bias or under/overcoverage, therefore a parametric bootstrapping is used to construct an ensemble of pseudo-experiment fits. Each pseudo-experiment fit provides a central value and uncertainty for each parameter, from the ensemble of which a distributions of central values and pulls can be constructed. The pull is

$$p = \frac{(\nu - \bar{\nu})}{\sigma_\nu}, \quad (4.51)$$

where  $\bar{\nu}$  is the value of the parameter used to generate the pseudo-experiments,  $\nu$  is the value found for the given pseudo-experiment and  $\sigma_\nu$  is its uncertainty. If the pull-

distribution has a non-zero mean this implies a bias in the central value which can be corrected for if necessary. A non-unit width implies under/overcoverage which results in an incorrect value for the statistical uncertainty from the direct fit. To correct this the statistical uncertainty can be obtained from the width of the distribution of parameter values in the pseudo-experiment ensemble. Full details are in Chapter 8.

A number of studies are performed to determine the systematic uncertainties associated with each parameter from a variety of sources, *e.g.* uncertainty on external inputs, uncertainties associated with background modelling. A covariance matrix for the parameters in the *CP* fit will be determined for each source. These can be summed, and their effects propagated to the interpretation to determine the systematic uncertainty on  $\gamma$ .

## 4.7 Summary

The basic analysis procedure is as follows:

1. Data and simulation samples are collected and processed as described in Chapter 3.
2. The basic selection is applied, followed by requirements on the output of a BDT algorithm to suppress combinatorial background, tighter PID cuts and kinematic vetoes. This is described in Chapter 5.
3. Simulated background samples are reweighted according to amplitude models. These are then used to determine the expected Dalitz binned distribution of the backgrounds in fully selected LHCb data and correct simulated the invariant mass distributions. This is described in Chapter 6.
4. Global invariant mass fits are performed to determine the quantity of each background present within the signal window for each  $D$  final state. This is described in Chapter 7.
5. Equation (4.48) is then fitted to the fully selected data, described in Chapter 8.
6. The parameters  $\gamma$ ,  $T_\alpha$  and  $\Delta\delta_\alpha$  are extracted from the values and covariance of  $x_\alpha^\pm$ ,  $y_\alpha^\pm$  with uncertainties determined according to the pseudo-experiment studies and systematic studies, described in Chapters 8 and 9.

The double Dalitz plane analysis is a novel method to measure the CKM angle  $\gamma$ . The  $B$  and  $D$  Dalitz planes of  $B^0 \rightarrow DK^+\pi^-$ ,  $D \rightarrow K_S^0 h^+ h^-$  decays are simultaneously binned and the binned signal expectation of Eq. (4.48) is fitted to data to extract Cartesian *CP* parameters from which  $\gamma$  can be extracted. Additional two and four body  $D$  decays are simultaneously fitted in the  $B$  plane to provide additional sensitivity to the fitted

parameters. This method is a generalisation of the single Dalitz analysis which is already used to great effect in LHCb. This allows it to use the same external inputs from Charm factories that the single Dalitz analysis uses, as well as the measurements of the  $D \rightarrow K_S^0 h^+ h^-$  decay distribution hadronic parameters measured in that analysis. It also benefits from the rich resonance structure of the  $B^0 \rightarrow DK^+ \pi^-$  Dalitz plane and the greater ratio between the suppressed and favoured  $B$  decay which results in larger interference effects and therefore higher inherent sensitivity to  $\gamma$ . However the high number of Dalitz bins means it requires a detailed understanding of the Dalitz distribution of prominent background decays since it is not possible to determine the binned signal populations via simultaneous invariant mass fits. This thesis presents the first time this analysis method has been used.





# 5 Selection

*“Oh, alright I’m go-, I’ll keep this.”*

---

Sean Lock

This chapter presents the methods used to perform an optimal selection on the LHCb dataset to remove as much background as possible and maximise statistical sensitivity. Care is also taken to ensure the  $D$  Dalitz plane efficiency is similar to that of the  $B^+ \rightarrow Dh^+$  analysis such that it is valid to use the measured  $R_i$  values as external inputs to the double Dalitz  $CP$  fit. Section 5.1 was performed by myself, Section 5.2 was performed by my analysis partner Yuya Shimizu and Section 5.3 was a joint effort.

## 5.1 Basic selection

The first stage of selection consists of basic rectangular cuts to ensure each event meets basic requirements which are known to significantly reduce the presence of background decays whilst maintaining a high signal efficiency.

A recent LHCb measurement of  $\gamma$  from a single Dalitz analysis of  $B^0 \rightarrow DK^{*0}$ ,  $D \rightarrow K_S^0 h^+ h^-$  decays [18] showed that the cuts in Table 5.1 result in a similar efficiency profile across the  $D$  Dalitz plane as in the single Dalitz analysis of  $B^+ \rightarrow Dh^+$  decays. The values of the recursive  $R_i$  parameters, which are fixed in the  $CP$  fit to the  $B^+ \rightarrow Dh^+$  analysis values, depend directly on this efficiency profile so it is essential that the selection presented here results in a similar efficiency profile. The primary difference between this selection and that of the  $B^0 \rightarrow DK^{*0}$  analysis is that any cuts that target the  $K^{*0}(892)$  resonance in the  $B$  Dalitz plane are omitted since this analysis utilises the full  $B$  Dalitz spectrum. Other small differences are illustrated in Table 5.1, the values in red are those used in the  $B^0 \rightarrow DK^{*0}$  analysis whereas in this analysis slightly looser cuts are used to allow for background studies. These cuts are chosen to perform a relatively loose selection since in later steps we perform more detailed studies to optimise the selection. The cuts shown in orange are relaxed to allow for the study of charmless background contributions in the sidebands of the  $D$  and  $K_S^0$  mass distributions, as discussed in Section 5.2.9. Due

to these differences in selection with the  $B^0 \rightarrow DK^{*0}$  analysis the efficiency profile across the  $D$  Dalitz plane is checked for compatibility with the single Dalitz  $B^+ \rightarrow Dh^+$  analysis in Section 5.3.2.

In Table 5.1,  $m(X)$  refers to the invariant mass of the  $X$  particle candidate according to the DecayTreeFitter (DTF) algorithm, which greatly improves kinematic resolution [86], and  $m_{\text{PDG}}(X)$  refers to the PDG value of the particle mass [7].

For the  $D^0$  mass cut if a  $K_S^0$  is produced by the  $D$  decay then the mass of the  $K_S^0$  is constrained to its PDG value, if no  $K_S^0$  is produced the invariant mass of the  $D^0$  candidate has no such constraint. Similarly for the  $K_S^0$  mass cut the mass of the  $D^0$  is constrained to its PDG value. The requirement “Has Rich Hits” ensures that each final state particle candidate produced sufficient Cherenkov light in the LHCb RICH sub-detectors to ensure accurate PID is available for each particle. “Solo  $X_{\text{PIDY}}$ ” refers to the PID variable corresponding to whether or not the kaon or pion originating from the  $B$  decay is a  $Y$  particle. Momentum cuts are applied to all final state particles as the RICH sub-detectors can only perform high significance kaon-pion separation for particles with momentum lower than 100 GeV/ $c$ .

In addition to the cuts in Table 5.1 the following trigger requirements are applied, the same as in Ref. [18]. Run 1:

- L0 Global TIS or L0 Hadron TOS
- HLT1 TrackAllL0 TOS
- HLT2Topo2BodyBBDT TOS or HLT2Topo3BodyBBDT TOS or HLT2Topo4BodyBBDT TOS

Run 2:

- L0Global TIS or L0Hadron TOS
- HLT1TrackMVA TOS or HLT1TwoTrackMVA TOS
- HLT2Topo2Body TOS or HLT2Topo3Body TOS or HLT2Topo4Body TOS

For a given trigger line an event passes as “triggered on signal” (TOS) if it is triggered due to particles that correspond to a signal candidate passing the requirements, if it is instead triggered by other particles passing the requirements it is passed as “triggered independently of signal”.

The L0 hadron TOS requirement selects particles with high transverse energy in the ECAL, however this has a low efficiency so the global TIS requirement is added to counteract this inefficiency [87]. The global TIS requirement corresponds to events where the other  $b$  of the  $b\bar{b}$  pair hadronises to a hadron that satisfies any of the L0

trigger lines. The HLT1 decisions require a high transverse momentum track(s) with a significant displacement of all primary vertices, as these are typical properties of beauty or charm decays, based on a partial event reconstruction. Given that the rate of events is significantly reduced by the first two stages of triggering the HLT2 can use a more detailed reconstruction of each event for selection. In Run 1 this included the reconstruction of long tracks but in Run 2 it used a complete, fully aligned reconstruction. The  $N$ -body topological trigger lines select events with  $N$  track vertices with large transverse momenta, significant displacement from the primary vertex and a topology compatible with that of a  $b$  hadron decay [50]. This selection is performed using a so-called bonsai boosted decision tree (BBDT) trained on track transverse momenta and the perpendicular distance of closest approach between each track and the PV (impact parameter) [88].

Base cuts	
$ m(D) - m_{\text{PDG}}(D^0) $	$< 25 \text{ MeV}/c^2$
$ m(K_S^0) - m_{\text{PDG}}(K_S^0) $	$< 15 \text{ MeV}/c^2$
DecayTreeFit converged	True
Has Rich Hits	True
Loose PID Cuts	
Solo $K_{\text{PIDK}}^\pm$	$> -10 > 5$
Solo $\pi_{\text{PIDK}}^\pm$	$< 20 < 3$
$D$ -child $K_{\text{PIDK}}^\pm$	$> -10 > -5$
$D$ -child $\pi_{\text{PIDK}}^\pm$	$< 20$
$K^\pm$ momentum	$< 100 \text{ GeV}/c$
$\pi^\pm$ momentum	$< 100 \text{ GeV}/c$
Background suppressing cuts	
$D$ flight-distance significance	$> 0.5$
$K_S^0$ flight-distance $\chi^2$	$> 49$ (LL only)
Semileptonic suppressing cuts	
$D$ -child $\pi_{\text{PIDe}}^\pm$	$< 0$
$D$ -child $\pi_{\text{isMuon}}^\pm$	$= 0$
$D$ -child $K_{\text{isMuon}}^\pm$	$= 0$

Table 5.1: Summary of the preselection cuts. Cuts written in orange are relaxed when studying the impact of charmless backgrounds. Cuts written in red are used in the  $B^0 \rightarrow DK^{*0}$  analysis and given for comparison.

For each event the  $B$ , and where applicable  $D$ , Dalitz plane coordinates are calculated from the four-momentum of each final state particle with appropriate DTF constraints applied to improve the resolution. Using the Laura++ package [21] and PDG mass values [89] the corresponding square Dalitz variables are calculated.

Table 5.2 shows the efficiency of this initial selection on the truth-matched simulated signal sample. This efficiency is calculated relative to the number of events in the signal simulated data after all data acquisition and processing steps prior to the selection detailed

in Table 5.1. The background rejection, estimated from the  $B$  mass sidebands in the data sample, is  $\sim 90\%$ .

Year	Polarity	2011		2012		2015	
		Up	Down	Up	Down	Up	Down
$D \rightarrow K^+ K^-$		0.625 $\pm$ 0.002	0.628 $\pm$ 0.002	0.604 $\pm$ 0.001	0.604 $\pm$ 0.001	0.607 $\pm$ 0.002	0.608 $\pm$ 0.002
$D \rightarrow \pi^+ \pi^-$		0.623 $\pm$ 0.002	0.614 $\pm$ 0.002	0.601 $\pm$ 0.001	0.594 $\pm$ 0.001	0.590 $\pm$ 0.002	0.580 $\pm$ 0.002
$D \rightarrow K^\pm \pi^\mp$		0.606 $\pm$ 0.002	0.615 $\pm$ 0.002	0.589 $\pm$ 0.001	0.589 $\pm$ 0.001	0.589 $\pm$ 0.001	0.589 $\pm$ 0.001
$D \rightarrow K^\pm \pi^\mp \pi^+ \pi^-$		0.587 $\pm$ 0.001	0.589 $\pm$ 0.001	0.561 $\pm$ 0.001	0.561 $\pm$ 0.001	0.551 $\pm$ 0.001	0.556 $\pm$ 0.001
$D \rightarrow \pi^\pm K^\mp \pi^+ \pi^-$		0.587 $\pm$ 0.001	0.591 $\pm$ 0.001	0.565 $\pm$ 0.001	0.562 $\pm$ 0.001	0.555 $\pm$ 0.001	0.561 $\pm$ 0.001
$D \rightarrow \pi^+ \pi^- \pi^+ \pi^-$		0.588 $\pm$ 0.002	0.588 $\pm$ 0.002	0.564 $\pm$ 0.001	0.564 $\pm$ 0.001	0.553 $\pm$ 0.003	0.561 $\pm$ 0.003
$D \rightarrow K_S^0 \pi^+ \pi^-$ DD		0.606 $\pm$ 0.001	0.608 $\pm$ 0.001	0.591 $\pm$ 0.001	0.591 $\pm$ 0.001	0.570 $\pm$ 0.002	0.575 $\pm$ 0.002
$D \rightarrow K_S^0 \pi^+ \pi^-$ LL		0.549 $\pm$ 0.001	0.550 $\pm$ 0.001	0.508 $\pm$ 0.001	0.506 $\pm$ 0.001	0.521 $\pm$ 0.002	0.523 $\pm$ 0.002
$D \rightarrow K_S^0 K^+ K^-$ DD		0.569 $\pm$ 0.001	0.569 $\pm$ 0.001	0.554 $\pm$ 0.001	0.554 $\pm$ 0.001	0.548 $\pm$ 0.003	0.546 $\pm$ 0.003
$D \rightarrow K_S^0 K^+ K^-$ LL		0.560 $\pm$ 0.002	0.558 $\pm$ 0.002	0.521 $\pm$ 0.002	0.520 $\pm$ 0.002	0.535 $\pm$ 0.004	0.544 $\pm$ 0.004
Year	Polarity	2016		2017		2018	
		Up	Down	Up	Down	Up	Down
$D \rightarrow K^+ K^-$		0.595 $\pm$ 0.001	0.594 $\pm$ 0.001	0.604 $\pm$ 0.001	0.604 $\pm$ 0.001	0.587 $\pm$ 0.001	0.592 $\pm$ 0.001
$D \rightarrow \pi^+ \pi^-$		0.582 $\pm$ 0.001	0.584 $\pm$ 0.001	0.593 $\pm$ 0.001	0.597 $\pm$ 0.001	0.569 $\pm$ 0.001	0.574 $\pm$ 0.001
$D \rightarrow K^\pm \pi^\mp$		0.586 $\pm$ 0.001	0.587 $\pm$ 0.001	0.596 $\pm$ 0.001	0.594 $\pm$ 0.001	0.580 $\pm$ 0.001	0.579 $\pm$ 0.001
$D \rightarrow K^\pm \pi^\mp \pi^+ \pi^-$		0.551 $\pm$ 0.001	0.550 $\pm$ 0.001	0.559 $\pm$ 0.001	0.563 $\pm$ 0.001	0.545 $\pm$ 0.001	0.546 $\pm$ 0.001
$D \rightarrow \pi^\pm K^\mp \pi^+ \pi^-$		0.555 $\pm$ 0.001	0.554 $\pm$ 0.001	0.565 $\pm$ 0.001	0.565 $\pm$ 0.001	0.550 $\pm$ 0.001	0.548 $\pm$ 0.001
$D \rightarrow \pi^+ \pi^- \pi^+ \pi^-$		0.552 $\pm$ 0.001	0.553 $\pm$ 0.001	0.559 $\pm$ 0.001	0.561 $\pm$ 0.001	0.545 $\pm$ 0.001	0.549 $\pm$ 0.001
$D \rightarrow K_S^0 \pi^+ \pi^-$ DD		0.571 $\pm$ 0.001	0.572 $\pm$ 0.001	0.578 $\pm$ 0.001	0.579 $\pm$ 0.001	0.572 $\pm$ 0.001	0.572 $\pm$ 0.001
$D \rightarrow K_S^0 \pi^+ \pi^-$ LL		0.523 $\pm$ 0.001	0.523 $\pm$ 0.001	0.530 $\pm$ 0.001	0.529 $\pm$ 0.001	0.517 $\pm$ 0.001	0.517 $\pm$ 0.001
$D \rightarrow K_S^0 K^+ K^-$ DD		0.542 $\pm$ 0.001	0.542 $\pm$ 0.001	0.549 $\pm$ 0.001	0.546 $\pm$ 0.001	0.544 $\pm$ 0.001	0.543 $\pm$ 0.001
$D \rightarrow K_S^0 K^+ K^-$ LL		0.534 $\pm$ 0.001	0.534 $\pm$ 0.001	0.546 $\pm$ 0.002	0.538 $\pm$ 0.002	0.527 $\pm$ 0.001	0.532 $\pm$ 0.001

Table 5.2: Preselection efficiency on signal MC samples

## 5.2 Selection

PID cuts are first optimised and applied to the solo kaon and pion to remove a significant amount of misidentified background. A BDT is then trained and an optimal cut on the BDT response is used to remove combinatorial background decays. PID cuts are then applied to the particles produced from the decay of the  $D$  meson. Kinematic vetoes are used to remove specific backgrounds by searching for peaks in the invariant mass distributions of various combinations of final state particles. Finally a study is performed to reduce the contributions of charmless  $B$  decays.

### 5.2.1 PID cuts on $B$ companion particles

The PID cut applied for a solo kaon is  $\text{ProbNN}_K(1 - \text{ProbNN}_\pi)(1 - \text{ProbNN}_p) > 0.2$  and  $\text{ProbNN}_\pi(1 - \text{ProbNN}_K)(1 - \text{ProbNN}_p) > 0.2$  for a solo pion. A  $\text{ProbNN}_X$  variable can be interpreted as the probability that the associated particle candidate has the identity  $X$ . These variables are an improved set of PID variables based on the likelihoods described in Section 3.2.3. They are created via a multivariate method which takes into account additional information such as correlations between the sub-detectors [46]. Typically the distributions of these variables in simulated data does not sufficiently reproduce that observed in data, therefore a correction is applied by resampling these distributions based on the corresponding distributions found in LHCb data [90]. The cut value of 0.2 was determined by maximising the  $S/\sqrt{S+B}$  figure of merit (FOM). A simple invariant mass fit was used to estimate the values of  $S$  and  $B$ . Since the goal of these cuts are to remove backgrounds such as  $B^0 \rightarrow D\pi^+\pi^-$  and  $\bar{A}_b^0 \rightarrow DK^+\bar{p}$  decays the value of  $B$  was taken as the yield of these decays within the signal window and  $S$  is the yield of the signal decay. The mass fit was performed for the cut value of 0.2 to obtain an initial FOM value which was then extrapolated to other values based on the cut efficiency in simulation. One difference between this cut and that in Ref. [72] is the addition of the  $\text{ProbNN}_p$  variable which was introduced here to suppress  $\Lambda_b^0$  backgrounds.

### 5.2.2 Boosted decision tree

In order to remove combinatorial backgrounds, the **XGBoost** package [91] was used to train a boosted decision tree (BDT). Using a separate BDT for each final state was tested but found to have a negligible improvement on selection power compared to one for each decay topology. For simplicity one BDT was trained for each of the following topologies,  $D \rightarrow K_S^0 h^+ h^-$  DD,  $D \rightarrow K_S^0 h^+ h^-$  LL,  $D \rightarrow h^+ h^-$ , and  $D \rightarrow h^+ h^- h^+ h^-$ . The final states chosen as representatives for each topology were  $D \rightarrow K_S^0 \pi^+ \pi^-$  DD,  $D \rightarrow K_S^0 \pi^+ \pi^-$  LL,

$D \rightarrow K^+K^-$ , and  $D \rightarrow \pi^+\pi^-\pi^+\pi^-$  respectively as these are the most sensitive to  $\gamma$ . The same BDT response cut value is used for each final state of a given topology.

The training datasets consisted of the signal simulation to model the signal decay and data from the  $B^0$  candidate high invariant mass sideband,  $m_B > 5.5 \text{ GeV}/c^2$ , to model combinatorial backgrounds.

Since the data in the high mass sideband is used in the invariant mass fits it is necessary to check the robustness of the BDT training. Therefore 4-fold cross-validation was employed to obtain four independent BDTs such that it can be confirmed that the training results in similar performance with different training samples and such that each event can be filtered by a BDT that was not trained on it. This also allows for larger training samples to be used. For four equally sized data groups, A, B, C, and D, a BDT is trained on three of the groups and evaluated on the 4th.

The data from Run 1 and Run 2 were obtained under different experimental conditions and had different stripping-level selection applied, to account for these differences separate BDTs were trained for each run.

Most of the input variables used for the training are common across the four  $D$  decay topologies, apart from a couple of variables related to the  $D$  children. The input variables are summarised in Table 5.3. The distributions of the BDT output for the training and testing samples are shown in Fig. 5.1 for the  $D \rightarrow K_S^0 h^+ h^-$  DD decay. In all cases the signal and background are well separated with negligible over-training as evidenced by the good agreement in distributions between the training and test samples.

All of the data and simulation can then be processed by the BDTs and assigned a response value. A cut on this response value is optimised with respect to the  $S/\sqrt{S+B}$  FOM, where  $S$  is the number of expected signal candidates and  $B$  is the number of expected combinatorial background candidates. Nominal values of  $S$ ,  $B$  and the FOM are determined by an invariant mass fit performed as described in Chapter 7 with a BDT response cut of  $> 0.7$ . This is then extrapolated to other BDT response cuts according to their efficiency relative to the nominal cut in the signal simulation and the high mass sideband data. This is performed with the data summed over the  $B$  flavours and Runs 1 and 2, a simultaneous optimisation with the runs fitted separately was attempted but was determined to provide a negligible improvement in background rejection. Examples of the results obtained are shown as BDT cut *vs.*  $S/\sqrt{S+B}$  plots in Fig. 5.2 with the optimal cut shown as a red dashed line, and specified in Table 5.4. The distributions of each input variable for the  $D \rightarrow K_S^0 \pi^+ \pi^-$  DD BDT are shown in Figs. A.1 to A.4 and the feature importances are shown in Fig. A.5.



Common variables
DTF $\chi^2$ per degrees of freedom
$B^0/D^0$ cylindrical distance between initial and final vertices
Asymmetry of the transverse momentum of non-signal associated tracks in the vicinity of the candidate $B^0$
$B^0/D^0$ impact parameter with respect to its primary vertex
Angle between the $B^0/D^0$ momentum direction and the direction from the previous vertex to the decay vertex
$B^0/D^0$ maximum distance of closest approach of subsequent tracks
$B^0$ /solo kaon/pion impact parameter with respect to its primary vertex
$B^0$ flight distance $\chi^2$ with respect to its primary vertex
$B^0/D^0$ /solo kaon/pion momentum
$B^0/D^0$ /solo kaon/pion transverse momentum
$B^0/D^0$ vertex fit $\chi^2$ per degrees of freedom
$D \rightarrow K_S^0 h^+ h^-$
Angle between the $K_S^0$ direction and the primary vertex
$K_S^0$ flight distance significance
Largest non- $K_S^0$ decay product impact parameter with respect to the decay vertex
Smallest non- $K_S^0$ decay product impact parameter with respect to the decay vertex
$D \rightarrow h^+ h^-$ & $D \rightarrow h^+ h^- h^+ h^-$
Largest decay product impact parameter with respect to the decay vertex
Largest decay product transverse momentum
Smallest decay product impact parameter with respect to the decay vertex
Smallest decay product transverse momentum

Table 5.3: Summary of the variables used for BDT training.

Decay category	Optimal BDT cut
$D \rightarrow K_S^0 h^+ h^-$ LL	0.92
$D \rightarrow K_S^0 h^+ h^-$ DD	0.92
$D \rightarrow h^+ h^-$	0.88
$D \rightarrow h^+ h^- h^+ h^-$	0.96

 Table 5.4: The optimal BDT cut values determined by maximising the  $S/\sqrt{S+B}$  FOM.

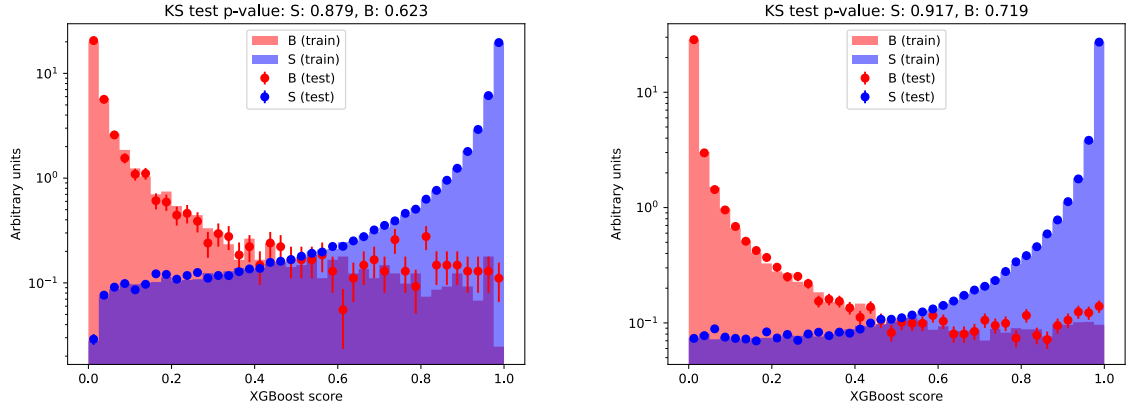


Figure 5.1: The BDT response in Run 1 (left) and Run 2 (right) for the  $D \rightarrow K_S^0 h^+ h^-$  DD topology for the respective samples A. The training (testing) samples are shown as solid histograms (points with errors) for the signal (blue) and background (red). The  $p$ -value of the Kolomogorov-Smirnov (KS) test between the training and testing samples are shown at the top of the plots.

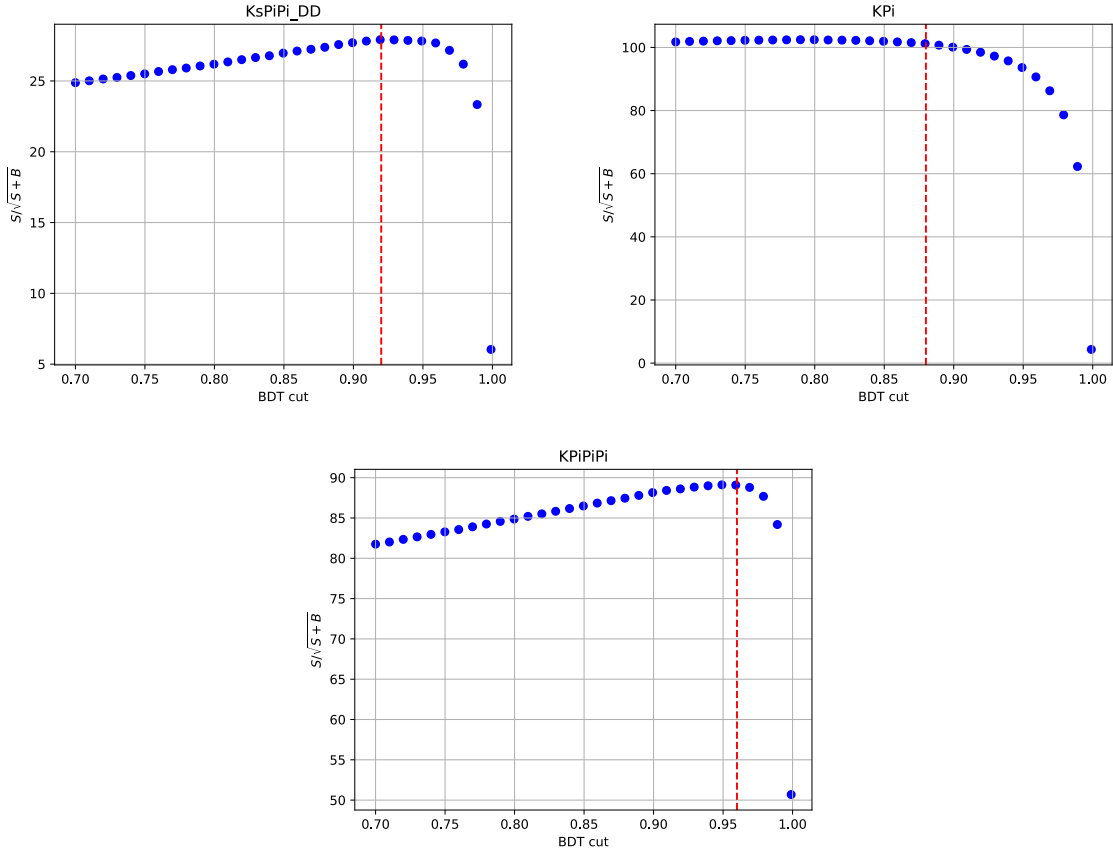


Figure 5.2: Summary of the FOM ( $S/\sqrt{S+B}$ ) *vs.* BDT cut plots for  $D \rightarrow K_S^0 h^+ h^-$  DD (top),  $D \rightarrow K^\pm \pi^\mp$  (middle) and  $D \rightarrow K^\pm \pi^\mp \pi^+ \pi^-$  (bottom). The value with a BDT cut at 0.7 is calculated from the mass fit and the rest from the efficiency. The working points chosen are shown with a red dashed line.

### 5.2.3 PID cut on $D$ children

For the two-body  $D$  modes it is required that  $\text{ProbNN}_K \times (1 - \text{ProbNN}_\pi) > 0.1$  for the kaon from the  $D$  and  $\text{ProbNN}_\pi \times (1 - \text{ProbNN}_K) > 0.1$  for the pion from the  $D$ . These selections were based on the studies in Ref. [92]. Studies based on the  $D \rightarrow K^\pm \pi^\mp$  simulation PID resampling showed that the ratio of events reconstructed as  $D \rightarrow K^+ K^-$  ( $D \rightarrow \pi^+ \pi^-$ ) to those reconstructed as  $D \rightarrow K^\pm \pi^\mp$  after all the selection criteria is  $1.1 \times 10^{-4}$  ( $1.5 \times 10^{-4}$ ) and  $1.8 \times 10^{-4}$  ( $2.0 \times 10^{-4}$ ) for Runs 1 and 2, respectively. Based on the fitted yield of the  $D \rightarrow K^\pm \pi^\mp$  mode obtained from the mass fit in Chapter 7 ( $\sim 5500$  for each  $B^0$  flavour), the number of expected  $D \rightarrow K^\pm \pi^\mp$  events mis-reconstructed as  $D \rightarrow K^+ K^-$  or  $D \rightarrow \pi^+ \pi^-$  would be  $\sim 1$ , which is considered to be negligible. For the  $D \rightarrow K_S^0 K^+ K^-$  mode, the kaon from the  $D$  decay is required to pass a very loose PID cut of  $\text{ProbNN}_K \times (1 - \text{ProbNN}_\pi) > 0.003$ . This cut suppresses the cross-feed from other  $D \rightarrow K_S^0 h^+ h'^-$  modes while keeping more than 98% of the signal. The cut value is chosen to have a similar signal efficiency as the PID cut in Ref. [80]. For the  $D \rightarrow K^\pm \pi^\mp \pi^+ \pi^-$  mode, the kaon from the  $D$  decay is required to pass  $\text{ProbNN}_K \times (1 - \text{ProbNN}_\pi) > 0.1$ , and the two pions with opposite charge to the kaon must satisfy  $\text{ProbNN}_\pi \times (1 - \text{ProbNN}_K) > 0.1$ . Concerning the  $D \rightarrow \pi^+ \pi^- \pi^+ \pi^-$  mode, the pions with the same charge as the kaon from the  $B$  must satisfy  $\text{ProbNN}_\pi \times (1 - \text{ProbNN}_K) > 0.1$ .

### 5.2.4 Double misidentification

Another source of background is a decay for which final state kaon and pion candidates are simultaneously misidentified as each other. The most significant case of this is when a favoured  $D \rightarrow K^\pm \pi^\mp$  decay is doubly misidentified and mimics its suppressed counterpart. Although the likelihood of a double misidentification is low, the background contribution could be significant given the relatively high BF of the favoured decay compared to the suppressed decay. The magnitude of this effect was studied using truth-matched simulated data. Doubly misidentified solo kaons and pions were found to account for  $\sim 1\%$  of the suppressed  $D \rightarrow K^\pm \pi^\mp$  yield, and the proportion from doubly misidentified  $D$  children was found to be even smaller, so this is considered to be a negligible effect but could be assessed as a source of systematic uncertainty.

### 5.2.5 $D^*(2010)^-$ veto

The decay  $B^0 \rightarrow D^*(2010)^- K^+$  followed by  $D^*(2010)^- \rightarrow D \pi^-$  makes a substantial contribution to the decay of interest since it has the same final state and a large branching fraction. These decays however are not of interest for this measurement as the peak of the  $D^*(2010)^-$  is too narrow to give significant sensitivity to  $\gamma$ . In order to remove it,

events with either  $m(D\pi)$  or  $m(DK_\pi)$  within  $\pm 2.5 \text{ MeV}/c^2$  of the known  $D^*(2010)^-$  mass are vetoed, where mass constraints on the  $D$  and  $K_S^0$  are applied where applicable.  $K_\pi$  denotes a kaon evaluated under the pion mass hypothesis. This veto is applied to all  $D$  final states.

### 5.2.6 $D^-$ , $D^0$ , and $D_s^+$ veto

Another source of background originates from particle tracks associated with the wrong vertices. For example the decay  $B \rightarrow D^- X$ ,  $D^- \rightarrow K^+ \pi^- \pi^-$  could be reconstructed as a signal candidate if one of the particles produced from the  $D$  decay are reconstructed as a solo kaon or pion from a  $B^0 \rightarrow DK^+ \pi^-$  decay. In order to identify such backgrounds one can search for peaking contributions in the invariant mass distribution of various combinations of the final state particle candidates. In the case of  $B \rightarrow D^- X$ ,  $D^- \rightarrow K^+ \pi^- \pi^-$  one would expect a peak around the known mass of the  $D^-$  meson in the distribution of  $m(K^+{}_B \pi^-{}_{B/D} \pi^-{}_D)$ , where  $\pi^-{}_{B/D}$  is either a  $B$  or  $D$  child pion,  $K^+{}_B$  is a solo particle from the  $B$  decay and  $\pi^-{}_D$  is a  $D$  child. This background can then be vetoed by removing decays within  $15 \text{ MeV}/c^2$  of the  $D^-$  mass. Table 5.5 presents the full list of vetoed particle candidate combinations with the corresponding invariant mass distributions shown in Figs. 5.3 and 5.4.

Final state	Mass combination
$D \rightarrow \pi^+ \pi^-$	$m(K^+{}_B \pi^-{}_B \pi^-{}_D)$ $m(K^+{}_B \pi^-{}_D)$
$D \rightarrow K_S^0 \pi^+ \pi^-$	$m(K^+{}_B \pi^-{}_D)$ $m(K_S^0 K^+{}_B)$
$D \rightarrow K_S^0 K^+ K^-$	$m(K_S^0 K_B K_D)$
$D \rightarrow \pi^+ \pi^- \pi^+ \pi^-$	$m(K^+{}_B \pi^-{}_D \pi^-{}_D)$ $m(K^+{}_B \pi^-{}_D)$ $m(K^+{}_B \pi^-{}_D \pi^+{}_D \pi^-{}_D)$ $m(\pi^+{}_B \pi^-{}_D \pi^+{}_D \pi^-{}_D)$
$D \rightarrow K^\pm \pi^\mp \pi^+ \pi^-$	$m(K^+{}_B \pi^-{}_D \pi^+{}_D \pi^-{}_D)$ $m(\pi^+{}_B \pi^-{}_D \pi^+{}_D \pi^-{}_D)$

Table 5.5: All particle candidate combinations that are vetoed for certain  $D$  final states.

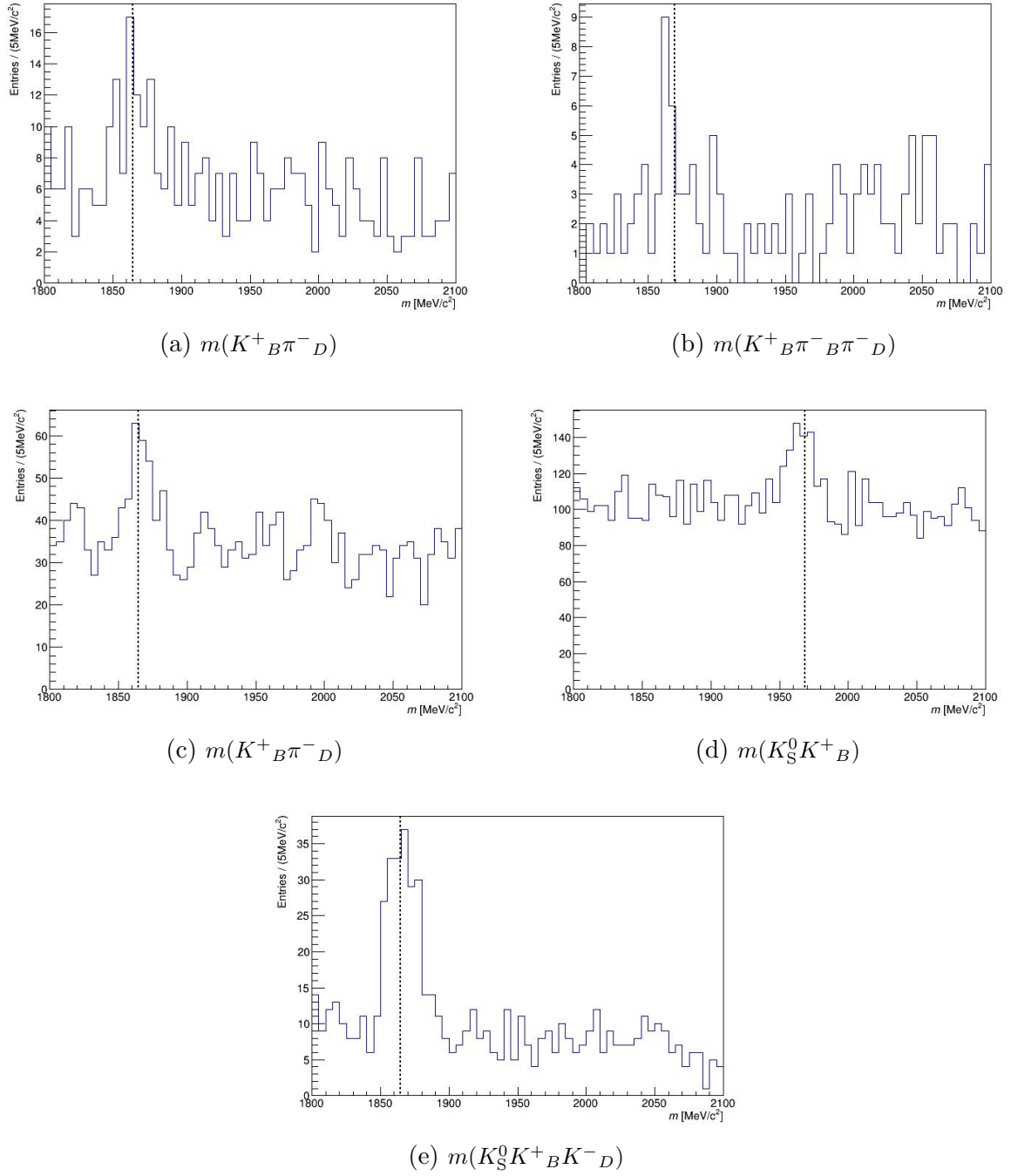


Figure 5.3: Distributions of mis-reconstructed masses for  $D \rightarrow \pi^+ \pi^-$  decays (top row),  $D \rightarrow K_S^0 \pi^+ \pi^-$  decays (second row),  $D \rightarrow K_S^0 K^+ K^-$  decays (third row). The dashed lines indicate the known mass of the  $D^0$  (left and bottom),  $D^-$  (top right), and  $D_s^+$  (middle right). Vetoes of  $\pm 15 \text{ MeV}/c^2$  are applied around the known  $D$  masses.

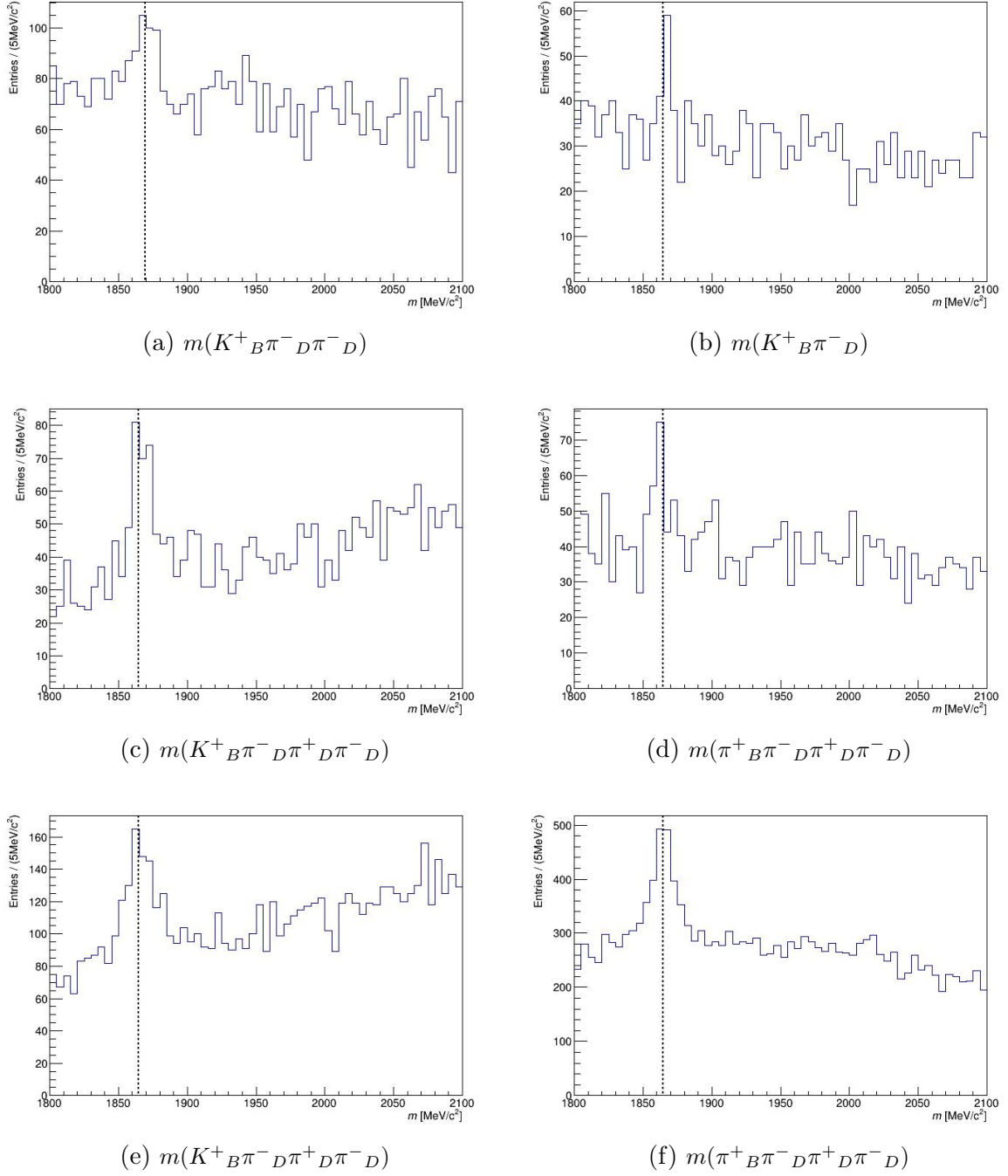


Figure 5.4: Distributions of mis-reconstructed masses for  $D \rightarrow \pi^+ \pi^- \pi^+ \pi^-$  decays (top and middle rows) and  $D \rightarrow K^\pm \pi^\mp \pi^+ \pi^-$  decays (bottom row). The dashed lines indicate the known mass of the  $D^-$  (top left) and  $D^0$  (the others). Vetoes of  $\pm 15 \text{ MeV}/c^2$  are applied around the known  $D$  masses.

### 5.2.7 Double $D^0$ veto

Decays of  $B_{(s)}^0 \rightarrow D^0 \bar{D}^0$  also contribute to the  $DK\pi$  final state, which results in a peak at the  $D^0$  mass in the distribution of  $m(K_B\pi_B)$ . In order to remove this background,  $m(K_B\pi_B)$  is required to be more than  $25 \text{ MeV}/c^2$  away from the  $D$  mass. This veto is applied on all the  $D$  modes. The  $m(K_B\pi_B)$  distribution for the  $D \rightarrow K_S^0 \pi^+ \pi^-$  DD mode is shown in Fig. 5.5.

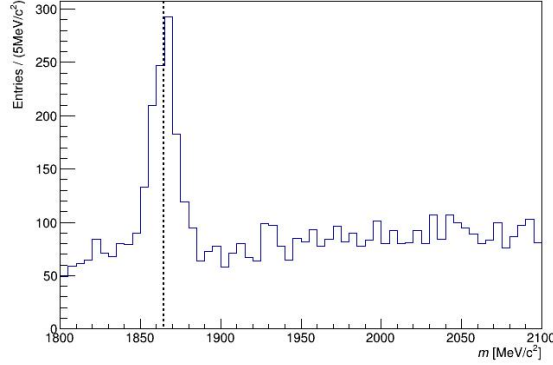


Figure 5.5: The distribution of  $m(K_B\pi_B)$  for  $D \rightarrow K_S^0 \pi^+ \pi^-$  DD. The dashed line indicates the mass of  $D^0$ .

### 5.2.8 $B^+$ veto

A similar source of background is a  $B^+ \rightarrow DK^+$  ( $B^+ \rightarrow D\pi^+$ ) decay where a random  $\pi^-$  ( $K^-$ ) is mistaken to be a true solo  $\pi^-$  ( $K^-$ ) to mimic a  $B^0 \rightarrow DK^+\pi^-$  decay. This is removed by vetoing events, for all  $D$  final states, within  $25 \text{ MeV}/c^2$  of the known  $B^+$  mass in the  $m(D\pi)$  and  $m(DK)$  invariant mass spectra. These are shown in Fig. 5.6.

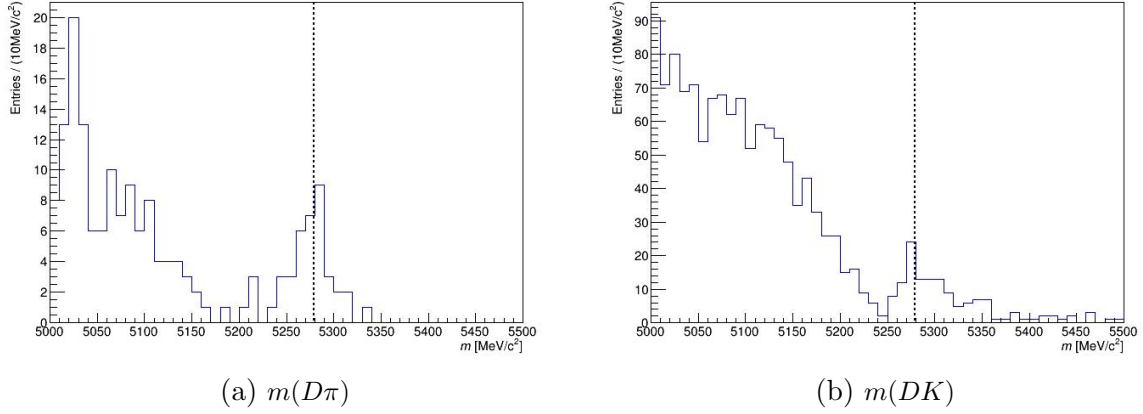


Figure 5.6: The distribution of  $m(D\pi)$  and  $m(DK)$  for  $D \rightarrow K_S^0 \pi^+ \pi^-$  DD. The dashed line indicates the known mass of the  $B^+$ . A veto of  $\pm 25 \text{ MeV}/c^2$  is applied around the known  $B$  mass.

### 5.2.9 Charmless suppression

Another source of background decays is a  $B$  decay to a charmless final state that mimics one of the signal final states under consideration. This can be mitigated by a cut on the flight-distance significance (FDS) of the candidate  $D$  meson as shown in Table 5.1. It was found that although this requirement is sufficient for the  $D \rightarrow K_S^0 h^+ h^-$  decays, a significant amount of charmless background remains for the other signal final states. For the  $D \rightarrow K^+ K^-$ ,  $D \rightarrow K^\pm \pi^\mp$  and  $D \rightarrow K^\pm \pi^\mp \pi^+ \pi^-$  final states a cut of  $\text{FDS}_D > 3$  is used, inherited from Ref. [19]. For the remaining final states a study was performed using data for which the full selection was applied besides the  $D$  mass and  $\text{FDS}_D$  cuts in Table 5.1 and the BDT was retrained without the DTF  $\chi^2$  per degrees of freedom, which is a strong discriminant against sideband decays in the  $D$  mass spectrum. The exact definitions of the sidebands in each final state are chosen to avoid contributions from misidentified backgrounds and are stated in Table 5.6.

Final state	Sideband definition
$D \rightarrow K_S^0 K^+ K^-$	$m_D \in (1770 \text{ MeV}/c^2, 1820 \text{ MeV}/c^2)$
$D \rightarrow K^+ K^-$	$m_D \in (1895 \text{ MeV}/c^2, 1920 \text{ MeV}/c^2)$
$D \rightarrow \pi^+ \pi^- \pi^+ \pi^-$	$m_D \in (1810 \text{ MeV}/c^2, 1830 \text{ MeV}/c^2)$
All others	$m_D \in (1910 \text{ MeV}/c^2, 1960 \text{ MeV}/c^2)$

Table 5.6: Sideband definitions for the various signal final states.

The yield of the charmless background contribution is then estimated using a fit to the  $B$  candidate invariant mass distribution in the  $D$  sideband. The ratio of the charmless background to the signal is then determined over a range of  $\text{FDS}_D$  cut values to ensure charmless backgrounds contribute less than  $\sim 5\%$  of the events in the signal



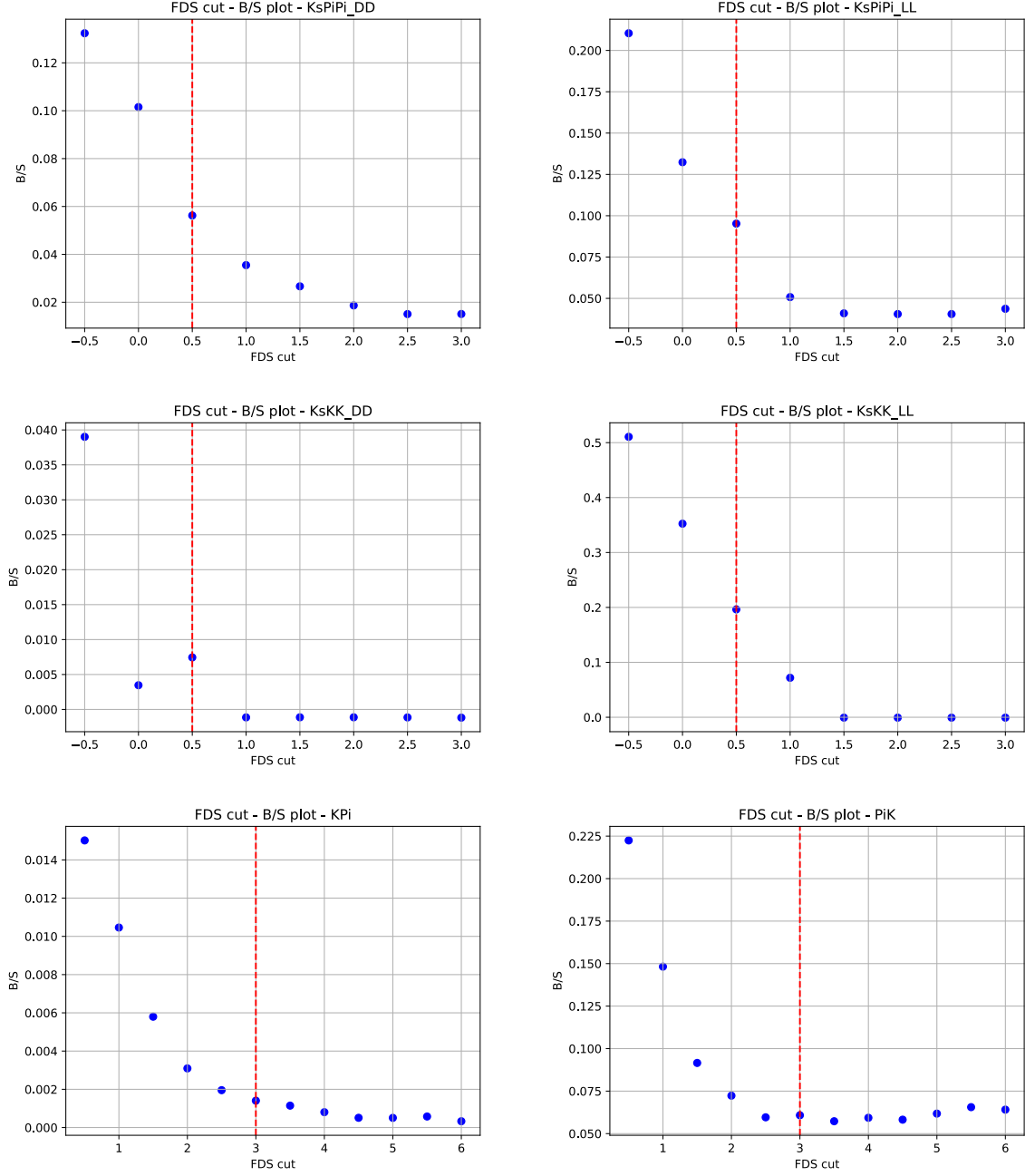


Figure 5.7:  $B/S$  as a function of  $FDS_D$  for  $D \rightarrow K_S^0 \pi^+ \pi^-$  (top),  $D \rightarrow K_S^0 K^+ K^-$  (middle), and  $D \rightarrow K^\pm \pi^\mp$  (bottom).

region. The background to signal ratio as a function of the  $FDS_D$ , and the chosen cut value, is shown for each decay mode in Figs. 5.7 and 5.8. This optimisation results in cut values of  $FDS_D > 0.5$  for  $D \rightarrow K_S^0 h^+ h^-$ ,  $FDS_D > 3$  for  $D \rightarrow K^+ K^-$ ,  $D \rightarrow K^\pm \pi^\mp$  and  $D \rightarrow K^\pm \pi^\mp \pi^+ \pi^-$ ,  $FDS_D > 4.5$  for  $D \rightarrow \pi^+ \pi^-$ , and  $FDS_D > 5$  for  $D \rightarrow \pi^+ \pi^- \pi^+ \pi^-$ .

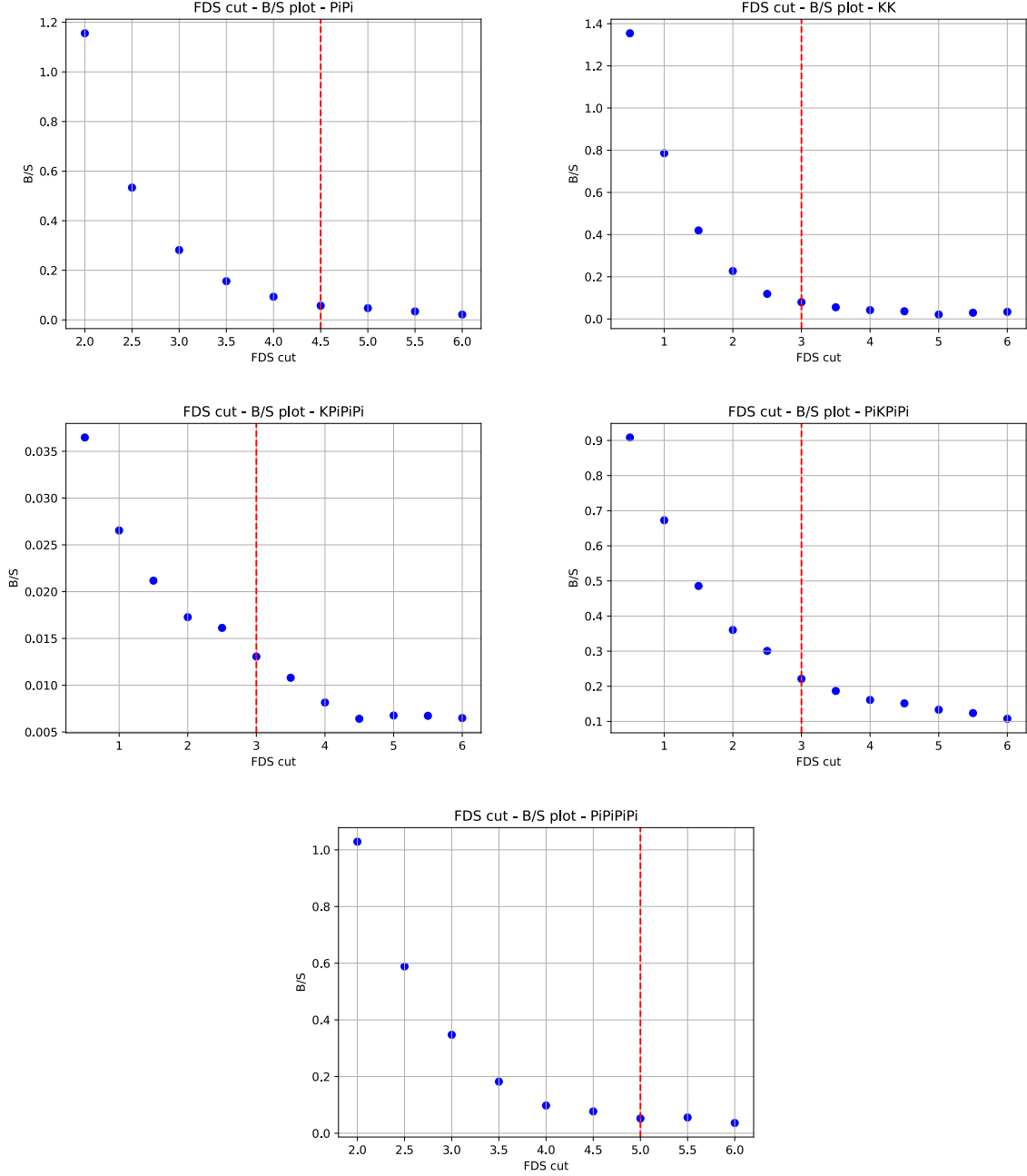


Figure 5.8:  $B/S$  as a function of  $FDS_D$  for  $D \rightarrow \pi^+\pi^-$  and  $D \rightarrow K^+K^-$  (top),  $D \rightarrow K^\pm\pi^\mp\pi^+\pi^-$  (middle), and  $D \rightarrow \pi^+\pi^-\pi^+\pi^-$  (bottom).

## 5.3 Selection results

### 5.3.1 Multiple candidates

The multiple candidate rate in data after the full selection is shown in Table 5.7. The obtained rate is in general low, particularly for the decays within the signal mass window defined in Chapter 7. Therefore no selection is applied to remove the multiple candidates.

Decay	Multiple candidate rate (%)	
	All	In the signal window
$D \rightarrow K^+ K^-$	$0.41 \pm 0.04$	$0.13 \pm 0.07$
$D \rightarrow \pi^+ \pi^-$	$0.55 \pm 0.08$	$0.12 \pm 0.12$
$D \rightarrow K^\pm \pi^\mp$	$0.28 \pm 0.02$	$0.09 \pm 0.03$
$D \rightarrow \pi^\pm K^\mp$	$0.46 \pm 0.02$	$0.07 \pm 0.03$
$D \rightarrow \pi^+ \pi^- \pi^+ \pi^-$	$2.04 \pm 0.08$	$0.45 \pm 0.16$
$D \rightarrow K^\pm \pi^\mp \pi^+ \pi^-$	$1.81 \pm 0.04$	$0.89 \pm 0.08$
$D \rightarrow \pi^\pm K^\mp \pi^+ \pi^-$	$2.92 \pm 0.04$	$1.02 \pm 0.1$
$D \rightarrow K_S^0 \pi^+ \pi^-$ DD	$1.67 \pm 0.07$	$0.56 \pm 0.15$
$D \rightarrow K_S^0 \pi^+ \pi^-$ LL	$1.96 \pm 0.1$	$1.23 \pm 0.33$
$D \rightarrow K_S^0 K^+ K^-$ DD	$1.47 \pm 0.16$	$0.29 \pm 0.29$
$D \rightarrow K_S^0 K^+ K^-$ LL	$1.4 \pm 0.21$	$1.02 \pm 0.72$

Table 5.7: Multiple candidate rate in data after the full selection.

### 5.3.2 The $D$ Dalitz efficiency profiles

As discussed in Section 4.3 the values of  $R_i$  from the single Dalitz  $B^+ \rightarrow Dh^+$  analysis are external inputs to this analysis and as the selection applied to data is slightly different between the analyses it must be checked that the  $D$  Dalitz plane efficiency profiles are similar.

To obtain efficiency profiles across the  $D$  Dalitz planes, simulated samples were generated uniformly flat in the  $D \rightarrow K_S^0 h^+ h^-$  phase space for  $B^0 \rightarrow DK^+ \pi^-$  and  $B^+ \rightarrow D\pi^+$  decays and their respective selections applied as shown in Figs. 5.9 and 5.10. The ratio of these simulation samples is shown in Fig. 5.11. In general these show that the different selections result in similar efficiency profiles. However this is not sufficient to ensure that the use of  $R_i$  values from the single Dalitz  $B^+ \rightarrow Dh^+$  analysis is valid. It must also be checked with simulated data generated according to the amplitude distribution of the  $D$  decays. This accounts for the possibility of a small variation in efficiency at a point with a high amplitude resulting in different  $R_i$  values that are valid for the different analyses. Figures 5.12 to 5.13 show the distribution of the simulated data generated according to an amplitude model for the  $D$  decay in the  $D$  Dalitz plane bins, demonstrating good agreement. Small residual differences will be assessed as a source of systematic uncertainty.

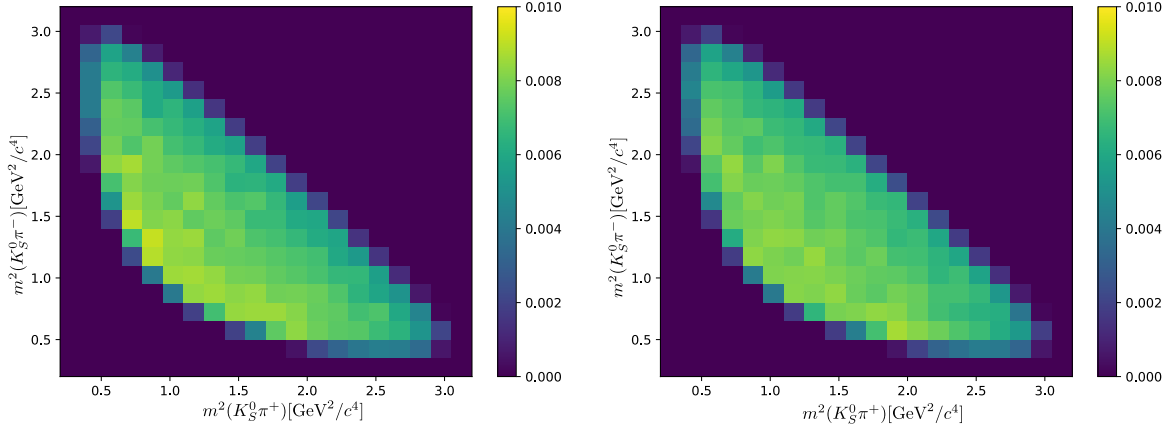


Figure 5.9: The distribution of the simulation samples in the  $D$  Dalitz plane for (top)  $B^+ \rightarrow D\pi^+$  and (bottom)  $B^0 \rightarrow DK^+\pi^-$  for  $D \rightarrow K_S^0\pi^+\pi^-$  DD.

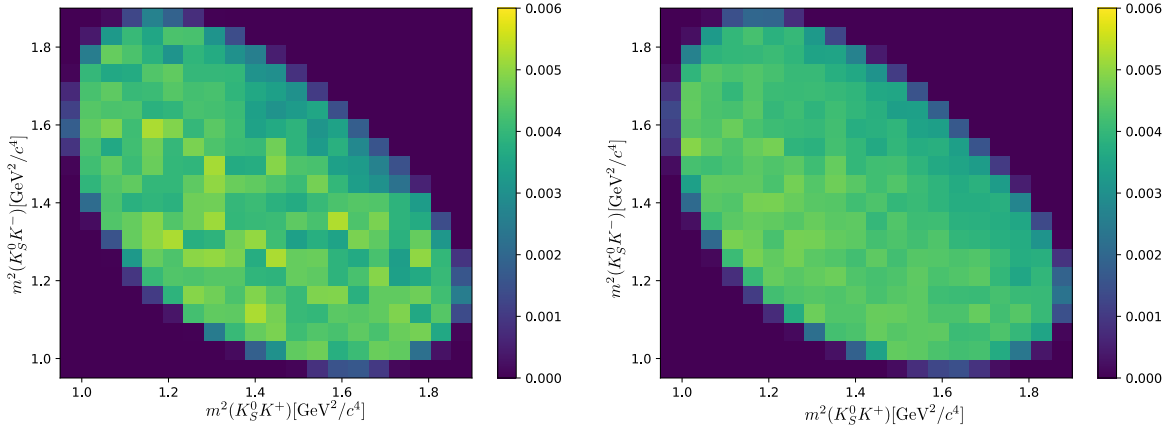


Figure 5.10: The distribution of the simulation samples in the  $D$  Dalitz plane for (top)  $B^+ \rightarrow D\pi^+$  and (bottom)  $B^0 \rightarrow DK^+\pi^-$  for  $D \rightarrow K_S^0 K^+ K^-$  DD.

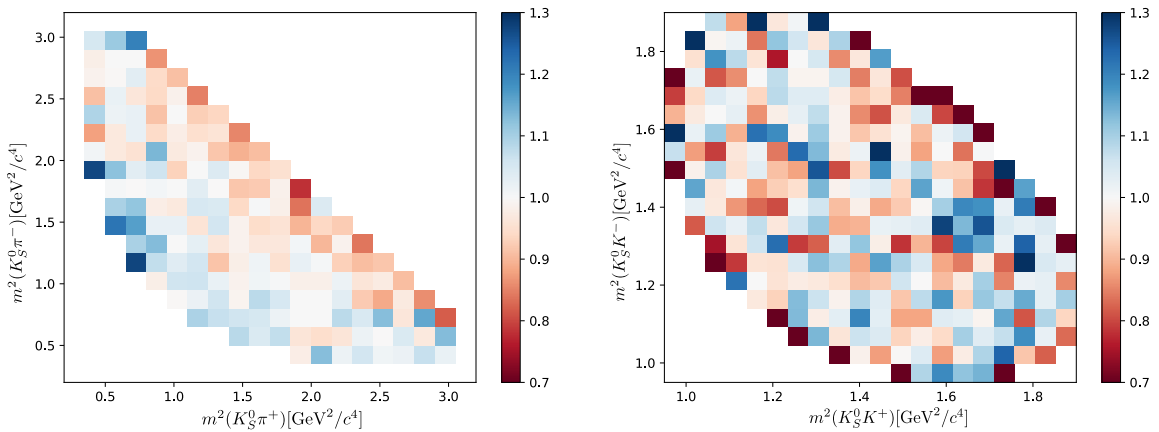


Figure 5.11: The ratio of the distribution of the simulation samples between the  $B^+ \rightarrow D\pi^+$  analysis and this analysis in the  $D$  Dalitz plane for the  $D \rightarrow K_S^0\pi^+\pi^-$  decay (top) and  $D \rightarrow K_S^0 K^+ K^-$  decay (bottom) when the  $K_S^0$  is reconstructed with DD tracks.

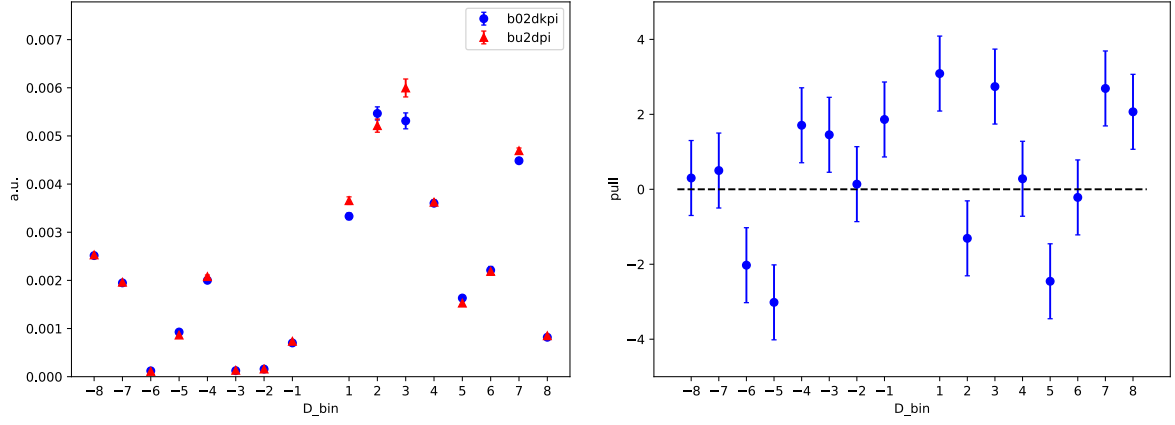


Figure 5.12: The fraction of simulated  $D \rightarrow K_S^0 \pi^+ \pi^-$  DD decays, reweighted according to the  $D$  amplitude model, in each of the  $D$  Dalitz bins.  $B^+ \rightarrow D\pi^+$  decays with the selection from the single Dalitz  $B^+ \rightarrow Dh^+$  analysis are shown in red,  $B^0 \rightarrow DK^+\pi^-$  decays with the selection from this analysis are shown in blue.

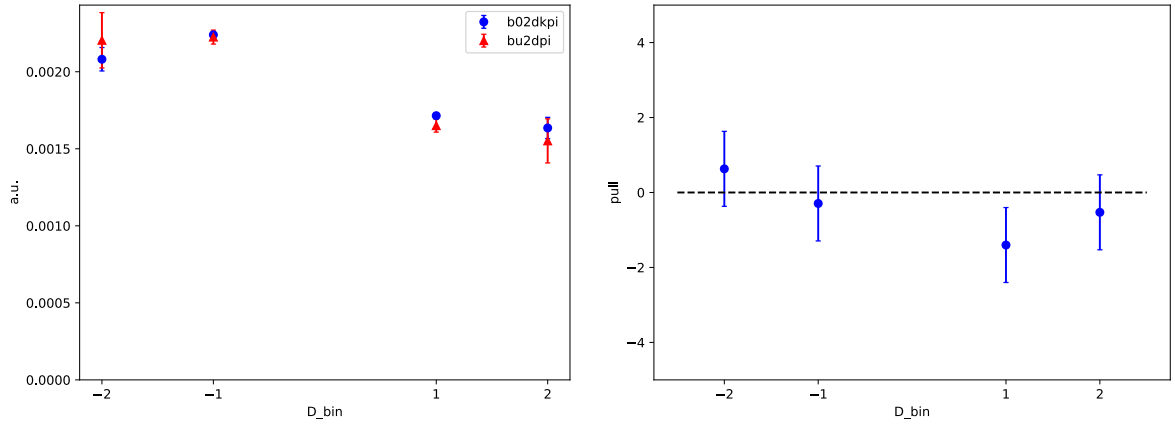


Figure 5.13: The fraction of simulated  $D \rightarrow K_S^0 K^+ K^-$  DD decays, generated according to the  $D$  amplitude model, in each of the  $D$  Dalitz bins.  $B^+ \rightarrow D\pi^+$  decays with the selection from the single Dalitz  $B^+ \rightarrow Dh^+$  analysis are shown in red,  $B^0 \rightarrow DK^+\pi^-$  decays with the selection from this analysis are shown in blue.

Another assumption made in this analysis, which is cross-checked here, is that the efficiency maps across the  $B$  Dalitz and  $D$  Dalitz plot are independent. This is confirmed by overlaying the distributions of the  $D$  Dalitz variables for each  $B$  bin in data simulated according to the appropriate  $D$  amplitude model [93, 94] and reweighted according to the appropriate  $B$  amplitude model after selection is applied [73]. Such plots are shown for each  $D \rightarrow K_S^0 h^+ h^-$  DD decays in Figs. 5.14 to 5.16 together with the ratio with respect to Bin 4, which has the largest entries in the simulation sample. They show no significant difference in the  $D$  Dalitz variable distributions for the different  $B$  bins.

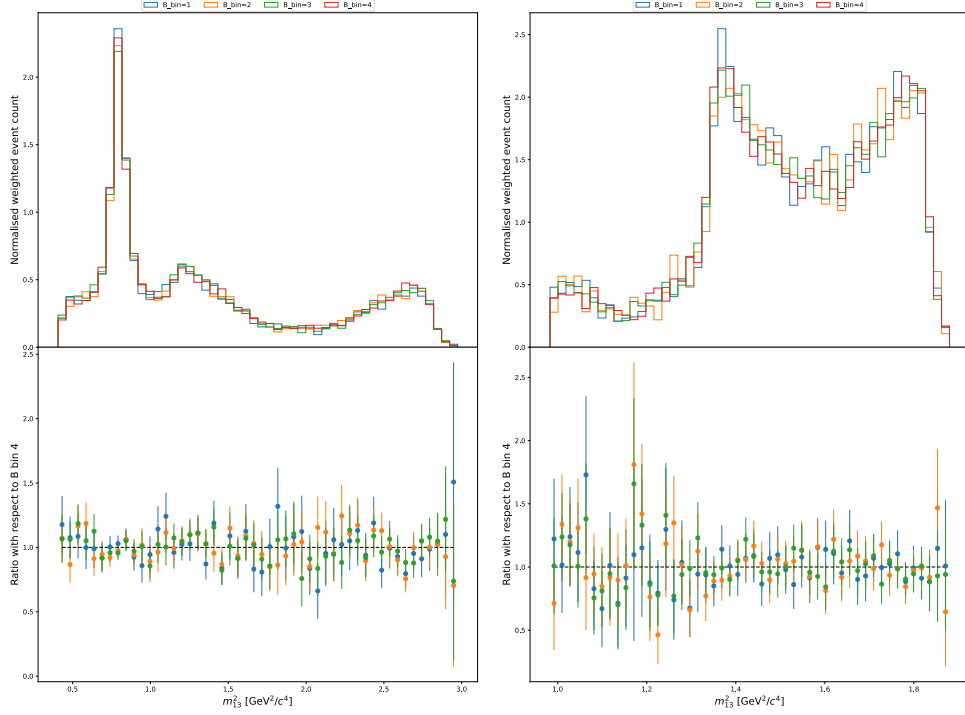


Figure 5.14: The distributions of the Dalitz variables  $D \rightarrow K_S^0 \pi^+ \pi^- m_{K_S^0 \pi^+}^2$  (left) and  $D \rightarrow K_S^0 K^+ K^- m_{K_S^0 K^+}^2$  (right) for each  $B$  bin and their ratio with respect to Bin 4.

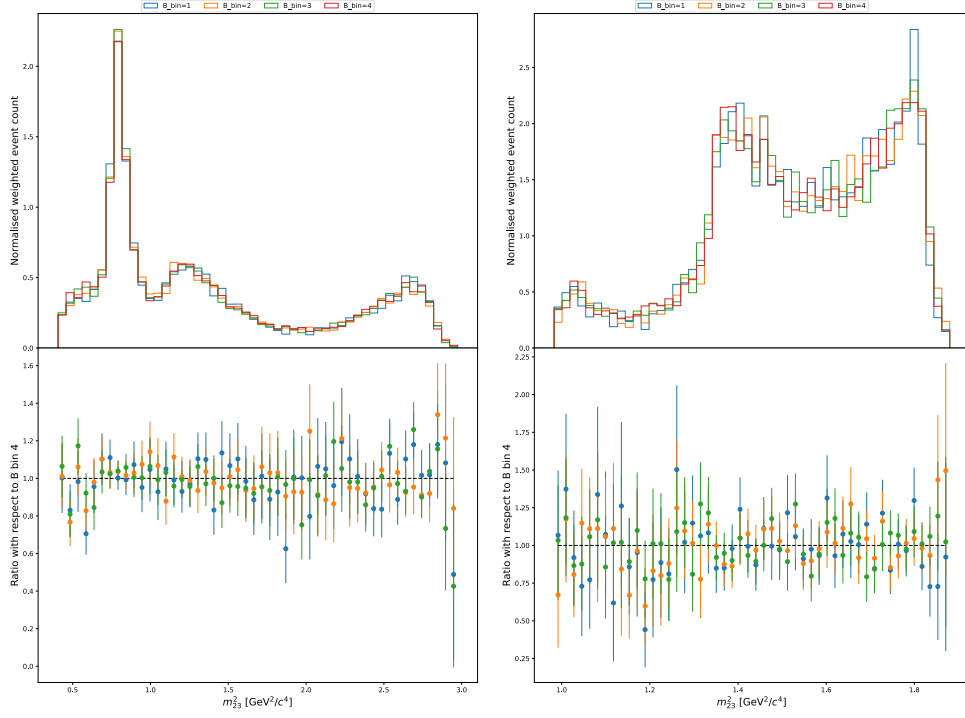


Figure 5.15: The distributions of the Dalitz variables  $D \rightarrow K_S^0 \pi^+ \pi^- m_{K_S^0 \pi^-}^2$  (left) and  $D \rightarrow K_S^0 K^+ K^- m_{K_S^0 K^-}^2$  (right) for each  $B$  bin and their ratio with respect to Bin 4.

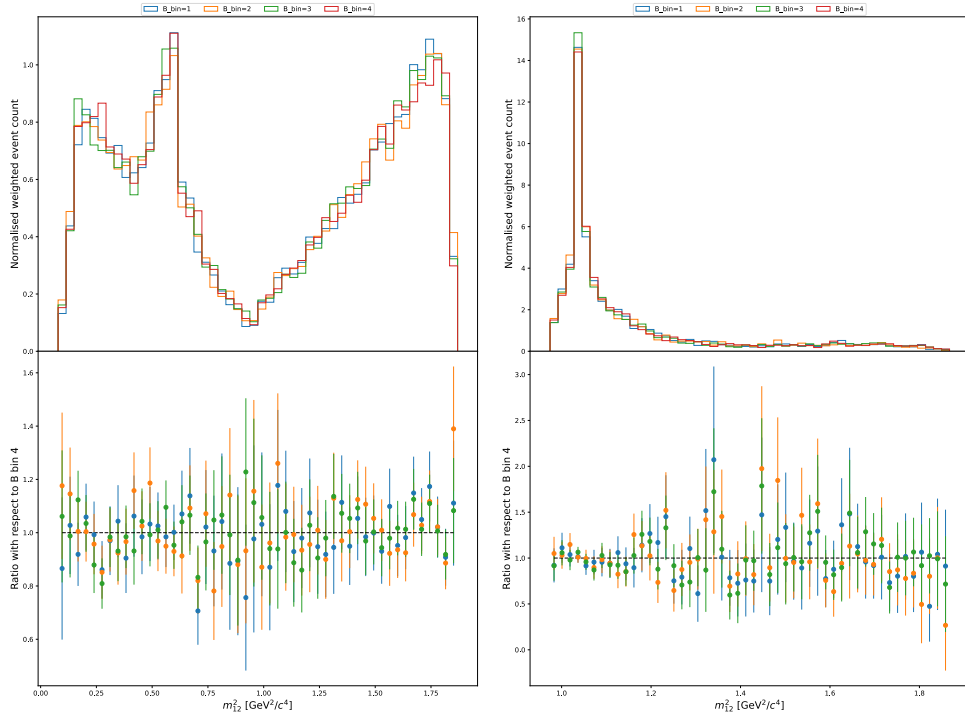


Figure 5.16: The distributions of the Dalitz variables  $D \rightarrow K_S^0 \pi^+ \pi^- m_{\pi^+ \pi^-}^2$  (left) and  $D \rightarrow K_S^0 K^+ K^- m_{K^+ K^-}^2$  (right) for each  $B$  bin and their ratio with respect to Bin 4.

## 5.4 Summary

Following the initial data collection and preparation for analysis, as described in Section 3.4, this chapter has described the full data selection that is applied. First the basic selection in Section 5.1 is applied to remove a significant amount of background data whilst maintaining a high signal efficiency. Next an optimised PID cut is applied to the solo particles to minimise the contributions from backgrounds associated with misidentified final state particles. A BDT is then trained and its response cut optimised to minimise the presence of combinatorial backgrounds. Another PID cut is then applied to children of the  $D$  decay, based on previous studies of LHCb data, and the effect of double misidentification is determined to be negligible. Kinematic vetoes are used to remove backgrounds originating from track-vertex misidentifications and finally a study is performed to estimate the presence of charmless backgrounds. In Section 5.3 the results of the selection are studied, in particular the efficiency profiles across the  $D$  Dalitz planes are studied to determine their compatibility with external measurements of the recursive  $R_i$  parameters. Now that the full selection has been applied the data is ready for fitting of the  $B$  invariant mass distributions, but first reweighting must be applied to the simulated datasets so that they can be used to model the invariant mass and Dalitz distributions of background decays.





# 6 Reweighting of backgrounds

“I don’t know if that’s a true statement, but let’s suppose it is.”

---

Caroline Konstnar

The work presented in Section 6.2.5 was performed by a postdoctoral research assistant Luis Miguel Garcia Martin but it is crucial to understand where this input comes from in the  $CP$  fit. Section 6.3 presents work of my analysis partner Yuya. The remaining work is my own.

## 6.1 Background fractions

As described in Section 4.5 in order to account for the presence of background decays one must determine how many decays each background contributes to each Dalitz bin. One requirement for this is to understand what fraction of each background populates each bin when reconstructed as the signal  $B^0 \rightarrow DK^+\pi^-$  decay, denoted as  $f_{\alpha,i}^b$  in Eq. (4.48). The other requirement is to determine the total number of each background decay present in the signal window via the use of invariant mass fits. These yields are shown in Tables 7.5 to 7.15. Estimates of these fractions are obtained from simulated datasets that model the true amplitude distribution of each background as well as the effects of the mis-reconstruction and the selection that is applied to the data. The approach is to first generate a simulated dataset that is flat in the square Dalitz plane of the  $B$  decay, and in the case of  $D \rightarrow K_S^0 h^+ h^-$  decays is generated according to an accurate physical model of the  $D$  decay amplitude distribution which is known to appropriately model the data [93, 94]. Each simulated event can then be weighted according to the model amplitude of the decay at its true Dalitz coordinates in the  $B$  Dalitz plane. The fraction in each bin can then be calculated as the sum of the weights in the bin divided by the total weight across all bins.

For  $D \rightarrow K_S^0 h^+ h^-$  decays the fractions are first determined for the  $B$  and  $D$  Dalitz planes separately and then multiplied to obtain the fraction in bin  $(\alpha, i)$ . This results in a lower uncertainty on the fractions and therefore a smaller systematic uncertainty.

## 6.2 Kinematic reweighting

As described above the simulated datasets are reweighted according to amplitude models for each background decay. Due to the different properties and current knowledge of each decay they are modelled in different ways and therefore weights are acquired via different methods.

Not all of the backgrounds seen in the mass fits in Chapter 7 have reweighting applied because there is no model available, however this modelling is only essential for the decays that have significant contributions to the distribution within the  $B^0$  mass signal window. All reweighted decays besides the  $\bar{\Lambda}_b^0 \rightarrow D^{(*)}K^+\bar{p}$  and  $\Lambda_b^0 \rightarrow D^{(*)}p\pi^-$  have models available but thanks to the proton PID cuts applied in Chapter 5 their contribution is minimised. The Dalitz distribution of  $\bar{\Lambda}_b^0 \rightarrow DK^+\bar{p}$  and  $\Lambda_b^0 \rightarrow Dp\pi^-$  decays in LHCb data are used as a proxy for their Dalitz distribution.

The various background modelling methods are summarised in Table 6.1 and described in more detail below. Figure 6.1 shows the square Dalitz distribution for each background decay model. All backgrounds are generated as flavour specific in the simulation. The combinatorial background is a special case and is not modelled using reweighted simulation but based on an extrapolation from sidebands in data as discussed in Section 6.2.5.

$B$ Decay	Model Type	Source
$\bar{B}_s^0 \rightarrow DK^+\pi^-$	Laura++ isobar	Ref. 95
$B^0 \rightarrow D\pi^+\pi^-$	Laura++ isobar	Ref. 96
$B^0 \rightarrow D^*K^+\pi^-$	Signal projection of LHCb data	Ref. 97
$\bar{B}_s^0 \rightarrow D^*K^+\pi^-$	Signal projection of LHCb data	Ref. 97
$B^0 \rightarrow D^*\pi^+\pi^-$	Signal projection of LHCb data	Ref. 97
$\Lambda_b^0 \rightarrow Dp\pi^-$	Selected LHCb data	Ref. 98
$\Lambda_b^0 \rightarrow D^*p\pi^-$	Selected LHCb data	Ref. 98
$\bar{\Lambda}_b^0 \rightarrow DK^+\bar{p}$	Selected LHCb data	Ref. 99
$\bar{\Lambda}_b^0 \rightarrow D^*K^+\bar{p}$	Selected LHCb data	Ref. 99
Combinatorial	Polynomial extrapolation	Sideband data

Table 6.1: Type of model used for each background and their source.

### 6.2.1 Laura++

Using this package LHCb has developed isobar models for  $B^0 \rightarrow D\pi^+\pi^-$  and  $\bar{B}_s^0 \rightarrow DK^+\pi^-$  decays. This can weight a sample generated flat in the square Dalitz plane according to a given model, it accounts for the flat generation by multiplying the weight by a Jacobian which corresponds to the appropriate coordinate transformation as explained in Ref. 21.

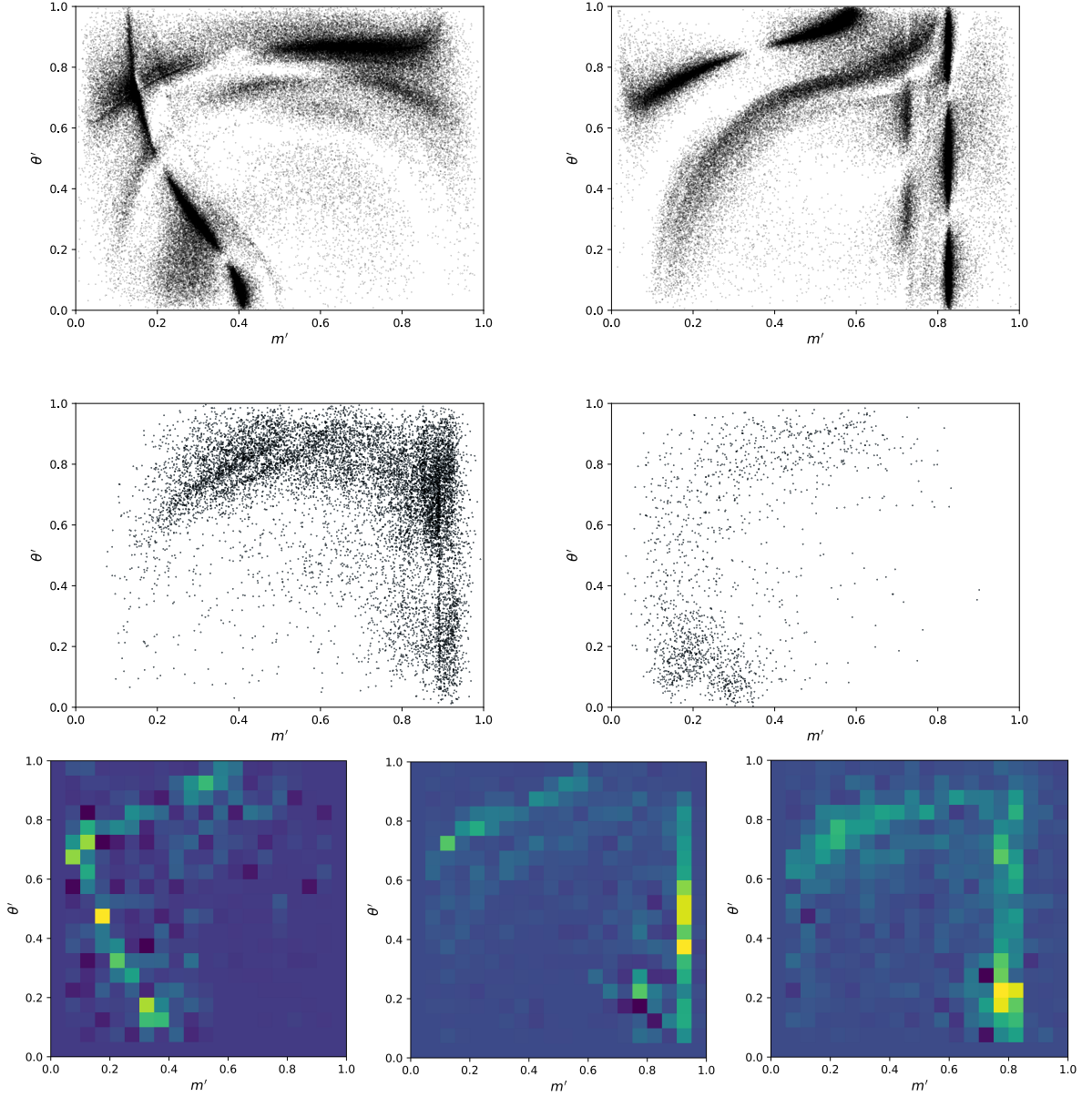


Figure 6.1: Square Dalitz plane distributions of the models used to reweight the background simulation samples. Top: events generated from the Laura++ model of  $B^0 \rightarrow D\pi^+\pi^-$  (left) and  $\bar{B}_s^0 \rightarrow DK^+\pi^-$  (right) decays. Middle: observed events for the  $\Lambda_b^0 \rightarrow Dp\pi^-$  (left) and  $\bar{\Lambda}_b^0 \rightarrow DK^+\bar{p}$  (right) decays. Bottom: signal projected data events for the  $B^0 \rightarrow D^*K^+\pi^-$  (left),  $\bar{B}_s^0 \rightarrow D^*K^+\pi^-$  (middle) and  $B^0 \rightarrow D^*\pi^+\pi^-$  (right) decays.

For a given event in the simulation sample, with true square Dalitz position  $(m', \theta')$ , the weight is determined according to

$$w(m', \theta') = |J(m', \theta')| |A(m', \theta')|^2 / |A|_{\max}^2, \quad (6.1)$$

where  $J(m', \theta')$  is the value of the Jacobian at the given position,  $A(m', \theta')$  is the amplitude obtained from the model at the given position and  $|A|_{\max}^2$  is the maximum amplitude-

squared across the Dalitz plane.

### 6.2.2 Signal projected measurements

`Laura++` can not be used to model decays with non-spin-0 final states, therefore efficiency corrected signal distributions from LHCb measurements is used to model the contributions from  $B^0 \rightarrow D^* K^+ \pi^-$ ,  $\bar{B}_s^0 \rightarrow D^* K^+ \pi^-$  and  $B^0 \rightarrow D^* \pi^+ \pi^-$  decays. The relevant information for the background channels of interest is available in Ref. [100], the distributions can be seen in Fig. 6.1. As can be seen here these projections are provided as uniformly binned histograms of the square Dalitz plane. A weight is obtained for each point in the square Dalitz plane by comparing the entries in the corresponding bin of the signal projection with the population of the same bin in a `RapidSim` sample [101], generated flat in the square Dalitz plane.

This weight is defined as

$$w(m', \theta') = \frac{P_{i,j}^S / S_{i,j}^S}{P_{i,j}^F / S_{i,j}^F} \frac{\sum_{j'} \sum_{i'} P_{i',j'}^F}{\sum_{j'} \sum_{i'} P_{i',j'}^S}, \quad (6.2)$$

where  $i, j$  denotes the bin of the uniformly-binned square Dalitz plane corresponding to a given  $(m', \theta')$ ,  $P$  ( $S$ ) denotes the population (size) of the bin and a superscript  $S$  ( $F$ ) denotes the observed data (flat) histogram. The inclusion of an `EvtGen`-flat square Dalitz histogram accounts for the non-uniform `EvtGen` generation at the boundaries [102].

### 6.2.3 Background polluted Dalitz distributions

For the background originating from a  $\Lambda_b^0$  decay there are no complete amplitude model descriptions available. There are also no signal projections (*i.e.* background subtracted) distributions published. Consequently, the observed Dalitz distributions of the  $\Lambda_b^0 \rightarrow D p \pi^-$  and  $\bar{\Lambda}_b^0 \rightarrow D K^+ \bar{p}$  decays from Refs. [98, 99] are the only possible sources of information about the amplitude distribution of these decays. The distributions are of fully selected data but include some small level of background, this will also have the full LHCb acceptance and efficiency effects already present in the distribution. The amount of the  $\Lambda_b^0$  decays that infiltrate the signal window is relatively small so imperfect modeling is a small effect.

Measurements of the Dalitz distribution of  $\Lambda_b^0 \rightarrow D^* p \pi^-$  ( $\bar{\Lambda}_b^0 \rightarrow D^* K^+ \bar{p}$ ) have not been performed so it is assumed that the  $\Lambda_b^0 \rightarrow D p \pi^-$  ( $\bar{\Lambda}_b^0 \rightarrow D K^+ \bar{p}$ ) Dalitz distribution is close enough to serve as a model for this decay as well, *i.e.* it is assumed that the  $D^{*0}$  version of a  $D^0$  mode has an identical  $B$  Dalitz distribution.

An adaptive binning scheme is used to bin the square Dalitz plane such that each bin contains an equal number of events. This results in a weight mapping that is detailed in the regions of high amplitude density while maintaining statistical significance in each bin.

Figure 6.2 (Fig. 6.3) shows the square Dalitz distribution of  $\Lambda_b^0 \rightarrow Dp\pi^-$  ( $\Lambda_b^0 \rightarrow DpK^-$ ) and the adaptive binning derived from it.

For a given event in the simulation sample, with true square Dalitz coordinates  $(m', \theta')$  its weight is obtained as

$$W = \frac{P_R(m', \theta')/S_R(m', \theta')}{P_F(m', \theta')/S_F(m', \theta')}, \quad (6.3)$$

where  $P_{R(F)}(m', \theta')$  is the population of the bin corresponding to the point  $(m', \theta')$  in the square Dalitz plane in the resonance (flat) sample and  $S_{R(F)}(m', \theta')$  is the size of that bin.

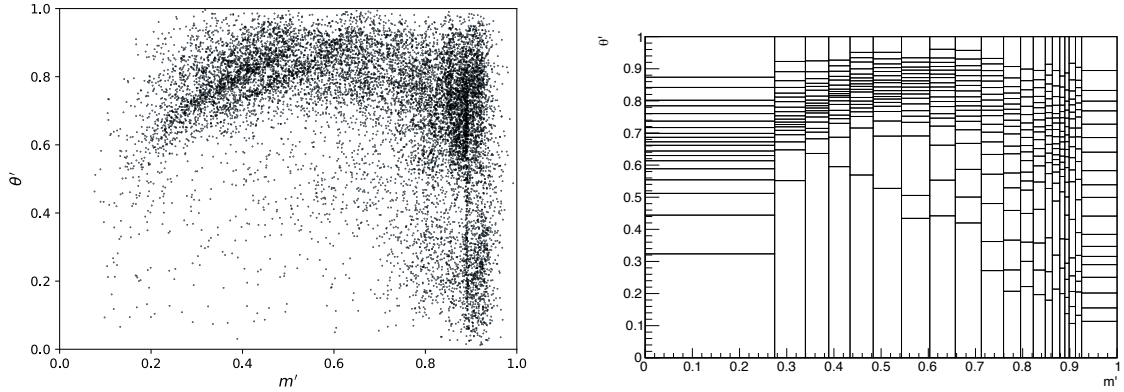


Figure 6.2: Measured square Dalitz distribution of  $\Lambda_b^0 \rightarrow Dp\pi^-$  decays from Ref. [98] (left) and the adaptive binning scheme derived from it (right).

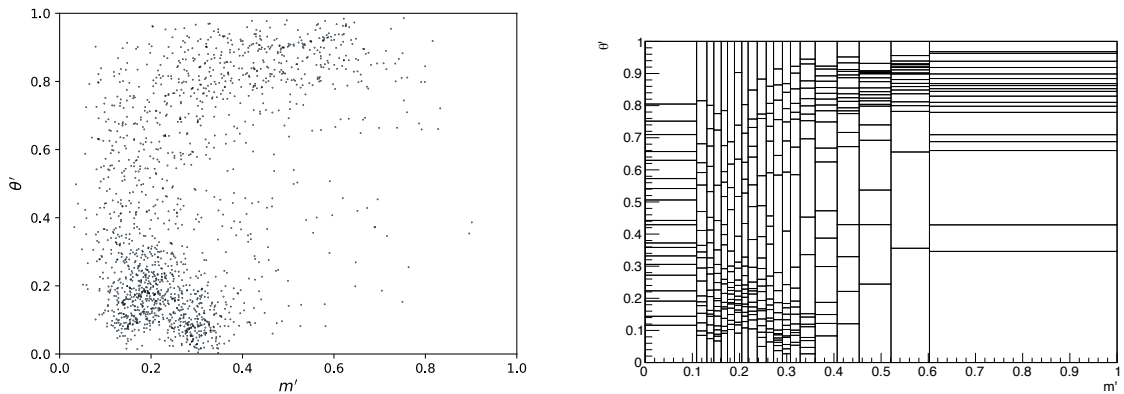


Figure 6.3: Measured square Dalitz distribution of  $\Lambda_b^0 \rightarrow DK^+\bar{p}$  decays from Ref. [99] (left) and the adaptive binning scheme derived from it (right).

### 6.2.4 Model reweighting results

Figures 6.4 to 6.7 show a comparison between the efficiency corrected models and the reweighted truth distributions in  $m'$  and  $\theta'$  for each modelled background decay. This verifies that the per-event reweighting has been applied correctly. These plots were made using 2018 Magnet Up simulation for the  $D \rightarrow K^+ K^-$  final state but the results for the other  $D$  decays are, as expected, extremely similar. Note that the uncertainty on the efficiency corrected model distributions depends on the method used to obtain the initial model distribution. In the case of  $B^0 \rightarrow D^* K^+ \pi^-$  decays the integral of the sweight distribution is considerably smaller than that of the  $B_s^0 \rightarrow D^* K^- \pi^+$  and  $B^0 \rightarrow D^* \pi^+ \pi^-$  distributions, hence the larger uncertainties.

Figure 6.7 shows a slight discrepancy between the distribution of the reweighted simulated data and the efficiency corrected model, likely due to the low amount of simulated data available after full selection. This is expected to have a negligible effect on the final result since the  $\Lambda_b^0$  decay backgrounds are suppressed by the proton PID rejection.

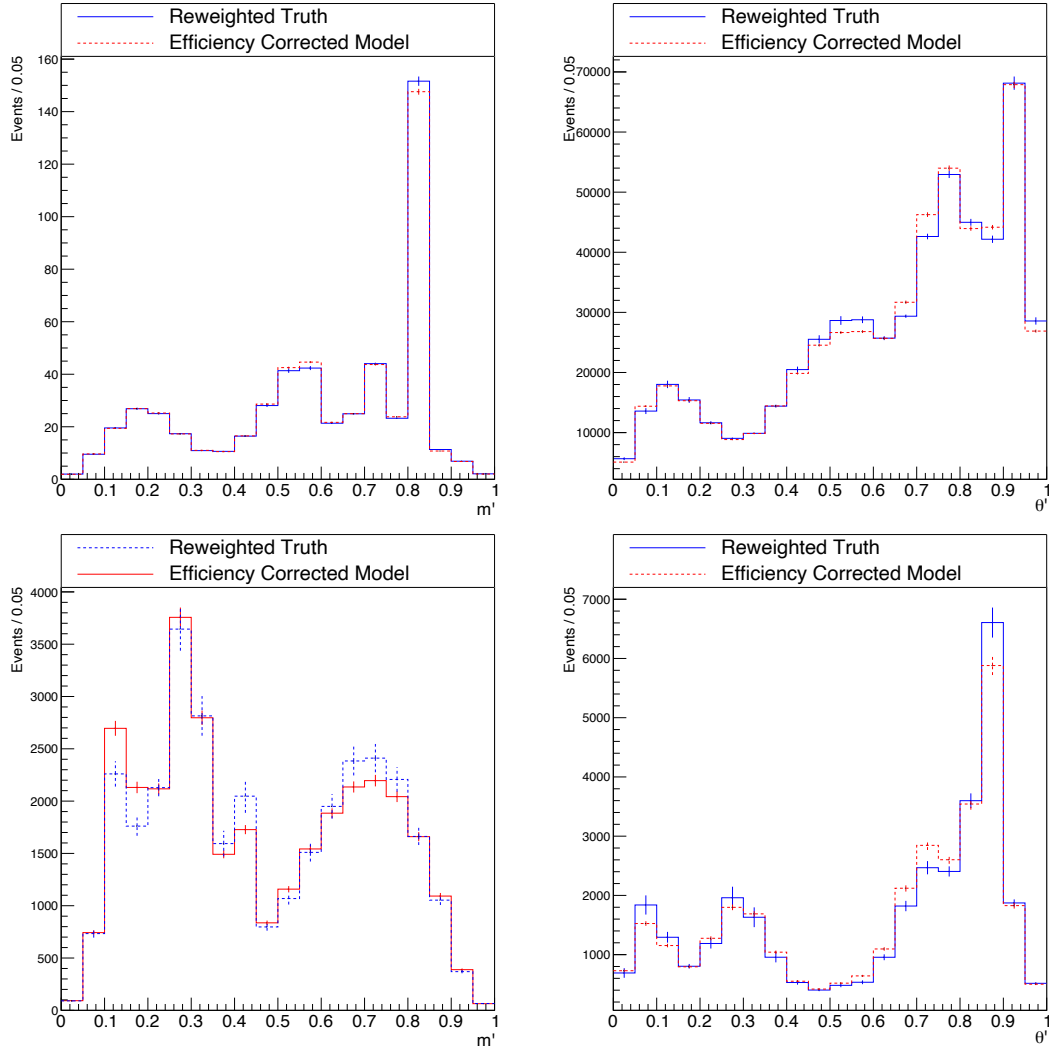


Figure 6.4: Comparison between the reweighted simulation truth and efficiency corrected model  $m'$  (left) and  $\theta'$  (right) distributions for  $\bar{B}_s^0 \rightarrow DK^+\pi^-$  (top) and  $B^0 \rightarrow D\pi^+\pi^-$  (bottom) decays.



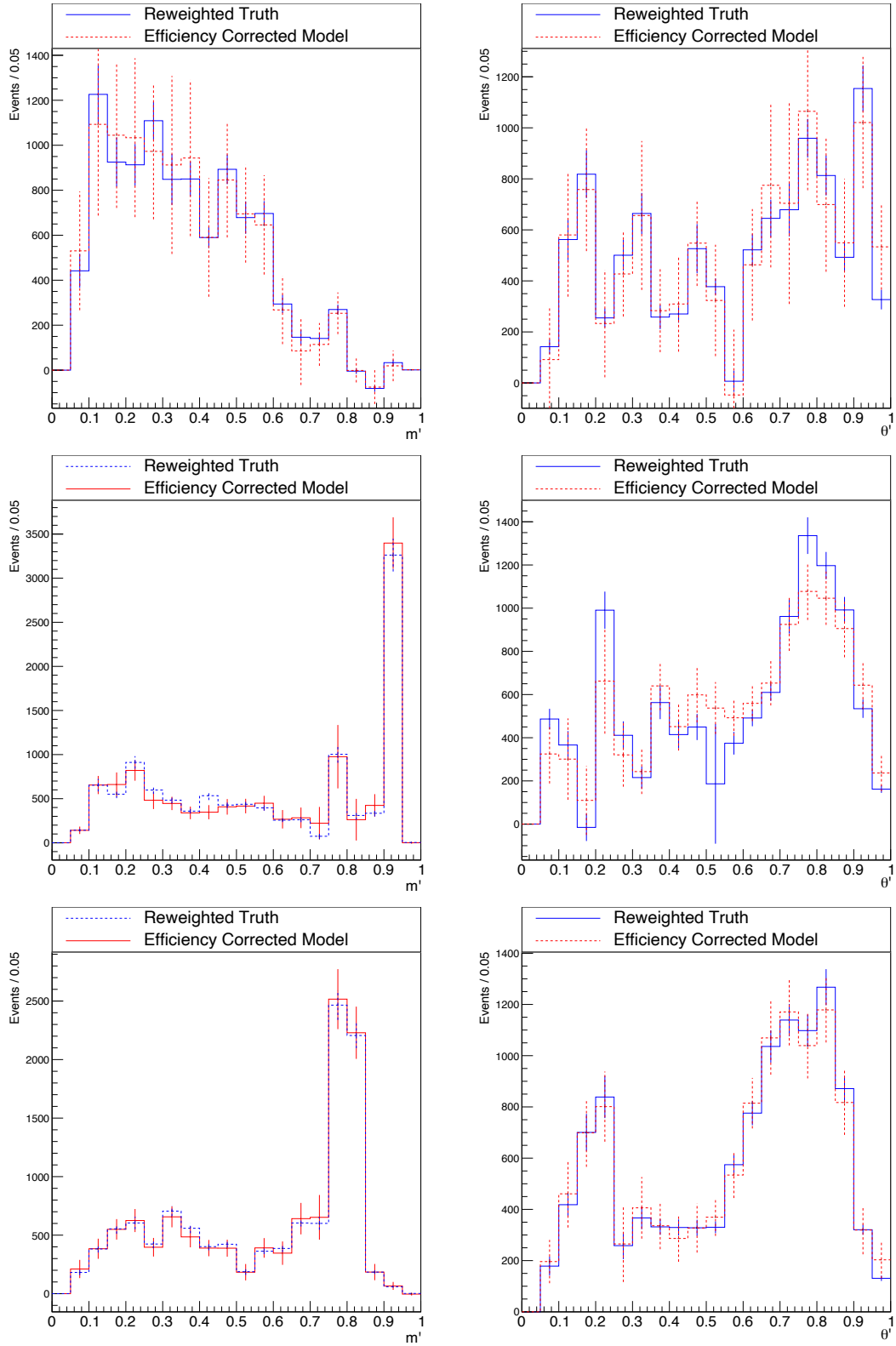


Figure 6.5: Comparison between the reweighted simulation truth and efficiency corrected model  $m'$  (left) and  $\theta'$  (right) distributions for  $B^0 \rightarrow D^*K^+\pi^-$  (top),  $\bar{B}_s^0 \rightarrow D^*K^+\pi^-$  (middle) and  $B^0 \rightarrow D^*\pi^+\pi^-$  (bottom) decays.

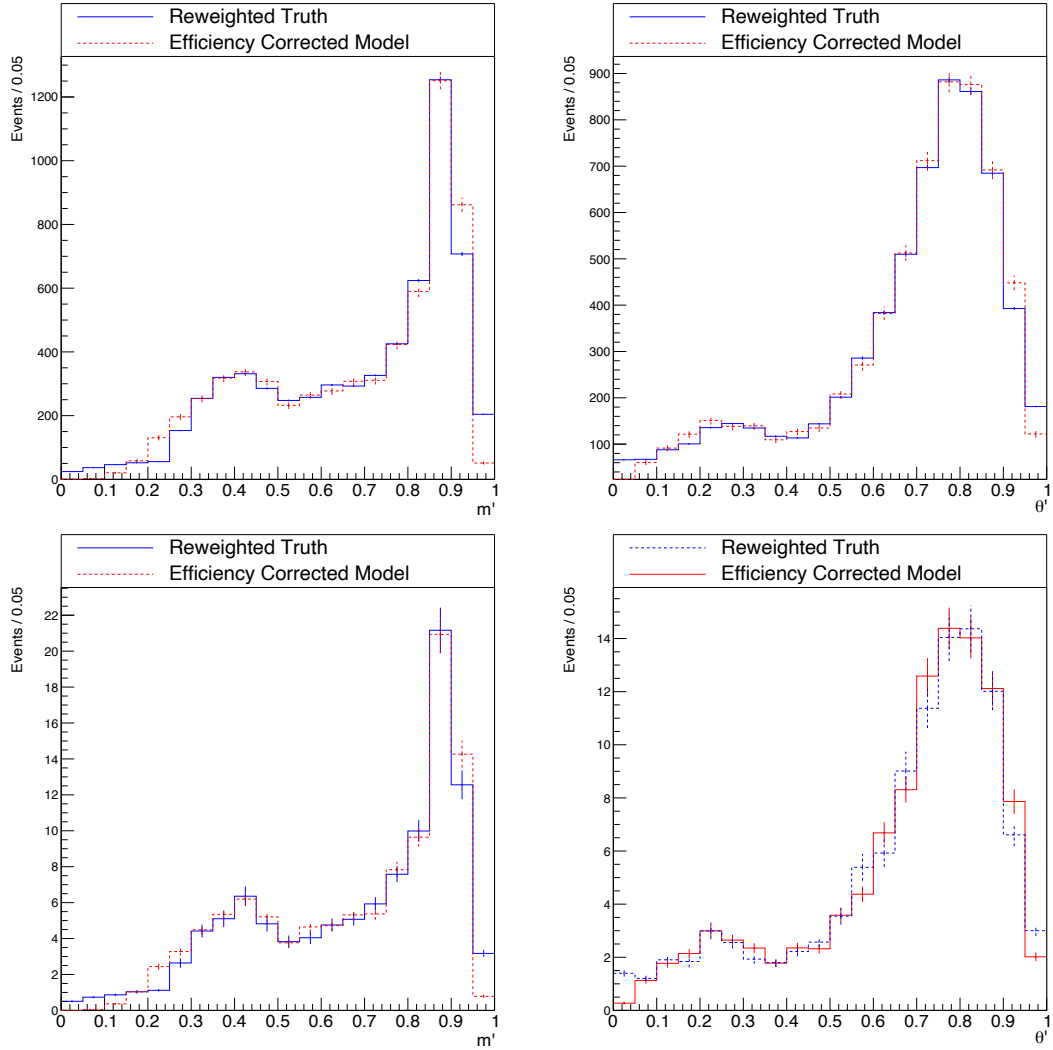


Figure 6.6: Comparison between the reweighted simulation truth and efficiency corrected model  $m'$  (left) and  $\theta'$  (right) distributions for  $\Lambda_b^0 \rightarrow Dp\pi^-$  (top),  $\Lambda_b^0 \rightarrow D^*p\pi^-$  (bottom) decays.

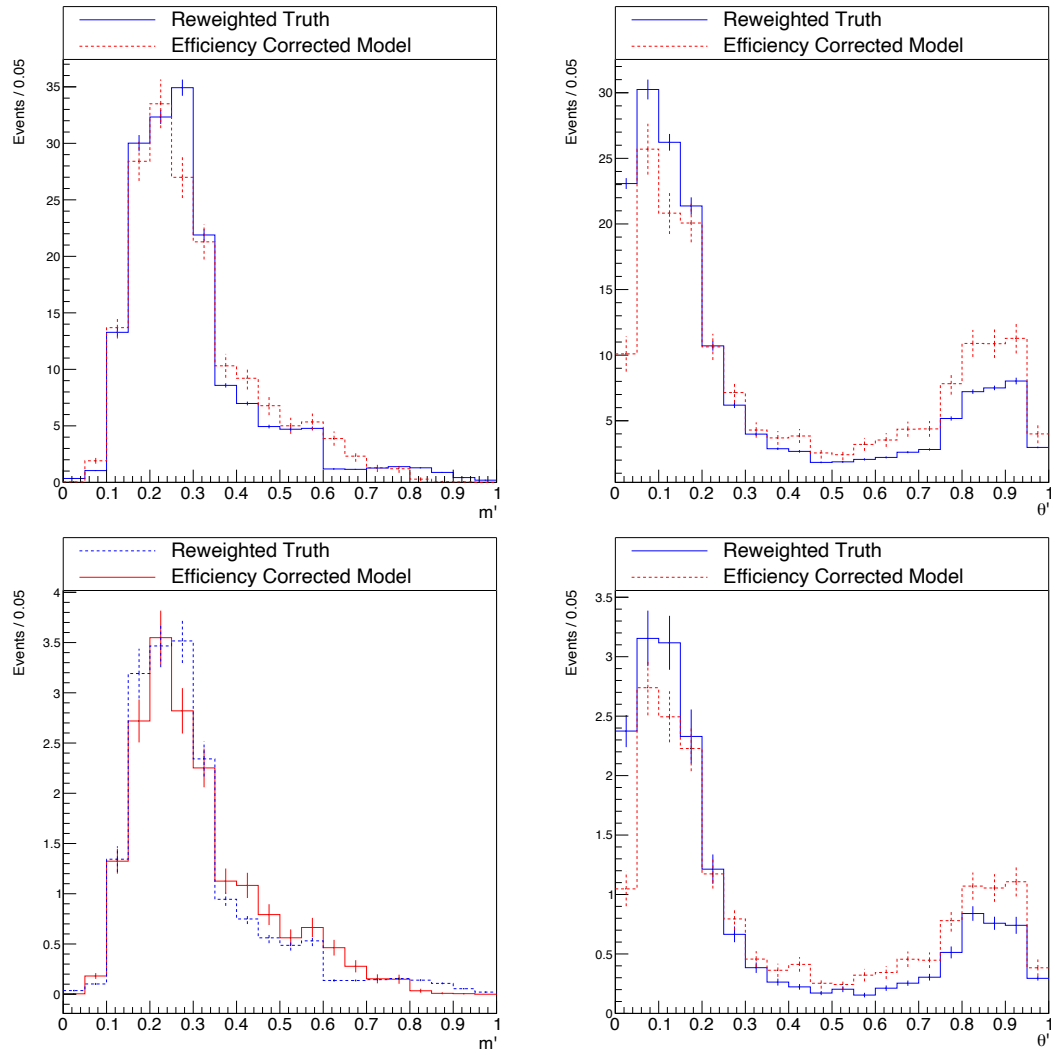


Figure 6.7: Comparison between the reweighted simulation truth and efficiency corrected model  $m'$  (left) and  $\theta'$  (right) distributions for  $\Lambda_b^0 \rightarrow DpK^-$  (top),  $\Lambda_b^0 \rightarrow D^*pK^-$  (bottom) decays.

### 6.2.5 Combinatorial background modelling

Combinatorial background events are those for which random combinations of final state tracks happen to mimic  $B^0 \rightarrow DK^+\pi^-$  decays. The majority of decays in the high mass sideband of the  $B^0$  candidate invariant mass distribution are combinatorial background decays so can be used to gain an understanding of how these are distributed across the Dalitz planes. However, the Dalitz plane phase space changes as a function of the  $B^0$  candidate invariant mass so some attempt must be made to predict how this evolves from the high mass sideband to the signal window.

A neural network method [103] was first attempted to perform this however it was found not to be optimal due to the low amount of sideband data. Instead the Dalitz binned distribution of combinatorial background is modelled with a first order polynomial. For each  $D$  final state a set of seven adjacent sidebands is defined, each with the same width as the signal window, starting at  $m(B) = 5442.4$  which is sufficiently high to ensure that each sideband in data contains almost completely pure combinatorial background. A visualisation of the signal region and sidebands is shown for the  $D \rightarrow K_S^0\pi^+\pi^-$  DD final state in Fig. 6.8. The combinatorial extrapolation procedure is performed separately for the  $B$  and  $D$  Dalitz planes in order to increase the statistics available for the extrapolation, *i.e.* it is assumed that the  $B$  and  $D$  Dalitz plane combinatorial fractions factorise. This is performed using the 5 bin binning for the  $B^0 \rightarrow DK^+\pi^-$  Dalitz plane since the resulting fractions can trivially be summed to obtain the nominal 4 bin binning. For each bin individually a first order polynomial is fitted to the fraction of the total events in that bin in each sideband window. Higher orders will be used for systematic studies. It is recognised that this is not an ideal method, particularly given the large fluctuations in these fractions along the sideband windows, however no alternative could be found and this will have to be revisited in later iterations of this analysis method. Figures 6.9 and 6.10 show the extrapolation fits in the  $B$  and  $D$  planes respectively for the  $D \rightarrow K_S^0\pi^+\pi^-$  DD final state.

## 6.3 Helicity weighting

One of the most significant backgrounds in the analysis originates from partially reconstructed  $B_s^0 \rightarrow D^*K^-\pi^+$  decays, which appear in the low-mass region when a soft pion or photon emitted from the neutral  $D^{*0}$  is missed in the reconstruction. The reconstructed mass of the  $B^0$  candidate depends on the momentum of the missing particle, which is related to the helicity state of the intermediate resonance. The LHCb simulation does not model the helicity states which results in an incorrect invariant mass distribution. Therefore the simulation must be reweighted according to the expected helicity distribu-

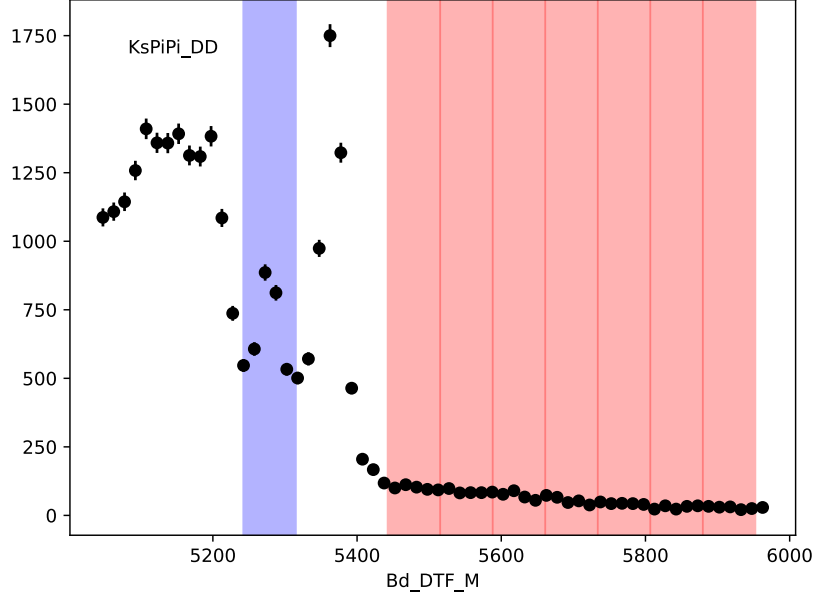


Figure 6.8: A visualisation of the signal window (blue) and the sidebands (red) used for the combinatorial background extrapolation in the  $D \rightarrow K_S^0 \pi^+ \pi^-$  DD final state.

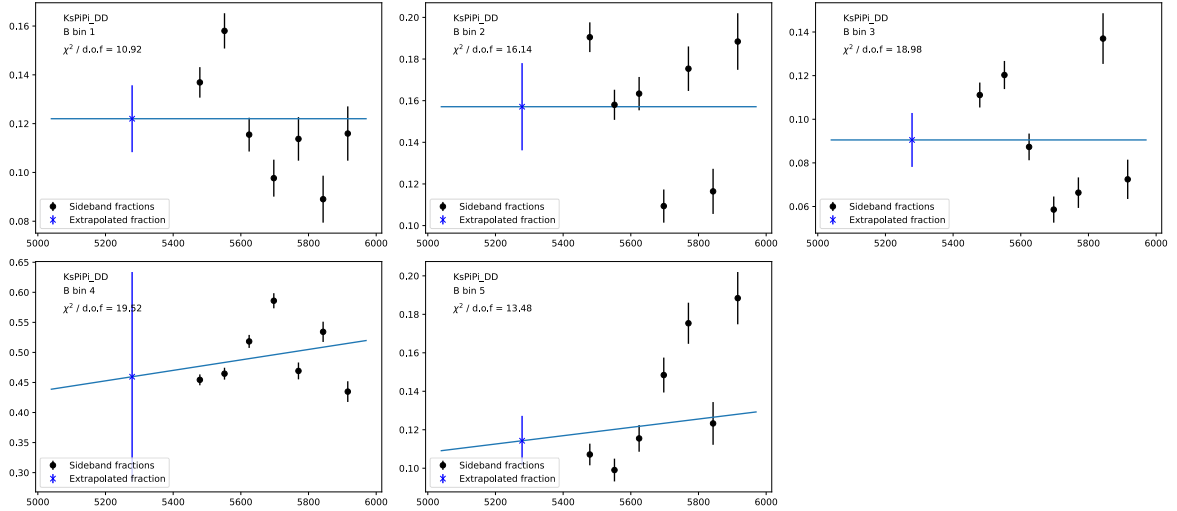


Figure 6.9: Combinatorial background extrapolation fits in the  $B$  Dalitz plane for the  $D \rightarrow K_S^0 \pi^+ \pi^-$  DD final state.

tions. Only the two dominant contributing resonant components are considered. These are  $D^{*0} K^{*0}$  and  $D_{s1}^- \pi^+$  for  $\bar{B}_s^0 \rightarrow D^* K^+ \pi^-$ , and  $D^{*0} K^{*0}$  and  $D_1^- K^+$  for  $B^0 \rightarrow D^* K^+ \pi^-$ . In the case of the  $D^{*0} K^{*0}$  resonance, the helicity angle is defined as the angle between the momentum vector of the  $K^+$  in the  $K^{*0}$  rest frame and the momentum vector of the  $K^{*0}$  in the  $B_s^0$  or  $B^0$  rest frame. For the  $D_{s1}^- \pi^+$  ( $D_1^- K^+$ ) resonance it is defined as the angle between the momentum vector of the  $\gamma$  or  $\pi^0$  in the  $D^{*0}$  rest frame and the momentum vector of the  $D^{*0}$  in the  $D_{s1}^-$  ( $D_1^-$ ) rest frame. Given that the spin structure of the resonant components is known, a per-event weight is derived based on the expected

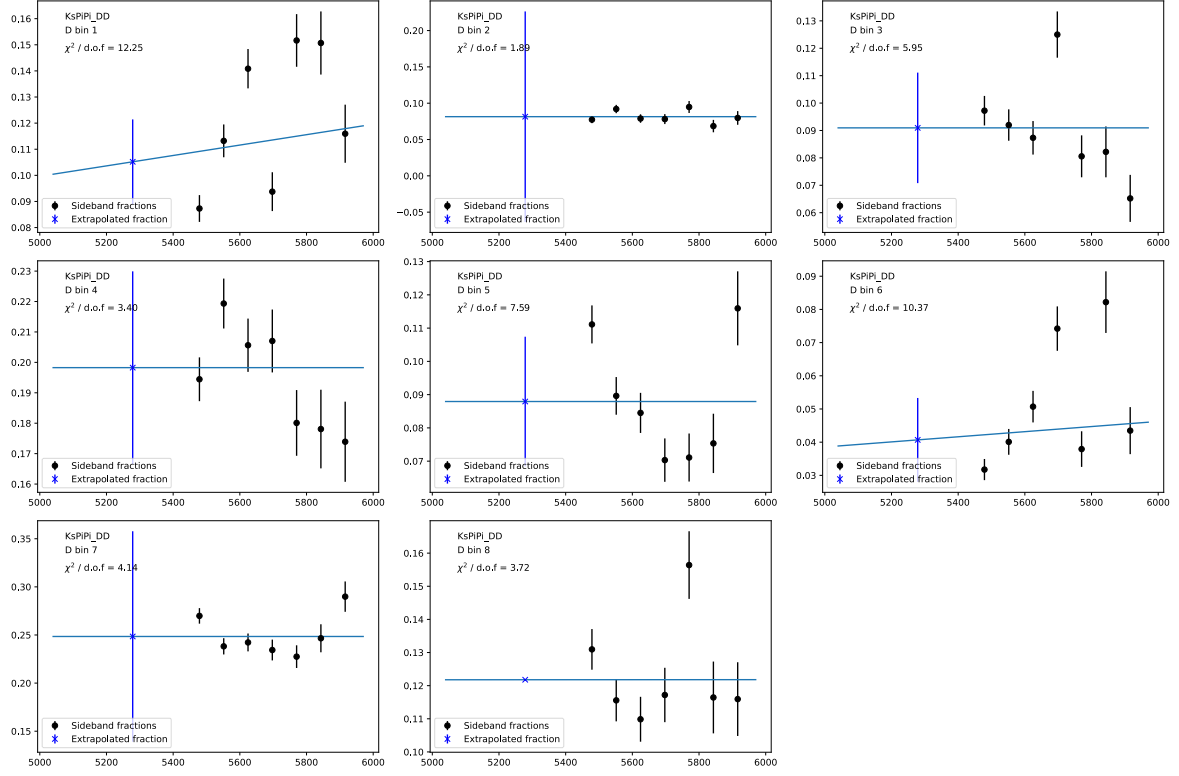


Figure 6.10: Combinatorial background extrapolation fits in the  $D$  Dalitz plane for the  $D \rightarrow K_S^0 \pi^+ \pi^-$  DD final state.

distribution of the helicity angle(s).

### 6.3.1 $B_s^0 \rightarrow D_{s1}^- (\rightarrow \bar{D}^{*0} K^-) \pi^+$

The helicity angle distributions for  $D^* \rightarrow D\gamma$  and  $D^* \rightarrow D\pi^0$  have been derived in the  $B_{(s)}^0 \rightarrow D_{s1}(2536)^\mp K^\pm$  LHCb analysis [104]. These distributions are in general dependent on three decay angles. Integrating over the angles that are not relevant for this analysis results in an expression with a dependence on the angle of interest,  $\theta$ . The relevant distribution for  $D^* \rightarrow D\gamma$  mode can then be written as

$$\frac{d\sigma}{d\cos\theta} \propto k^2 + (1 - k^2) \cos^2 \theta, \quad (6.4)$$

and for the  $D^* \rightarrow D\pi^0$  mode it is

$$\frac{d\sigma}{d\cos\theta} \propto k^2 + 1 + (k^2 - 1) \cos^2 \theta, \quad (6.5)$$

where  $k$  is related to the ratio of the different helicity couplings, measured to be  $k = 1.93 \pm 0.06 \pm 0.08$  [104].

### 6.3.2 $B^0 \rightarrow D_1^-(\rightarrow \bar{D}^{*0}\pi^-)K^+$

In this mode, the expression for the angular distributions is of the form

$$\frac{d\sigma}{d\cos\theta} \propto 1 + A_{D_1} \cos^2\theta, \quad (6.6)$$

where  $A_{D_1}$  is the polarisation amplitude which is equal to  $5.73 \pm 0.25$  [89].

### 6.3.3 $B_s^0 \rightarrow \bar{D}^{*0}\bar{K}^{*0}(\rightarrow K^-\pi^+)$ , $B^0 \rightarrow \bar{D}^{*0}K^{*0}(\rightarrow K^+\pi^-)$

These decays are a transition of a scalar to two vectors. In this case, the helicity states of  $D^{*0}$  and  $K^{*0}$  can be (0,0), (1,1), or (-1,-1). The angular distribution of the  $D^{*0}$  child particles is the same for (1,1) and (-1,-1), so only four unique categories need to be modelled: (0,0) or (1,1) with  $D^0\gamma$  or  $D^0\pi^0$ . The dependence of the amplitude on the helicity angle can be expressed as the following.

- (0,0),  $D^0\gamma$  mode

$$\frac{d\sigma}{d\cos\theta} \propto \sin^2\theta \quad (6.7)$$

- (0,0),  $D^0\pi^0$  mode

$$\frac{d\sigma}{d\cos\theta} \propto \cos^2\theta \quad (6.8)$$

- (1,1),  $D^0\gamma$  mode

$$\frac{d\sigma}{d\cos\theta} \propto 1 + \cos^2\theta \quad (6.9)$$

- (1,1),  $D^0\pi^0$  mode

$$\frac{d\sigma}{d\cos\theta} \propto \sin^2\theta \quad (6.10)$$

### 6.3.4 Reweighting procedure

Each event is classified as one of the decay categories above based on the final state invariant masses,  $m(K\pi)$  and  $m(D^0K)$  or  $m(D^0\pi)$  with the following criteria:

- $|m(K\pi) - m_{K^{*0}}| < 100 \text{ MeV}/c^2 \implies B_s^0 \rightarrow \bar{D}^{*0}\bar{K}^{*0}(\rightarrow K^-\pi^+)$  or  $B^0 \rightarrow \bar{D}^{*0}K^{*0}(\rightarrow K^+\pi^-)$
- $|m(D^0K) - m_{D_{s1}}| < 10 \text{ MeV}/c^2 \implies B_s^0 \rightarrow D_{s1}^-(\rightarrow \bar{D}^{*0}K^-)\pi^+$
- $|m(D^0\pi) - m_{D_1}| < 40 \text{ MeV}/c^2 \implies B^0 \rightarrow D_1^-(\rightarrow \bar{D}^{*0}\pi^-)K^+$

If the event does not fall into any of these categories the weight is 1, *i.e.* no weighting is applied, otherwise the weight is calculated based on the expressions above with normalisation taken into account. When the category is  $K^{*0}$ , the event is assigned a weight for the (0,0) helicity state with a probability  $p = 1/3$  and for the (1,1) state with  $p = 2/3$ .

### 6.3.5 Reweighted helicity angle distributions

The distribution of the helicity angle with and without the helicity reweighting for  $D \rightarrow K_S^0 \pi^+ \pi^-$  DD at the level of the basic selection described in Section 5.1 is shown in Figs. 6.11 to 6.16.

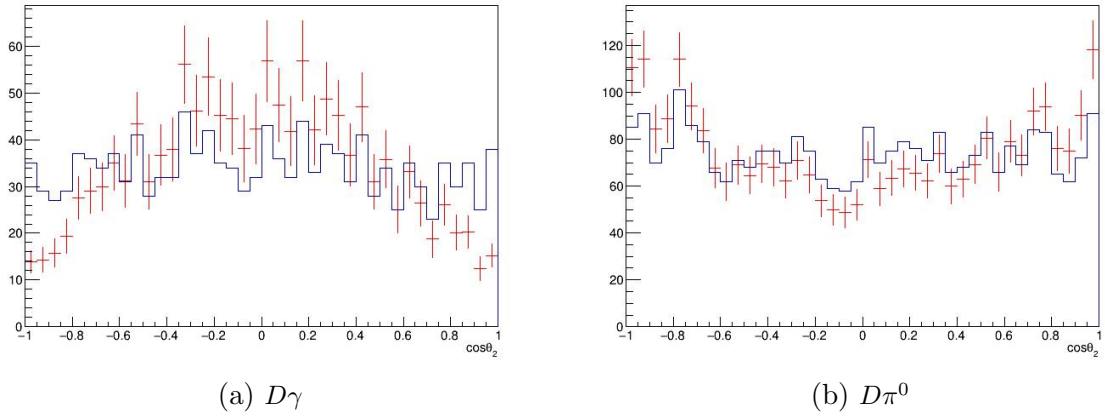


Figure 6.11: The distribution of the helicity angle with and without the helicity reweighting for  $B_s^0 \rightarrow D_{s1}^- (\rightarrow \bar{D}^{*0} K^-) \pi^+$ .

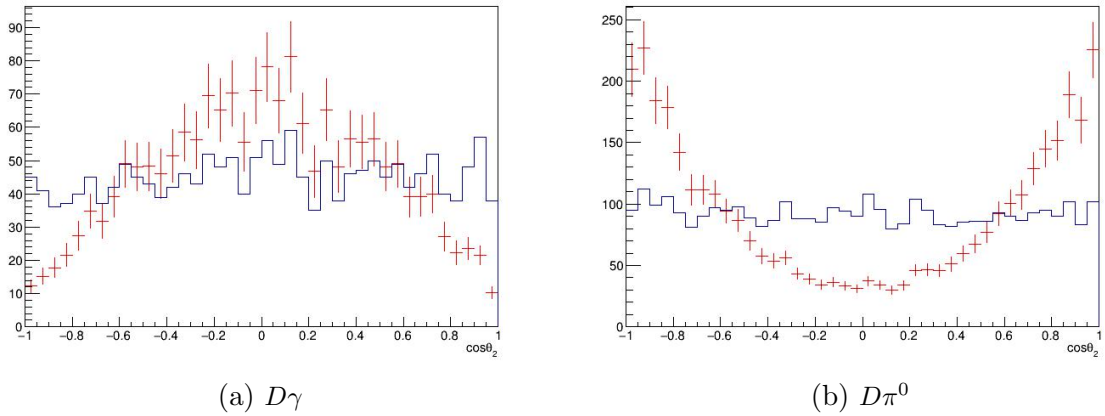


Figure 6.12: The distribution of the helicity angle with and without the helicity reweighting for  $B^0 \rightarrow D_1^- (\rightarrow \bar{D}^{*0} \pi^-) K^+$ .



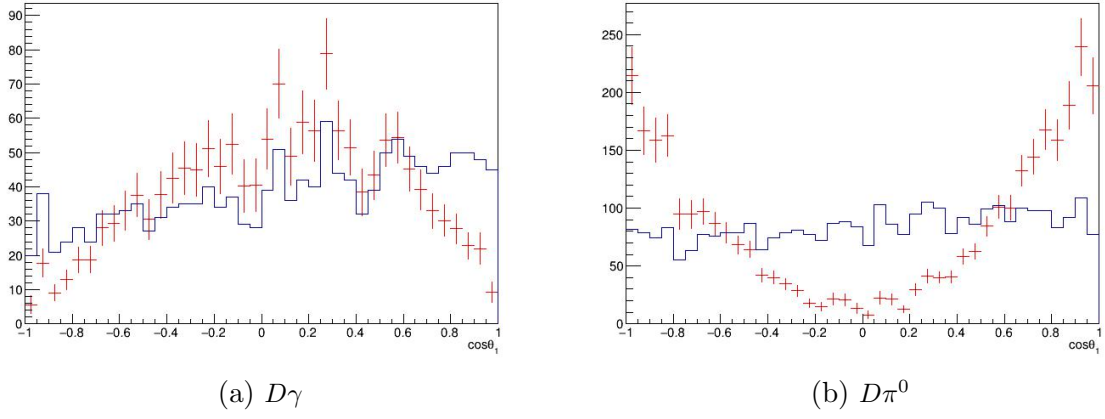


Figure 6.13: The distribution of the helicity angle with and without the helicity reweighting for  $B_s^0 \rightarrow \bar{D}^{*0} \bar{K}^{*0}$  with the helicity state (0,0).

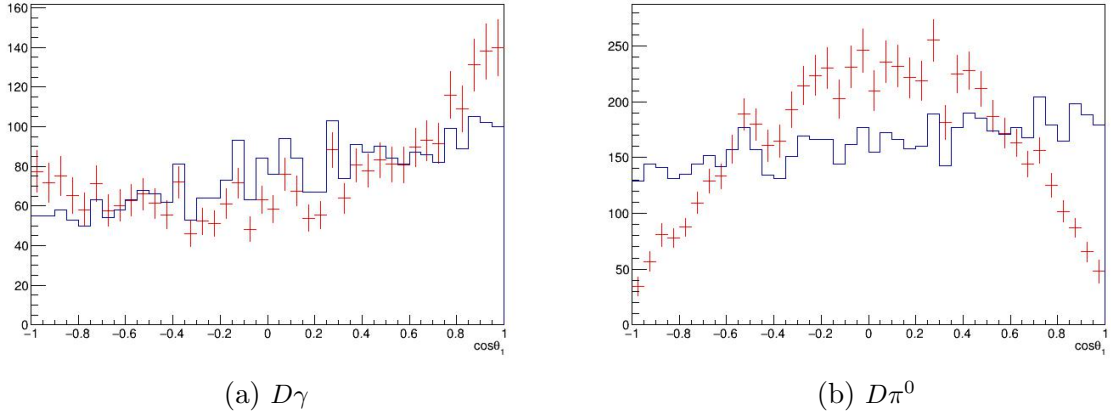


Figure 6.14: The distribution of the helicity angle with and without the helicity reweighting for  $B_s^0 \rightarrow \bar{D}^{*0} \bar{K}^{*0}$  with the helicity state (1,1).

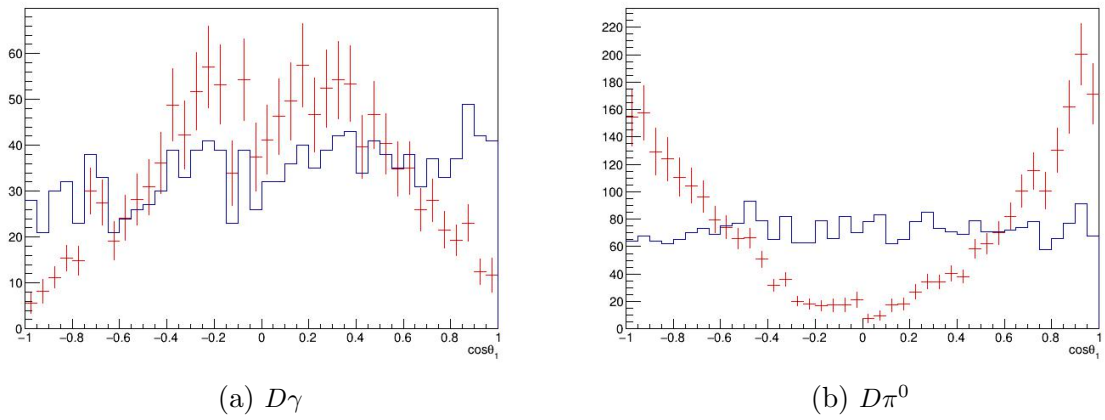


Figure 6.15: The distribution of the helicity angle with and without the helicity reweighting for  $B^0 \rightarrow \bar{D}^{*0} K^{*0}$  with the helicity state (0,0).

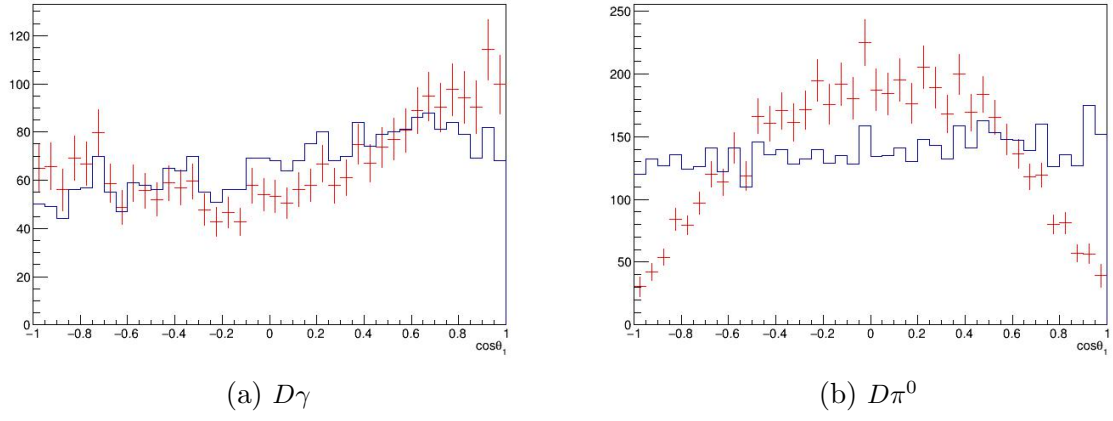


Figure 6.16: The distribution of the helicity angle with and without the helicity reweighting for  $B^0 \rightarrow \bar{D}^{*0} K^{*0}$  with the helicity state (1,1).

### 6.3.6 Reweighted mass distributions

The  $B^0$  invariant mass distribution with and without the helicity weights for each resonance is shown in Figs. 6.17 to 6.24.

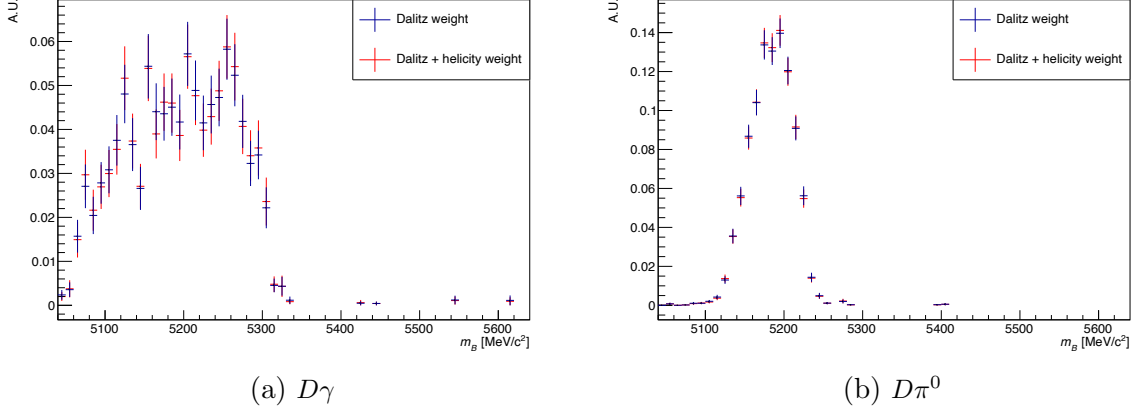


Figure 6.17: The distribution of the  $B^0$  mass with and without the helicity reweighting for  $B_s^0 \rightarrow D_{s1}^- (\rightarrow \bar{D}^{*0} K^-) \pi^+$ .

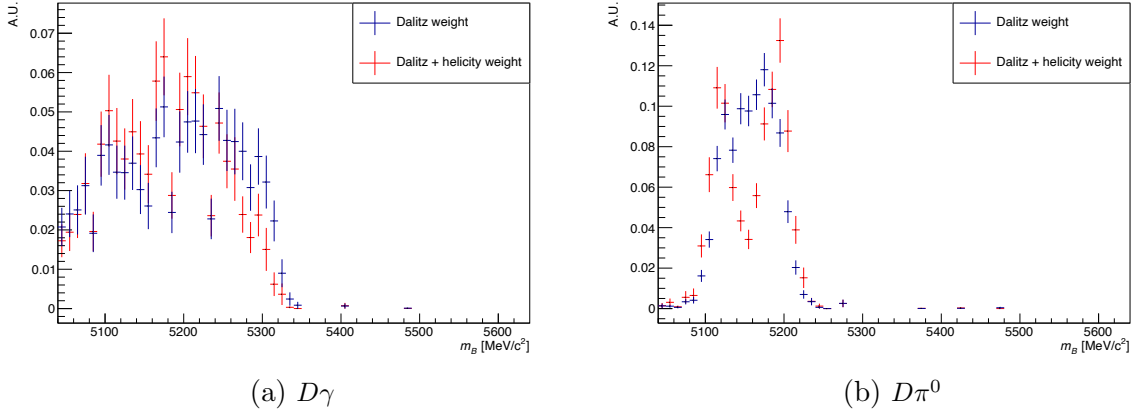


Figure 6.18: The distribution of the  $B^0$  mass with and without the helicity reweighting for  $B_s^0 \rightarrow \bar{D}^{*0} \bar{K}^{*0}$  with the helicity state (0,0).

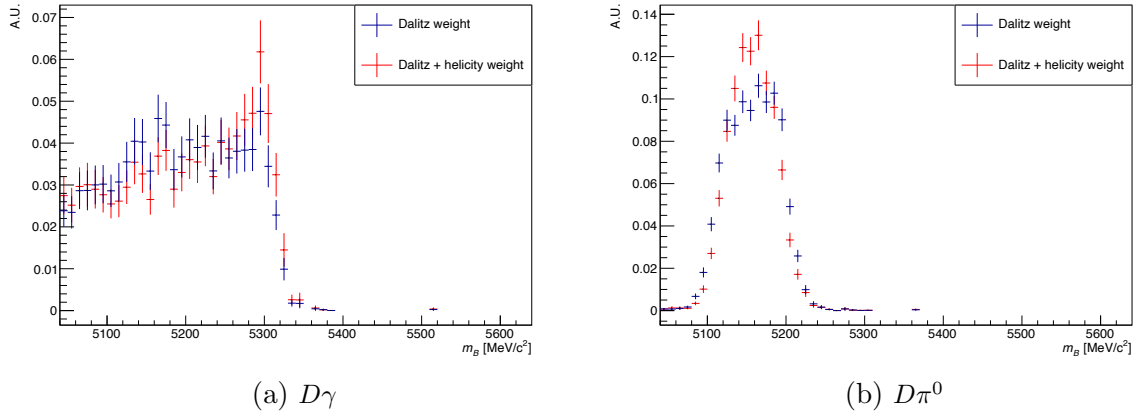


Figure 6.19: The distribution of the  $B^0$  mass with and without the helicity reweighting for  $B_s^0 \rightarrow \bar{D}^{*0} \bar{K}^{*0}$  with the helicity state (1,1).

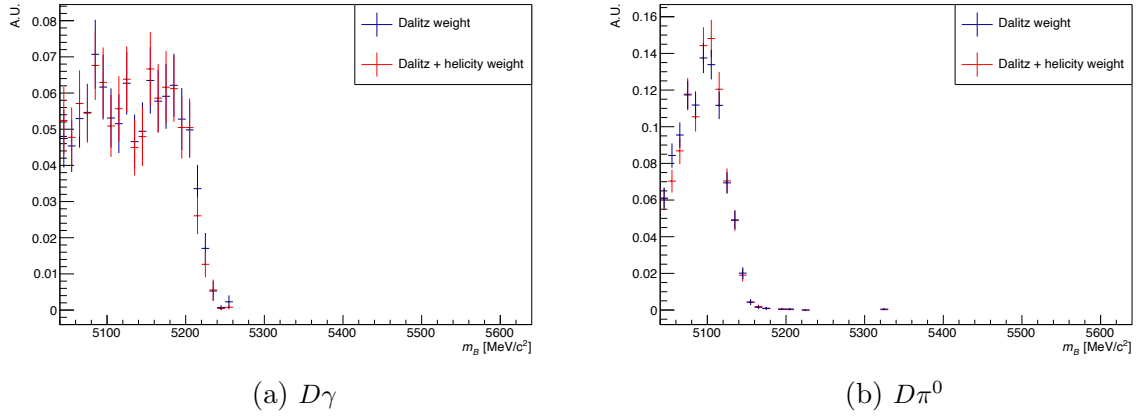


Figure 6.20: The distribution of the  $B^0$  mass with and without the helicity reweighting for  $B^0 \rightarrow D_1^- (\rightarrow \bar{D}^{*0} \pi^-) K^+$ .

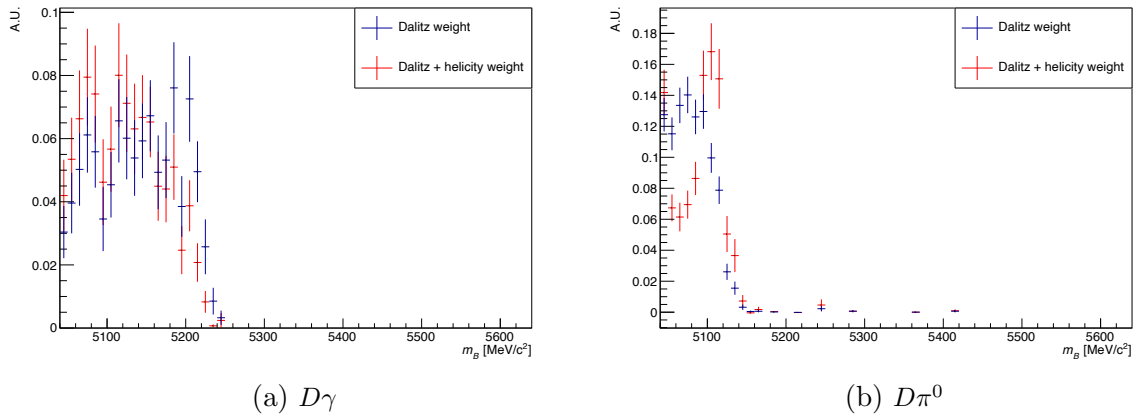


Figure 6.21: The distribution of the  $B^0$  mass with and without the helicity reweighting for  $B^0 \rightarrow \bar{D}^{*0} K^{*0}$  with the helicity state (0,0).

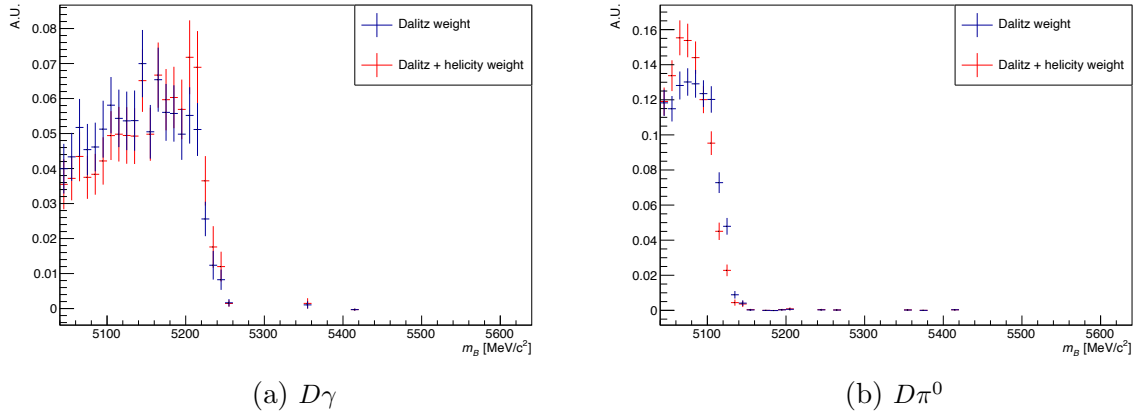


Figure 6.22: The distribution of the  $B^0$  mass with and without the helicity reweighting for  $B^0 \rightarrow \bar{D}^{*0} K^{*0}$  with the helicity state (1,1).

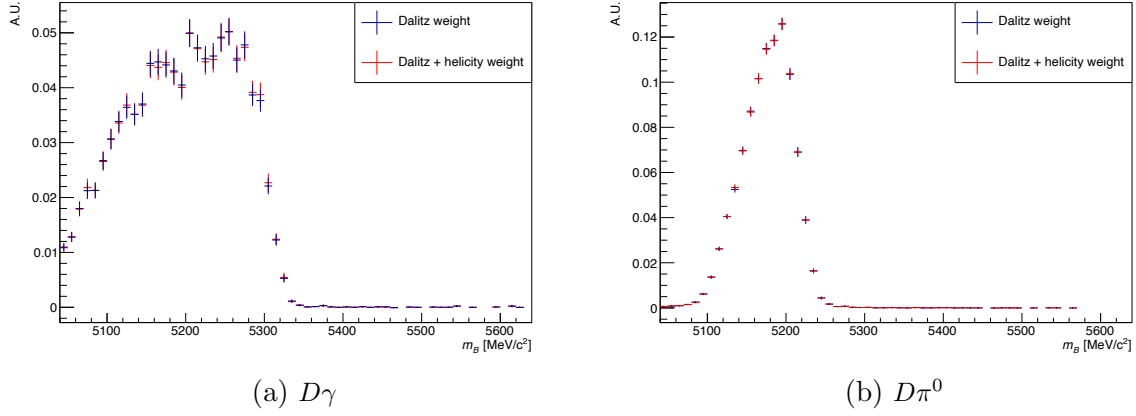


Figure 6.23: The distribution of the  $B^0$  mass with and without the helicity reweighting for  $B_s^0 \rightarrow \bar{D}^{*0} K^- \pi^+$  for all the modes included.

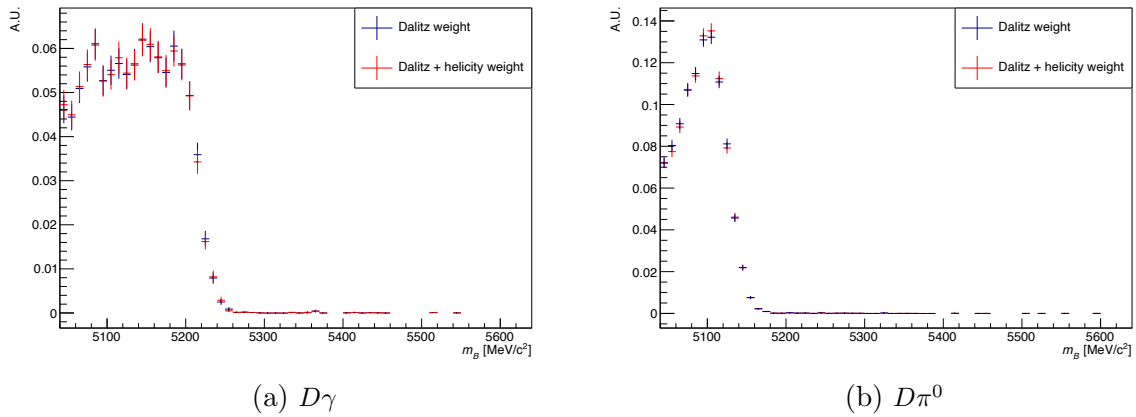


Figure 6.24: The distribution of the  $B^0$  mass with and without the helicity reweighting for  $B^0 \rightarrow D^* K^+ \pi^-$  for all the modes included.

## 6.4 Summary

This chapter has described all the methods used to reweight the LHCb simulation samples such that they properly model the Dalitz and/or helicity distributions in LHCb data. This is essential to model the invariant  $B$  mass distributions which are studied in Chapter 7 and correctly estimate distribution of the most prominent background decays within the signal window for input into the  $CP$  fit described in Chapter 8. Dalitz modelling is performed with a variety of input models utilising a number of different methods, a data driven approach is applied to the combinatorial background Dalitz distribution, and helicity reweighting is performed based on previous LHCb analyses.



## 7 Invariant mass fits

*“I never use mathematics, or statistics, or calculations,  
or anything at all like that because I can’t do it.  
So I just hope for the best.”*

---

Dr Irving Finkel

The work presented in this chapter was not performed by myself but by my analysis partner Yuya. Nevertheless this is a crucial part of the analysis so I have provided a concise explanation.

### 7.1 Strategy

As explained in Section 4.5 since the selection does not eliminate 100% of all background decays one must estimate how many remain in the data so that they can be accounted for in the  $CP$  fit. Chapter 6 explained how the fraction of each background source within each Dalitz bin is predicted. The global invariant mass fits account for the other factor of the final term in Eq. (4.48),  $y^b$ .

#### 7.1.1 Components of the fit

An invariant mass fit is performed by fitting an ensemble of PDFs via an unbinned extended maximum-likelihood fit to the distribution of the  $B^0$  candidate invariant mass in data. The PDFs and their shape parameters are determined by considering the distribution of each background decay and the signal decay in simulation, choosing an appropriate PDF to model each one. Each component PDF is first fitted to the corresponding simulation in order to determine the values of its shape parameters. The data are then fitted simultaneously for both  $B^0$  flavours, in each  $D$  final state. Some of the shape parameters are fixed to the values from the fit to the simulation samples, some parameters are free to float to account for differences between the data and the simulation. A number of different PDF shapes are used which are then summed to form the per-decay ensembles



and the total ensemble,

- a Gaussian distribution, defined as

$$p_G(x; \mu, \sigma) = \frac{1}{\sqrt{2\pi}\sigma} \exp \left[ \frac{-(x - \mu)^2}{2\sigma^2} \right]. \quad (7.1)$$

- a Crystal Ball distribution [105], defined as

$$p_{CB}(x; \mu, \sigma, \alpha, n) = N \begin{cases} \exp \left[ \frac{-(x-\mu)^2}{2\sigma^2} \right], & \text{if } \frac{x-\mu}{\sigma} > -\alpha \\ A(B - \frac{x-\mu}{\sigma})^{-n}, & \text{if } \frac{x-\mu}{\sigma} \leq -\alpha \end{cases} \quad (7.2)$$

where

$$A = \left( \frac{n}{|\alpha|} \right)^n \exp \left[ \frac{-|\alpha|^2}{2} \right], \quad (7.3)$$

$$B = \frac{n}{|\alpha|} - |\alpha|, \quad (7.4)$$

$$N = \frac{1}{\sigma(C + D)}, \quad (7.5)$$

$$C = \frac{n}{|\alpha|(n-1)} \exp \left[ \frac{-|\alpha|^2}{2} \right], \quad (7.6)$$

$$D = \sqrt{\frac{\pi}{2}} \left( 1 + \operatorname{erf} \left[ \frac{|\alpha|}{\sqrt{2}} \right] \right). \quad (7.7)$$

- and a Horns distribution [106], defined as

$$\begin{aligned} p_H(x; R, a, b, f, \sigma, \xi) = & \int_a^b \left( y - \frac{a+b}{2} \right)^2 \left( f p_G(y; x, \sigma) + (1-f) p_G(y; x, R\sigma) \right) \\ & \times \left( \frac{1-\xi}{b-a} y + \frac{b\xi - a}{b-a} \right) dy. \end{aligned} \quad (7.8)$$

RooDini [106] PDFs are also used to model the helicity structure of partially reconstructed  $D^{*0}$  decays. Table 7.1 details which backgrounds are included for which  $D$  final states. Not every background is included for every  $D$  final state as some are not expected to, or not seen to, contribute significantly. In the following, it is assumed that the simulation samples have been weighted with the Dalitz, PID and helicity weights where applicable.

Component	<i>D</i> decay modes for which the component is included		
	$KK/\pi\pi/K_S^0 hh/\pi\pi\pi\pi$	$K\pi/K\pi\pi\pi$	$\pi K/\pi K\pi\pi$
Combinatorial	✓	✓	✓
$B^0 \rightarrow D^* K^+ \pi^-$	✓	✓	✓
$B_s^0 \rightarrow D^* K^- \pi^+$	✓	✓	✓
$B^0 \rightarrow D^{(*)} \pi^+ \pi^-$	✓	✓	✓
$B^0 \rightarrow D^{(*)} K^+ K^-$	✓	✓	✓
$B_s^0 \rightarrow D^{(*)} K^+ K^-$	✓	✓	✓
$\Lambda_b^0 \rightarrow D^{(*)} p \pi^-$	✓		✓
$\bar{\Lambda}_b^0 \rightarrow D^{(*)} K^+ \bar{p}$	✓	✓	
$B^+ \rightarrow DK^+ \pi^+ \pi^-$	✓	✓	
$B^+ \rightarrow D \pi^+ \pi^+ \pi^-$	✓	✓	✓
$B^0 \rightarrow DK_{(1,2)}^{(*)}$	✓	✓	
$B_s^0 \rightarrow D\bar{K}_{(1,2)}^{(*)}$	✓		✓

Table 7.1: Summary of background components taken into account depending on the *D* decay modes.

## 7.2 Determining the PDF shapes

Unless otherwise specified in the fit to data all the parameters are fixed to values found from fits to simulated data to model each decay mode separately, besides the mean of each total PDF for the modelled decays which is allowed to move by a global mass shift parameter,  $\Delta m$ .

### 7.2.1 $B^0 \rightarrow DK^+ \pi^-$ and $B_s^0 \rightarrow DK^- \pi^+$

The mass distributions of these decays are identical besides a different mean due to the different initial *B* meson, therefore the PDF used for the  $B_s^0 \rightarrow DK^- \pi^+$  decay is simply the PDF used for the  $B^0 \rightarrow DK^+ \pi^-$  decay but shifted in mean by the PDG value of the  $B^0$ – $B_s^0$  mass difference,  $87.42 \pm 0.14$  MeV/ $c^2$  [7]. As these modes are fully reconstructed and the final state particles are correctly identified the invariant mass distributions can be modelled as a sum of a double crystal balls (DCBs) and a Gaussian. The means of all three PDFs and the widths of the crystal balls are also shared. The width of the Gaussian is a fixed ratio of the crystal ball widths.

### 7.2.2 $B^0 \rightarrow D^* K^+ \pi^-$ and $B_s^0 \rightarrow D^* K^- \pi^+$

The final state particles of these decays are correctly identified however a  $\pi^0$  or  $\gamma$  emitted from the decay of the  $D^{*0}$  is not reconstructed resulting in a broad helicity dependent distribution in the lower mass region of the invariant mass distribution. A `RooHornsDini` [106] PDF is used to model the helicity distribution of these decays by considering the  $D^* \rightarrow D\pi^0$  and  $D^* \rightarrow D\gamma$  contributions separately. As in the case of the  $B^0 \rightarrow DK^+\pi^-$  and  $B_s^0 \rightarrow DK^-\pi^+$  decays the  $B^0 \rightarrow D^*(\rightarrow D\pi^0)K^+\pi^-$  and  $\bar{B}_s^0 \rightarrow D^*(\rightarrow D\pi^0)K^+\pi^-$  decays should have similar mass distributions however due to the lower mass region of the decays the distribution of the  $B^0 \rightarrow D^*(\rightarrow D\pi^0)K^+\pi^-$  decay is cut off by the lower limit of the invariant mass. Therefore the  $\bar{B}_s^0 \rightarrow D^*(\rightarrow D\pi^0)K^+\pi^-$  distribution is modelled with a DCB function with independent means and widths but  $n_1$  fixed to 0. The yield of  $B^0 \rightarrow D^*(\rightarrow D\pi^0)K^+\pi^-$  is a free parameter, whilst that of  $\bar{B}_s^0 \rightarrow D^*(\rightarrow D\pi^0)K^+\pi^-$  is a fraction of the  $\bar{B}_s^0 \rightarrow DK^+\pi^-$  yield,  $f_{\bar{B}_s^0 \rightarrow D^* K^+ \pi^-}$ . These are shared among all the  $D$  final states and  $B$  flavours. The yield of the  $D^* \rightarrow D\gamma$  mode varies as a fixed fraction of the floating  $D^* \rightarrow D\pi^0$  yield according to their difference in branching fractions and efficiencies. This is done for all  $D^*$  background decays.

### 7.2.3 Partially reconstructed background with $DK_{(1,2)}^{(*)}(\rightarrow K^\pm \pi^\mp \pi^0)$

Decays of a  $B^0$  or  $B_s^0$  to some excited kaon state can be mis-reconstructed as the signal decay when the  $\pi^0$  from the excited kaon is missed during reconstruction. The main contributions come from  $K_1(1270)$ ,  $K_1(1400)$ ,  $K^*(1410)$  and  $K_2^*(1430)$  states. As some of the branching ratios of  $B^0$  or  $B_s^0$  decaying to  $DK_{(1,2)}^{(*)}$  are not known it is assumed that the branching ratios are the same for all of the kaon excited states. The branching ratios of the excited kaon to the relevant final state particles are taken from Ref. [7]. `RapidSim` [101] with `EvtGen` [102] models are used to generate a “cocktail” of simulation samples for these decays. Although these are possibly not as accurate as the full LHCb simulation, it has been shown that for the partially reconstructed background  $B^+ \rightarrow DK^+\pi^+\pi^-$  in the  $B^0 \rightarrow DK^{*0}$  analysis [107] the mass distributions obtained from this are a good proxy for those acquired from full simulation. These mass distributions are then modelled with the `RooHornsDini` function. The yield of  $B^0 \rightarrow D^0 K_{(1,2)}^{(*)}$  varies as a fixed fraction of the floating  $B^0 \rightarrow D^*(\rightarrow D\pi^0)K^+\pi^-$  yield,  $f_{B^0 \rightarrow D^0 K_{(1,2)}^{(*)}}$ , as does the yield of  $B_s^0 \rightarrow \bar{D}^0 \bar{K}_{(1,2)}^{(*)}$  as a fraction of the  $\bar{B}_s^0 \rightarrow D^*(\rightarrow D\pi^0)K^+\pi^-$  yield,  $f_{B_s^0 \rightarrow \bar{D}^0 \bar{K}_{(1,2)}^{(*)}}$ . These fractions are floated and shared among all the  $D$  final states and  $B$  flavours.

### 7.2.4 $B^0 \rightarrow D\pi^+\pi^-$

The  $B^0 \rightarrow D\pi^+\pi^-$  decay can be mis-reconstructed as  $B^0 \rightarrow DK^+\pi^-$  when a pion is mis-identified as a kaon. A PID selection is imposed on the reconstructed kaon to mitigate this however there is still some residual contribution that needs to be accounted for in the mass fit. A pion-kaon mis-identification results in the background peaking slightly above the true  $B^0$  mass. The mass shape is modelled with a DCB shape with shared mean but different widths,  $n_1$  fixed to 0.9 and  $n_2$  fixed to 1.0. The yield of  $B^0 \rightarrow D\pi^+\pi^-$  is a free parameter for the  $D \rightarrow K^\pm\pi^\mp$ ,  $D \rightarrow K_S^0\pi^+\pi^-$  LL,  $D \rightarrow K^\pm\pi^\mp\pi^+\pi^-$  modes and shared between the two  $B$  flavours, to increase the consistency of the fit, assuming no  $CP$  violation. The yield for the  $D \rightarrow \pi^\pm K^\mp$  mode is the same as that for the  $D \rightarrow K^\pm\pi^\mp$  mode since the only difference is the charge of the mis-identified  $B$  child kaon. The same constraint is applied for the  $D \rightarrow K^\pm\pi^\mp\pi^+\pi^-$  and  $D \rightarrow \pi^\pm K^\mp\pi^+\pi^-$  modes. For the other  $D$  modes, the yield of  $B^0 \rightarrow D\pi^+\pi^-$  is related to the yield in a reference  $D$  mode,  $D \rightarrow K^\pm\pi^\mp$  for  $D \rightarrow h^+h^-$ ,  $D \rightarrow K_S^0\pi^+\pi^-$  LL for  $D \rightarrow K_S^0h^+h^-$  and  $D \rightarrow K^\pm\pi^\mp\pi^+\pi^-$  for  $D \rightarrow \pi^+\pi^-\pi^+\pi^-$ , by a fixed ratio according to their differences in branching fraction and efficiency.

### 7.2.5 $B^0 \rightarrow D^*\pi^+\pi^-$

Similar to the  $B^0 \rightarrow D^*K^+\pi^-$  mode, the  $B^0 \rightarrow D^*\pi^+\pi^-$  decay appears in the  $B$  candidate invariant mass distribution when a soft neutral particle from the  $D^*$  decay is missed, and a pion is misidentified as a kaon. A `RooHornsDini` function is used for the  $D\pi^0$  mode and a DCB function without shared mean or width for the  $D\gamma$  mode. The yield of the  $D^* \rightarrow D\pi^0$  mode is varied as a fixed fraction of the  $B^0 \rightarrow D\pi^+\pi^-$  yield according to their differences in branching fraction and efficiency.

### 7.2.6 $B^+ \rightarrow DK^+\pi^+\pi^-$

This decay mode is reconstructed as  $B^0 \rightarrow DK^+\pi^-$  when the pion with the same charge as the kaon is not reconstructed. The distribution is described with a `RooHornsDini` function. The yield is varied as a fixed fraction of the  $B^0 \rightarrow D^*(\rightarrow D\pi^0)K^+\pi^-$  yield according to their differences in branching fraction and efficiency.

### 7.2.7 $B^+ \rightarrow D\pi^+\pi^+\pi^-$

This decay mode is reconstructed as  $B^0 \rightarrow DK^+\pi^-$  when one of the two pions of the same charge is missed and one of the other pions is misidentified as a kaon. Although the missing pion shifts the  $B$  candidate mass down, the pion-kaon mis-identification

also shifts it up resulting in a distribution with a non-negligible presence in the signal window. The mass distribution is described with a `RooHornsDini` function. Similar to the  $B^0 \rightarrow D\pi^+\pi^-$  background, the yield is a free parameter for the  $D \rightarrow K^\pm\pi^\mp$ ,  $D \rightarrow K_S^0\pi^+\pi^-$  LL,  $D \rightarrow K^\pm\pi^\mp\pi^+\pi^-$  modes, and shared between the  $B$  flavours. For the  $D \rightarrow \pi^\pm K^\mp$  mode, the yield is varied as a fixed fraction of the  $D \rightarrow K^\pm\pi^\mp$  mode according to their difference in efficiency. Since this efficiency takes into account the stripping level efficiency this fraction incorporates the fact that the  $B^+ \rightarrow D\pi^+\pi^+\pi^-$  background can pollute the  $D \rightarrow K^\pm\pi^\mp$  and  $D \rightarrow \pi^\pm K^\mp$  data at different rates. The same fraction is used to relate the  $D \rightarrow K^\pm\pi^\mp\pi^+\pi^-$  yield and the  $D \rightarrow \pi^\pm K^\mp\pi^+\pi^-$  yield. For the other  $D$  modes, the yield of  $B^+ \rightarrow D\pi^+\pi^+\pi^-$  is related to the yield in the reference  $D$  mode,  $D \rightarrow K^\pm\pi^\mp$  for  $D \rightarrow h^+h^-$ ,  $D \rightarrow K_S^0\pi^+\pi^-$  LL for  $D \rightarrow K_S^0h^+h^-$ ,  $D \rightarrow K^\pm\pi^\mp\pi^+\pi^-$  for  $D \rightarrow \pi^+\pi^-\pi^+\pi^-$ , by a fixed fraction according to their differences in branching fraction and efficiency.

### 7.2.8 Other peaking backgrounds

The following misidentified (and partially reconstructed for decays with a  $D^*$ ) backgrounds need to be taken into account in the mass fit. The decays with two kaons are reconstructed as signal when one of the kaons is misidentified as a pion.  $\bar{A}_b^0 \rightarrow DK^+\bar{p}$  requires a proton-pion mis-identification and  $\Lambda_b^0 \rightarrow Dp\pi^-$  requires a proton-kaon mis-identification. These backgrounds have small yields after selection so are modelled with histogram templates for simplicity. The yields of all the mis-identified background components are varied as a fixed fraction of the  $B^0 \rightarrow D\pi^+\pi^-$  yield for each  $D$  mode. This incorporates the fragmentation ratio in the case of  $B_s^0$  or  $\Lambda_b^0$  decays [108], the branching fractions of the  $B$  decays [89], and the efficiency ratio. The yields of the partially reconstructed misidentified background components are varied as a fixed fraction of the fully reconstructed misidentified background components according to their efficiency differences. Unlike for the  $B^0 \rightarrow D^*\pi^+\pi^-$  background in Section 7.2.5, there is no branching fraction measured for these partially reconstructed backgrounds so it is assumed that the branching fractions are the same for the fully and partially reconstructed backgrounds.

## 7.3 Fit to data

The distributions of the  $B^0$  candidate invariant mass, with the DTF constraints applied, have been fitted simultaneously for each of the  $D$  final states and both  $B$  flavours. The width of the DCB function for the signal mode and the slope of the exponential combinatorial background are floated. All the other shape parameters are fixed to the values obtained from the fit to the simulation samples. In addition to the shape parameters,

a global mass shift  $\Delta m$  is introduced in order to take into account differences in the track momentum scale between data and simulation. This is floated and shared between all the mass fit components and the fit categories. The yields  $N$  are free parameters for each flavour of the signal,  $B_s^0 \rightarrow DK^-\pi^+$ ,  $B^0 \rightarrow D^*(\rightarrow D\pi^0)K^+\pi^-$  for all the  $D$  modes, and  $B^0 \rightarrow D\pi^+\pi^-$  and  $B^+ \rightarrow D\pi^+\pi^+\pi^-$  for the  $D \rightarrow K^\pm\pi^\mp$ ,  $D \rightarrow K_S^0\pi^+\pi^-$  LL and  $D \rightarrow K^\pm\pi^\mp\pi^+\pi^-$  modes. The yields of the other components are related to one of the above yields by a fraction parameter. Gaussian constraining some of the fraction parameters was found to result in inconsistent fits across the  $D$  categories. Consequently, most of these parameters are fixed. Variations of the parameters within their uncertainties is considered as a source of systematic uncertainty.

The fit results are shown in Figs. 7.1 to 7.9 for each  $D$  mode. Note that although the fitted distribution shows some discrepancy in the partially reconstructed backgrounds,  $m_B \lesssim 5240 \text{ MeV}/c^2$ , this is not expected to have a significant effect on the final extraction of  $\gamma$ , since that depends on a fit to data in the signal window, and it can be assessed as a source of systematic uncertainty. The fitted parameters are summarised in Tables 7.2 to 7.4. The signal window is defined as the interval  $\mu \pm 3\sigma$ , where  $\sigma$  is the fitted width of the signal peak and  $\mu$  is its mean. The yields within this window are computed by integrating the PDFs. The computed yields are summarised in Tables 7.5 to 7.15. The uncertainties include the errors propagated from the  $N$  (global yield) or  $f$  parameters.

Parameter	Value			
	$KK$	$\pi\pi$	$K\pi$	$\pi K$
$\sigma_B[\text{MeV}/c^2]$	$11.7 \pm 0.2$	$11.7 \pm 0.3$	$11.28 \pm 0.06$	
$p_0$	$-0.0036 \pm 0.0003$	$-0.0018 \pm 0.0004$	$-0.0049 \pm 0.0001$	$-0.0019 \pm 0.0001$
$N_{B^0 \rightarrow DK\pi}$	$666 \pm 36$	$219 \pm 20$	$5827 \pm 89$	$1074 \pm 68$
$N_{\bar{B}^0 \rightarrow DK\pi}$	$646 \pm 35$	$204 \pm 20$	$5753 \pm 88$	$1054 \pm 67$
$N_{B_s^0 \rightarrow DK\pi}$	$2100 \pm 40$	$659 \pm 22$	$267 \pm 32$	$19220 \pm 120$
$N_{\bar{B}_s^0 \rightarrow DK\pi}$	$1983 \pm 39$	$668 \pm 22$	$270 \pm 32$	$19150 \pm 120$
$N_{\text{comb}}$	$1070 \pm 130$	$390 \pm 52$	$5980 \pm 280$	$3420 \pm 160$
$\bar{N}_{\text{comb}}$	$1120 \pm 130$	$366 \pm 51$	$5880 \pm 280$	$3490 \pm 170$
$N_{B^0 \rightarrow D\pi^0 K\pi}$	$407 \pm 41$	$158 \pm 20$	$4000 \pm 120$	$1 \pm 60$
$N_{\bar{B}^0 \rightarrow D\pi^0 K\pi}$	$439 \pm 41$	$162 \pm 20$	$3780 \pm 120$	$190 \pm 190$
$N_{B^0 \rightarrow D\pi\pi}$			$1421 \pm 29$	
$N_{B^+ \rightarrow D\pi\pi\pi}$			$2390 \pm 300$	
$\Delta m[\text{MeV}/c^2]$			$-1.94 \pm 0.05$	
$f_{B_s^0 \rightarrow D\pi^0 K\pi}$			$0.63 \pm 0.01$	
$f_{B_s^0 \rightarrow K^* \text{ cocktail}}$			$1.56 \pm 0.07$	

Table 7.2: Fit results for the two-body modes. The  $N$  and  $f$  parameters without (with) a bar are the yields and fractions for  $B^0$  ( $\bar{B}^0$ ), except for the kaon cocktails for which the yields are shared between the two flavours.

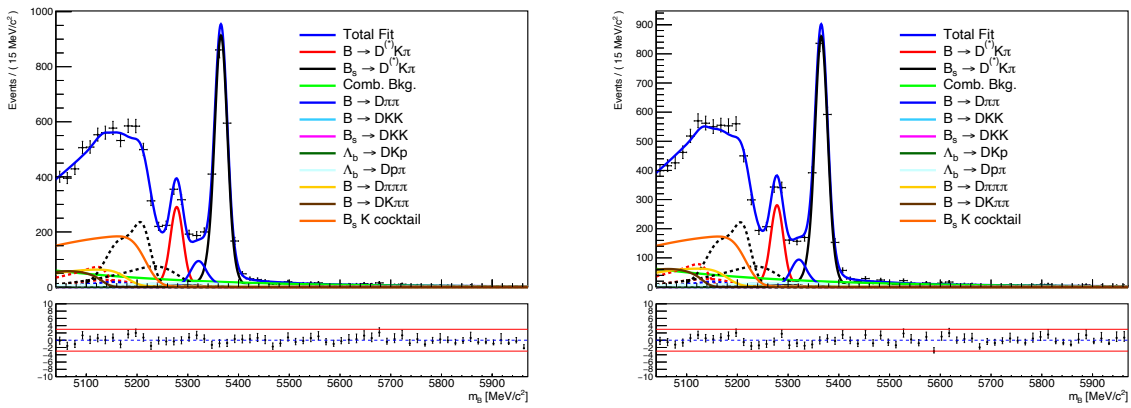
Parameter	Value			
	$K_S^0 \pi \pi$ LL	$K_S^0 \pi \pi$ DD	$K_S^0 K K$ LL	$K_S^0 K K$ DD
$\sigma_B [\text{MeV}/c^2]$	$12.2 \pm 0.3$	$12.2 \pm 0.3$	$12 \pm 1$	$12.5 \pm 0.7$
$p_0$	$-0.0025 \pm 0.0003$	$-0.0030 \pm 0.0002$	$-0.0025 \pm 0.0004$	$-0.0030 \pm 0.0004$
$N_{B^0 \rightarrow DK\pi}$	$324 \pm 25$	$631 \pm 37$	$33 \pm 10$	$95 \pm 14$
$N_{\bar{B}^0 \rightarrow DK\pi}$	$291 \pm 25$	$597 \pm 36$	$47 \pm 10$	$75 \pm 14$
$N_{B_s^0 \rightarrow DK\pi}$	$931 \pm 27$	$1656 \pm 42$	$123 \pm 12$	$221 \pm 14$
$N_{\bar{B}_s^0 \rightarrow DK\pi}$	$860 \pm 27$	$1652.847 \pm 40$	$120 \pm 11$	$210 \pm 15$
$N_{\text{comb}}$	$670 \pm 78$	$1891 \pm 144$	$320 \pm 48$	$324 \pm 51$
$\bar{N}_{\text{comb}}$	$811 \pm 88$	$1693 \pm 131$	$247 \pm 40$	$402 \pm 62$
$N_{B^0 \rightarrow D\pi^0 K\pi}$	$190 \pm 34$	$238 \pm 67$	$16 \pm 13$	$22 \pm 18$
$N_{\bar{B}^0 \rightarrow D\pi^0 K\pi}$	$234 \pm 35$	$268 \pm 67$	$26 \pm 12$	$11 \pm 20$
$N_{B^0 \rightarrow D\pi\pi}$	$135 \pm 8$			
$N_{B^+ \rightarrow D\pi\pi\pi}$	$403 \pm 76$			
$\Delta m [\text{MeV}/c^2]$		$-1.94 \pm 0.05$		
$f_{B_s^0 \rightarrow D\pi^0 K\pi}$		$0.630 \pm 0.008$		
$f_{B_s^0 \rightarrow K^* \text{ cocktail}}$		$1.56 \pm 0.07$		

Table 7.3: Fit results for the three-body modes. The  $N$  and  $f$  parameters without (with) a bar are the yields and fractions for  $B^0$  ( $\bar{B}^0$ ), except for the kaon cocktails for which the yields are shared between the two flavours.

Parameter	Value		
	$\pi\pi\pi\pi$	$K\pi\pi\pi$	$\pi K\pi\pi$
$\sigma_B [\text{MeV}/c^2]$	$12.6 \pm 0.3$	$12.04 \pm 0.07$	
$p_0$	$-0.0029 \pm 0.0002$	$-0.0047 \pm 0.0001$	$-0.0023 \pm 0.0001$
$N_{B^0 \rightarrow DK\pi}$	$453 \pm 32$	$4949 \pm 86$	$1076 \pm 67$
$N_{\bar{B}^0 \rightarrow DK\pi}$	$411 \pm 31$	$4665 \pm 84$	$847 \pm 65$
$N_{B_s^0 \rightarrow DK\pi}$	$1273 \pm 34$	$223 \pm 35$	$16420 \pm 120$
$N_{\bar{B}_s^0 \rightarrow DK\pi}$	$1223 \pm 35$	$252 \pm 36$	$16490 \pm 120$
$N_{\text{comb}}$	$1568 \pm 120$	$9160 \pm 290$	$6820 \pm 230$
$\bar{N}_{\text{comb}}$	$1714 \pm 131$	$9300 \pm 290$	$6980 \pm 230$
$N_{B^0 \rightarrow D\pi^0 K\pi}$	$256 \pm 35$	$2980 \pm 110$	$1 \pm 54$
$N_{\bar{B}^0 \rightarrow D\pi^0 K\pi}$	$232 \pm 36$	$2830 \pm 110$	$300 \pm 180$
$N_{B^0 \rightarrow D\pi\pi}$		$1338 \pm 32$	
$N_{B^+ \rightarrow D\pi\pi\pi}$		$1980 \pm 250$	
$\Delta m [\text{MeV}/c^2]$		$-1.94 \pm 0.05$	
$f_{B_s^0 \rightarrow D\pi^0 K\pi}$		$0.630 \pm 0.008$	
$f_{B_s^0 \rightarrow K^* \text{ cocktail}}$		$1.56 \pm 0.07$	

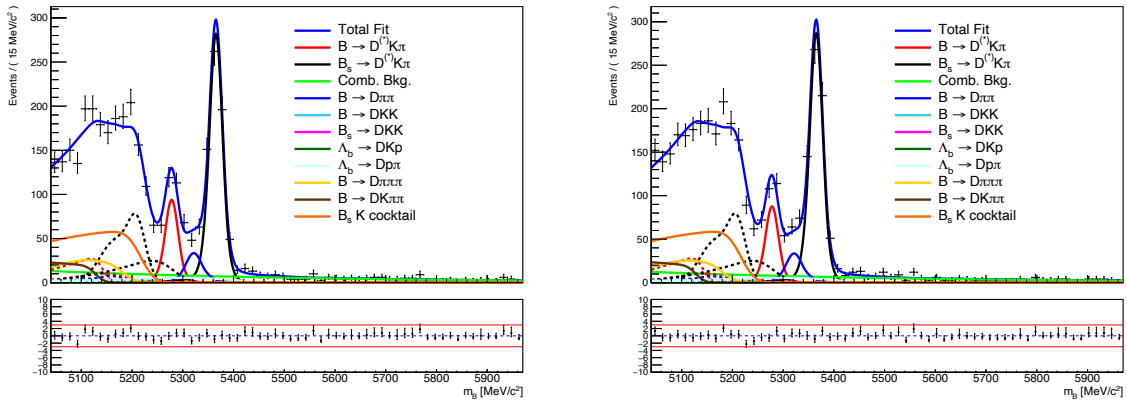
Table 7.4: Fit results for the four-body modes. The  $N$  and  $f$  parameters without (with) a bar are the yields and fractions for  $B^0$  ( $\bar{B}^0$ ), except for the kaon cocktails for which the yields are shared between the two flavours.

Yield	$B^0$	$\bar{B}^0$
$B^0 \rightarrow DK^+\pi^-$	$631.3 \pm 34.2$	$611.7 \pm 33.3$
$\bar{B}_s^0 \rightarrow DK^+\pi^-$	$32.9 \pm 0.8$	$31.0 \pm 0.8$
Combinatorial	$119.8 \pm 14.7$	$125.5 \pm 14.6$
$B^0 \rightarrow D^*(\rightarrow D\pi^0)K^+\pi^-$	$0.5 \pm 0.0$	$0.5 \pm 0.0$
$B^0 \rightarrow D^*(\rightarrow D\gamma)K^+\pi^-$	$1.0 \pm 0.1$	$1.1 \pm 0.1$
$\bar{B}_s^0 \rightarrow D^*(\rightarrow D\pi^0)K^+\pi^-$	$20.6 \pm 0.5$	$19.4 \pm 0.4$
$\bar{B}_s^0 \rightarrow D^*(\rightarrow D\gamma)K^+\pi^-$	$210.8 \pm 4.6$	$199.0 \pm 4.5$
$B^0 \rightarrow D\pi^+\pi^-$	$82.9 \pm 1.7$	$82.9 \pm 1.7$
$B^0 \rightarrow D^*(\rightarrow D\pi^0)\pi^+\pi^-$	$1.8 \pm 0.0$	$1.8 \pm 0.0$
$B^0 \rightarrow D^*(\rightarrow D\gamma)\pi^+\pi^-$	$7.1 \pm 0.1$	$7.1 \pm 0.1$
$B^0 \rightarrow DK^+K^-$	$7.5 \pm 0.2$	$7.5 \pm 0.2$
$B^0 \rightarrow D^*(\rightarrow D\pi^0)K^+K^-$	$0.0 \pm 0.0$	$0.0 \pm 0.0$
$B^0 \rightarrow D^*(\rightarrow D\gamma)K^+K^-$	$0.0 \pm 0.0$	$0.0 \pm 0.0$
$B_s^0 \rightarrow DK^+K^-$	$4.1 \pm 0.1$	$4.1 \pm 0.1$
$B_s^0 \rightarrow D^*(\rightarrow D\pi^0)K^+K^-$	$0.0 \pm 0.0$	$0.0 \pm 0.0$
$B_s^0 \rightarrow D^*(\rightarrow D\gamma)K^+K^-$	$0.1 \pm 0.0$	$0.1 \pm 0.0$
$\bar{\Lambda}_b^0 \rightarrow DK^+\bar{p}$	$2.6 \pm 0.1$	$2.6 \pm 0.1$
$\bar{\Lambda}_b^0 \rightarrow D^*(\rightarrow D\pi^0)K^+\bar{p}$	$0.2 \pm 0.0$	$0.2 \pm 0.0$
$\bar{\Lambda}_b^0 \rightarrow D^*(\rightarrow D\gamma)K^+\bar{p}$	$0.3 \pm 0.0$	$0.3 \pm 0.0$
$\bar{\Lambda}_b^0 \rightarrow Dp\pi^-$	$62.9 \pm 1.3$	$62.9 \pm 1.3$
$\bar{\Lambda}_b^0 \rightarrow D^*(\rightarrow D\pi^0)p\pi^-$	$6.6 \pm 0.1$	$6.6 \pm 0.1$
$\bar{\Lambda}_b^0 \rightarrow D^*(\rightarrow D\gamma)p\pi^-$	$6.6 \pm 0.1$	$6.6 \pm 0.1$
$B^+ \rightarrow D\pi^+\pi^+\pi^-$	$6.2 \pm 0.8$	$6.2 \pm 0.8$
$B^+ \rightarrow DK^+\pi^+\pi^-$	$0.3 \pm 0.0$	$0.3 \pm 0.0$
$B_s^0 \rightarrow D\bar{K}_{(1,2)}^{(*)}$	$15.9 \pm 0.6$	$15.0 \pm 0.6$

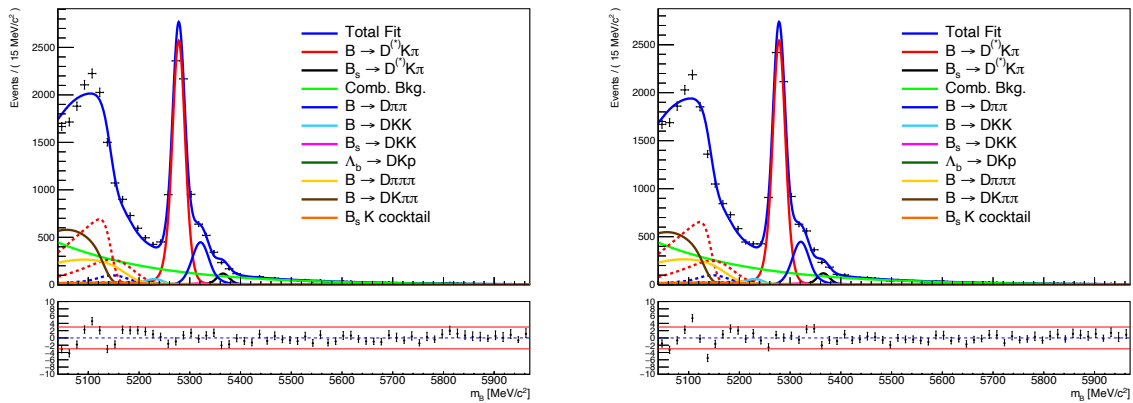
Table 7.5: Yields per  $B$  flavour within  $\mu \pm 3\sigma$  for  $D \rightarrow K^+K^-$ .Figure 7.1:  $D \rightarrow K^+K^-$  from  $B^0$  (left) and from  $\bar{B}^0$  (right).



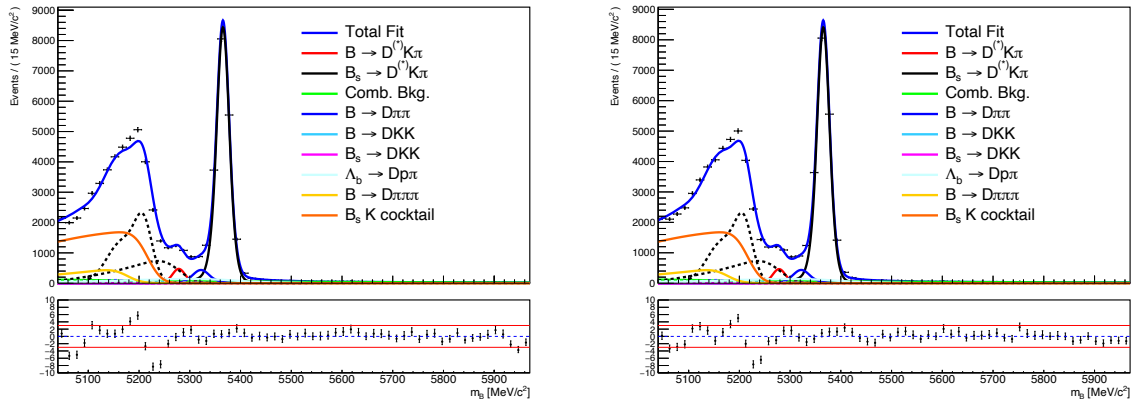
Yield	$B^0$	$\bar{B}^0$
$B^0 \rightarrow DK^+\pi^-$	$207.0 \pm 19.2$	$192.7 \pm 18.8$
$\bar{B}_s^0 \rightarrow DK^+\pi^-$	$10.7 \pm 0.5$	$10.9 \pm 0.5$
Combinatorial	$39.9 \pm 6.6$	$37.4 \pm 6.4$
$B^0 \rightarrow D^*(\rightarrow D\pi^0)K^+\pi^-$	$0.2 \pm 0.0$	$0.2 \pm 0.0$
$B^0 \rightarrow D^*(\rightarrow D\gamma)K^+\pi^-$	$0.3 \pm 0.0$	$0.3 \pm 0.0$
$\bar{B}_s^0 \rightarrow D^*(\rightarrow D\pi^0)K^+\pi^-$	$6.9 \pm 0.2$	$7.0 \pm 0.2$
$\bar{B}_s^0 \rightarrow D^*(\rightarrow D\gamma)K^+\pi^-$	$70.0 \pm 2.4$	$71.0 \pm 2.4$
$B^0 \rightarrow D\pi^+\pi^-$	$29.9 \pm 0.6$	$29.9 \pm 0.6$
$B^0 \rightarrow D^*(\rightarrow D\pi^0)\pi^+\pi^-$	$0.7 \pm 0.0$	$0.7 \pm 0.0$
$B^0 \rightarrow D^*(\rightarrow D\gamma)\pi^+\pi^-$	$2.5 \pm 0.1$	$2.5 \pm 0.1$
$B^0 \rightarrow DK^+K^-$	$3.0 \pm 0.1$	$3.0 \pm 0.1$
$B^0 \rightarrow D^*(\rightarrow D\pi^0)K^+K^-$	$0.0 \pm 0.0$	$0.0 \pm 0.0$
$B^0 \rightarrow D^*(\rightarrow D\gamma)K^+K^-$	$0.0 \pm 0.0$	$0.0 \pm 0.0$
$B_s^0 \rightarrow DK^+K^-$	$1.7 \pm 0.0$	$1.7 \pm 0.0$
$B_s^0 \rightarrow D^*(\rightarrow D\pi^0)K^+K^-$	$0.0 \pm 0.0$	$0.0 \pm 0.0$
$B_s^0 \rightarrow D^*(\rightarrow D\gamma)K^+K^-$	$0.0 \pm 0.0$	$0.0 \pm 0.0$
$\bar{\Lambda}_b^0 \rightarrow DK^+\bar{p}$	$1.1 \pm 0.0$	$1.1 \pm 0.0$
$\bar{\Lambda}_b^0 \rightarrow D^*(\rightarrow D\pi^0)K^+\bar{p}$	$0.1 \pm 0.0$	$0.1 \pm 0.0$
$\bar{\Lambda}_b^0 \rightarrow D^*(\rightarrow D\gamma)K^+\bar{p}$	$0.1 \pm 0.0$	$0.1 \pm 0.0$
$\Lambda_b^0 \rightarrow Dp\pi^-$	$24.9 \pm 0.5$	$24.9 \pm 0.5$
$\Lambda_b^0 \rightarrow D^*(\rightarrow D\pi^0)p\pi^-$	$2.7 \pm 0.1$	$2.7 \pm 0.1$
$\Lambda_b^0 \rightarrow D^*(\rightarrow D\gamma)p\pi^-$	$2.7 \pm 0.1$	$2.7 \pm 0.1$
$B^+ \rightarrow D\pi^+\pi^+\pi^-$	$2.6 \pm 0.3$	$2.6 \pm 0.3$
$B^+ \rightarrow DK^+\pi^+\pi^-$	$0.1 \pm 0.0$	$0.1 \pm 0.0$
$B_s^0 \rightarrow D\bar{K}_{(1,2)}^*$	$5.0 \pm 0.2$	$5.1 \pm 0.2$

 Table 7.6: Yields per  $B$  flavour within  $\mu \pm 3\sigma$  for  $D \rightarrow \pi^+\pi^-$ 

 Figure 7.2:  $D \rightarrow \pi^+\pi^-$  from  $B^0$  (left) and from  $\bar{B}^0$  (right)

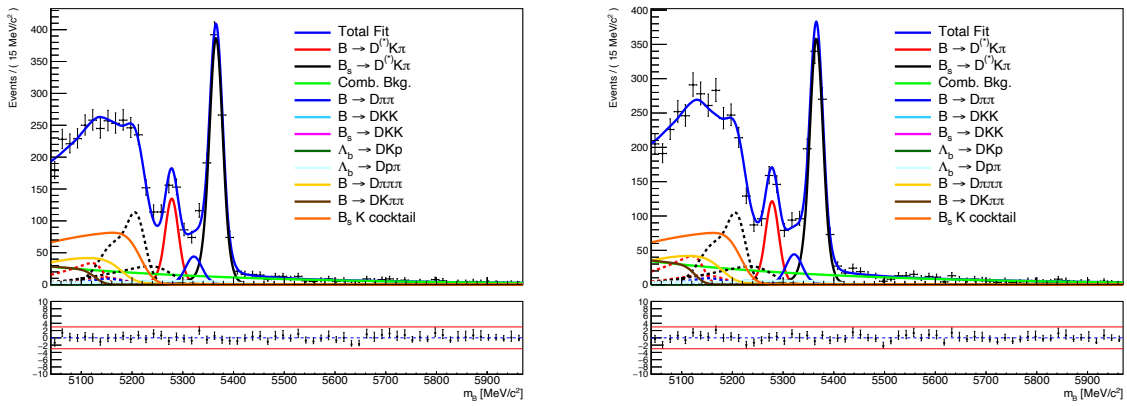
Yield	$B^0$	$\bar{B}^0$
$B^0 \rightarrow DK^+\pi^-$	$5497.2 \pm 83.6$	$5427.8 \pm 82.8$
$\bar{B}_s^0 \rightarrow DK^+\pi^-$	$4.0 \pm 0.5$	$4.0 \pm 0.5$
Combinatorial	$625.8 \pm 27.0$	$615.6 \pm 26.8$
$B^0 \rightarrow D^*(\rightarrow D\pi^0)K^+\pi^-$	$4.0 \pm 0.1$	$3.8 \pm 0.1$
$B^0 \rightarrow D^*(\rightarrow D\gamma)K^+\pi^-$	$7.4 \pm 0.2$	$7.0 \pm 0.2$
$\bar{B}_s^0 \rightarrow D^*(\rightarrow D\pi^0)K^+\pi^-$	$2.2 \pm 0.3$	$2.2 \pm 0.3$
$\bar{B}_s^0 \rightarrow D^*(\rightarrow D\gamma)K^+\pi^-$	$26.3 \pm 3.2$	$26.7 \pm 3.2$
$B^0 \rightarrow D\pi^+\pi^-$	$388.8 \pm 7.9$	$388.8 \pm 7.9$
$B^0 \rightarrow D^*(\rightarrow D\pi^0)\pi^+\pi^-$	$9.0 \pm 0.2$	$9.0 \pm 0.2$
$B^0 \rightarrow D^*(\rightarrow D\gamma)\pi^+\pi^-$	$21.0 \pm 0.4$	$21.0 \pm 0.4$
$B^0 \rightarrow DK^+K^-$	$34.7 \pm 0.7$	$34.7 \pm 0.7$
$B^0 \rightarrow D^*(\rightarrow D\pi^0)K^+K^-$	$0.0 \pm 0.0$	$0.0 \pm 0.0$
$B^0 \rightarrow D^*(\rightarrow D\gamma)K^+K^-$	$0.0 \pm 0.0$	$0.0 \pm 0.0$
$B_s^0 \rightarrow DK^+K^-$	$20.4 \pm 0.4$	$20.4 \pm 0.4$
$B_s^0 \rightarrow D^*(\rightarrow D\pi^0)K^+K^-$	$0.0 \pm 0.0$	$0.0 \pm 0.0$
$B_s^0 \rightarrow D^*(\rightarrow D\gamma)K^+K^-$	$0.6 \pm 0.0$	$0.6 \pm 0.0$
$\bar{\Lambda}_b^0 \rightarrow DK^+\bar{p}$	$27.8 \pm 0.6$	$27.8 \pm 0.6$
$\bar{\Lambda}_b^0 \rightarrow D^*(\rightarrow D\pi^0)K^+\bar{p}$	$2.1 \pm 0.0$	$2.1 \pm 0.0$
$\bar{\Lambda}_b^0 \rightarrow D^*(\rightarrow D\gamma)K^+\bar{p}$	$2.7 \pm 0.1$	$2.7 \pm 0.1$
$B^+ \rightarrow D\pi^+\pi^+\pi^-$	$42.3 \pm 5.2$	$42.3 \pm 5.2$
$B^+ \rightarrow DK^+\pi^+\pi^-$	$1.2 \pm 0.0$	$1.2 \pm 0.0$
$B_s^0 \rightarrow D\bar{K}_{(1,2)}^{(*)}$	$1.8 \pm 0.2$	$1.8 \pm 0.2$

Table 7.7: Yields per  $B$  flavour within  $\mu \pm 3\sigma$  for  $D \rightarrow K^\pm\pi^\mp$ Figure 7.3:  $D \rightarrow K^\pm\pi^\mp$  from  $B^0$  (left) and from  $\bar{B}^0$  (right)

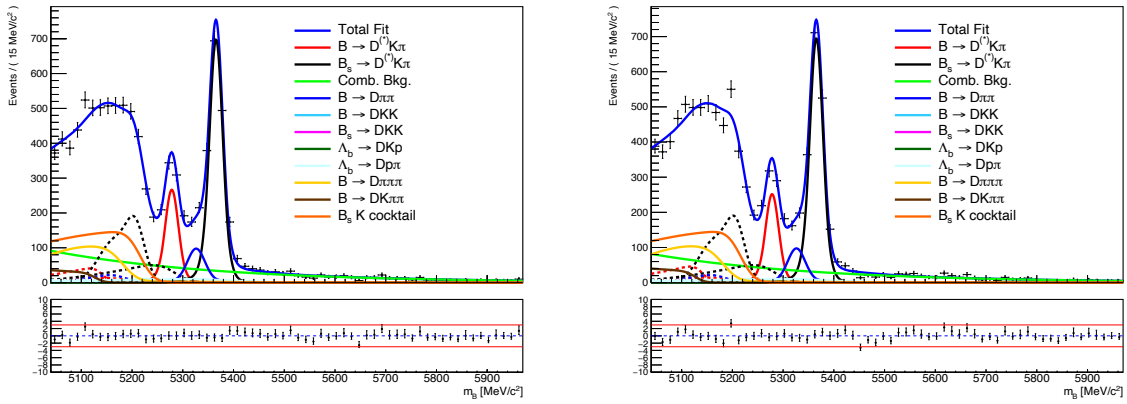
Yield	$B^0$	$\bar{B}^0$
$B^0 \rightarrow DK^+\pi^-$	$1013.4 \pm 63.9$	$994.3 \pm 63.6$
$\bar{B}_s^0 \rightarrow DK^+\pi^-$	$287.4 \pm 2.4$	$286.4 \pm 2.3$
Combinatorial	$336.0 \pm 19.8$	$342.9 \pm 20.3$
$B^0 \rightarrow D^*(\rightarrow D\pi^0)K^+\pi^-$	$0.0 \pm 0.0$	$0.2 \pm 0.2$
$B^0 \rightarrow D^*(\rightarrow D\gamma)K^+\pi^-$	$0.0 \pm 0.0$	$0.4 \pm 0.3$
$\bar{B}_s^0 \rightarrow D^*(\rightarrow D\pi^0)K^+\pi^-$	$155.1 \pm 2.1$	$154.5 \pm 2.0$
$\bar{B}_s^0 \rightarrow D^*(\rightarrow D\gamma)K^+\pi^-$	$1894.5 \pm 24.9$	$1887.6 \pm 23.4$
$B^0 \rightarrow D\pi^+\pi^-$	$354.2 \pm 7.2$	$354.2 \pm 7.2$
$B^0 \rightarrow D^*(\rightarrow D\pi^0)\pi^+\pi^-$	$10.2 \pm 0.2$	$10.2 \pm 0.2$
$B^0 \rightarrow D^*(\rightarrow D\gamma)\pi^+\pi^-$	$23.6 \pm 0.5$	$23.6 \pm 0.5$
$B^0 \rightarrow DK^+K^-$	$31.5 \pm 0.7$	$31.5 \pm 0.7$
$B^0 \rightarrow D^*(\rightarrow D\pi^0)K^+K^-$	$0.0 \pm 0.0$	$0.0 \pm 0.0$
$B^0 \rightarrow D^*(\rightarrow D\gamma)K^+K^-$	$0.0 \pm 0.0$	$0.0 \pm 0.0$
$\bar{B}_s^0 \rightarrow DK^+K^-$	$20.7 \pm 0.4$	$20.7 \pm 0.4$
$\bar{B}_s^0 \rightarrow D^*(\rightarrow D\pi^0)K^+K^-$	$0.0 \pm 0.0$	$0.0 \pm 0.0$
$\bar{B}_s^0 \rightarrow D^*(\rightarrow D\gamma)K^+K^-$	$0.6 \pm 0.0$	$0.6 \pm 0.0$
$\Lambda_b^0 \rightarrow Dp\pi^-$	$608.1 \pm 12.3$	$608.1 \pm 12.3$
$\Lambda_b^0 \rightarrow D^*(\rightarrow D\pi^0)p\pi^-$	$62.0 \pm 1.3$	$62.0 \pm 1.3$
$\Lambda_b^0 \rightarrow D^*(\rightarrow D\gamma)p\pi^-$	$70.2 \pm 1.4$	$70.2 \pm 1.4$
$B^+ \rightarrow D\pi^+\pi^+\pi^-$	$22.5 \pm 2.8$	$22.5 \pm 2.8$
$B_s^0 \rightarrow D\bar{K}_{(1,2)}^{(*)}$	$128.2 \pm 4.2$	$127.7 \pm 4.2$

 Table 7.8: Yields per  $B$  flavour within  $\mu \pm 3\sigma$  for  $D \rightarrow \pi^\pm K^\mp$ 

 Figure 7.4:  $D \rightarrow \pi^\pm K^\mp$  from  $B^0$  (left) and from  $\bar{B}^0$  (right)

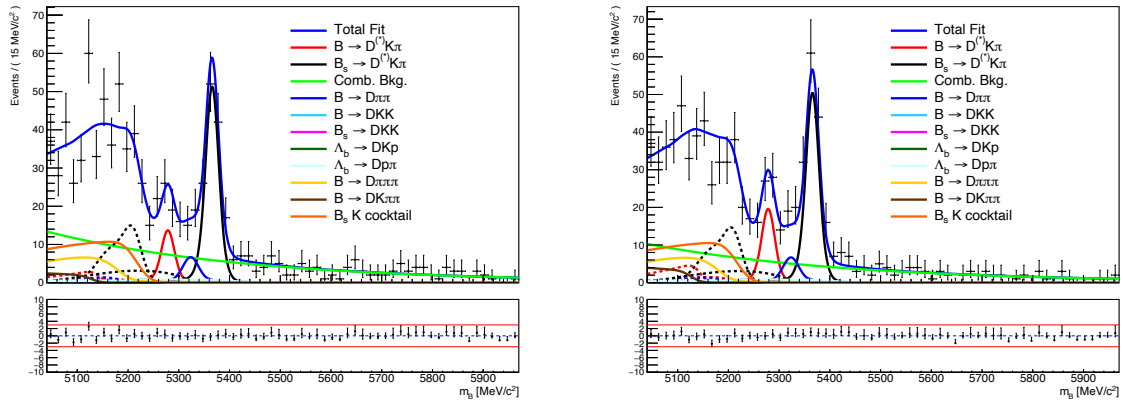
Yield	$B^0$	$\bar{B}^0$
$B^0 \rightarrow DK^+\pi^-$	$306.3 \pm 23.9$	$275.2 \pm 23.2$
$\bar{B}_s^0 \rightarrow DK^+\pi^-$	$16.6 \pm 0.7$	$15.3 \pm 0.7$
Combinatorial	$75.4 \pm 9.8$	$91.3 \pm 11.3$
$B^0 \rightarrow D^*(\rightarrow D\pi^0)K^+\pi^-$	$0.2 \pm 0.0$	$0.2 \pm 0.0$
$B^0 \rightarrow D^*(\rightarrow D\gamma)K^+\pi^-$	$0.3 \pm 0.0$	$0.3 \pm 0.0$
$\bar{B}_s^0 \rightarrow D^*(\rightarrow D\pi^0)K^+\pi^-$	$10.8 \pm 0.3$	$10.0 \pm 0.3$
$\bar{B}_s^0 \rightarrow D^*(\rightarrow D\gamma)K^+\pi^-$	$79.6 \pm 2.5$	$73.6 \pm 2.5$
$B^0 \rightarrow D\pi^+\pi^-$	$43.8 \pm 2.6$	$43.8 \pm 2.6$
$B^0 \rightarrow D^*(\rightarrow D\pi^0)\pi^+\pi^-$	$0.9 \pm 0.1$	$0.9 \pm 0.1$
$B^0 \rightarrow D^*(\rightarrow D\gamma)\pi^+\pi^-$	$2.3 \pm 0.1$	$2.3 \pm 0.1$
$B^0 \rightarrow DK^+K^-$	$4.1 \pm 0.3$	$4.1 \pm 0.3$
$B^0 \rightarrow D^*(\rightarrow D\pi^0)K^+K^-$	$0.0 \pm 0.0$	$0.0 \pm 0.0$
$B^0 \rightarrow D^*(\rightarrow D\gamma)K^+K^-$	$0.0 \pm 0.0$	$0.0 \pm 0.0$
$B_s^0 \rightarrow DK^+K^-$	$1.7 \pm 0.1$	$1.7 \pm 0.1$
$B_s^0 \rightarrow D^*(\rightarrow D\pi^0)K^+K^-$	$0.0 \pm 0.0$	$0.0 \pm 0.0$
$B_s^0 \rightarrow D^*(\rightarrow D\gamma)K^+K^-$	$0.0 \pm 0.0$	$0.0 \pm 0.0$
$\bar{\Lambda}_b^0 \rightarrow DK^+\bar{p}$	$1.5 \pm 0.1$	$1.5 \pm 0.1$
$\bar{\Lambda}_b^0 \rightarrow D^*(\rightarrow D\pi^0)K^+\bar{p}$	$0.2 \pm 0.0$	$0.2 \pm 0.0$
$\bar{\Lambda}_b^0 \rightarrow D^*(\rightarrow D\gamma)K^+\bar{p}$	$0.1 \pm 0.0$	$0.1 \pm 0.0$
$\Lambda_b^0 \rightarrow Dp\pi^-$	$26.6 \pm 1.6$	$26.6 \pm 1.6$
$\Lambda_b^0 \rightarrow D^*(\rightarrow D\pi^0)p\pi^-$	$4.8 \pm 0.3$	$4.8 \pm 0.3$
$\Lambda_b^0 \rightarrow D^*(\rightarrow D\gamma)p\pi^-$	$3.6 \pm 0.2$	$3.6 \pm 0.2$
$B^+ \rightarrow D\pi^+\pi^+\pi^-$	$6.4 \pm 1.2$	$6.4 \pm 1.2$
$B^+ \rightarrow DK^+\pi^+\pi^-$	$0.1 \pm 0.0$	$0.2 \pm 0.0$
$B_s^0 \rightarrow D\bar{K}_{(1,2)}^*$	$8.0 \pm 0.3$	$7.4 \pm 0.3$

Table 7.9: Yields per  $B$  flavour within  $\mu \pm 3\sigma$  for  $D \rightarrow K_S^0\pi^+\pi^-$  LLFigure 7.5:  $D \rightarrow K_S^0\pi^+\pi^-$  LL from  $B^0$  (left) and from  $\bar{B}^0$  (right)

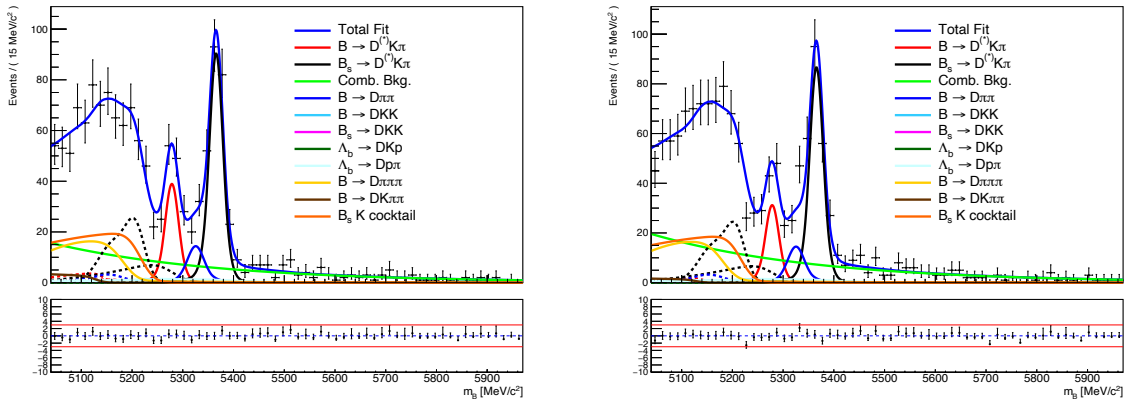
Yield	$B^0$	$\bar{B}^0$
$B^0 \rightarrow DK^+\pi^-$	$598.4 \pm 34.6$	$566.3 \pm 33.7$
$\bar{B}_s^0 \rightarrow DK^+\pi^-$	$28.6 \pm 1.0$	$28.5 \pm 1.0$
Combinatorial	$217.8 \pm 17.8$	$195.1 \pm 16.1$
$B^0 \rightarrow D^*(\rightarrow D\pi^0)K^+\pi^-$	$0.2 \pm 0.1$	$0.2 \pm 0.1$
$B^0 \rightarrow D^*(\rightarrow D\gamma)K^+\pi^-$	$0.6 \pm 0.2$	$0.7 \pm 0.2$
$\bar{B}_s^0 \rightarrow D^*(\rightarrow D\pi^0)K^+\pi^-$	$17.6 \pm 0.5$	$17.5 \pm 0.5$
$\bar{B}_s^0 \rightarrow D^*(\rightarrow D\gamma)K^+\pi^-$	$153.9 \pm 4.3$	$153.6 \pm 4.2$
$B^0 \rightarrow D\pi^+\pi^-$	$81.3 \pm 4.9$	$81.3 \pm 4.9$
$B^0 \rightarrow D^*(\rightarrow D\pi^0)\pi^+\pi^-$	$1.8 \pm 0.1$	$1.8 \pm 0.1$
$B^0 \rightarrow D^*(\rightarrow D\gamma)\pi^+\pi^-$	$6.8 \pm 0.4$	$6.8 \pm 0.4$
$B^0 \rightarrow DK^+K^-$	$6.5 \pm 0.4$	$6.5 \pm 0.4$
$B^0 \rightarrow D^*(\rightarrow D\pi^0)K^+K^-$	$0.0 \pm 0.0$	$0.0 \pm 0.0$
$B^0 \rightarrow D^*(\rightarrow D\gamma)K^+K^-$	$0.0 \pm 0.0$	$0.0 \pm 0.0$
$B_s^0 \rightarrow DK^+K^-$	$3.2 \pm 0.2$	$3.2 \pm 0.2$
$B_s^0 \rightarrow D^*(\rightarrow D\pi^0)K^+K^-$	$0.0 \pm 0.0$	$0.0 \pm 0.0$
$B_s^0 \rightarrow D^*(\rightarrow D\gamma)K^+K^-$	$0.1 \pm 0.0$	$0.1 \pm 0.0$
$\bar{\Lambda}_b^0 \rightarrow DK^+\bar{p}$	$2.7 \pm 0.2$	$2.7 \pm 0.2$
$\bar{\Lambda}_b^0 \rightarrow D^*(\rightarrow D\pi^0)K^+\bar{p}$	$0.2 \pm 0.0$	$0.2 \pm 0.0$
$\bar{\Lambda}_b^0 \rightarrow D^*(\rightarrow D\gamma)K^+\bar{p}$	$0.3 \pm 0.0$	$0.3 \pm 0.0$
$\Lambda_b^0 \rightarrow Dp\pi^-$	$47.5 \pm 2.9$	$47.5 \pm 2.9$
$\Lambda_b^0 \rightarrow D^*(\rightarrow D\pi^0)p\pi^-$	$9.8 \pm 0.6$	$9.8 \pm 0.6$
$\Lambda_b^0 \rightarrow D^*(\rightarrow D\gamma)p\pi^-$	$7.5 \pm 0.5$	$7.5 \pm 0.5$
$B^+ \rightarrow D\pi^+\pi^+\pi^-$	$15.0 \pm 2.8$	$15.0 \pm 2.8$
$B^+ \rightarrow DK^+\pi^+\pi^-$	$0.1 \pm 0.0$	$0.1 \pm 0.0$
$B_s^0 \rightarrow D\bar{K}_{(1,2)}^*$	$14.1 \pm 0.6$	$14.1 \pm 0.6$

 Table 7.10: Yields per  $B$  flavour within  $\mu \pm 3\sigma$  for  $D \rightarrow K_S^0\pi^+\pi^-$  DD

 Figure 7.6:  $D \rightarrow K_S^0\pi^+\pi^-$  DD from  $B^0$  (left) and from  $\bar{B}^0$  (right)

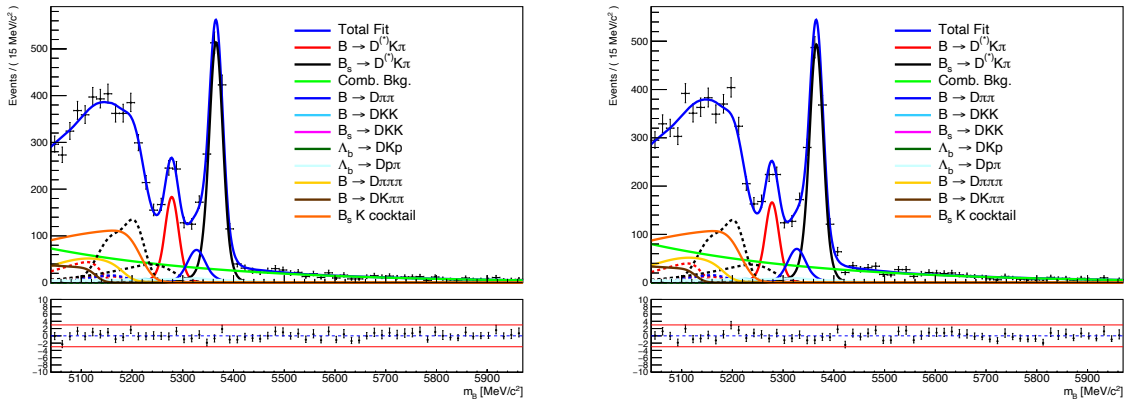
Yield	$B^0$	$\bar{B}^0$
$B^0 \rightarrow DK^+\pi^-$	$30.8 \pm 9.6$	$44.0 \pm 9.6$
$\bar{B}_s^0 \rightarrow DK^+\pi^-$	$2.1 \pm 0.3$	$2.1 \pm 0.3$
Combinatorial	$35.2 \pm 6.0$	$27.1 \pm 5.0$
$B^0 \rightarrow D^*(\rightarrow D\pi^0)K^+\pi^-$	$0.0 \pm 0.0$	$0.0 \pm 0.0$
$B^0 \rightarrow D^*(\rightarrow D\gamma)K^+\pi^-$	$0.0 \pm 0.0$	$0.0 \pm 0.0$
$\bar{B}_s^0 \rightarrow D^*(\rightarrow D\pi^0)K^+\pi^-$	$1.4 \pm 0.1$	$1.4 \pm 0.1$
$\bar{B}_s^0 \rightarrow D^*(\rightarrow D\gamma)K^+\pi^-$	$11.1 \pm 1.1$	$10.9 \pm 1.0$
$B^0 \rightarrow D\pi^+\pi^-$	$6.0 \pm 0.4$	$6.0 \pm 0.4$
$B^0 \rightarrow D^*(\rightarrow D\pi^0)\pi^+\pi^-$	$0.1 \pm 0.0$	$0.1 \pm 0.0$
$B^0 \rightarrow D^*(\rightarrow D\gamma)\pi^+\pi^-$	$0.4 \pm 0.0$	$0.4 \pm 0.0$
$B^0 \rightarrow DK^+K^-$	$0.5 \pm 0.0$	$0.5 \pm 0.0$
$B^0 \rightarrow D^*(\rightarrow D\pi^0)K^+K^-$	$0.0 \pm 0.0$	$0.0 \pm 0.0$
$B^0 \rightarrow D^*(\rightarrow D\gamma)K^+K^-$	$0.0 \pm 0.0$	$0.0 \pm 0.0$
$B_s^0 \rightarrow DK^+K^-$	$0.3 \pm 0.0$	$0.3 \pm 0.0$
$B_s^0 \rightarrow D^*(\rightarrow D\pi^0)K^+K^-$	$0.0 \pm 0.0$	$0.0 \pm 0.0$
$B_s^0 \rightarrow D^*(\rightarrow D\gamma)K^+K^-$	$0.0 \pm 0.0$	$0.0 \pm 0.0$
$\bar{\Lambda}_b^0 \rightarrow DK^+\bar{p}$	$0.2 \pm 0.0$	$0.2 \pm 0.0$
$\bar{\Lambda}_b^0 \rightarrow D^*(\rightarrow D\pi^0)K^+\bar{p}$	$0.0 \pm 0.0$	$0.0 \pm 0.0$
$\bar{\Lambda}_b^0 \rightarrow D^*(\rightarrow D\gamma)K^+\bar{p}$	$0.0 \pm 0.0$	$0.0 \pm 0.0$
$\Lambda_b^0 \rightarrow Dp\pi^-$	$3.7 \pm 0.2$	$3.7 \pm 0.2$
$\Lambda_b^0 \rightarrow D^*(\rightarrow D\pi^0)p\pi^-$	$0.7 \pm 0.0$	$0.7 \pm 0.0$
$\Lambda_b^0 \rightarrow D^*(\rightarrow D\gamma)p\pi^-$	$0.5 \pm 0.0$	$0.5 \pm 0.0$
$B^+ \rightarrow D\pi^+\pi^+\pi^-$	$1.0 \pm 0.2$	$1.0 \pm 0.2$
$B^+ \rightarrow DK^+\pi^+\pi^-$	$0.0 \pm 0.0$	$0.0 \pm 0.0$
$B_s^0 \rightarrow D\bar{K}_{(1,2)}^*$	$1.0 \pm 0.1$	$0.9 \pm 0.1$

Table 7.11: Yields per  $B$  flavour within  $\mu \pm 3\sigma$  for  $D \rightarrow K_S^0 K^+ K^-$  LLFigure 7.7:  $D \rightarrow K_S^0 K^+ K^-$  LL from  $B^0$  (left) and from  $\bar{B}^0$  (right)

Yield	$B^0$	$\bar{B}^0$
$B^0 \rightarrow DK^+\pi^-$	$89.9 \pm 13.1$	$71.5 \pm 12.9$
$\bar{B}_s^0 \rightarrow DK^+\pi^-$	$3.9 \pm 0.4$	$3.8 \pm 0.4$
Combinatorial	$38.0 \pm 6.4$	$47.2 \pm 7.7$
$B^0 \rightarrow D^*(\rightarrow D\pi^0)K^+\pi^-$	$0.0 \pm 0.0$	$0.0 \pm 0.0$
$B^0 \rightarrow D^*(\rightarrow D\gamma)K^+\pi^-$	$0.1 \pm 0.0$	$0.0 \pm 0.0$
$\bar{B}_s^0 \rightarrow D^*(\rightarrow D\pi^0)K^+\pi^-$	$2.5 \pm 0.2$	$2.3 \pm 0.2$
$\bar{B}_s^0 \rightarrow D^*(\rightarrow D\gamma)K^+\pi^-$	$20.1 \pm 1.3$	$19.2 \pm 1.4$
$B^0 \rightarrow D\pi^+\pi^-$	$12.9 \pm 0.8$	$12.9 \pm 0.8$
$B^0 \rightarrow D^*(\rightarrow D\pi^0)\pi^+\pi^-$	$0.2 \pm 0.0$	$0.2 \pm 0.0$
$B^0 \rightarrow D^*(\rightarrow D\gamma)\pi^+\pi^-$	$1.0 \pm 0.1$	$1.0 \pm 0.1$
$B^0 \rightarrow DK^+K^-$	$0.9 \pm 0.1$	$0.9 \pm 0.1$
$B^0 \rightarrow D^*(\rightarrow D\pi^0)K^+K^-$	$0.0 \pm 0.0$	$0.0 \pm 0.0$
$B^0 \rightarrow D^*(\rightarrow D\gamma)K^+K^-$	$0.0 \pm 0.0$	$0.0 \pm 0.0$
$B_s^0 \rightarrow DK^+K^-$	$0.5 \pm 0.0$	$0.5 \pm 0.0$
$B_s^0 \rightarrow D^*(\rightarrow D\pi^0)K^+K^-$	$0.0 \pm 0.0$	$0.0 \pm 0.0$
$B_s^0 \rightarrow D^*(\rightarrow D\gamma)K^+K^-$	$0.0 \pm 0.0$	$0.0 \pm 0.0$
$\bar{\Lambda}_b^0 \rightarrow DK^+\bar{p}$	$0.4 \pm 0.0$	$0.4 \pm 0.0$
$\bar{\Lambda}_b^0 \rightarrow D^*(\rightarrow D\pi^0)K^+\bar{p}$	$0.0 \pm 0.0$	$0.0 \pm 0.0$
$\bar{\Lambda}_b^0 \rightarrow D^*(\rightarrow D\gamma)K^+\bar{p}$	$0.0 \pm 0.0$	$0.0 \pm 0.0$
$\Lambda_b^0 \rightarrow Dp\pi^-$	$6.8 \pm 0.4$	$6.8 \pm 0.4$
$\Lambda_b^0 \rightarrow D^*(\rightarrow D\pi^0)p\pi^-$	$1.4 \pm 0.1$	$1.4 \pm 0.1$
$\Lambda_b^0 \rightarrow D^*(\rightarrow D\gamma)p\pi^-$	$0.9 \pm 0.1$	$0.9 \pm 0.1$
$B^+ \rightarrow D\pi^+\pi^+\pi^-$	$2.4 \pm 0.5$	$2.4 \pm 0.5$
$B^+ \rightarrow DK^+\pi^+\pi^-$	$0.0 \pm 0.0$	$0.0 \pm 0.0$
$B_s^0 \rightarrow D\bar{K}_{(1,2)}^{(*)}$	$2.0 \pm 0.1$	$1.9 \pm 0.1$

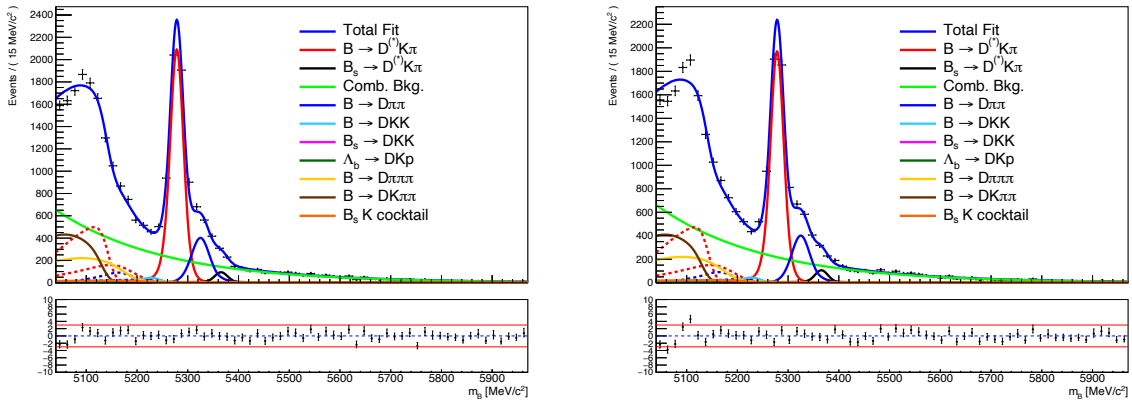
 Table 7.12: Yields per  $B$  flavour within  $\mu \pm 3\sigma$  for  $D \rightarrow K_S^0 K^+ K^-$  DD

 Figure 7.8:  $D \rightarrow K_S^0 K^+ K^-$  DD from  $B^0$  (left) and from  $\bar{B}^0$  (right)

Yield	$B^0$	$\bar{B}^0$
$B^0 \rightarrow DK^+\pi^-$	$428.7 \pm 30.0$	$389.1 \pm 29.5$
$\bar{B}_s^0 \rightarrow DK^+\pi^-$	$24.2 \pm 1.0$	$23.2 \pm 1.0$
Combinatorial	$185.8 \pm 15.5$	$203.2 \pm 16.9$
$B^0 \rightarrow D^*(\rightarrow D\pi^0)K^+\pi^-$	$0.4 \pm 0.1$	$0.3 \pm 0.1$
$B^0 \rightarrow D^*(\rightarrow D\gamma)K^+\pi^-$	$0.5 \pm 0.1$	$0.5 \pm 0.1$
$\bar{B}_s^0 \rightarrow D^*(\rightarrow D\pi^0)K^+\pi^-$	$15.9 \pm 0.5$	$15.2 \pm 0.5$
$\bar{B}_s^0 \rightarrow D^*(\rightarrow D\gamma)K^+\pi^-$	$120.0 \pm 3.5$	$115.3 \pm 3.5$
$B^0 \rightarrow D\pi^+\pi^-$	$63.3 \pm 1.5$	$63.3 \pm 1.5$
$B^0 \rightarrow D^*(\rightarrow D\pi^0)\pi^+\pi^-$	$1.9 \pm 0.0$	$1.9 \pm 0.0$
$B^0 \rightarrow D^*(\rightarrow D\gamma)\pi^+\pi^-$	$6.7 \pm 0.2$	$6.7 \pm 0.2$
$B^0 \rightarrow DK^+K^-$	$5.1 \pm 0.1$	$5.1 \pm 0.1$
$B^0 \rightarrow D^*(\rightarrow D\pi^0)K^+K^-$	$0.0 \pm 0.0$	$0.0 \pm 0.0$
$B^0 \rightarrow D^*(\rightarrow D\gamma)K^+K^-$	$0.0 \pm 0.0$	$0.0 \pm 0.0$
$B_s^0 \rightarrow DK^+K^-$	$3.0 \pm 0.1$	$3.0 \pm 0.1$
$B_s^0 \rightarrow D^*(\rightarrow D\pi^0)K^+K^-$	$0.0 \pm 0.0$	$0.0 \pm 0.0$
$B_s^0 \rightarrow D^*(\rightarrow D\gamma)K^+K^-$	$0.1 \pm 0.0$	$0.1 \pm 0.0$
$\bar{\Lambda}_b^0 \rightarrow DK^+\bar{p}$	$2.3 \pm 0.1$	$2.3 \pm 0.1$
$\bar{\Lambda}_b^0 \rightarrow D^*(\rightarrow D\pi^0)K^+\bar{p}$	$0.2 \pm 0.0$	$0.2 \pm 0.0$
$\bar{\Lambda}_b^0 \rightarrow D^*(\rightarrow D\gamma)K^+\bar{p}$	$0.3 \pm 0.0$	$0.3 \pm 0.0$
$\Lambda_b^0 \rightarrow Dp\pi^-$	$38.7 \pm 0.9$	$38.7 \pm 0.9$
$\Lambda_b^0 \rightarrow D^*(\rightarrow D\pi^0)p\pi^-$	$7.7 \pm 0.2$	$7.7 \pm 0.2$
$\Lambda_b^0 \rightarrow D^*(\rightarrow D\gamma)p\pi^-$	$5.7 \pm 0.1$	$5.7 \pm 0.1$
$B^+ \rightarrow D\pi^+\pi^+\pi^-$	$5.7 \pm 0.7$	$5.7 \pm 0.7$
$B^+ \rightarrow DK^+\pi^+\pi^-$	$0.1 \pm 0.0$	$0.1 \pm 0.0$
$B_s^0 \rightarrow D\bar{K}_{(1,2)}^{(*)}$	$12.2 \pm 0.5$	$11.7 \pm 0.5$

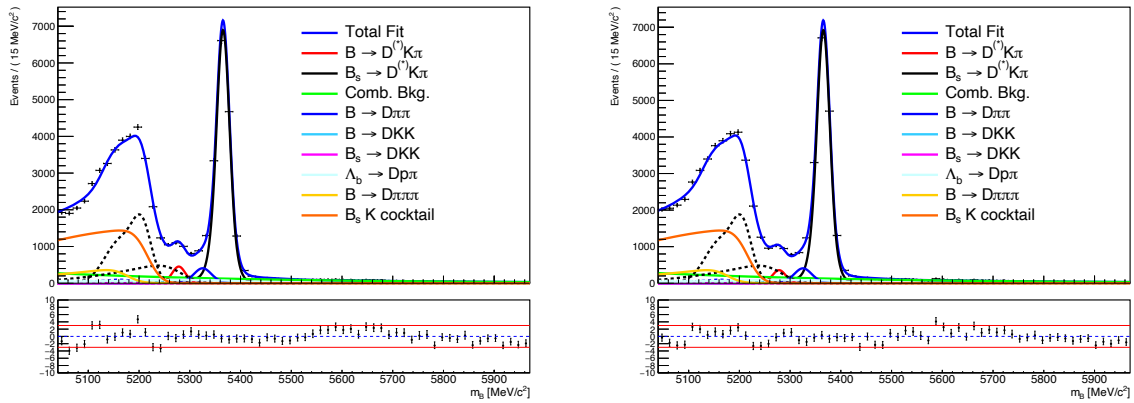
Table 7.13: Yields per  $B$  flavour within  $\mu \pm 3\sigma$  for  $D \rightarrow \pi^+\pi^-\pi^+\pi^-$ Figure 7.9:  $D \rightarrow \pi^+\pi^-\pi^+\pi^-$  from  $B^0$  (left) and from  $\bar{B}^0$  (right)



Yield	$B^0$	$\bar{B}^0$
$B^0 \rightarrow DK^+\pi^-$	$4678.2 \pm 80.8$	$4409.7 \pm 79.1$
$\bar{B}_s^0 \rightarrow DK^+\pi^-$	$3.8 \pm 0.6$	$4.3 \pm 0.6$
Combinatorial	$1033.6 \pm 30.6$	$1049.4 \pm 30.6$
$B^0 \rightarrow D^*(\rightarrow D\pi^0)K^+\pi^-$	$2.1 \pm 0.1$	$2.0 \pm 0.1$
$B^0 \rightarrow D^*(\rightarrow D\gamma)K^+\pi^-$	$6.8 \pm 0.3$	$6.5 \pm 0.3$
$\bar{B}_s^0 \rightarrow D^*(\rightarrow D\pi^0)K^+\pi^-$	$2.3 \pm 0.4$	$2.6 \pm 0.4$
$\bar{B}_s^0 \rightarrow D^*(\rightarrow D\gamma)K^+\pi^-$	$19.3 \pm 3.1$	$21.9 \pm 3.1$
$B^0 \rightarrow D\pi^+\pi^-$	$359.9 \pm 8.7$	$359.9 \pm 8.7$
$B^0 \rightarrow D^*(\rightarrow D\pi^0)\pi^+\pi^-$	$12.1 \pm 0.3$	$12.1 \pm 0.3$
$B^0 \rightarrow D^*(\rightarrow D\gamma)\pi^+\pi^-$	$28.3 \pm 0.7$	$28.3 \pm 0.7$
$B^0 \rightarrow DK^+K^-$	$26.1 \pm 0.6$	$26.1 \pm 0.6$
$B^0 \rightarrow D^*(\rightarrow D\pi^0)K^+K^-$	$0.0 \pm 0.0$	$0.0 \pm 0.0$
$B^0 \rightarrow D^*(\rightarrow D\gamma)K^+K^-$	$0.0 \pm 0.0$	$0.0 \pm 0.0$
$B_s^0 \rightarrow DK^+K^-$	$15.0 \pm 0.4$	$15.0 \pm 0.4$
$B_s^0 \rightarrow D^*(\rightarrow D\pi^0)K^+K^-$	$0.0 \pm 0.0$	$0.0 \pm 0.0$
$B_s^0 \rightarrow D^*(\rightarrow D\gamma)K^+K^-$	$0.3 \pm 0.0$	$0.3 \pm 0.0$
$\bar{\Lambda}_b^0 \rightarrow DK^+\bar{p}$	$23.0 \pm 0.6$	$23.0 \pm 0.6$
$\bar{\Lambda}_b^0 \rightarrow D^*(\rightarrow D\pi^0)K^+\bar{p}$	$2.2 \pm 0.1$	$2.2 \pm 0.1$
$\bar{\Lambda}_b^0 \rightarrow D^*(\rightarrow D\gamma)K^+\bar{p}$	$2.5 \pm 0.1$	$2.5 \pm 0.1$
$B^+ \rightarrow D\pi^+\pi^+\pi^-$	$37.5 \pm 4.6$	$37.5 \pm 4.6$
$B^+ \rightarrow DK^+\pi^+\pi^-$	$1.0 \pm 0.0$	$0.9 \pm 0.0$
$B_s^0 \rightarrow D\bar{K}_{(1,2)}^{(*)}$	$1.8 \pm 0.3$	$2.1 \pm 0.3$

 Table 7.14: Yields per  $B$  flavour within  $\mu \pm 3\sigma$  for  $D \rightarrow K^\pm\pi^\mp\pi^+\pi^-$ 

 Figure 7.10:  $D \rightarrow K^\pm\pi^\mp\pi^+\pi^-$  from  $B^0$  (left) and from  $\bar{B}^0$  (right)

Yield	$B^0$	$\bar{B}^0$
$B^0 \rightarrow DK^+\pi^-$	$1016.8 \pm 63.5$	$801.0 \pm 61.1$
$\bar{B}_s^0 \rightarrow DK^+\pi^-$	$280.4 \pm 2.8$	$281.6 \pm 2.7$
Combinatorial	$746.3 \pm 28.8$	$763.2 \pm 29.4$
$B^0 \rightarrow D^*(\rightarrow D\pi^0)K^+\pi^-$	$0.0 \pm 0.0$	$0.2 \pm 0.1$
$B^0 \rightarrow D^*(\rightarrow D\gamma)K^+\pi^-$	$0.0 \pm 0.0$	$0.7 \pm 0.4$
$\bar{B}_s^0 \rightarrow D^*(\rightarrow D\pi^0)K^+\pi^-$	$168.8 \pm 2.4$	$169.6 \pm 2.3$
$\bar{B}_s^0 \rightarrow D^*(\rightarrow D\gamma)K^+\pi^-$	$1421.7 \pm 19.9$	$1427.9 \pm 18.7$
$B^0 \rightarrow D\pi^+\pi^-$	$346.1 \pm 8.3$	$346.1 \pm 8.3$
$B^0 \rightarrow D^*(\rightarrow D\pi^0)\pi^+\pi^-$	$13.3 \pm 0.3$	$13.3 \pm 0.3$
$B^0 \rightarrow D^*(\rightarrow D\gamma)\pi^+\pi^-$	$29.5 \pm 0.7$	$29.5 \pm 0.7$
$B^0 \rightarrow DK^+K^-$	$27.5 \pm 0.7$	$27.5 \pm 0.7$
$B^0 \rightarrow D^*(\rightarrow D\pi^0)K^+K^-$	$0.0 \pm 0.0$	$0.0 \pm 0.0$
$B^0 \rightarrow D^*(\rightarrow D\gamma)K^+K^-$	$0.0 \pm 0.0$	$0.0 \pm 0.0$
$B_s^0 \rightarrow DK^+K^-$	$15.5 \pm 0.4$	$15.5 \pm 0.4$
$B_s^0 \rightarrow D^*(\rightarrow D\pi^0)K^+K^-$	$0.0 \pm 0.0$	$0.0 \pm 0.0$
$B_s^0 \rightarrow D^*(\rightarrow D\gamma)K^+K^-$	$0.3 \pm 0.0$	$0.3 \pm 0.0$
$\Lambda_b^0 \rightarrow Dp\pi^-$	$428.2 \pm 10.3$	$428.2 \pm 10.3$
$\Lambda_b^0 \rightarrow D^*(\rightarrow D\pi^0)p\pi^-$	$82.2 \pm 2.0$	$82.2 \pm 2.0$
$\Lambda_b^0 \rightarrow D^*(\rightarrow D\gamma)p\pi^-$	$60.4 \pm 1.5$	$60.4 \pm 1.5$
$B^+ \rightarrow D\pi^+\pi^+\pi^-$	$20.0 \pm 2.5$	$20.0 \pm 2.5$
$B_s^0 \rightarrow D\bar{K}_{(1,2)}^{(*)}$	$133.5 \pm 4.3$	$134.1 \pm 4.4$

Table 7.15: Yields per  $B$  flavour within  $\mu \pm 3\sigma$  for  $D \rightarrow \pi^\pm K^\mp \pi^+ \pi^-$ Figure 7.11:  $D \rightarrow \pi^\pm K^\mp \pi^+ \pi^-$  from  $B^0$  (left) and from  $\bar{B}^0$  (right)

## 7.4 Pseudo-experiment studies

The stability of the mass fit is verified with pseudo-experiments. Based on the fit results to data, 250 pseudo-experiments are generated and fitted. Invalid fits are rejected as they are deemed not to represent the real fit to data, Figs. 7.12 and 7.13 show the pull plots obtained from the successful fits. The variable names listed correspond to the variables shown in Tables 7.2 to 7.4. The means are consistent with zero and the widths are consistent with unity for the majority of the parameters. The proportion of parameters consistent with a mean of zero is 56.4%, 89.7%, 100% within  $1\sigma$ ,  $2\sigma$ ,  $3\sigma$ , respectively.

This result shows that for a dataset similar to that of the present data, within statistical fluctuations, the fitting procedure is robust. The pull distribution means consistent with zero show that the determined parameter values are typically unbiased and the pull distribution widths consistent with unity show that the statistical uncertainties on these parameters are correctly estimated.

## 7.5 Summary

This chapter explains the method used to determine how much signal and background is present within the signal window of the  $B$  candidate invariant mass, *i.e.* the fully selected dataset from which  $\gamma$  will be extracted in Chapter 8. The yields of each background,  $y^b$ , shown in Tables 7.5 to 7.15 are used in the background expectation term for the Dalitz bin populations in Eq. (4.48). Together with the Dalitz bin distribution fractions,  $f_{\alpha,i}^b$ , which are determined based on the modelling described in Chapter 6 this completes the necessary information about the expected presence of backgrounds in the LHCb data.

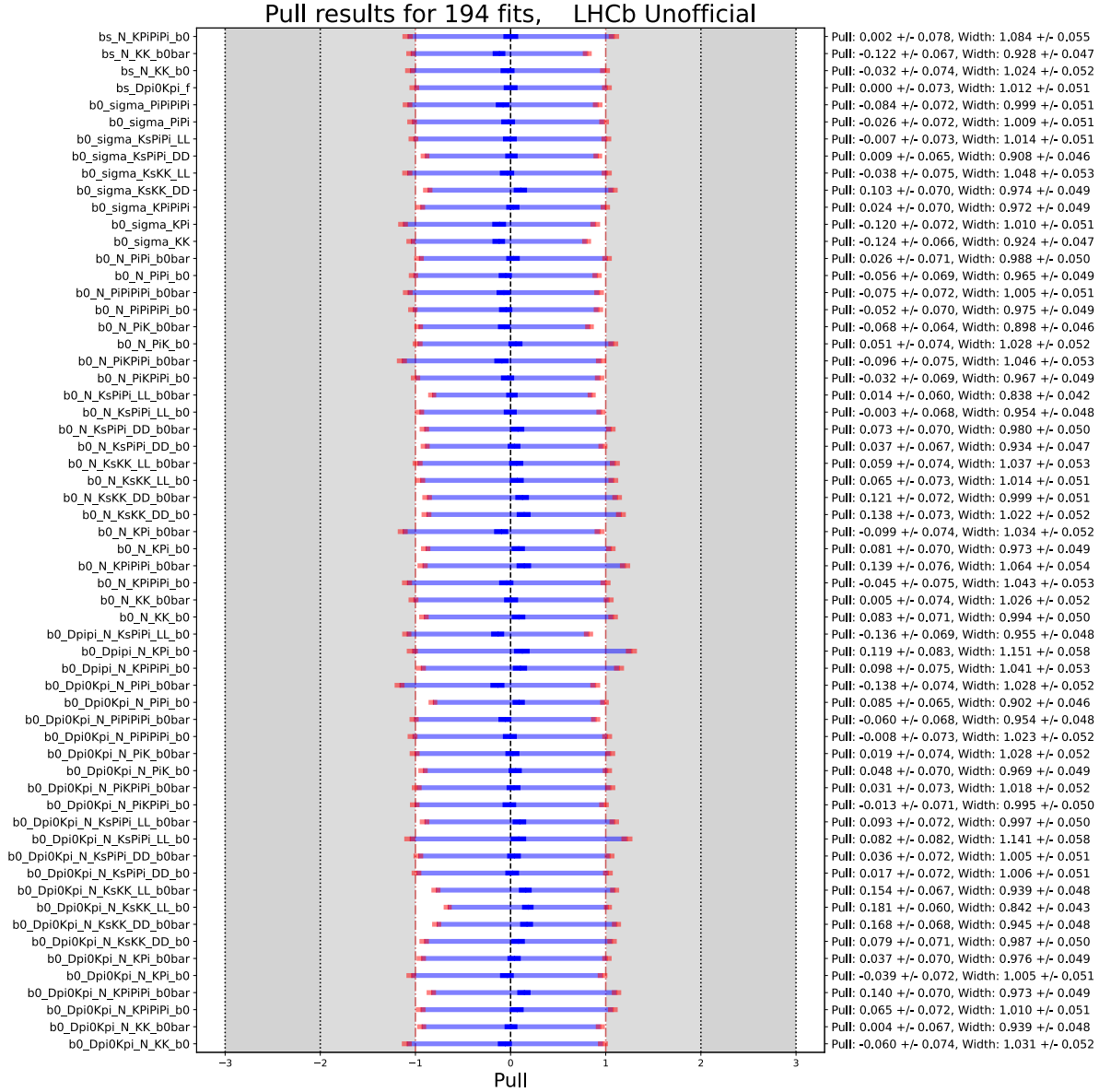


Figure 7.12: Summary of the pulls obtained from the mass fits to the pseudo-experiments. Showing all parameters in a single plot would be too dense so the remaining parameters are shown in a second plot, Fig. 7.13. Solid blue is the mean and its uncertainty of the pull distribution, translucent blue is the width of the pull distribution and red shows its uncertainty.

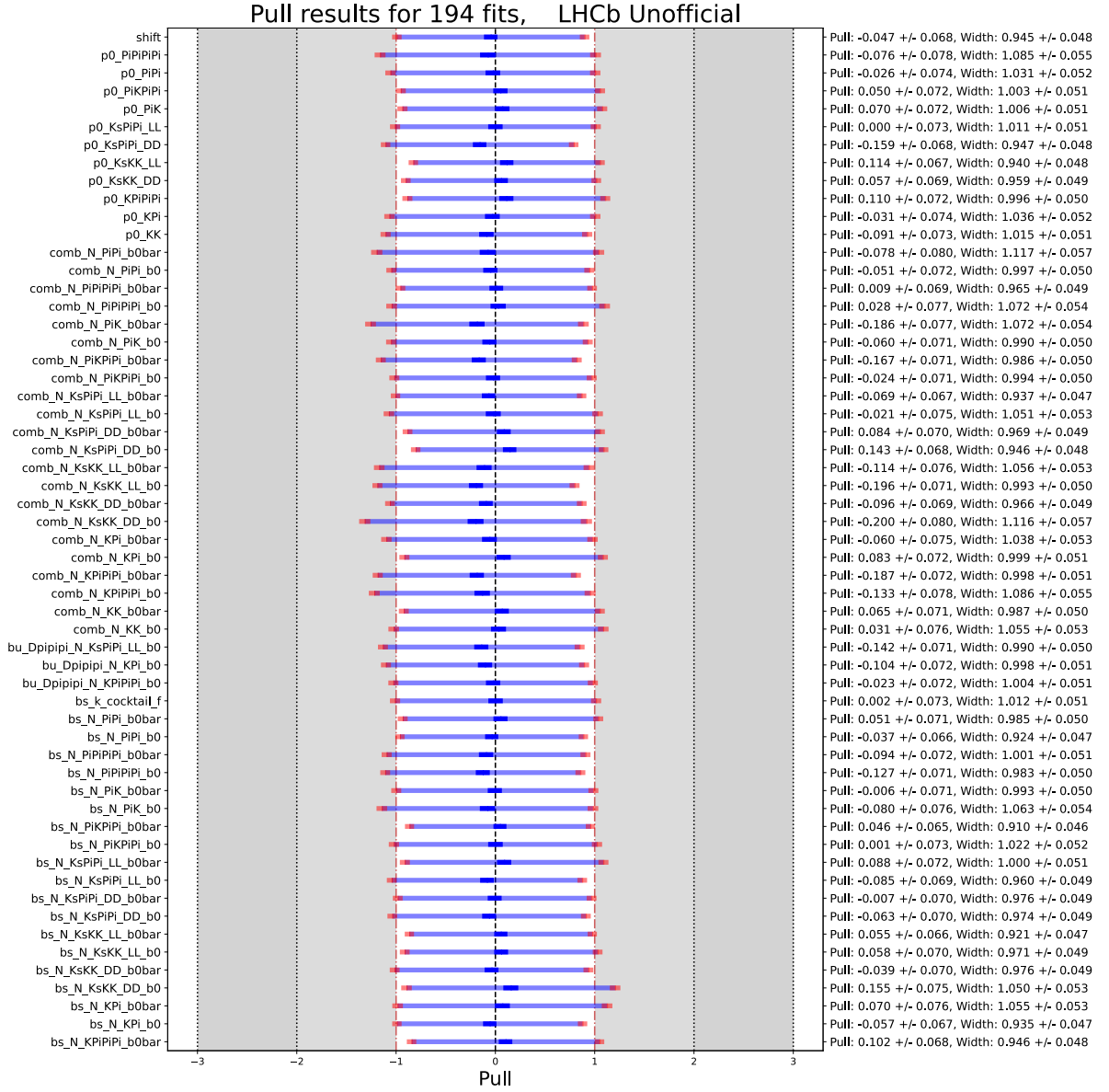


Figure 7.13: Summary of the pulls obtained from the mass fits to the pseudo-experiments. This plot shows the second half of all of the fit parameters, with the first set shown in Fig. 7.13.

## 8 $CP$ fit and interpretation

*“One in 20 people have been a victim of crime,  
which means that 19 out of 20 people must be criminals.  
No wonder we need police.”*

---

Philomena Cunk

This chapter explains the configuration of the double Dalitz fit to extract  $CP$  parameters  $x_\alpha^\pm$  and  $y_\alpha^\pm$ , and the method to interpret these parameters in terms of  $\gamma$  and related parameters,  $T_\alpha$  and  $\Delta\delta_\alpha$ , is also explained. Previous LHCb measurements are reproduced to help verify that the fitter is configured correctly. The results of the fit to data and pseudo-experiment studies are presented, with the value of  $\gamma$  blinded.

### 8.1 $CP$ fit

#### 8.1.1 Choice of parameterisation

The parameterisation of the signal expectation used in Eq. (4.39) is one of many possible parameterisations for modelling the binned signal populations of the double Dalitz  $B^0 \rightarrow DK^+\pi^-$  decay. It was not the first or simplest parameterisation considered for this analysis so it is necessary to summarise the problems with other possible parameterisations.

The first parameterisation to be considered was the simple Cartesian parameterisation where rather than having four unique Cartesian parameters per  $B$  Dalitz bin as in the case of Eq. (4.39) there is a single pair of Cartesian parameters common to all  $B$  Dalitz bins. They are defined as

$$x = \cos(\gamma), \quad y = \sin(\gamma), \quad (8.1)$$

with the general expectation equation being

$$N_{\alpha,i}^\pm = h_D^\pm \left\{ \bar{\kappa}_\alpha F_{\mp i} + \kappa_\alpha F_{\pm i} + 2\sqrt{\kappa_\alpha F_{+i} \bar{\kappa}_\alpha F_{-i}} [(\chi_\alpha c_i \mp \sigma_\alpha s_i)x \mp (\sigma_\alpha c_i \mp \chi_\alpha s_i)y] \right\}, \quad (8.2)$$

One downfall of this parameterisation is the lack of knowledge of the strong-phase param-

eters of the  $B$  Dalitz plane,  $\chi_\alpha$ ,  $\sigma_\alpha$ . Equation (8.2) is invariant under the transformation

$$x \mapsto cx \tag{8.3}$$

$$y \mapsto cy \tag{8.4}$$

$$\chi_\alpha \mapsto c^{-1}\chi_\alpha \quad \forall \alpha \in \mathbb{N}_{\leq 5} \tag{8.5}$$

$$\sigma_\alpha \mapsto c^{-1}\sigma_\alpha \quad \forall \alpha \in \mathbb{N}_{\leq 5}, \tag{8.6}$$

where  $c \in \mathbb{R}, c \neq 0$ . If this invariance is not broken by the addition of constraints then for any given set of  $N_{\alpha,i}^\pm$  values there is an infinite number of values of  $x, y, \chi_\alpha$  and  $\sigma_\alpha$  that correspond to a solution of Eq. (8.2). Since this is the first measurement of these strong-phase parameters and their only constraint,  $\chi_\alpha^2 + \sigma_\alpha^2 \leq 1 \forall \alpha \in \mathbb{N}_{\leq 5}$ , is not strict, the only way to resolve this ambiguity is to not freely float  $y$  in the fits and instead calculate it as  $y = \sqrt{1 - x^2}$ . This removes the independence between  $x$  and  $y$  and therefore offers no benefit over simply using the polar form Eq. (4.27) to avoid the ambiguity.

Following this realisation the next parameterisation that was attempted was to fall back on Eq. (4.27) where  $\gamma$  itself is floated in the  $CP$  fit. It has been shown in other analyses that a parameterisation such as this is problematic in cases where the values of  $\gamma$  and its uncertainty are such that  $\gamma$  is close to the zeroes of the cosine or sine functions. This results in unstable fits and poor quality pull distributions such that one can not have confidence in the result. It was found that this particular analysis can indeed suffer from this. Consequently the next parameterisation to be considered is the Cartesian parameterisation represented by Eq. (4.39), repeated here for ease of reading

$$N_{\alpha,i}^\pm = h_D^\pm [\bar{\kappa}_\alpha F_{\mp i} + \kappa_\alpha F_{\pm i} + 2\sqrt{\bar{\kappa}_\alpha \kappa_\alpha} F_{-i} F_{+i} (c_i x_\alpha^\pm \mp s_i y_\alpha^\pm)]. \tag{4.39}$$

This is the parameterisation used in this analysis however it does still have a few ambiguities one should be careful of when developing the  $CP$  fit.

### 8.1.2 Ambiguities

There are certain transformations for which Eq. (4.39) is invariant. These result in an infinite number of valid minima to which the fitter may converge instead of the true minima. Without resolving these ambiguities one cannot be confident that the fit to measure  $\gamma$  finds the correct value of all parameters.

**$h_D^\pm$  and  $(\bar{\kappa})_\alpha$** 

Equation (4.39) is invariant under the transformations

$$h_D^\pm \mapsto c h_D^\pm \quad \forall D \text{ final states}, \quad (8.7)$$

$$(\bar{\kappa})_\alpha \mapsto c^{-1} (\bar{\kappa})_\alpha \quad \forall \alpha \in \mathbb{N}_{\leq 5}, \quad (8.8)$$

where  $c \in \mathbb{R}, c \neq 0$ .

This ambiguity is resolved by enforcing the condition that the sum of all  $(\bar{\kappa})_\alpha$  is 1, as explained in Section 4.6.1 this is achieved by multiplying the global likelihood by a Gaussian term whose mean is the difference between this sum and 1. Another way to resolve this would be to use a recursive parameterisation similar to that described in Section 4.1.4 but for the  $(\bar{\kappa})_\alpha$  instead. As explained in Section 4.1.4 this parameterisation was motivated in the single Dalitz  $B^+ \rightarrow Dh^+$  analysis by the fact that simply floating the  $F_{\pm i}$  parameters and enforcing their sum to be one resulted in fit instabilities and high correlations between the  $F_{\pm i}$  parameters, however in the double Dalitz analysis no improvement was observed when the recursive parameterisation for the  $B$  Dalitz plane. For the sake of simplicity therefore it was decided to float the  $(\bar{\kappa})_\alpha$  parameters directly. This ambiguity is also possible between the  $h_D^\pm$  and  $F_{\pm i}$  parameters however use of the recursive parameterisation for the  $D$  planes resolves the ambiguity. Furthermore due to the assumption that the  $D$  Dalitz plane efficiency profile in this analysis is similar to that of the  $B^+ \rightarrow Dh^+$  analysis the relevant parameters are fixed in the  $CP$  fit.

 **$\kappa_\alpha$  polynomials**

Another source of ambiguity is one that is slightly more subtle and usually of little consequence but can be confusing when first encountered. If one considers all the parameters of Eq. (4.39) to be constant besides the  $(\bar{\kappa})_\alpha$  parameters then one can realise that this is a bivariate polynomial in terms of  $(\kappa_\alpha, \bar{\kappa}_\alpha)$

$$a\bar{\kappa}_\alpha + b\kappa_\alpha + c\sqrt{\kappa_\alpha\bar{\kappa}_\alpha} - d = 0, \quad (8.9)$$

where  $a, b, c, d \in \mathbb{R}$ . Therefore for a single set of values of  $a, b, c, d$  there can be an infinite number of solutions to which the fitter may converge defined by the values of the  $a, b, c, d$ . This is illustrated by Fig. 8.1 where the true values of  $(\bar{\kappa})_\alpha$  are such that  $\kappa_1 = \bar{\kappa}_1 = 0.5$ , *i.e.* only the first  $B$  Dalitz bin is populated, but the same argument applies for any choice of true  $(\sqrt{\kappa_1}, \sqrt{\bar{\kappa}_1})$ . However, the shape of this curve depends on the values of  $a, b, c, d$  therefore each  $D$  decay mode and each  $D$  Dalitz bin of the  $D \rightarrow K_S^0 h^+ h^-$  decay modes has a different shaped curve, each of which must pass through the true values of the  $(\bar{\kappa})_\alpha$  parameters. If multiple  $D$  final states are fitted at once then the fitter can only converge



to points where these ambiguous curves cross each other, this means that to resolve this ambiguity one simply needs to fit enough final states simultaneously such that there is a unique crossing point. As shown by Fig. 8.1 it should be sufficient to include both the favoured and suppressed  $D \rightarrow K^\pm \pi^\mp$  final states to resolve this ambiguity. This can be understood by considering that given the known value of  $r_{D,K\pi}$  the expectation of the favoured (suppressed) mode is dominated by the  $\bar{\kappa}_\alpha$  ( $\kappa_\alpha$ ) term such that a small deviation from the polynomial curve results in a relatively large change in the expected population. In the  $CP$  fit this ambiguity is of little concern since the  $D \rightarrow K_S^0 \pi^+ \pi^-$  mode alone has 40  $D$  Dalitz bins per  $B$  Dalitz bin, each with different  $D$  Dalitz parameter values, which in addition to the constraint that the sum of  $(\bar{\kappa})_\alpha$  is unity is sufficient to resolve the ambiguity.

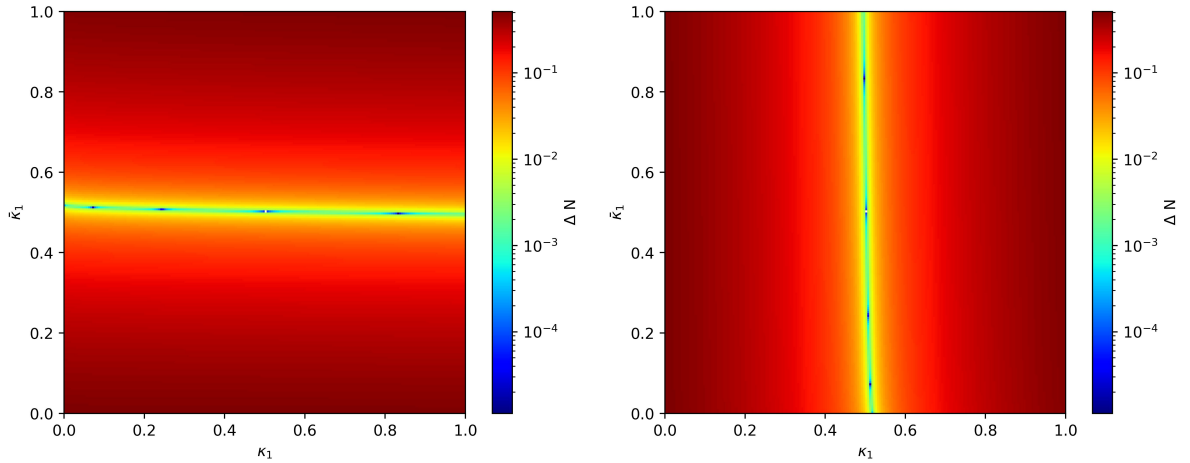


Figure 8.1: Bands of ambiguous solutions when fitting only the favoured (left) or suppressed (right)  $D \rightarrow K^\pm \pi^\mp$  decay. The  $z$ -axis shows the absolute difference between the expectation and the true expectation.

### 8.1.3 Parameter constraints

As already explained, the sum of the  $B$  population fraction Dalitz plane parameters  $(\bar{\kappa})_\alpha$  must sum to unity which is enforced by the addition of a Gaussian term to the likelihood. For the  $F_{\pm i}$  parameters this is enforced by fixing them according to the values of the  $R_i$  values measured in the single Dalitz  $B^+ \rightarrow Dh^+$  analysis. There is one other class of constraints that could be applied in the  $CP$  fit. These are the only physically motivated constraints that can be applied to the strong-phase parameters, the unit-disk constraints

$$T_\alpha^2 \equiv \chi_\alpha^2 + \sigma_\alpha^2 \leq 1 \quad \forall \alpha \in \mathbb{N}_{\leq \mathcal{M}}, \quad (8.10)$$

$$c_i^2 + s_i^2 \leq 1 \quad \forall \pm i \in \mathbb{N}_{\leq \mathcal{N}}. \quad (8.11)$$

However the central value of  $s_5$  from the external measurements in Table 4.2 is 1.022 and therefore this constraint cannot be used for the  $D$  plane strong phases. For the  $B$  Dalitz plane this constraint is not used as it is unlikely to provide any benefit to the fit based on studies using a simple implementation, and to implement it in such a way to avoid introducing bias is complicated.

### 8.1.4 Fitter verifications

A set of test fits have been determined that can be performed to test if the  $CP$  fit and interpretation are producing valid results. This is done by reproducing the results of previous LHCb analyses, albeit with slight modifications of the fit configuration to match the method of implementation in this analysis. The primary modification is, as explained in Sections 4.1.5 and 4.7, that the single Dalitz  $B^+ \rightarrow Dh^+$  analysis uses a simultaneous per-bin mass fit and  $CP$  fit whereas the double Dalitz analysis performs a global mass fit to provide background decay event yields which are then fixed in the  $CP$  fit. This means that a recreation of the  $B^+ \rightarrow Dh^+$   $CP$  fit can not be expected to exactly match the results of the original analysis as the only information available to the  $CP$  fit in this recreation is the signal yields according to the  $B^+ \rightarrow Dh^+$  per-bin mass fit, not the mass distributions or correlations themselves. Nevertheless it is encouraging that it can be shown that the double Dalitz fitter can obtain a  $CP$  fit result close to the original  $B^+ \rightarrow Dh^+$  analysis result to prove that the expectation equations are implemented correctly.

#### Single Dalitz $B^+ \rightarrow DK^+$ $CP$ -parameter-only reproduction

This check is performed by running the fitter assuming a single  $B$  bin and fitting the  $D$  Dalitz plane population expectation equations to the binned signal populations found in the previous  $B^+ \rightarrow Dh^+$  analysis for the  $B^+ \rightarrow DK^+$  mode only. The values used are shown in Tables 8.1 and 8.2 and copied from Ref. [56]. The only parameters floated are the normalisations and  $CP$  parameters for the  $B^+ \rightarrow DK^+$  decay. The fitted expectation is

$$N_i^\pm = h^\pm \left\{ F_{\mp i} + r_B^2 F_{\pm i} + 2r_B \sqrt{F_{+i} F_{-i}} [c_i x_\pm \mp s_i y_\pm] \right\}, \quad (8.12)$$

and the  $CP$  parameters are defined as

$$x_\pm = r_B \cos(\delta_B \pm \gamma), \quad (8.13)$$

$$y_\pm = r_B \sin(\delta_B \pm \gamma). \quad (8.14)$$

The recursive binned population fraction parameters,  $R_i$ , are fixed to the values found in the  $B^+ \rightarrow Dh^+$  analysis, and the strong-phase parameters,  $c_i$  and  $s_i$ , are fixed to combined CLEO-c and BES-III values. If the fitter is configured correctly it should be

able to produce a measurement of  $\gamma$  consistent with that found in the real single Dalitz  $B^+ \rightarrow Dh^+$  analysis. By default the fitter parameterises the likelihood distribution for the signal yields as Poisson distributed. However, since the yields for the  $B^+ \rightarrow Dh^+$  analysis are obtained from an invariant mass fit, a Gaussian likelihood is used for this cross check.

Figure 8.2 shows the Cartesian  $CP$  parameters contours obtained from the cross-check, along with the  $-2\ln\mathcal{L}$  profile obtained when interpreting these in terms of  $\gamma$ . Table 8.3 shows the values of the  $CP$  parameters extracted from this fitter compared to those found in the  $B^+ \rightarrow Dh^+$  analysis. There is extremely good agreement between the two which gives high confidence that the fitter is working as expected.

Bin $i$	LL		DD	
	$N_i^+$	$N_i^-$	$N_i^+$	$N_i^-$
-8	$138 \pm 13$	$66 \pm 9$	$290 \pm 19$	$123 \pm 13$
-7	$70 \pm 10$	$264 \pm 18$	$197 \pm 17$	$650 \pm 29$
-6	$4 \pm 3$	$137 \pm 13$	$17 \pm 5$	$286 \pm 18$
-5	$61 \pm 9$	$93 \pm 11$	$111 \pm 12$	$212 \pm 16$
-4	$126 \pm 12$	$180 \pm 15$	$329 \pm 20$	$390 \pm 22$
-3	$6 \pm 4$	$325 \pm 20$	$18 \pm 5$	$684 \pm 29$
-2	$1 \pm 2$	$353 \pm 20$	$9 \pm 4$	$735 \pm 29$
-1	$47 \pm 8$	$185 \pm 15$	$84 \pm 11$	$416 \pm 23$
1	$196 \pm 15$	$52 \pm 8$	$451 \pm 24$	$117 \pm 12$
2	$310 \pm 19$	$14 \pm 5$	$730 \pm 29$	$46 \pm 8$
3	$349 \pm 20$	$18 \pm 5$	$758 \pm 30$	$47 \pm 8$
4	$228 \pm 16$	$107 \pm 12$	$507 \pm 25$	$207 \pm 16$
5	$96 \pm 11$	$46 \pm 8$	$209 \pm 16$	$81 \pm 10$
6	$137 \pm 13$	$9 \pm 3$	$236 \pm 17$	$13 \pm 4$
7	$253 \pm 18$	$112 \pm 12$	$585 \pm 27$	$289 \pm 19$
8	$44 \pm 8$	$146 \pm 13$	$91 \pm 11$	$357 \pm 21$

Table 8.1: Binned signal populations observed in the  $B^+ \rightarrow Dh^+$  analysis for  $B^+ \rightarrow DK^+$ ,  $D \rightarrow K_S^0 \pi^+ \pi^-$  decays. From Ref. [56].

Bin $i$	LL		DD	
	$N_i^+$	$N_i^-$	$N_i^+$	$N_i^-$
-2	$100 \pm 11$	$65 \pm 9$	$212 \pm 16$	$142 \pm 13$
-1	$68 \pm 10$	$84 \pm 10$	$180 \pm 15$	$174 \pm 15$
1	$55 \pm 9$	$89 \pm 11$	$128 \pm 13$	$221 \pm 16$
2	$70 \pm 9$	$87 \pm 10$	$168 \pm 14$	$164 \pm 14$

Table 8.2: Binned signal populations observed in the  $B^+ \rightarrow Dh^+$  analysis for  $B^+ \rightarrow DK^+$ ,  $D \rightarrow K_S^0 K^+ K^-$  decays. From Ref. [56].

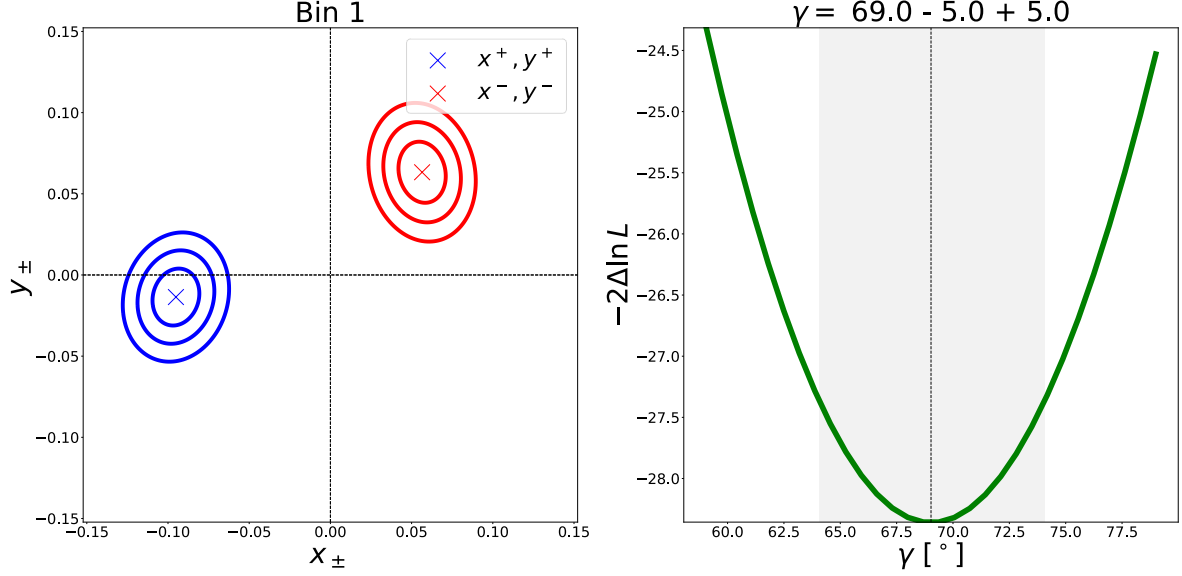


Figure 8.2: Cartesian  $CP$  parameters (left) and  $\chi^2$  profile for  $\gamma$  (right) extracted from the  $CP$  fit recreation of the  $B^+ \rightarrow Dh^+$  analysis with the  $B^+ \rightarrow DK^+$  data only.

Parameter	$B^+ \rightarrow Dh^+$ Measurement	Validation Result
$x_+^{DK}$	$(-9.3 \pm 1.0) \times 10^{-2}$	$(-9.5 \pm 1.0) \times 10^{-2}$
$y_+^{DK}$	$(-1.3 \pm 1.3) \times 10^{-2}$	$(-1.4 \pm 1.2) \times 10^{-2}$
$x_-^{DK}$	$(5.7 \pm 1.0) \times 10^{-2}$	$(5.6 \pm 1.0) \times 10^{-2}$
$y_-^{DK}$	$(6.6 \pm 1.0) \times 10^{-2}$	$(6.3 \pm 1.2) \times 10^{-2}$
$\gamma [^\circ]$	$68.7_{-5.1}^{+5.2}$	$69.0 \pm 5.0$
$r_B^{DK}$	$0.0904_{-0.0075}^{+0.0077}$	$0.0909 \pm 0.0072$
$\delta_B^{DK} [^\circ]$	$118.3_{-5.6}^{+5.5}$	$118.5 \pm 5.1$

Table 8.3: Comparison between the  $B^+ \rightarrow Dh^+$  analysis values of parameters of interest [56], and the values obtained by the double Dalitz fit with only the  $B^+ \rightarrow DK^+$  decay. Only statistical uncertainties are shown for the  $CP$  parameters to allow comparison, the other parameters only have total uncertainties quoted so it is expected that the uncertainties obtained should be slightly smaller since systematics are not accounted for here.

### Single Dalitz $B^+ \rightarrow Dh^+$ reproduction

This check uses the same procedure as above, but this time additionally including the  $B^+ \rightarrow D\pi^+$  mode as well as the  $B^+ \rightarrow DK^+$ . With the inclusion of the  $B^+ \rightarrow D\pi^+$  mode the recursive population fractions,  $R_i$ , can be floated as well as the  $B^+ \rightarrow D\pi^+$  normalisation parameters and  $CP$  parameters. The observed binned populations for  $B^+ \rightarrow D\pi^+$  decays are shown in Tables 8.4 and 8.5, also copied from Ref. [56]. The effective  $B^+ \rightarrow D\pi^+$   $CP$  parameters,  $x_{\xi}^{D\pi}$  and  $y_{\xi}^{D\pi}$ , are defined such that

$$x_{\pm}^{D\pi} = x_{\xi}^{D\pi} x_{\pm}^{DK} - y_{\xi}^{D\pi} y_{\pm}^{DK}, \quad (8.15)$$

$$y_{\pm}^{D\pi} = x_{\xi}^{D\pi} y_{\pm}^{DK} + y_{\xi}^{D\pi} x_{\pm}^{DK}. \quad (8.16)$$

Figure 8.3 shows the Cartesian *CP* parameter contours and the  $-2\ln\mathcal{L}$  profile of the interpretation for  $\gamma$ . Table 8.6 shows a comparison between the values of the *CP* parameters and recursive population fractions obtained in the original analysis and those using the double Dalitz fitter. The parameters  $r_B^{D\pi}$ ,  $\delta_B^{D\pi}$  are not extracted as this would require additional modifications to the fitter beyond the scope of this check.

Again the agreement between the original analysis and the double Dalitz fitter is incredibly good which gives further confidence that the fitter is correctly configured and can reproduce previous results with a high level of agreement.

Bin $i$	LL		DD	
	$N_i^+$	$N_i^-$	$N_i^+$	$N_i^-$
-8	$2056 \pm 46$	$735 \pm 28$	$5139 \pm 73$	$1603 \pm 42$
-7	$1760 \pm 43$	$3914 \pm 64$	$3968 \pm 65$	$9028 \pm 98$
-6	$121 \pm 11$	$1867 \pm 44$	$231 \pm 16$	$3932 \pm 63$
-5	$823 \pm 29$	$1392 \pm 38$	$1583 \pm 41$	$2833 \pm 55$
-4	$1667 \pm 42$	$2909 \pm 55$	$3819 \pm 64$	$6553 \pm 83$
-3	$134 \pm 12$	$4904 \pm 71$	$274 \pm 18$	$11104 \pm 107$
-2	$148 \pm 13$	$4695 \pm 69$	$376 \pm 21$	$10461 \pm 104$
-1	$655 \pm 26$	$2958 \pm 55$	$1384 \pm 39$	$6714 \pm 84$
1	$2859 \pm 54$	$658 \pm 26$	$6722 \pm 84$	$1402 \pm 39$
2	$4629 \pm 69$	$154 \pm 13$	$10653 \pm 104$	$323 \pm 19$
3	$4841 \pm 70$	$129 \pm 12$	$11146 \pm 107$	$245 \pm 17$
4	$2884 \pm 55$	$1675 \pm 42$	$6599 \pm 83$	$3893 \pm 64$
5	$1416 \pm 38$	$818 \pm 29$	$2988 \pm 56$	$1546 \pm 41$
6	$1924 \pm 44$	$126 \pm 12$	$3892 \pm 63$	$207 \pm 15$
7	$3868 \pm 63$	$1673 \pm 42$	$9373 \pm 99$	$3938 \pm 65$
8	$741 \pm 28$	$2004 \pm 45$	$1730 \pm 43$	$4885 \pm 71$

Table 8.4: Binned signal populations observed in the  $B^+ \rightarrow Dh^+$  analysis for  $B^+ \rightarrow D\pi^+$ ,  $D \rightarrow K_S^0\pi^+\pi^-$  decays. From Ref. [56].

Bin $i$	LL		DD	
	$N_i^+$	$N_i^-$	$N_i^+$	$N_i^-$
-2	$1298 \pm 37$	$888 \pm 31$	$2674 \pm 53$	$2005 \pm 46$
-1	$1358 \pm 38$	$971 \pm 32$	$2987 \pm 57$	$2284 \pm 50$
1	$1051 \pm 34$	$1304 \pm 37$	$2265 \pm 50$	$2853 \pm 55$
2	$990 \pm 32$	$1250 \pm 36$	$1959 \pm 46$	$2677 \pm 53$

Table 8.5: Binned signal populations observed in the  $B^+ \rightarrow Dh^+$  analysis for  $B^+ \rightarrow D\pi^+$ ,  $D \rightarrow K_S^0\pi^+\pi^-$  decays. From Ref. [56].

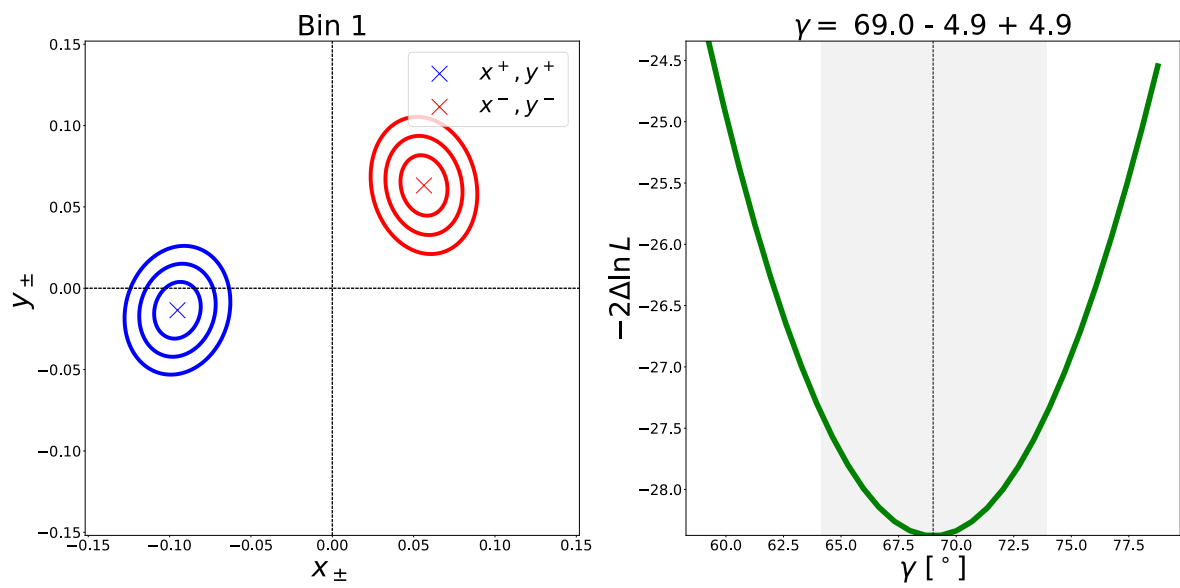


Figure 8.3: Cartesian  $CP$  parameters (left) and  $-2\ln\mathcal{L}$  profile for  $\gamma$  (right) extracted from the  $CP$  parameters in the  $B^+ \rightarrow Dh^+$  validation with both the  $B^+ \rightarrow DK^+$  and  $B^+ \rightarrow D\pi^+$  data. For simplicity this only shows the  $CP$  parameters for the  $B^+ \rightarrow DK^+$  decay, the corresponding parameters for the  $B^+ \rightarrow D\pi^+$  decay are omitted although Table 8.6 shows that the double Dalitz fitter reproduces the nominal  $B^+ \rightarrow Dh^+$  result very closely.

Parameter	$B^+ \rightarrow Dh^+$ Measurement	Validation Result
$x_+^{DK}$	$(-9.3 \pm 1.0) \times 10^{-2}$	$(-9.5 \pm 0.9) \times 10^{-2}$
$y_+^{DK}$	$(-1.3 \pm 1.3) \times 10^{-2}$	$(-1.4 \pm 1.2) \times 10^{-2}$
$x_-^{DK}$	$(5.7 \pm 1.0) \times 10^{-2}$	$(5.6 \pm 1.0) \times 10^{-2}$
$y_-^{DK}$	$(6.6 \pm 1.0) \times 10^{-2}$	$(6.3 \pm 1.2) \times 10^{-2}$
$x_\xi^{D\pi}$	$(-5.5 \pm 2.0) \times 10^{-2}$	$(-5.4 \pm 2.0) \times 10^{-2}$
$y_\xi^{D\pi}$	$(0.7 \pm 2.3) \times 10^{-2}$	$(0.7 \pm 2.3) \times 10^{-2}$
$R_{-8} (D \rightarrow K_S^0 \pi^+ \pi^- \text{ LL})$	$0.0243 \pm 0.0007$	$0.0242 \pm 0.0006$
$R_{-7}$	$0.1304 \pm 0.0014$	$0.1304 \pm 0.0014$
$R_{-6}$	$0.0734 \pm 0.0012$	$0.0733 \pm 0.0011$
$R_{-5}$	$0.0584 \pm 0.0011$	$0.0584 \pm 0.0011$
$R_{-4}$	$0.1281 \pm 0.0017$	$0.1282 \pm 0.0016$
$R_{-3}$	$0.2472 \pm 0.0024$	$0.2473 \pm 0.0021$
$R_{-2}$	$0.3147 \pm 0.0033$	$0.3148 \pm 0.0027$
$R_{-1}$	$0.2851 \pm 0.0033$	$0.2852 \pm 0.0031$
$R_1$	$0.0906 \pm 0.0024$	$0.0907 \pm 0.0024$
$R_2$	$0.0224 \pm 0.0015$	$0.0222 \pm 0.0013$
$R_3$	$0.0204 \pm 0.0013$	$0.0205 \pm 0.0013$
$R_4$	$0.2638 \pm 0.0039$	$0.264 \pm 0.004$
$R_5$	$0.1752 \pm 0.0039$	$0.175 \pm 0.004$
$R_6$	$0.0316 \pm 0.0021$	$0.0314 \pm 0.0020$
$R_7$	$0.4541 \pm 0.0062$	$0.454 \pm 0.006$
$R_{-8} (D \rightarrow K_S^0 \pi^+ \pi^- \text{ DD})$	$0.0240 \pm 0.0004$	$0.0240 \pm 0.0004$
$R_{-7}$	$0.1362 \pm 0.0009$	$0.1362 \pm 0.0009$
$R_{-6}$	$0.0670 \pm 0.0008$	$0.0670 \pm 0.0007$
$R_{-5}$	$0.0537 \pm 0.0007$	$0.0536 \pm 0.0007$
$R_{-4}$	$0.1276 \pm 0.0011$	$0.1277 \pm 0.0010$
$R_{-3}$	$0.2470 \pm 0.0016$	$0.2470 \pm 0.0014$
$R_{-2}$	$0.3126 \pm 0.0021$	$0.3125 \pm 0.0018$
$R_{-1}$	$0.2879 \pm 0.0022$	$0.2880 \pm 0.0021$
$R_1$	$0.0842 \pm 0.0016$	$0.0842 \pm 0.0016$
$R_2$	$0.0229 \pm 0.0010$	$0.0229 \pm 0.0009$
$R_3$	$0.0179 \pm 0.0009$	$0.0178 \pm 0.0008$
$R_4$	$0.2649 \pm 0.0026$	$0.2649 \pm 0.0026$
$R_5$	$0.1452 \pm 0.0024$	$0.1453 \pm 0.0024$
$R_6$	$0.0238 \pm 0.0012$	$0.0237 \pm 0.0012$
$R_7$	$0.4402 \pm 0.0040$	$0.440 \pm 0.004$
$R_{-2} (D \rightarrow K_S^0 K^+ K^- \text{ LL})$	$0.2068 \pm 0.0044$	$0.207 \pm 0.004$
$R_{-1}$	$0.2800 \pm 0.0054$	$0.280 \pm 0.005$
$R_1$	$0.5076 \pm 0.0070$	$0.508 \pm 0.007$
$R_{-2} (D \rightarrow K_S^0 K^+ K^- \text{ DD})$	$0.2024 \pm 0.0029$	$0.2023 \pm 0.0029$
$R_{-1}$	$0.2885 \pm 0.0038$	$0.289 \pm 0.004$
$R_1$	$0.5218 \pm 0.0048$	$0.522 \pm 0.005$
$\gamma[^\circ]$	$68.7_{-5.1}^{+5.2}$	$69.0 \pm 4.9$
$r_B$	$0.0904_{-0.0075}^{+0.0077}$	$0.0909 \pm 0.0072$
$\delta_B^{DK}[^\circ]$	$118.3_{-5.6}^{+5.5}$	$118.5 \pm 5.2$

Table 8.6: Comparison between the  $B^+ \rightarrow Dh^+$  analysis values of parameters of interest [56] and the values obtained by the double Dalitz fitter. Only statistical uncertainties are shown for the CP parameters to allow comparison, the other parameters only have total uncertainties quoted so it is expected that the uncertainties obtained should be slightly smaller since systematics are not accounted for here.

### 8.1.5 Fit configuration

The fit configuration is as follows:

- As explained in Section 4.2.2 each decay mode has a single normalisation parameter,  $h_D$ , to allow for sensitivity to the total per- $B$ -flavour asymmetries. The  $D \rightarrow K_S^0 h^+ h^-$  modes however have per- $B$ -flavour normalisation parameters,  $h_D^\pm$ , to avoid bias from  $K_S^0$  material interaction effects [63].
- All parameters with externally measured values are fixed to the values in Table 4.2 all other parameters float.
- The Cartesian parameters are defined as in Eq. (4.36).
- The fraction of each background expected in each bin is fixed to that predicted by the background modelling in Chapter 6
- The yield of each background is fixed to the global mass fit yield value obtained in Chapter 7.
- The population fraction parameters in the  $B$  plane,  $\langle \bar{\kappa} \rangle_\alpha$ , are constrained such that they sum to unity.

It has been found in pseudo-experiment studies that when fitting with a large number of parameters floating, if their start values are not close to the true values the fitter is unable to converge on the minimum. To mitigate this a guided fit is used to try guide the fitter towards a valid minimum. This is done by performing several fits with different parameters fixed/floating:

1. Fix all parameters to their starting values and float only the population fraction parameters of the  $B$  Dalitz plane.
2. Fix the population fraction parameters of the  $B$  Dalitz plane and float  $x_\alpha^\pm, y_\alpha^\pm$ .
3. Float all parameters besides the fixed external parameters.

### 8.1.6 Data CP fit results

Figure 8.4 shows the Cartesian parameters obtained in the fit and their  $1 - 3\sigma$  contours. This illustrates that most of the sensitivity to  $CP$  violation originates from bins 1 and 2 of the  $B$  Dalitz plane as the  $CP$  violation observables are less compatible with the origin than in bins 3 and 4. Figures 8.5 to 8.9 show a comparison between the data and the fitted expectation for each decay mode. Uncertainties are shown for the populations in



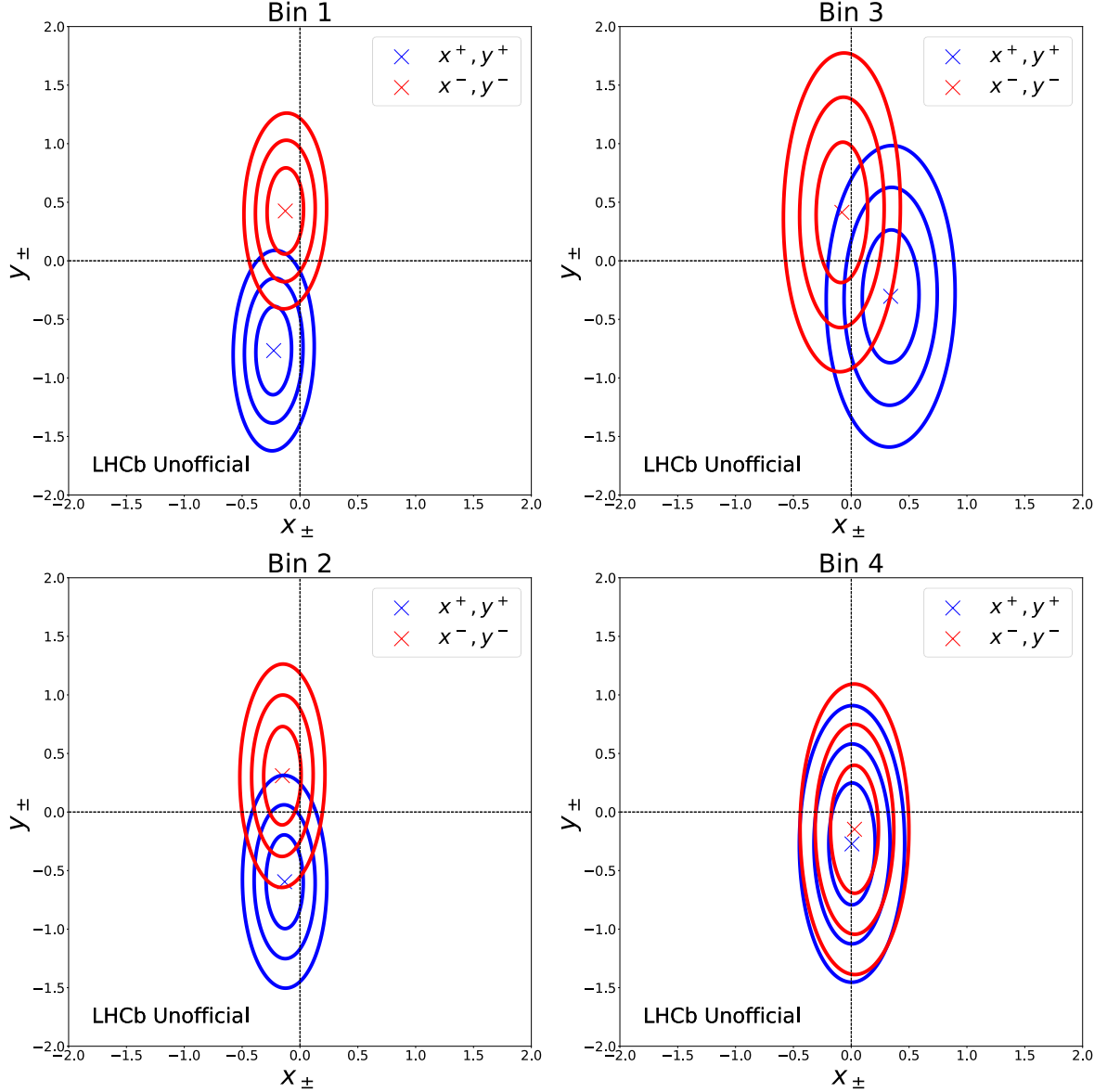


Figure 8.4: Cartesian parameters obtained in the *CP* fit and their  $1 - 3\sigma$  contours. For simplicity of calculation the contours are plotted using a multivariate Gaussian distribution constructed from the covariance matrix of the Cartesian parameters for the given bin *i.e.* the contours do not account for correlations between the *B* Dalitz bins.

data, however for some modes they are miniscule due to being Poisson uncertainties of large populations. It is noted that some bins show a significant departure between the data and fitted expectation, however these are few of the many observables and typically occur in bin 3 or 4 of the *B* Dalitz plane from which very little of the sensitivity to *CP* violation originates. The overall fit quality is represented by the  $\chi^2$  per degrees of freedom for the nominal fit to data which is 1.22 (3 SF). Table 8.7 shows the central values of all free parameters in the fit and their uncertainties. The corresponding correlation matrix can be found in Appendix B.

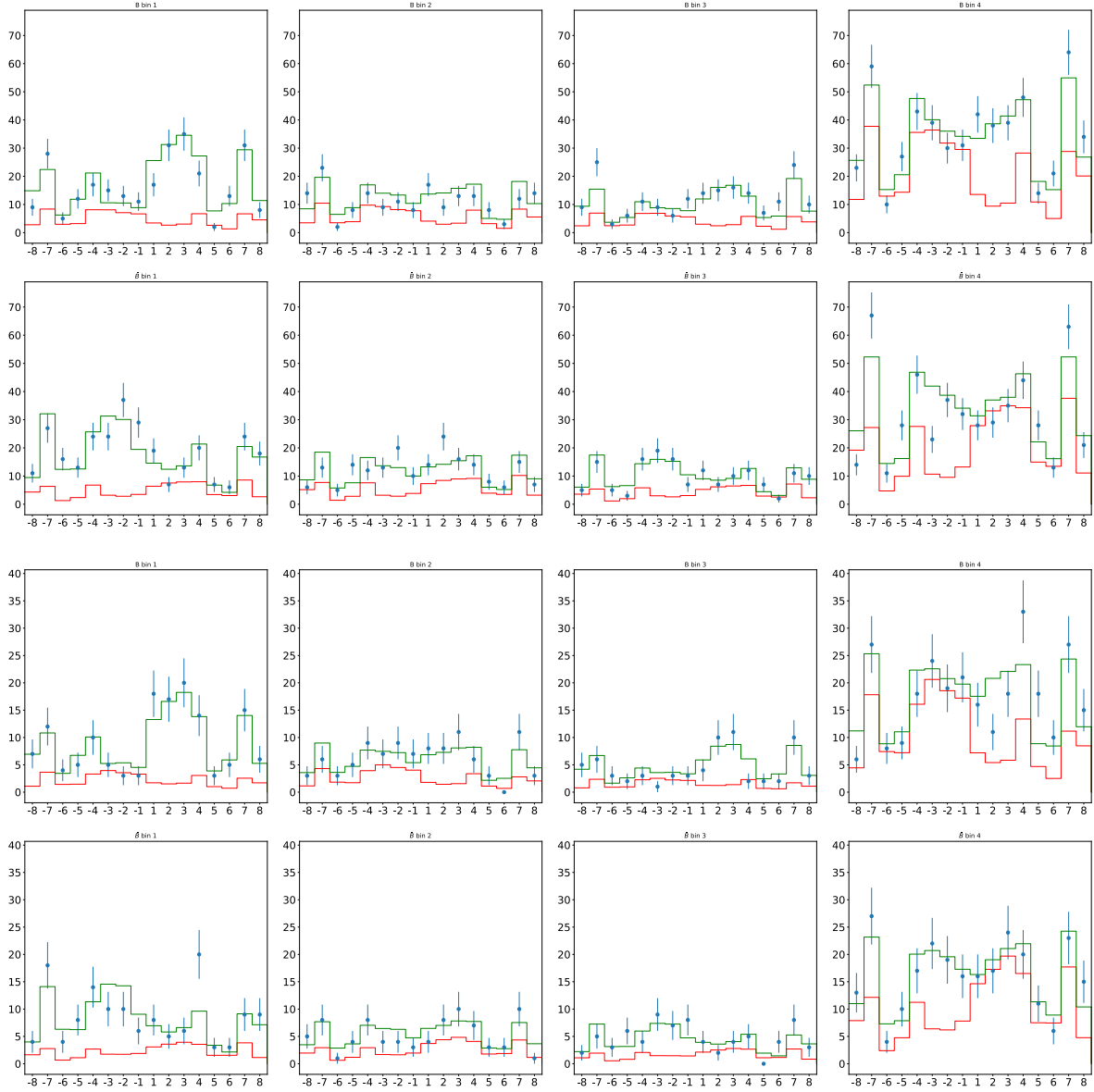


Figure 8.5: Comparison between the data (blue) and fitted expectation (green) for  $D \rightarrow K_S^0 \pi^+ \pi^-$  DD (top),  $D \rightarrow K_S^0 \pi^+ \pi^-$  LL (bottom). The fixed background expectation is shown in red, and the total fitted expectation is shown in green.

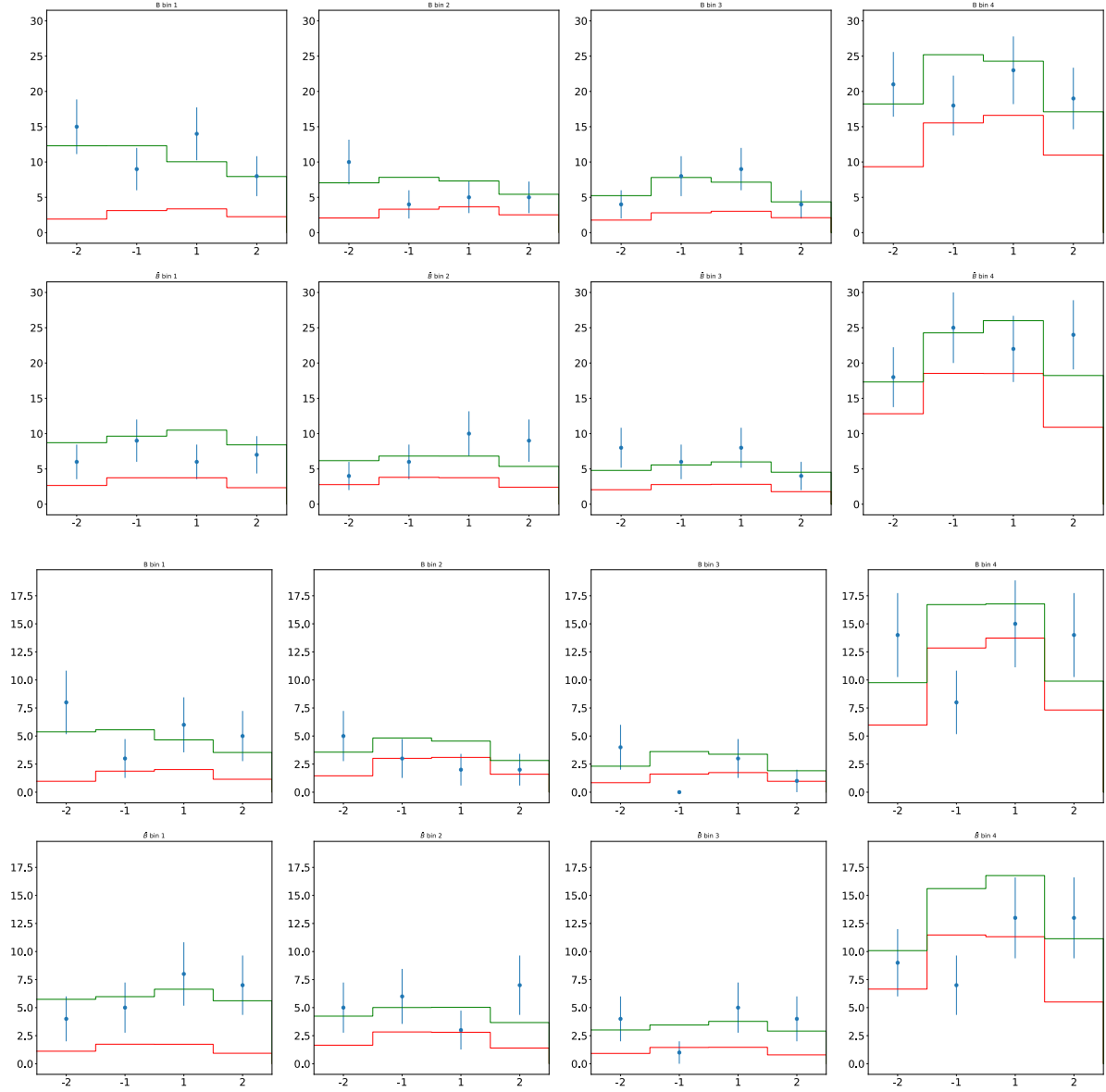


Figure 8.6: Comparison between the data (blue) and fitted expectation (green) for  $D \rightarrow K_S^0 K^+ K^-$  DD (top) and  $D \rightarrow K_S^0 K^+ K^-$  LL (bottom). The fixed background expectation is shown in red, and the total fitted expectation is shown in green.

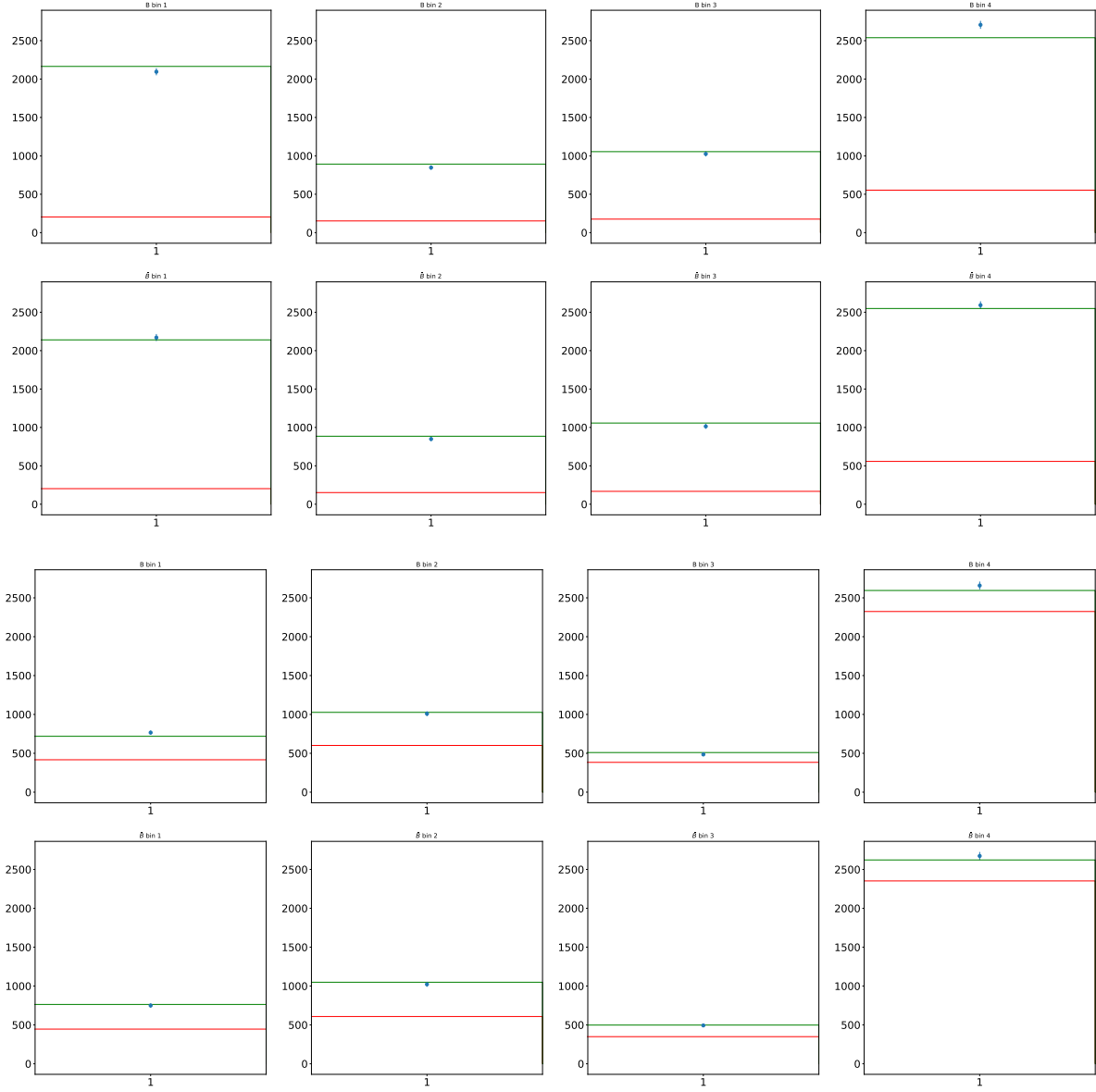


Figure 8.7: Comparison between the data (blue) and fitted expectation (green) for  $D \rightarrow K^\pm \pi^\mp$  (top),  $D \rightarrow \pi^\pm K^\mp$  (bottom). The fixed background expectation is shown in red, and the total fitted expectation is shown in green.

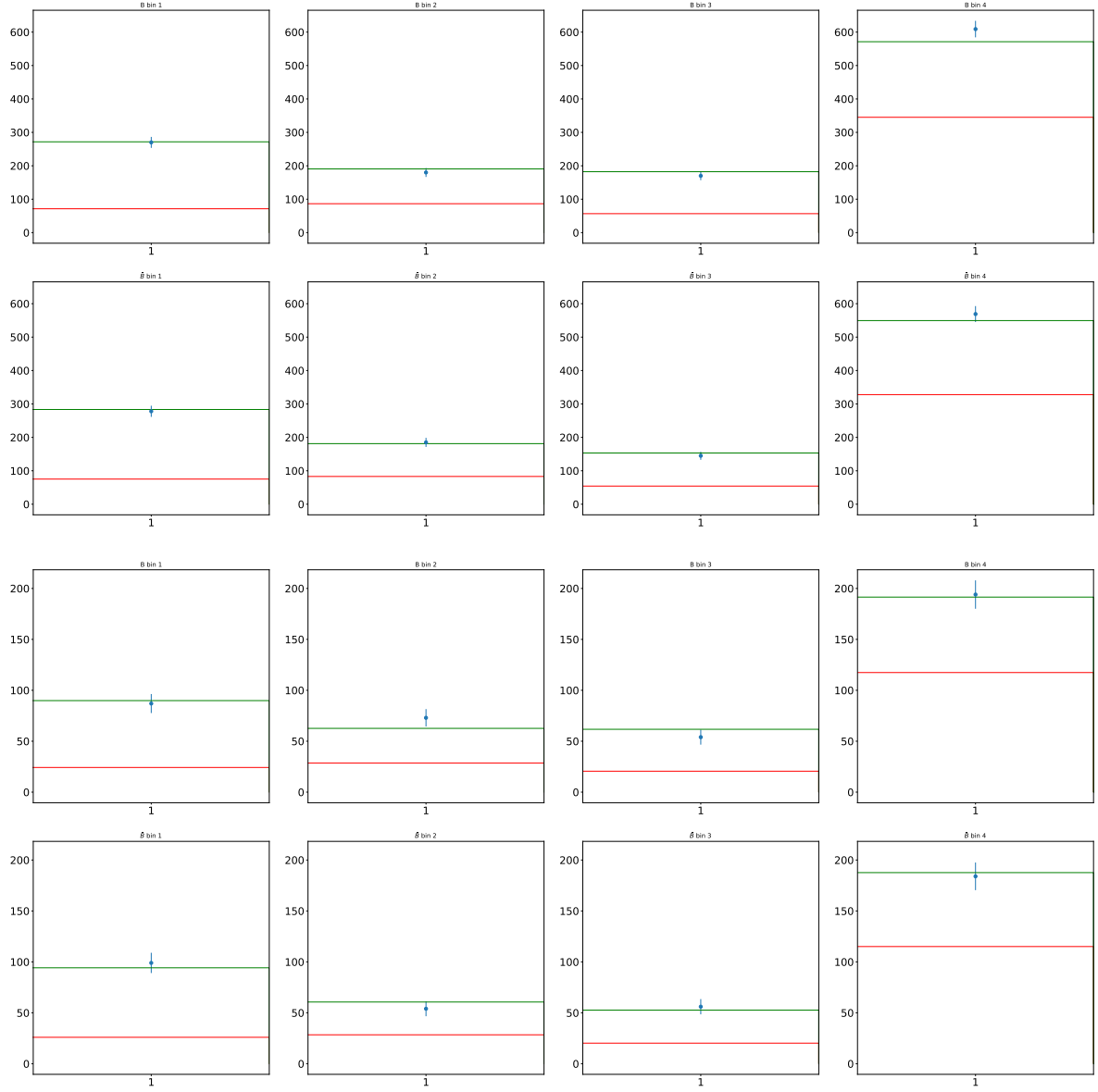


Figure 8.8: Comparison between the data (blue) and fitted expectation (green) for  $D \rightarrow K^+K^-$  (top) and  $D \rightarrow \pi^+\pi^-$  (bottom). The fixed background expectation is shown in red, and the total fitted expectation is shown in green.

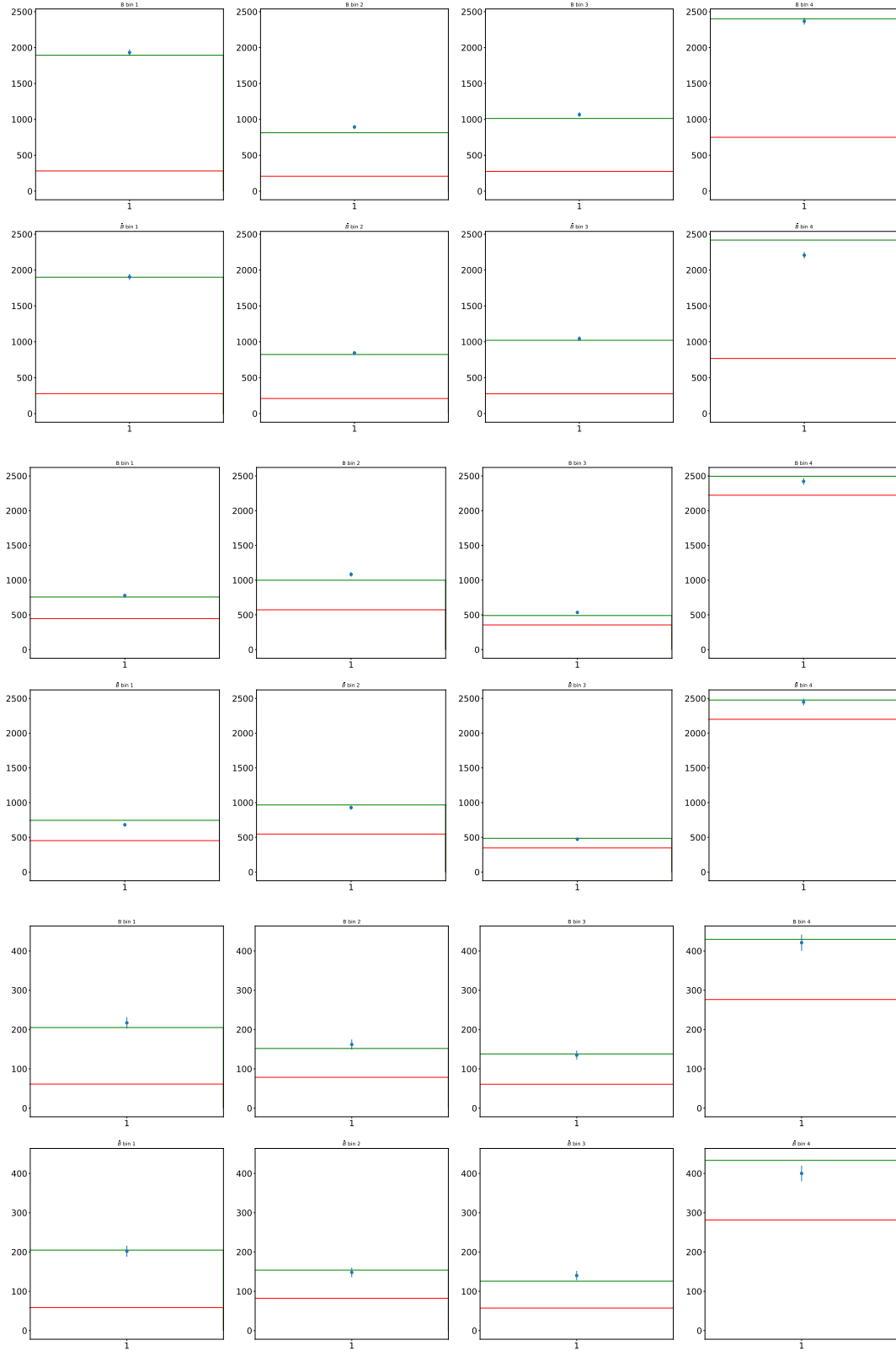


Figure 8.9: Comparison between the data (blue) and fitted expectation (green) for  $D \rightarrow K^\pm \pi^\mp \pi^+ \pi^-$  (top),  $D \rightarrow \pi^\pm K^\mp \pi^+ \pi^-$  (middle) and  $D \rightarrow \pi^+ \pi^- \pi^+ \pi^-$  (bottom). The fixed background expectation is shown in red, and the total fitted expectation is shown in green.

Parameter	Value $\pm$ Uncertainty
$x_1^+$	$-0.11 \pm 0.10$
$y_1^+$	$-0.78 \pm 0.24$
$x_1^-$	$-0.06 \pm 0.10$
$y_1^-$	$0.44 \pm 0.24$
$x_2^+$	$-0.06 \pm 0.10$
$y_2^+$	$-0.60 \pm 0.26$
$x_2^-$	$-0.11 \pm 0.10$
$y_2^-$	$0.30 \pm 0.27$
$x_3^+$	$0.38 \pm 0.16$
$y_3^+$	$-0.24 \pm 0.37$
$x_3^-$	$-0.02 \pm 0.14$
$y_3^-$	$0.42 \pm 0.39$
$x_4^+$	$0.05 \pm 0.13$
$y_4^+$	$-0.27 \pm 0.34$
$x_4^-$	$0.01 \pm 0.14$
$y_4^-$	$-0.15 \pm 0.36$
$h_{D \rightarrow K_S^0 \pi^+ \pi^-, DD}^+$	$622 \pm 32$
$h_{D \rightarrow K_S^0 \pi^+ \pi^-, LL}^+$	$328 \pm 22$
$h_{D \rightarrow K_S^0 K^+ K^-, DD}^+$	$102 \pm 13$
$h_{D \rightarrow K_S^0 K^+ K^-, LL}^+$	$38 \pm 9$
$h_{D \rightarrow K_S^0 \pi^+ \pi^-, DD}^-$	$615 \pm 32$
$h_{D \rightarrow K_S^0 \pi^+ \pi^-, LL}^-$	$283 \pm 22$
$h_{D \rightarrow K_S^0 K^+ K^-, DD}^-$	$82 \pm 12$
$h_{D \rightarrow K_S^0 K^+ K^-, LL}^-$	$55 \pm 9$
$h_{D \rightarrow K^\pm \pi^\mp}$	$11119 \pm 115$
$h_{D \rightarrow \pi^\pm K^\mp}$	$2293 \pm 93$
$h_{D \rightarrow K^+ K^-}$	$1283 \pm 48$
$h_{D \rightarrow \pi^+ \pi^-}$	$421 \pm 27$
$h_{D \rightarrow \pi^+ \pi^- \pi^+ \pi^-}$	$885 \pm 41$
$h_{D \rightarrow K^\pm \pi^\mp \pi^+ \pi^-}$	$9240 \pm 110$
$h_{D \rightarrow \pi^\pm K^\mp \pi^+ \pi^-}$	$2276 \pm 89$
$\kappa_1$	$0.0410 \pm 0.0060$
$\bar{\kappa}_1$	$0.2947 \pm 0.0079$
$\kappa_2$	$0.0592 \pm 0.0079$
$\bar{\kappa}_2$	$0.1110 \pm 0.0038$
$\kappa_3$	$0.0197 \pm 0.0030$
$\bar{\kappa}_3$	$0.1356 \pm 0.0041$
$\kappa_4$	$0.0374 \pm 0.0061$
$\bar{\kappa}_4$	$0.3015 \pm 0.0081$

Table 8.7: Central values and uncertainties determined for all floating parameters in the *CP* fit. The  $\chi^2$  per degrees of freedom for the nominal fit to data is 1.22 (3 SF).

### 8.1.7 Pseudo-experiment studies

The *CP* fitter was developed to generate ensembles of pseudo-experiments to test that it provides robust and consistent results when fitting pseudo-experiments based on the result from the fit to data.

#### Generation

A pseudo-experiment is generated by calculating the total population expectation of each bin according Eq. (4.48) and then fluctuating each population according to its corresponding Poisson distribution. If any parameters are constrained to external measurements they are fluctuated within their constraint distribution prior to calculating the expectation [109].

This method of pseudo-experiment generation is often referred to as a parametric bootstrapping based on the data fit result. The model values used are the values each parameter is fitted to in the corresponding data fit. The pseudo-experiments generated in this way and their *CP* fit results are discussed in Section 8.1.7 and their interpretation results are discussed in Section 8.2.1.

#### Pseudo-experiment pull studies

An ensemble of 1000 pseudo-experiments is generated and fitted to estimate any biases inherent in the fit. A fit result is only included in the pull distribution if it has converged to a valid minimum with a positive-definite covariance matrix. The distribution of pulls,  $(x - \hat{x})/\sigma_x$ , where  $\sigma_x$  is the uncertainty of the parameter, should be a unit Gaussian if the fit is unbiased and the uncertainty estimate has proper coverage. A deviation from a unit Gaussian implies that the fitter is biased, so either the source of bias must be determined and mitigated, or one can adjust the output of the fitter to account for this known bias when fitting the real data.

The pseudo-experiment study results for the nominal fit configuration are summarised below. The pull distributions for each fitted parameter when generating ensembles from the nominal fit configuration are summarised in Figure 8.10. These pseudo-experiments are generated based on the central values obtained for each parameter in the fit to data. This shows that the fit is statistically well behaved, with negligible bias and robust coverage, as all fitted parameters have pull means (widths) consistent with zero (unity). Consequently, all central values and uncertainties presented for parameters determined directly by the *CP* fit come directly from the fitter itself.



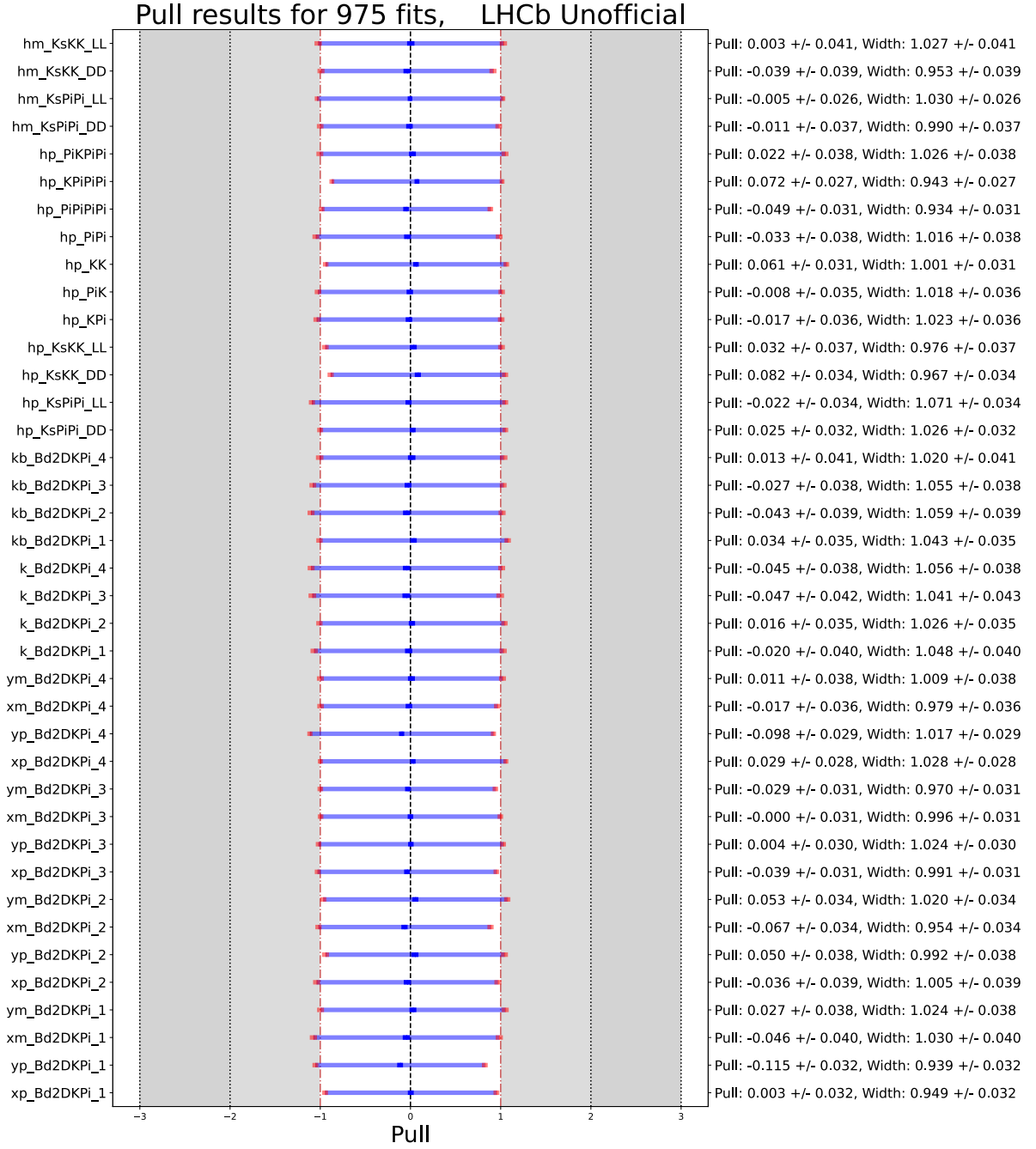


Figure 8.10: Pull results for the double Dalitz fit using pseudo-experiments generated with parameter values determined by the fit to data. Solid blue is the mean and its uncertainty of the pull distribution, translucent blue is the width of the pull distribution and red shows its uncertainty.

## 8.2 Interpretation results

### 8.2.1 Pseudo-experiment studies

Figure 8.11 shows the pull results obtained from the interpretation of the same pseudo-experiments presented in Fig. 8.10. Deviations from zero are visible for the coherence factors in bins 3 and 4, and deviations from widths of one are seen, most significantly for  $\gamma$ . This is due to the known coverage issue [110] on  $\gamma$  when the value of  $r_\alpha$  or  $T_\alpha$  is close to 0. It is known that the Cartesian parameters, shown in Fig. 8.4, are statistically well behaved. However extracting  $\gamma$  from these (which is half the opening angle between the two Cartesian points) is problematic when the circles are close to or consistent with the origin. It can be seen in Fig. 8.4 that the sensitivity to  $\gamma$  is incredibly low in bin 4, where the circles are both close to the origin. Bin 3 exhibits similar, albeit not as severe, behaviour. This causes the inconsistency in the interpretation pulls in Fig. 8.11. Fortunately the pseudo-experiment ensemble itself can be used to extract the statistical uncertainty for each parameter. The bias in the coherence parameters is yet to be resolved however there remains a couple methods that may help. Fits will become unstable as the parameter value approaches zero which, when  $T_\alpha$  is allowed to obtain negative values, results in two distinct toy distributions above and below zero. Negative values of  $T_\alpha$  are unphysical, they also correspond to a shift of  $\pi/2$  in their corresponding  $\Delta\delta_\alpha$  so one method to resolve this could be to perform the following transformations for any toys where  $T_\alpha$  is negative,

$$T_\alpha \mapsto -T_\alpha \quad (8.17)$$

$$\Delta\delta_\alpha \mapsto \Delta\delta_\alpha - \pi. \quad (8.18)$$

Alternatively the allowed limits for  $T_\alpha$  in the fit could be restricted only to the physically allowed region,  $T_\alpha > 0$ , and the uncertainty determined using the Feldman-Cousins method [111].

### 8.2.2 Data $CP$ fit interpretation results (currently blinded)

Table 8.8 shows the values of  $(\gamma, T_\alpha, \Delta\delta_\alpha)$  obtained from the bootstrapped interpretation of the  $CP$  fit to data. The most notable result being,  $\gamma = (68.6 \pm 6.8)^\circ$ , where  $\gamma$  is blinded and the uncertainty is statistical only. Blinding is achieved by adding  $b^\circ$  to  $\gamma$  immediately after extraction, where  $b^\circ$  is a fixed value determined from a seeded random sampling of a Gaussian of width  $6^\circ$ . In addition Table 8.8 provides  $r_\alpha$  values in each bin derived from the ratio of  $\bar{\kappa}_\alpha$ ,  $\kappa_\alpha$  values found in Section 8.1.6, with their uncertainty and correlation propagated.

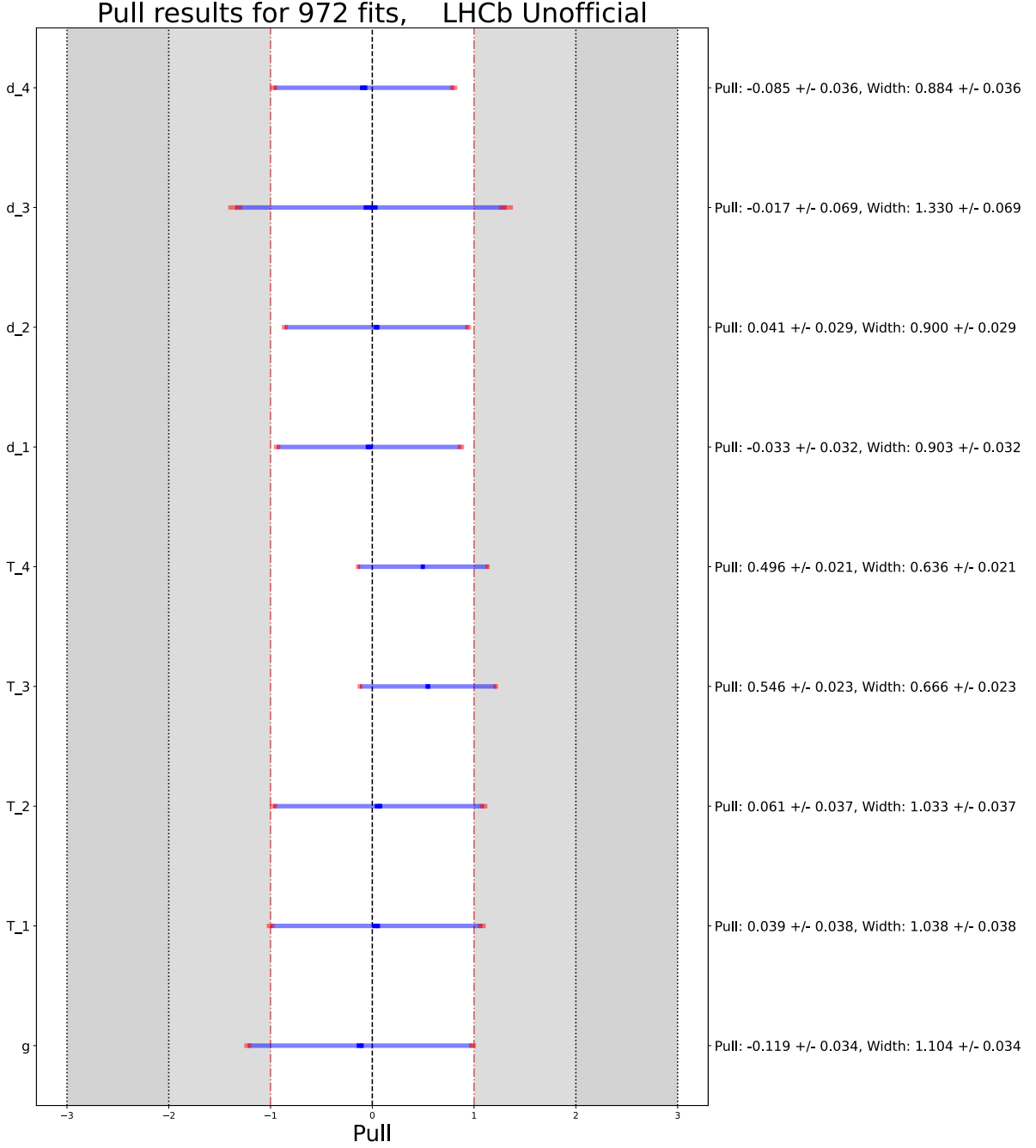


Figure 8.11: Pull results following the interpretation to extract  $\gamma$  for the double Dalitz fit using pseudo-experiments generated with parameter values determined by the fit to data. Solid blue is the mean and its uncertainty of the pull distribution, translucent blue is the width of the pull distribution and red shows its uncertainty.

### 8.2.3 Sensitivity to $\gamma$

Since the full systematics of the double Dalitz analysis are yet to be computed and the analysis is still blinded with respect to the value of  $\gamma$ , one can only interpret the meaning of its statistical uncertainty.

Parameter	Value $\pm$ Uncertainty
$\gamma[^\circ]$	$68.8 \pm 6.8$
$\delta_1[^\circ]$	$178.6 \pm 4.9$
$\delta_2[^\circ]$	$183.0 \pm 6.9$
$\delta_3[^\circ]$	$248 \pm 60$
$\delta_4[^\circ]$	$186 \pm 60$
$T_1$	$0.61 \pm 0.18$
$T_2$	$0.50 \pm 0.17$
$T_3$	$0.27 \pm 0.12$
$T_4$	$0.18 \pm 0.13$
$r_1 = \sqrt{\kappa_1/\bar{\kappa}_1}$	$0.373 \pm 0.028$
$r_2 = \sqrt{\kappa_2/\bar{\kappa}_2}$	$0.730 \pm 0.050$
$r_3 = \sqrt{\kappa_3/\bar{\kappa}_3}$	$0.381 \pm 0.029$
$r_4 = \sqrt{\kappa_4/\bar{\kappa}_4}$	$0.352 \pm 0.029$

Table 8.8: Central values and uncertainties determined for all floating parameters in the interpretation of the  $CP$  fit result.  $\gamma$  is blinded by shifting the central value by a random amount.

The statistical uncertainty on  $\gamma$  from this first ever double Dalitz analysis of  $B^0 \rightarrow DK^+\pi^-$  decays is  $6.8^\circ$ . The uncertainty obtained from a combination of the results of the  $B^0 \rightarrow DK^{*0}$ ,  $D \rightarrow h^+h^-$  &  $D \rightarrow h^+h^-h^+h^-$  and the  $B^0 \rightarrow DK^{*0}$ ,  $D \rightarrow K_S^0 h^+h^-$  analyses results in a value of  $\gamma = (63.3 \pm 7.2)^\circ$  where the uncertainty includes both the statistical and systematic uncertainties [18,19]. Certainly once the systematic uncertainties are fully calculated and taken into account the uncertainty on  $\gamma$  from the double Dalitz analysis will most likely be greater than  $7.2^\circ$ . This may seem surprising since this analysis utilises a larger dataset and additional resonant effects that should result in greater sensitivity to  $CP$  violation effects. However, as explained in Section 4.4, the statistical sensitivity to  $\gamma$  depends on the binning definition of the Dalitz planes and as is briefly mentioned in Section 4.2 the  $B^0 \rightarrow DK^+\pi^-$  Dalitz binning used in this analysis is not believed to be optimal. In Ref. [73] the  $B^0 \rightarrow DK^+\pi^-$  Dalitz binning was optimised by maximising the binning quality factor of Eq. (4.47) and assuming that the data consists of pure signal. Although it is possible that such a method can result in a binning that is close to optimal even in the presence of backgrounds, it does not guarantee it as clearly illustrated by the inability to fit the data without merging bins four and five of the binning scheme. Figure 10.7 shows the distribution of the uncertainty on  $\gamma$  in an ensemble of pseudo-experiments based on the  $B^0 \rightarrow DK^+\pi^-$  model of Ref. [73] with no background decays present and the distribution with the same model but with the background description in the nominal fit to data of this analysis present. This shows that the sensitivity to  $\gamma$  is significantly decreased due to the presence of these backgrounds. In future analyses, to optimise the sensitivity to  $\gamma$ , it will be beneficial to find additional methods of background suppression and to optimise the binning with the distribution of

the remaining background decays accounted for.

Table 8.9 shows the values of  $\bar{\kappa}_\alpha$ ,  $r_\alpha$ , and  $T_\alpha$  predicted by the model Ref. [73] and measured in this analysis. There is clearly some discrepancy between the model expectation and the measured parameters. These are key observables as the per-bin sensitivity to  $CP$  violation is proportional to combinations of these parameters, *i.e.* the per-bin magnitude of the interference term in the signal expectation and population share. Figure 10.7 shows the distribution of the uncertainty on  $\gamma$  in an ensemble of pseudo-experiments based on the  $B^0 \rightarrow DK^+\pi^-$  model and the distribution corresponding to the result of the fit to data, where both use the background description in the nominal fit to data of this analysis. The model ensemble is generated with the original five bin  $B$  Dalitz binning to represent the model in the original version of the analysis in Ref. [73]. This shows that due to the slight difference in hadronic parameter values, once the effect of backgrounds is included, this analysis has obtained sensitivity to  $\gamma$  slightly better than expected based on the model.

Parameter	Model Value	Value $\pm$ Uncertainty
$\bar{\kappa}_1$	0.3105	$0.2947 \pm 0.0079$
$\bar{\kappa}_2$	0.1188	$0.1110 \pm 0.0038$
$\bar{\kappa}_3$	0.1683	$0.1356 \pm 0.0041$
$\bar{\kappa}_4$	0.3458	$0.3015 \pm 0.0081$
$r_1$	0.218	$0.373 \pm 0.028$
$r_2$	0.508	$0.730 \pm 0.050$
$r_3$	0.138	$0.381 \pm 0.029$
$r_4$	0.348	$0.352 \pm 0.029$
$T_1$	0.84	$0.61 \pm 0.18$
$T_2$	0.80	$0.50 \pm 0.17$
$T_3$	0.69	$0.27 \pm 0.12$
$T_4$	0.25	$0.18 \pm 0.13$

Table 8.9: Model values and experimentally determined values of the  $\bar{\kappa}_\alpha$ ,  $r_\alpha$  and  $T_\alpha$  hadronic parameters.

### 8.3 Summary

This chapter explains how all of the results of Chapters 5 to 7 are brought together to extract  $\gamma$  from the LHCb data. The choice of parameterisation of the Dalitz bin population expectation equations is justified with greater detail than in Section 4.2.3 and it is explained how ambiguities inherent to these equations are removed. Studies performed to validate the fit setup by reproducing previous LHCb measurements are presented, followed by an explanation of the double Dalitz fit parameterisation. The results of this fit are then presented, followed by pseudo-experiment studies to verify the

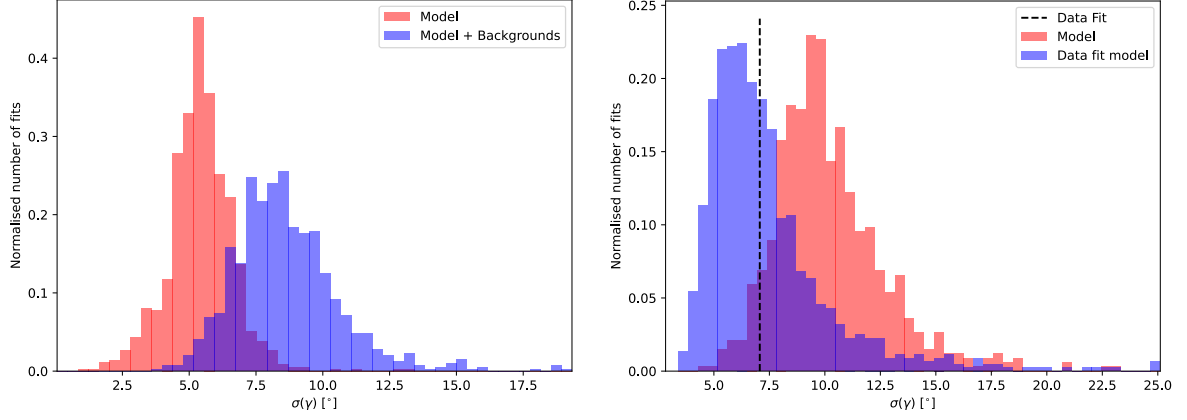


Figure 8.12: Left: Distribution of the uncertainty on  $\gamma$  in fits to pseudodata generated based on the  $B^0 \rightarrow DK^+\pi^-$  model of Ref. [73] with no background decays present (red) and with the background decays observed in this analysis present (blue). Both ensembles are generated using the 5 bin Dalitz binning from Ref. [73]. Right: Distribution of the uncertainty on  $\gamma$  in fits to pseudodata generated based on the  $B^0 \rightarrow DK^+\pi^-$  model of Ref. [73] with the background decays observed in this analysis present (red) and the distribution corresponding to pseudodata generated based on the result of the  $CP$  fit to data with background decays present (blue).

stability of the result and identify biases. Finally the statistical sensitivity to  $\gamma$  obtained in this analysis is discussed and compared with the expectation based on the  $B^0 \rightarrow DK^+\pi^-$  model. The only remaining step of this analysis is to evaluate the systematic uncertainties, this is explained in Chapter 9.



## 9 Systematic uncertainties

*“If we took maths out of the equation it would be much easier.  
Couldn’t we use something else instead of numbers?”*

---

Philomena Cunk

At the time of writing, the systematic uncertainties of this analysis are yet to be fully computed. Section 9.1 summarises the sources of systematic uncertainty, those discussed in Sections 9.1.4 to 9.1.11 have not had their associated uncertainty calculated yet. Section 9.2 presents the results of those calculated thus far only in terms of the uncertainty on  $x_{\alpha}^{\pm}$ ,  $y_{\alpha}^{\pm}$  parameters. The determination of the systematic uncertainties is a joint effort between myself and my supervisor but has been put to the side while I finish this thesis.

The main types of systematic uncertainties under consideration, in decreasing order of the expected size of their contribution, are those originating from

- Background modelling and pollution
- Use of external inputs for  $CP$  fit parameters, and their interplay with the selection efficiency where appropriate
- PID corrections
- Invariant mass fit parameterisations
- $CP$  violation in backgrounds
- Bin migration

Background modelling leading the systematics is based on the observation that the  $CP$  fit is very sensitive to the background pollution, assessed by performing fits to ensembles of pseudo-experiments with and without backgrounds included. The rest of this ordering is motivated by the measurements of  $\gamma$  using  $B^0 \rightarrow DK^{*0}$  decays [18, 19].



## 9.1 Systematic methodologies

The systematic uncertainties are determined by obtaining a covariance matrix for the  $x_\alpha^\pm, y_\alpha^\pm$  parameters which is then propagated to the interpretation to determine the systematic uncertainty on  $\gamma$  and the other extracted parameters.

### 9.1.1 External inputs

As explained in Section 4.3 the  $CP$  fit uses a vast number of external input parameters originating from a variety of measurements at the LHCb, CLEO-c and BES III experiments. In the  $CP$  fit these parameters are fixed to the provided central values so the uncertainties on these original measurements are yet to be taken into account. Therefore a systematic uncertainty must be associated with each of these inputs, this is achieved by performing the  $CP$  fit to data where the parameter of interest is fixed to a random value obtained from an appropriate distribution instead of its reported central value. This is repeated a number of times to obtain the covariance matrix for the  $x_\alpha^\pm, y_\alpha^\pm$  parameters according to

$$\text{cov}(x, y) = \frac{1}{N} \sum_i^N (x_i - \bar{x})(y_i - \bar{y}), \quad (9.1)$$

where  $N$  is the number of generated input values and  $x_i, y_i$  are the  $i$ -th values of the fitted parameters  $x$  and  $y$ . For a single input parameter the appropriate distribution from which to obtain the ensemble of input values is simply the Gaussian distribution according to its reported central value and uncertainty. For a group of input parameters, such as the  $c_i$  and  $s_i$  parameters of the  $D \rightarrow K_S^0 h^+ h^-$  decays, the appropriate distribution is the multivariate Gaussian according to the central values and covariance matrix of the parameters.

#### Strong phases in $D \rightarrow K_S^0 h^+ h^-$ decays

For the  $c_i$  and  $s_i$  parameters of the  $D \rightarrow K_S^0 h^+ h^-$  decays the values and covariance matrices are obtained from combinations of CLEO-c and BES-III results [65, 66]. These same values are used as input to the LHCb single Dalitz  $B^+ \rightarrow Dh^+$  analysis [56]. Given that both the single Dalitz  $B^+ \rightarrow Dh^+$  analysis and this analysis can be used as inputs to the LHCb  $\gamma$  combination care must be taken to control any correlations between these analyses, one source is the systematic uncertainties associated with these  $c_i$  and  $s_i$  parameters. Therefore the analyses use a common ensemble of  $c_i, s_i$  values when calculating systematic uncertainties, 1000 sets of  $(c_i, s_i)$  values generated from the multivariate Gaussian defined by their central values and covariance matrix, separately

for  $D \rightarrow K_S^0 K^+ K^-$  and  $D \rightarrow K_S^0 \pi^+ \pi^-$ . This systematic appears in Table 9.1 under the column labelled “ $c_i, s_i$ ”.

### Binned Dalitz distribution in $D \rightarrow K_S^0 h^+ h^-$ decays

The  $R_i$  values used are taken from the LHCb single Dalitz  $B^+ \rightarrow Dh^+$  analysis and are fixed in the  $CP$  fit 56. The systematic is calculated using an ensemble of 1000 sets of  $R_i$  values generated from the multivariate Gaussian defined by their central values and covariance matrix. This systematic appears under the column labelled “ $R_i$ ” in Table 9.1.

### 9.1.2 Efficiency variations across the Dalitz space

The statistical uncertainty on the  $R_i$  input parameters is accounted for as a source of systematic above in Section 9.1.1. The correct values of  $R_i$  that correspond to a given dataset depend on the selection efficiency profile across the  $D$  Dalitz planes, therefore the different selection criteria in the analysis from which the  $R_i$  values originate and the criteria of this analysis could result in a systematic effect. Section 5.3.2 shows that the efficiency profiles of the LHCb single Dalitz  $B^+ \rightarrow Dh^+$  analysis from which the input values originate is broadly compatible with those of this analysis, however any residual differences result in an additional source of systematic uncertainty. To compute the systematic the  $R_i$  values are corrected to those that would have been computed in the  $B^+ \rightarrow Dh^+$  analyses had the efficiency profile been the same as in this analysis. This is done according to the ratios of the values shown in Figs. 5.12 and 5.13, *i.e.* the  $D$  Dalitz bin population fractions in simulated  $B^+ \rightarrow D\pi^+$  ( $B^0 \rightarrow DK^+\pi^-$ ) data following the selection of the single Dalitz  $B^+ \rightarrow Dh^+$  analysis (double Dalitz) analysis. The  $CP$  fit to data is performed with these new  $R_i$  values and the systematic uncertainty is determined to be the difference between the nominal and new fit results. This systematic appears under the column labelled “Dalitz efficiency” in Table 9.1.

A similar systematic can also be determined for the  $c_i$  and  $s_i$  parameters.

### 9.1.3 Background yield uncertainty

The total amount of each background source present in the fully selected data in each decay mode is fixed in the  $CP$  fit according to the values presented in Tables 7.5 to 7.15. To determine the systematic uncertainty associated with the uncertainty on these values an ensemble of 250 variations in which the values are randomly varied according to their covariance in the mass fit result is produced. The data fit is then repeatedly performed with the yields fixed according to each variation and the  $x_\alpha^\pm, y_\alpha^\pm$  covariance matrix is extracted from the fit results. This systematic appears under the column labelled

“Background yield” in Table 9.1.

### 9.1.4 Background source binned distribution

In the  $CP$  fit the fraction of each background source present in each Dalitz bin is fixed according to the distribution of weighted simulated data samples, therefore there is a systematic uncertainty associated with the uncertainties of these fractions. The simulated samples are reweighted according to the methods described in Chapter 6. The systematic uncertainty is determined by generating an ensemble of 250 variations in which the background fractions are randomly varied according to  $\sqrt{\sum w^2}$ . The data fit is then repeated with the background fractions fixed to each variation and the systematic is computed from the covariance of the ensemble.

### 9.1.5 Factorisation of $B$ plane and $D$ plane

Another potential source of systematic uncertainty, which is expected to be small, is the assumption that the Dalitz binned distribution of  $B^0 \rightarrow DK^+\pi^-$  decays factorise between the  $B$  and  $D$  Dalitz planes. This allows one to write Eq. (4.39) in terms of the  $(\bar{\kappa})_\alpha$  and  $F_{\pm i}$  parameters rather than a combined distribution parameter and therefore greatly simplifies the analysis. The plots shown in Figs. 5.14 to 5.16 demonstrate that the  $D$  Dalitz distribution does not exhibit any differences depending on the  $B$  bin, but the residuals of these plots will be used to compute the associated systematic uncertainty.

### 9.1.6 PID correction

Within the invariant mass fit, from which the amount of background infiltrating the fully selected data is determined, various relative contributions of backgrounds are fixed according to PID efficiencies computed using simulated data. The associated systematic uncertainty can be determined by considering the statistical uncertainty on the values obtained from the simulated data and the uncertainties on the PID corrections themselves.

### 9.1.7 Mass fit parameterisation

Within the mass fit, various shape and relative yield parameters are fixed. Shape parameters are fixed from fits to simulated data and relative yields are fixed based on efficiencies calculated with simulated data and known branching fractions. For this systematic, each fixed parameter in the mass fit is varied within its statistical uncertainty over an ensemble of 250 pseudo-experiment ensembles. For each pseudo-experiment ensemble the mass and  $CP$  fit is re-run and the systematic is computed from the covariance of the ensemble.

### 9.1.8 Charmless contributions

In Section 5.2.9 cuts on the  $D$  flight distance significance are chosen in order to reduce the level of charmless contamination to below 5%. Therefore there will be some residual charmless contributions that are not accounted for in the nominal  $CP$  fit. In order to compute a related systematic uncertainty, the size of the potential charmless contribution is estimated from the study in Section 5.2.9 and ensembles of  $CP$  fit pseudo-experiment ensembles with this charmless background present are generated. Since the charmless contributions are heavily suppressed it is assumed that the charmless backgrounds populate the Dalitz bins uniformly since we are unlikely to be sensitive to any resonant structure. These pseudo-experiment ensembles are then fitted with the nominal fit configuration, *i.e.* no charmless background is accounted for, to obtain the relevant covariance matrix.

### 9.1.9 $CP$ violation in background decays

It is assumed that there is no  $CP$  violation in any of the backgrounds, *i.e.* the background distributions are identical for both  $B$  flavours. This assumption is expected to be reasonable as the background rates are generally small and the  $CP$  violation effects within them are also expected to be rather small. However, there will be some systematic effect from this which should be quantified.

### 9.1.10 Production and detection asymmetries

Currently the nominal fit sets the total production and detection asymmetry in each decay mode to zero. Values for the detection and production asymmetry in each decay mode can be computed which will then be fixed in the nominal fit. The systematic can then be computed by generating ensembles in which the values of the production and detection asymmetries are varied within their uncertainties and propagated through the  $CP$  fitter to the parameters of interest. As discussed in Section 4.2.2 these values will be calculated in the same way as in Ref. [19].

### 9.1.11 Bin migration

The effect of bin migrations can be determined by comparing the Dalitz bins corresponding to the true and reconstructed kinematic variables in simulated data generated/weighted according to appropriate decay models. Given the excellent kinematic resolution of LHCb this effect is expected to be small.

## 9.2 Results

Table [9.1](#) presents the systematic uncertainties of the  $x_{\alpha}^{\pm}$ ,  $y_{\alpha}^{\pm}$  parameters calculated thus far and compares them to the statistical uncertainties. Based on this it is expected that this measurement of  $\gamma$  will be statistically limited.

Parameter	Total Stat.	External inputs $c_i, s_i$		Background yield	Dalitz efficiency	Total Syst.	Syst. / Stat.
$x_1^+$	10	0.72	0.67	1.83	0.27	2.1	0.21
$y_1^+$	24	8.75	1.07	5.38	1.67	10	0.44
$x_1^-$	10	0.55	0.66	1.91	0.37	2.1	0.21
$y_1^-$	24	5.14	1.07	3.06	1.60	6.3	0.26
$x_2^+$	10	0.69	0.52	2.55	0.14	2.7	0.27
$y_2^+$	26	10.23	1.08	7.00	3.94	13	0.50
$x_2^-$	10	0.60	0.53	2.63	0.31	2.8	0.28
$y_2^-$	27	10.50	0.85	3.06	1.23	11	0.41
$x_3^+$	16	0.72	0.68	1.60	0.09	1.9	0.12
$y_3^+$	37	6.58	0.97	2.51	1.26	7.2	0.20
$x_3^-$	14	0.43	0.53	1.67	0.11	1.8	0.13
$y_3^-$	39	7.20	0.95	2.61	2.12	8.0	0.21
$x_4^+$	13	0.72	0.53	3.27	0.08	3.4	0.26
$y_4^+$	34	7.10	0.92	2.46	1.38	7.7	0.23
$x_4^-$	14	0.67	0.56	3.13	0.02	3.2	0.23
$y_4^-$	36	5.76	0.83	1.44	1.34	6.1	0.17
$\kappa_1$	0.60	0.04	0.02	0.18	0.01	0.19	0.31
$\bar{\kappa}_1$	0.79	0.05	0.03	0.32	0.03	0.33	0.41
$\kappa_2$	0.79	0.03	0.02	0.16	0.00	0.16	0.21
$\bar{\kappa}_2$	0.38	0.02	0.01	0.12	0.00	0.12	0.32
$\kappa_3$	0.30	0.02	0.01	0.13	0.01	0.13	0.44
$\bar{\kappa}_3$	0.41	0.02	0.01	0.15	0.01	0.15	0.37
$\kappa_4$	0.61	0.07	0.04	0.51	0.04	0.52	0.85
$\bar{\kappa}_4$	0.81	0.06	0.04	0.34	0.02	0.35	0.43

Table 9.1: Summary of systematic uncertainty contributions. The total statistical uncertainty is provided for reference. All uncertainties are quoted  $\times 100$  their actual values for ease of reading. The last two columns show the quadrature sum of each individual systematic contribution and the systematic uncertainty as a fraction of the statistical uncertainty, respectively.



# 10 Rare decays at the FCC-ee

*“So it’s all about sort of planting a seed, looking after each other  
... but I’m sort of guessing he enjoyed gardening anyway,  
part of the enjoyment was in planting that seed.”*

---

Karl Pilkington

This chapter presents a study performed to estimate the potential of BF measurements of  $b \rightarrow s\nu\bar{\nu}$  decays at the FCC-ee [27]. Sections 10.1 to 10.2 serve to introduce the topic and features no original work of my own. Section 10.3 explains the study performed and its results, which was developed alongside my supervisor Matt Kenzie with inspiration from the method used in Ref. [112]. Section 10.4 discusses the phenomenological implications of these measurements informed by the work of M  ril Reboud in Ref. [27]. Note that as the FCC designs are constantly evolving many of the exact values quoted with respect to collider and detector design and operation may be outdated.

## 10.1 Current status, prospects and limitations of $b \rightarrow s\nu\bar{\nu}$ measurements

Until recently there was no experimental evidence for any  $b \rightarrow s\nu\bar{\nu}$  decay however Belle II has now provided the first evidence for  $B^+ \rightarrow K^+\nu\bar{\nu}$  decays [113]. This measurement has determined the BF to be  $[2.3 \pm 0.5^{+0.5}_{-0.4}] \times 10^{-5}$ , a significance of  $3.5\sigma$ . This is in tension with the SM prediction of  $(5.58 \pm 0.37) \times 10^{-6}$  with a significance of  $2.7\sigma$ . For other  $b \rightarrow s\nu\bar{\nu}$  decays of mesons only upper limits have been set [114–116]. According to the predictions of the Belle II physics book, under the assumption of SM physics it is expected that  $B^+ \rightarrow K^+\nu\bar{\nu}$ ,  $B^0 \rightarrow K^{*0}\nu\bar{\nu}$  and  $B^+ \rightarrow K^{*+}\nu\bar{\nu}$  decays will be observed after Belle II has collected  $10 \text{ ab}^{-1}$  worth of data and with the full dataset of  $50 \text{ ab}^{-1}$  they will obtain BF measurements with relative uncertainties of  $\mathcal{O}(10\%)$ . Given that Belle II primarily operates at the  $\Upsilon(4S)$  resonance it will not be able to perform searches for  $b \rightarrow s\nu\bar{\nu}$  decays from any  $B_s^0$ ,  $B_c^+$  or  $A_b^0$  hadrons [117]. LHCb is unable to perform



any measurement of  $b \rightarrow s\nu\bar{\nu}$  decays due to its inability to infer the presence of a double neutrino final state with sufficient resolution.

To improve upon the measurements possible at current experiments a new facility must be built. This study explores how such a set of measurements could develop at the FCC-ee. It provides the first estimate of the sensitivity with which the BFs of  $B^0 \rightarrow K^{*0}\nu\bar{\nu}$ ,  $B_s^0 \rightarrow \phi\nu\bar{\nu}$ ,  $B^0 \rightarrow K_S^0\nu\bar{\nu}$  and  $\Lambda_b^0 \rightarrow \Lambda\nu\bar{\nu}$  decays could be measured at the FCC-ee, initial detector performance requirements and provides an analysis framework which can be developed to perform more detailed studies in the future.

## 10.2 The Future Circular Collider

The FCC collaboration is developing plans for construction of a circular collider at CERN to come into operation after the end of the LHC. The plan is to first run an electron-positron collider, the FCC-ee, and then upgrade it to a proton-proton collider, the FCC-hh. The FCC collaboration is currently preparing a final feasibility study report to submit to the CERN council in 2025 and has recently submitted a mid-term report [118]. To contribute to these reports physicists have been performing studies with simulated datasets to understand the potential physics reach of the FCC and to consider the detector design requirements.

### 10.2.1 FCC-ee

The current FCC-ee proposal is a  $\sim 91$  km long tunnel with four interaction points [5]. This will be operated over a course of 16 years starting in the late 2040s. It will have four running periods exploiting different centre-of-mass collision energies, the  $Z$  pole, the  $WW$  threshold, the Higgs factory  $ZH$  threshold, and the  $t\bar{t}$  pair threshold.

As summarised in Ref. [119] the  $Z$  pole and  $WW$  threshold runs have garnered the most interest from the flavour community. The  $Z$  pole run will produce a dataset orders of magnitude larger than at any previous experiment which will allow greater statistical sensitivity to be obtained in precision flavour measurements. The  $WW$  threshold run will allow for more precise measurements of the CKM matrix thanks to the large quantity of on-shell  $W$  bosons that will be produced. In the current baseline FCC-ee design these runs will yield  $6 \times 10^{12}$   $Z$  bosons and  $2.4 \times 10^8$   $WW$  pairs respectively, summed over all four interaction points. As illustrated by Table 10.1, the FCC-ee can be viewed as a “best of both worlds” scenario during the  $Z$  pole run when compared to the current flagship flavour experiments, LHCb and Belle II [33, 117]. Given the beauty production cross section in the LHCb acceptance  $\sim 1.5 \mu\text{b}$  and the expected integrated luminosity for the entire lifetime of the LHC  $300 \text{ fb}^{-1}$ , it is expected that over the lifetime of LHCb

$\mathcal{O}(10^{14})$  beauty hadrons will be produced in the LHCb acceptance [120,121]. For Belle II, the full  $50 \text{ ab}^{-1}$  with a beauty production cross section  $\sim 1 \text{ nb}$  is expected to correspond to producing  $\mathcal{O}(10^{11})$  beauty hadrons [117]. Given the  $Z \rightarrow b\bar{b}$  BF of 0.1512 the expected FCC-ee dataset of  $6 \times 10^{12}$   $Z$  bosons will correspond to  $\mathcal{O}(10^{12})$  beauty hadrons [7].

Attribute	$\Upsilon(4S)$	proton-proton	$Z^0$
All hadron species		✓	✓
High boost		✓	✓
Enormous production cross-section		✓	
Negligible trigger losses	✓		✓
Low backgrounds	✓		✓
Initial energy constraint	✓		(✓)

Table 10.1: Advantageous properties of Belle II ( $\Upsilon(4S)$ ), the LHC (proton-proton) and the FCC-ee ( $Z^0$ ). Reproduced from Ref. [122].

Note that although the FCC-ee will not have as high a production cross-section as the LHC the instantaneous luminosity will be much greater and produce the expected large dataset of  $Z$  bosons, this will result in the FCC-ee reproducing the LEP collider’s  $Z$  boson dataset in just a few minutes of operation. Table 10.1 also highlights the difference in initial energy constraints between Belle II and the FCC-ee. Unlike the  $\Upsilon(4S)$  resonance, hadrons produced from the  $Z$  decay do not have a known momentum although the distribution of momenta is well understood and the per-event initial  $B$  energy be determined via an iterative method as shown in Ref. [123]. Therefore the FCC-ee could fill the gaps in the capabilities of LHCb and Belle II, whilst also performing many other complementary measurements to a high precision.

### 10.2.2 The IDEA detector and simulation production

Since there will be four collision points it is sensible to expect that there may be one detector designed with a focus on optimising sensitivity to flavour measurements. One current detector idea from which a flavour experiment could be developed is the Innovative Detector for Electron-positron Accelerators (IDEA) [5]. This is the detector concept used for current flavour physics studies as it should provide the necessary PID performance.

The detector geometry is shown in Fig. 10.1. The inner detector features a silicon vertex detector (VTX) based on the ALICE ITS upgrade vertex detector. The drift chamber (DCH) provides tracking, momentum measurement and PID using a cluster counting method and is based on the KLOE and MEG2 detectors [124,125]. The DCH has been designed to be incredibly light to achieve high transparency. In the radial direction the total material corresponds to  $\sim 1.6\%$  of the radiation length,  $X_0$ , and  $\sim 5\%$   $X_0$  in the forward direction most of which is due to the end plates and front end electronics [126].

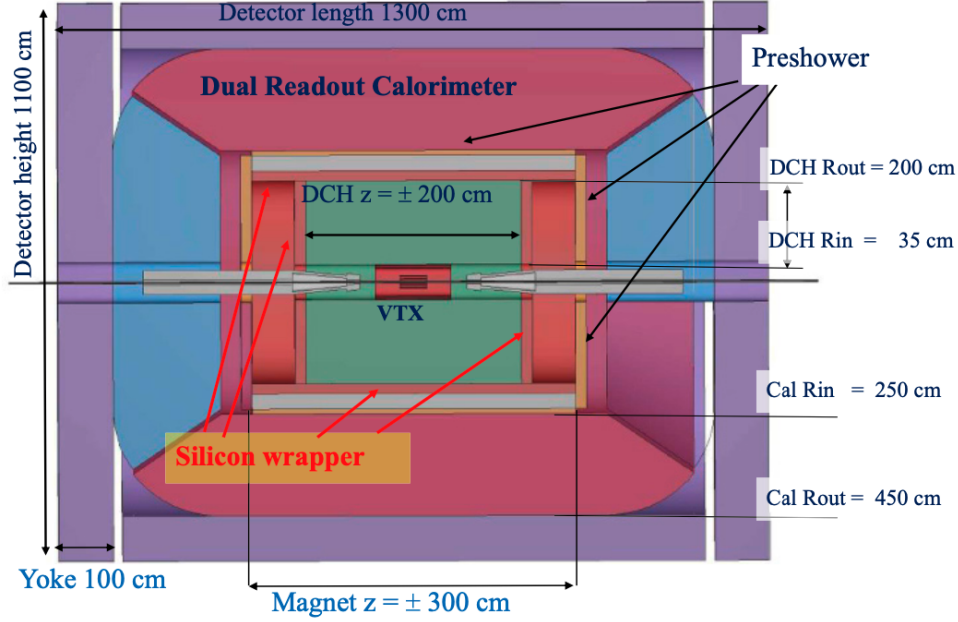


Figure 10.1: Cross-section of the IDEA detector concept. From Ref. [5].

The DCH is surrounded by a layer of silicon micro-strip detectors to provide a final spacial position measurement and a precise definition of the tracking acceptance. This is then surrounded by a thin solenoid which provides a 2T magnetic field, and a preshower detector. In between this and the solenoid return yoke is a dual readout calorimeter which provides full coverage up to within 100 mrad of the  $z$  axis [127]. The final sub-detector is a muon system embedded in the solenoid return yoke, this is currently based on the CMS phase-II upgrade detector as a cost-effective solution to covering the large area required.

In simulation production for FCC studies the detector response is provided by DELPHES [128] which models a tracking system, magnetic field, calorimeters and a muon system [129]. The K4SIMDELPHES [130] project is used to convert DELPHES objects to the EDM4HEP format [131]. Simulated datasets of specific decays and inclusive background samples are produced using PYTHIA with the leading order cross-section and no K-factor [132]. EVTGEN is used to model the decays of unstable particles [102] and PHOTOS generates final-state radiation [133]. Primary vertex smearing is implemented corresponding to the expected beam properties such that  $\sigma_x^{\text{PV}} = 4.5\mu\text{m}$ ,  $\sigma_y^{\text{PV}} = 20\text{nm}$ ,  $\sigma_z^{\text{PV}} = 0.3\text{mm}$ , where the axes are defined such that  $x$  is parallel to the radial direction of the collider,  $y$  is the vertical direction and  $z$  is parallel to the beam. Secondary and tertiary vertices are assumed to have perfect seeding and PID performance is assumed to be perfect, unless otherwise stated. For inclusive background samples  $10^{10}$  decays are generated for three categories,  $Z \rightarrow b\bar{b}$ ,  $Z \rightarrow c\bar{c}$ , and  $Z \rightarrow q\bar{q}$ , where  $q \in \{u, d, s\}$ . For each signal decay  $10^7$  decays are generated such that the  $B$  decay products kinematics are uniform in the phase space. In the case of  $B^0 \rightarrow K^{*0}\nu\bar{\nu}$  decays the  $K^{*0}$  resonance is purely  $K^*(892)^0 \rightarrow K^+\pi^-$

and for  $B_s^0 \rightarrow \phi\nu\bar{\nu}$  decays the  $\phi$  is purely  $\phi(1020) \rightarrow K^+K^-$ . All signal decays are generated with an equal admixture of  $b$ -hadron flavours.

## 10.3 Prospects for $b \rightarrow s\nu\bar{\nu}$ measurements at the FCC-ee

### 10.3.1 Basic sensitivity studies in an ideal detector

The analysis procedure is as follows:

1. For each event construct signal candidates, split the detector space into two hemispheres based on the thrust of the  $Z \rightarrow q\bar{q}$  products.
2. Apply basic selection requirements and cuts. This is referred to as the stage 0 selection.
3. Train a BDT on the difference between the two hemispheres in terms of measured energy, tracks, vertices, etc. This is referred to as the stage one selection.
4. Apply a loose BDT cut and candidate mass cut.
5. Train a second BDT on the candidate kinematics. This is referred to as the stage two selection.
6. Optimise BDT cuts according to the  $S/\sqrt{S+B}$  FOM, this is the inverse of the relative statistical uncertainty on the BF.

This analysis workflow is inspired by the analysis performed to study the potential of  $B_c^+ \rightarrow \tau^+\nu_\tau$  decay measurements at the FCC-ee however it deviates slightly after the first stage BDT [112]. In the  $B_c^+ \rightarrow \tau^+\nu_\tau$  study exclusive samples of selected  $Z \rightarrow b\bar{b}$  background decays are generated and used to optimise the BDT cuts. In the  $b \rightarrow s\nu\bar{\nu}$  analysis however bi-cubic splines are instead used to construct efficiency maps in terms of the BDT response values of the first and second stage BDTs. The full analysis workflow was applied to  $B^0 \rightarrow K^{*0}\nu\bar{\nu}$  and  $B_s^0 \rightarrow \phi\nu\bar{\nu}$  decays. Throughout this discussion the signal candidates,  $K^{*0}$  and  $\phi$ , will be referred to as  $Y$ .

#### Candidate construction and basic selection

For each decay a candidate was constructed for any vertex that was not the primary vertex and was followed by the correct number of tracks with PIDs and charge corresponding to that of its expected children. The child identities for each signal decay are shown in

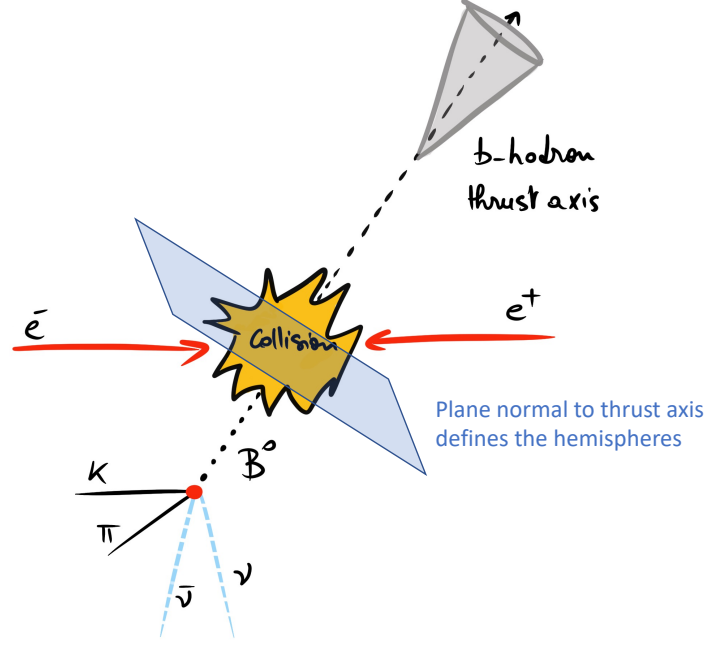


Figure 10.2: A pictorial representation of the definition of the thrust axis and the two event hemispheres for a  $B^0 \rightarrow K^{*0} \nu \bar{\nu}$  decay.

Table 10.2, it also shows the loose mass cuts that are applied later on. Each candidate is identified within a given hemisphere of the detector, defined according to the plane normal to the thrust axis. The thrust axis is defined as the unit vector,  $\hat{\mathbf{n}}$ , that maximises

$$T = \frac{\sum_i |\mathbf{p}_i \cdot \hat{\mathbf{n}}|}{\sum_i |\mathbf{p}_i|}, \quad (10.1)$$

where  $\mathbf{p}_i$  is the momentum vector of the  $i^{\text{th}}$  reconstructed particle in the event. This is a measure of the direction of the quark pair produced by the  $Z$  decay. Figure 10.2 shows a representation of the reconstruction of a  $B^0 \rightarrow K^{*0} \nu \bar{\nu}$  signal decay.

The stage 0 selection removes any events that don't have a primary vertex and a  $Y$  candidate whose momentum points towards the minimum energy hemisphere.

Decay	Candidate	Candidate Children	Candidate Mass Range [ $\text{GeV}/c^2$ ]
$B^0 \rightarrow K^{*0} \nu \bar{\nu}$	$K^{*0}$	$K^\pm \pi^\mp$	[0.65, 1.10]
$B_s^0 \rightarrow \phi \nu \bar{\nu}$	$\phi$	$K^+ K^-$	[1.00, 1.06]

Table 10.2: The children PID and candidate mass range required for constructing the candidate particle for each signal decay.

### First-stage BDT

The first BDT is designed to select for signal candidates based on the event topology and energy distribution. The XGBOOST package [134] is used to train the BDTs. A  $k$ -fold cross validation (with  $k = 4$ ) is used to avoid over-training. Separate BDTs are trained for each signal mode. The background training samples consist of inclusive background decays with each category appropriately weighted according to the known hadronic  $Z$  BFs: 0.1512 ( $Z \rightarrow b\bar{b}$ ), 0.1203 ( $Z \rightarrow c\bar{c}$ ) and 0.4276 ( $Z \rightarrow q\bar{q}$ ) [7].

The first stage BDT is trained using a sample of one million signal decays and one million background decays with the following input variables:

- Total reconstructed energy in each hemisphere,
- Total charged and neutral reconstructed energies of each hemisphere,
- Charged and neutral particle multiplicities in each hemisphere,
- Number of charged tracks used in the reconstruction of the primary vertex,
- Number of reconstructed vertices in the event,
- Number of candidates in the event,
- Number of reconstructed vertices in each hemisphere,
- Minimum, maximum and average radial distances of all decay vertices from the primary vertex.

Figure 10.3 shows the BDT response for each of the reconstructed decays and Fig. 10.4 shows how the efficiency depends on the minimum BDT response when applying a cut on the BDT response variable. This shows that the stage one selection is highly effective at rejecting the inclusive background decays. The integrated ROC score is 0.965 for both the  $B^0 \rightarrow K^{*0}\nu\bar{\nu}$  and  $B_s^0 \rightarrow \phi\nu\bar{\nu}$  decays. The feature importance and plots of the distribution in the signal and inclusive backgrounds, for  $B^0 \rightarrow K^{*0}\nu\bar{\nu}$ , is shown in Table C.1 and Figs. C.1 and C.2

### Second-stage BDT

The second-stage BDT is trained using a sample of one million signal decays and one million background decays which pass the preselection criteria of  $E_{\text{diff}} > 5 \text{ GeV}$  and  $\text{BDT1} > 0.6$ . This additional requirement on the value of  $E_{\text{diff}}$  is motivated by Fig. 10.5 which shows that considerable background can be removed with little reduction in signal efficiency.

The second-stage BDT is trained using the following input variables:

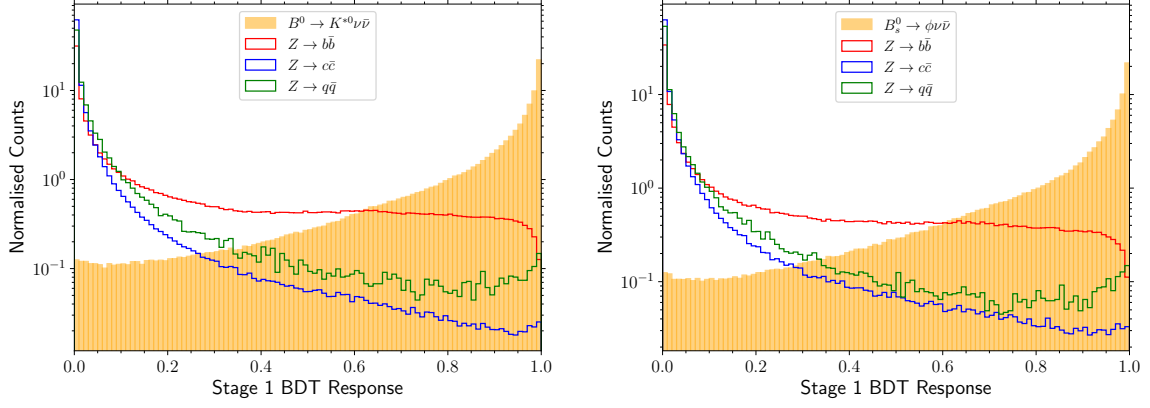


Figure 10.3: First stage BDT response for the  $B^0 \rightarrow K^{*0} \nu \bar{\nu}$  channel (left) and the  $B_s^0 \rightarrow \phi \nu \bar{\nu}$  channel (right). The relevant signal mode response is shown as the orange filled histogram, the inclusive background sample responses are shown in red, blue and green for  $Z \rightarrow b\bar{b}$ ,  $Z \rightarrow c\bar{c}$  and  $Z \rightarrow q\bar{q}$  (for  $q \in \{u, d, s\}$ ), respectively.

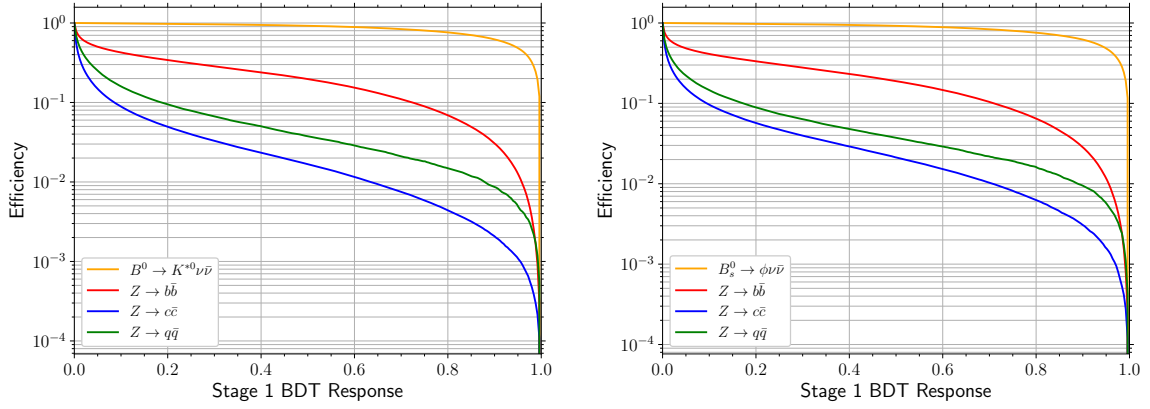


Figure 10.4: First stage BDT response cut efficiencies for the  $B^0 \rightarrow K^{*0} \nu \bar{\nu}$  channel (left) and the  $B_s^0 \rightarrow \phi \nu \bar{\nu}$  channel (right). The relevant signal mode response is shown as the orange line, the inclusive background sample responses are shown in red, blue and green for  $Z \rightarrow b\bar{b}$ ,  $Z \rightarrow c\bar{c}$  and  $Z \rightarrow q\bar{q}$  (for  $q \in \{u, d, s\}$ ), respectively.

- The intermediate candidate's reconstructed mass
- Number of intermediate candidates in the event
- The intermediate candidate's flight distance and vertex  $\chi^2$
- The  $x$ ,  $y$  and  $z$  components of the intermediate candidate's momentum
- Scalar momentum of the intermediate candidate
- Transverse and longitudinal impact parameters of the intermediate candidate
- Minimum, maximum and average transverse and longitudinal impact parameters of all other reconstructed decay vertices in the event

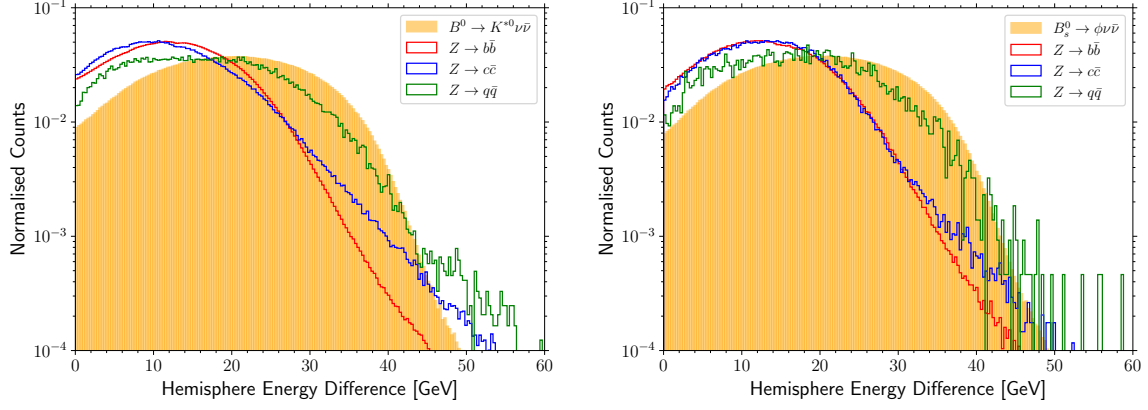


Figure 10.5: Distributions of the energy difference between the two hemispheres, after a loose cut on  $\text{BDT1} > 0.6$ , for the  $B^0 \rightarrow K^{*0}\nu\bar{\nu}$  channel (left) and  $B_s^0 \rightarrow \phi\nu\bar{\nu}$  channel (right). The relevant signal mode response is shown as the orange filled histogram, the inclusive background sample responses are shown in red, blue and green for  $Z \rightarrow b\bar{b}$ ,  $Z \rightarrow c\bar{c}$  and  $Z \rightarrow q\bar{q}$  (for  $q \in \{u, d, s\}$ ), respectively.

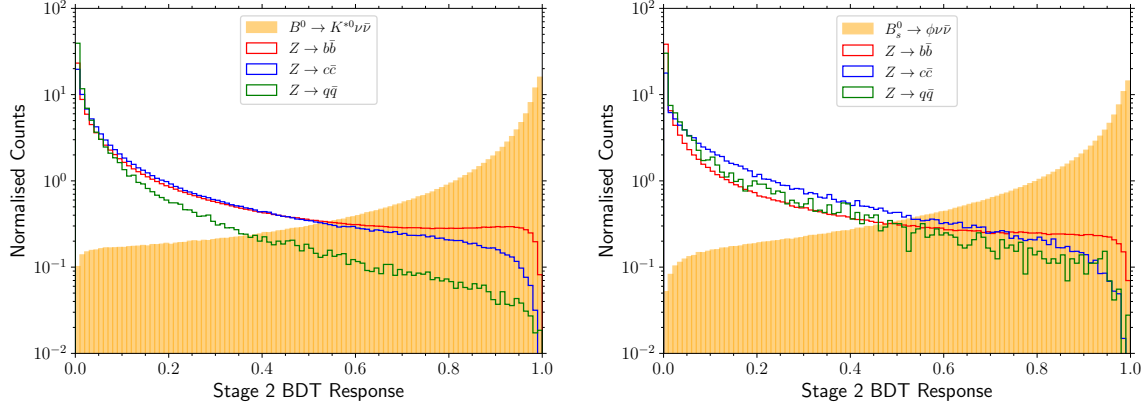


Figure 10.6: Second stage BDT response for the  $B^0 \rightarrow K^{*0}\nu\bar{\nu}$  channel (left) and the  $B_s^0 \rightarrow \phi\nu\bar{\nu}$  channel (right). The relevant signal mode response is shown as the orange filled histogram, the inclusive background sample responses are shown in red, blue and green for  $Z \rightarrow b\bar{b}$ ,  $Z \rightarrow c\bar{c}$  and  $Z \rightarrow q\bar{q}$  (for  $q \in \{u, d, s\}$ ), respectively.

- The angle between the intermediate candidate and the thrust axis
- Mass of the primary vertex candidate
- The nominal  $B$  candidate energy, defined as the  $Z$  mass minus all of the reconstructed energy apart from the candidate children

Figure 10.6 shows the second-stage BDT response for each of the reconstructed decays. The integrated ROC scores are 0.961 and 0.959 for the  $B^0 \rightarrow K^{*0}\nu\bar{\nu}$  and  $B_s^0 \rightarrow \phi\nu\bar{\nu}$  decays, respectively. The feature importance and plots of the distribution in the signal and inclusive backgrounds, for  $B^0 \rightarrow K^{*0}\nu\bar{\nu}$ , are shown in Table C.2 and Figs. C.4 and C.5



### Sensitivity estimate

The final step of the analysis is to optimise the BDT response cuts to maximise the sensitivity to the BF of each decay. The FOM to maximise is defined as

$$\text{FOM} = \frac{S}{\sqrt{S+B}}, \quad (10.2)$$

where  $S$  is the expected number of signal decays and  $B$  is the expected number of background decays based on the appropriately weighted sum of  $Z \rightarrow b\bar{b}$ ,  $Z \rightarrow c\bar{c}$  and  $Z \rightarrow q\bar{q}$  decays. The signal expectation is defined as

$$S = 2 N_Z \mathcal{B}(Z \rightarrow b\bar{b}) f_B \mathcal{B}(B \rightarrow Y \nu \bar{\nu}) \mathcal{B}(Y \rightarrow f) \epsilon_{\text{pre}}^s \epsilon_{\text{BDTs}}^s, \quad (10.3)$$

where  $N_Z$  is the number of  $Z$  bosons produced, the factor of two accounts for the two  $B$  flavours,  $f_B$  is the hadronisation fraction for the relevant  $B$  hadron,  $\mathcal{B}(B \rightarrow Y \nu \bar{\nu})$  is the BF for the given  $B$  decay,  $\mathcal{B}(Y \rightarrow f)$  is the BF of the intermediate resonance to the final state  $f$ ,  $\epsilon_{\text{pre}}^s$  is the signal efficiency of the initial selection, including the reconstruction and the loose cut on the stage 1 BDT), and  $\epsilon_{\text{BDTs}}^s$  is the signal efficiency of the two BDT score cuts. The background expectation is defined as

$$B = \sum_{f \in \{b\bar{b}, c\bar{c}, q\bar{q}\}} N_Z \mathcal{B}(Z \rightarrow f) \epsilon_{f,\text{pre}}^b \epsilon_{f,\text{BDTs}}^b, \quad (10.4)$$

where  $\mathcal{B}(Z \rightarrow f)$  is the relevant hadronic BF, and  $\epsilon_{f,\text{pre}}^b$ ,  $\epsilon_{f,\text{BDTs}}^b$  are the pre-selection and BDT cut efficiencies of the relevant background, respectively. This study assumed the following values of the parameters in Eqs. (10.3) and (10.4):

- $N_Z = 6 \times 10^{12}$ , the total number of  $Z$ -bosons produced in all collisions at the FCC-ee during the  $Z$  pole run.
- The hadronisation fraction of  $B$ -mesons from  $Z \rightarrow b\bar{b}$  decays are  $f_{B^0} = 0.43$  and  $f_{B_s^0} = 0.096$  [135].
- The SM predictions of the relevant decay BFs are provided in Table 2.2, although the sensitivity is also shown as a function of these BFs in Fig. 10.7.
- The intermediate resonance BFs are  $\mathcal{B}(K^{*0} \rightarrow K^+ \pi^-) = 2/3$  and  $\mathcal{B}(\phi \rightarrow K^+ K^-) = 0.491$ .
- The  $Z \rightarrow f$  BFs are  $\mathcal{B}(Z \rightarrow b\bar{b}) = 0.1512$ ,  $\mathcal{B}(Z \rightarrow c\bar{c}) = 0.1203$  and  $\mathcal{B}(Z \rightarrow q\bar{q}) = 0.4276$  [7].

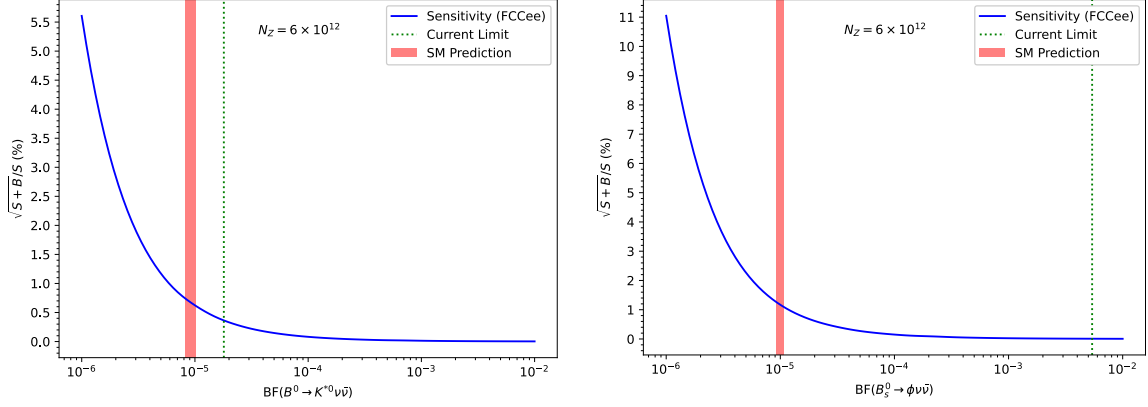


Figure 10.7: The expected sensitivity of the Tera-Z run at FCC-ee to the BF of  $B^0 \rightarrow K^{*0}\nu\bar{\nu}$  (left) and  $B_s^0 \rightarrow \phi\nu\bar{\nu}$  (right). Note that the  $B^0 \rightarrow K^{*0}\nu\bar{\nu}$  plot corresponds to assuming  $\mathcal{B}(K^{*0} \rightarrow K^+\pi^-) = 0.9975$ .

Mode	$N_S$	$N_B$	$\epsilon^s$	$\epsilon^{b\bar{b}}$	$\epsilon^{c\bar{c}}$	$\epsilon^{q\bar{q}}$	$S/B$	$\sqrt{S+B}/S$
$B^0 \rightarrow K^{*0}\nu\bar{\nu}$	144 K	1.13 M	3.5%	$\mathcal{O}(10^{-7})$	$\mathcal{O}(10^{-8})$	$\mathcal{O}(10^{-9})$	0.15	0.76%
$B_s^0 \rightarrow \phi\nu\bar{\nu}$	61 K	0.48 M	7.4%	$\mathcal{O}(10^{-7})$	$\mathcal{O}(10^{-9})$	$\mathcal{O}(10^{-9})$	0.13	1.20%

Table 10.3: The expected number of signal and background decays of the Tera-Z run at FCC-ee at the SM predictions for the  $B^0 \rightarrow K^{*0}\nu\bar{\nu}$  and  $B_s^0 \rightarrow \phi\nu\bar{\nu}$  decays. The signal and inclusive background efficiencies of the analysis chain are also shown along with the signal-to-background ratio and the expected sensitivity.

Given the strength with which the two-stage BDT selection rejects background decays one cannot simply optimise a cut on each BDT response score according to the efficiency directly from the inclusive background samples. Therefore a map of the selection efficiency is constructed, separately for the signal simulation and each inclusive background category, as a function of the BDT response cut values. This map is then interpolated with a bi-cubic spline which is used to find the BDT response cut values maximise the FOM.

Figure 10.7 shows the relative statistical uncertainty on the BFs as a function of the BF. Assuming SM BF the expected sensitivities are 0.53% for  $B^0 \rightarrow K^{*0}\nu\bar{\nu}$  and 1.20% for  $B_s^0 \rightarrow \phi\nu\bar{\nu}$ . The expected number of signal and background decays, along with the analysis chain efficiencies are shown in Table 10.3.

### Extrapolation to neutral modes

Studies of neutral reconstruction performance with IDEA at FCC-ee suggest that the  $K_S^0$  and  $\Lambda$  reconstruction efficiency could be  $\sim 80\%$  in the momentum range relevant for this analysis [136]. To estimate the sensitivity of BF measurements for  $B^0 \rightarrow K_S^0\nu\bar{\nu}$  and  $\Lambda_b^0 \rightarrow \Lambda\nu\bar{\nu}$  this efficiency and the SM BF are used to extrapolate the results of the  $B^0 \rightarrow K^{*0}\nu\bar{\nu}$  and  $B_s^0 \rightarrow \phi\nu\bar{\nu}$  studies using Eqs. (10.3) and (10.4).

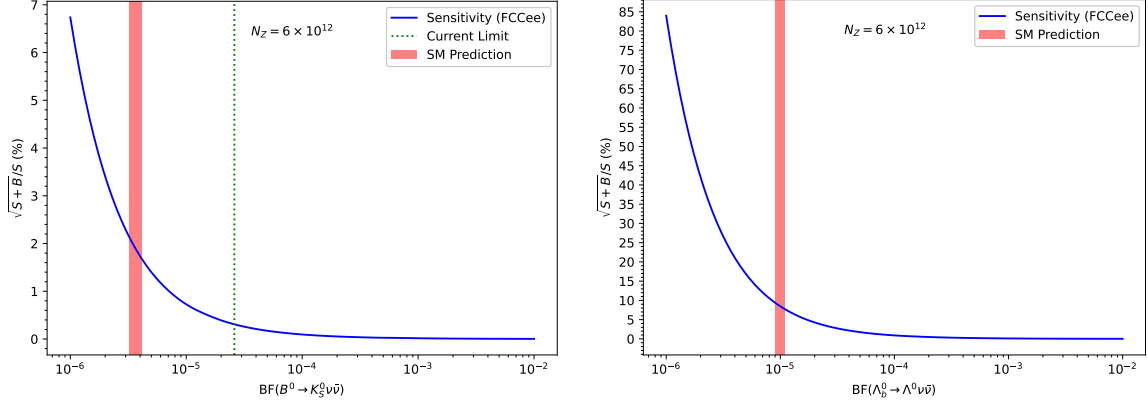


Figure 10.8: The expected sensitivity of the Tera-Z run at FCC-ee to the BF of  $B^0 \rightarrow K_S^0 \nu \bar{\nu}$  (left) and  $\Lambda_b^0 \rightarrow \Lambda \nu \bar{\nu}$  (right).

The values used for Eqs. (10.3) and (10.4) are  $f_{\Lambda_b^0} = 0.037$ ,  $\mathcal{B}(K_S^0 \rightarrow \pi^+ \pi^-) = 0.692$  and  $\mathcal{B}(\Lambda \rightarrow p \pi^-) = 0.639$ . This results in expected sensitivities (signal-to-background ratios), assuming SM BF's, of 3.37% (0.04) for  $B^0 \rightarrow K_S^0 \nu \bar{\nu}$  and 9.86% (0.015) for  $\Lambda_b^0 \rightarrow \Lambda \nu \bar{\nu}$ . The sensitivity as a function of the BF is shown in Fig. 10.8

### 10.3.2 Detector performance requirements

The above sensitivity studies were performed with simulation and reconstruction assuming perfect PID performance and vertex seeding. This provides a baseline estimate of the statistical sensitivity that could be achieved with this analysis method but in order to design a suitable experiment one must understand how this sensitivity will depend on detector performance. The studies below are the first with respect to this particular class of decays at the FCC-ee.

#### Study of particle-identification

Perfect PID implies all pions and kaons can be perfectly identified by the detector and assigned the correct mass hypothesis. Clearly this is an unrealistic expectation for any detector so this assumption is now relaxed by recomputing the signal efficiencies,  $\epsilon_{\text{pre}}^s$  and  $\epsilon_{\text{BDT}}^s$  of Eq. (10.3), after making random mass hypothesis swaps of kaon  $\rightarrow$  pion and pion  $\rightarrow$  kaon, based on an assumed mis-identification rate,  $f_{\text{misid}}$ . This incorporates the effect of double mis-identifications and will cause decays to fall outside of the mass window for the intermediate resonance, listed in Table 10.2

The results of this are shown in Fig. 10.9 in terms of the kaon-pion separation power in standard deviations,  $\sigma$ , *vs.* the expected degradation to the sensitivity. This shows that  $K - \pi$  separation of  $\sim 2\sigma$  would have a negligible impact on the uncertainty. The PID performance of the DCH proposed for the IDEA detector concept is expected to provide

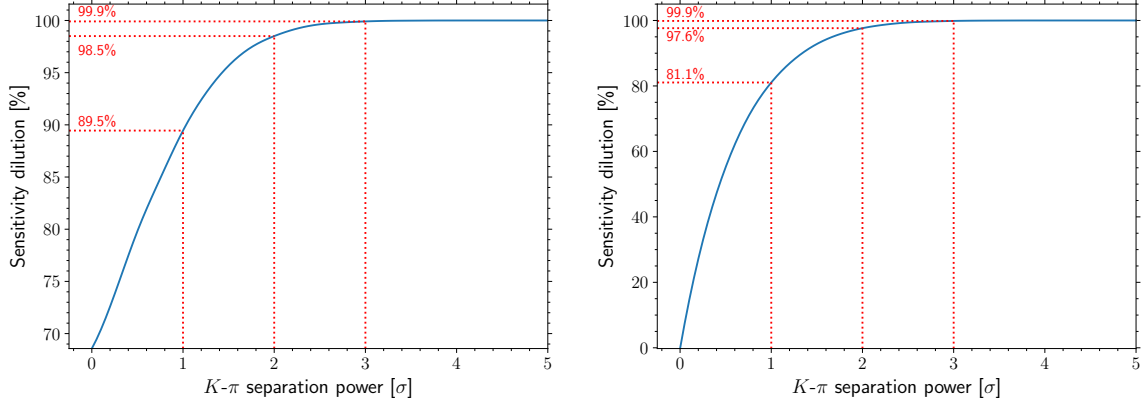


Figure 10.9: Degradation of the sensitivity to the BF, with respect to the nominal sensitivity assuming perfect PID, as a function of the kaon-pion separation power for the  $B^0 \rightarrow K^{*0}\nu\bar{\nu}$  decay (left) and  $B_s^0 \rightarrow \phi\nu\bar{\nu}$  decay (right).

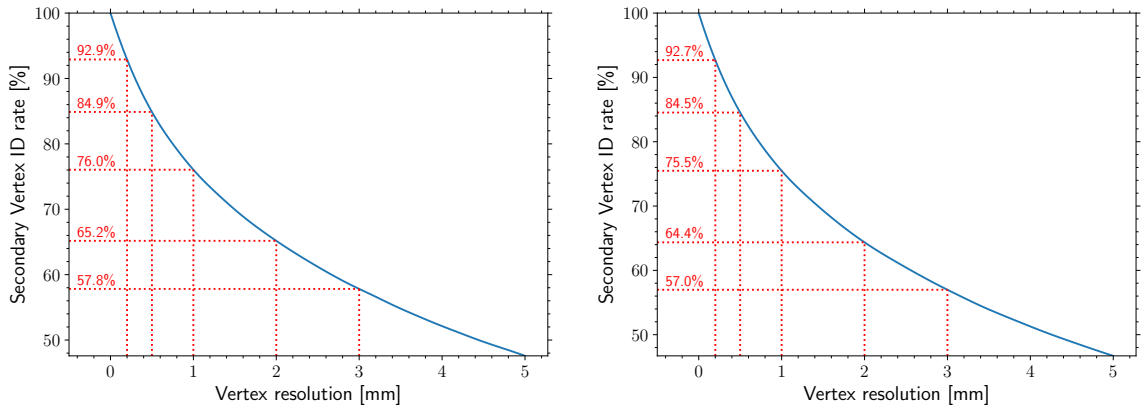


Figure 10.10: The correct secondary vertex association rate as a function of the expected vertex resolution for the  $B^0 \rightarrow K^{*0}\nu\bar{\nu}$  decay (left) and  $B_s^0 \rightarrow \phi\nu\bar{\nu}$  decay (right).

$K - \pi$  separation  $\gtrsim 2\sigma$  for particle momenta in the range  $[0.1, 0.850] \cup [1, 100]$  GeV/ $c$  so the baseline IDEA design should be sufficient for precise measurements of these decays [5].

### Study of imperfect vertex seeding

Perfect vertex seeding assumes that each vertex is correctly identified. However in a real experiment there will be a chance, depending on the vertex resolution, that an incorrect vertex is chosen. The dependence of sensitivity on this is studied by randomly selecting the wrong vertex during reconstruction, based on an assumed value of the vertex resolution, and propagating its effect through the analysis workflow. The results are shown in Fig. 10.10, which gives the secondary vertex identification rate as a function of the vertex resolution. This shows that the vertex resolution needs to be  $\lesssim 0.2$  mm. This is far above the expected vertex resolution of  $\sim 5 \mu\text{m}$  [5].

## Potential systematic effects

Systematic effects beyond the simple PID and vertex seeding will have to be considered in a real analysis. For example in the calculation of the BF from the signal yield, Eq. (10.3), there will be systematics related to knowledge of the selection efficiencies, hadronisation fragmentation and production fractions, decay multiplicities, and related BFs. Many of these quantities are currently best measured by the LEP experiments, but the FCC-ee experiments will naturally be able to improve upon this.

The most significant systematic for this analysis is due to the uncertainty of the  $Z \rightarrow b\bar{b}$  BF and the  $b$ -quark fragmentation fractions,  $f_B$ . The former is already known from LEP to three per mille precision [7] and will likely improvements from FCC-ee measurements. The latter, however, is currently only known to  $\sim 2\%$  precision [7] but it is expected that FCC-ee itself will be able to improve knowledge of these by an order of magnitude or more.

## 10.4 Implications of the FCC-ee prospects

### 10.4.1 SM implications

If one assumes these decays to be purely SM-like then their measurement can be used to constrain related SM parameters. As mentioned in Section 2.4 the two main sources of uncertainty in the prediction of the BFs is the CKM factor,  $\lambda_t$ , and the hadronic form factors.

#### Extraction of CKM elements.

As a first illustration of the potential of these measurements at FCC-ee, the precision of extracting  $|\lambda_t|^2$  from these decays is studied by using the form factors determined from lattice QCD (LQCD) and Eqs. (2.23) to (2.26).

Figure 10.11 shows the uncertainties on  $\lambda_t$  obtained from each decay compared to the recent determination from the flavour lattice averaging group. The form factors used in these extractions are the current values with a factor of ten improvement on the uncertainties since it is assumed that progress will be made in their determination over the next few decades.

#### Ratio of charged and neutral lepton BFs

There is also interest in ratios of the form

$$R_Y^{\ell/\nu} = \frac{\mathcal{B}(B \rightarrow Y \ell^+ \ell^-)}{\mathcal{B}(B \rightarrow Y \nu \bar{\nu})}, \quad (10.5)$$

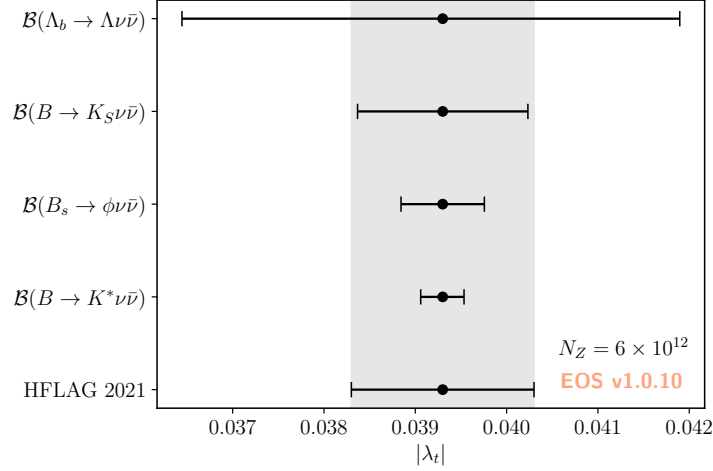


Figure 10.11: 68% probability ranges of CKM factor extractions assuming the branching ratios to be SM-like. Where the BF uncertainties are those determined in Section 10.3 and the form factors uncertainties are assumed to have reduced by a factor of ten by the time of the FCC-ee measurements. The results are compared with the value derived from  $|V_{cb}| = (40.0 \pm 1.0) \times 10^{-3}$ , extracted from  $B \rightarrow D\ell\nu$  decays [137].

where the branching ratio is integrated over the full kinematic range. These ratios benefit from numerous uncertainty cancellations which allow them to serve as sensitive probes of NP. These cancellations originate both from experimental sources such as the fragmentation fraction, BF of the normalization channel, and experimental efficiencies and from theory sources such as the CKM elements and local form factors [31].

Experimentally,  $R_{K^+}^{\mu/\nu}$  can be reconstructed using the world average measurement of  $B \rightarrow K\mu^+\mu^-$  decays [7] and the evidence for  $B \rightarrow K\nu\bar{\nu}$  decays presented by the Belle II collaboration [113]. Assuming uncorrelated uncertainties

$$R_{K^+}^{\mu/\nu}|_{2023} = 0.03 \pm 0.01. \quad (10.6)$$

Using world averages [7], at 90% CL

$$R_{K^{*+}}^{\mu/\nu}|_{2023} > 0.02, \quad R_{K^{*0}}^{\mu/\nu}|_{2023} > 0.07, \quad R_{\phi}^{\mu/\nu}|_{2023} > 2 \times 10^{-4}. \quad (10.7)$$

Theoretical predictions of  $R_M^{\ell/\nu}$  are hampered by long-range effects due to the charm loops and can be handled in a variety of ways [138, 139]. A precise measurement of these ratios at the FCC-ee would provide valuable information about these non-local effects. Assuming that the  $b \rightarrow s\nu\bar{\nu}$  mode will dominate the experimental uncertainties, the sensitivities expected for FCC-ee will permit a direct extraction of the shift to  $C_9^\ell$  with an accuracy of 8.7%, 13%, 22% and 37% for the  $B \rightarrow K$ ,  $B \rightarrow K^*$ ,  $B_s \rightarrow \phi$  and  $\Lambda_b^0 \rightarrow \Lambda$  decays respectively.

### 10.4.2 NP implications

In the WEFT one can introduce terms to the Hamiltonian to model the effects of potential NP such as right-handed neutrinos. These would then propagate to Eqs. (2.23) to (2.26) such that the BF of these decays can be used to probe for this NP. A full discussion of the interpretation in terms of the the NP WEFT can be found in Ref. [27]. It follows that measurements at the FCC-ee can be converted into constraints on the values of the left- and right-handed Wilson coefficients which can be combined to extract precise values.

Figure 10.12 shows the estimated constraints obtained at the end of the  $Z$  pole run compared to the current constraint derived from the experimental average of  $\mathcal{B}(B \rightarrow K\nu\bar{\nu})$  [113]. Clearly the measurement of  $b \rightarrow s\nu\bar{\nu}$  decays at the FCC-ee would provide a powerful test of NP models, especially when the results of various  $b$ -hadron species are combined.

## 10.5 Summary

This chapter has presented the current status of measurements of  $b \rightarrow s\nu\bar{\nu}$  decays and their prospects at current experiments. The current nominal specification of the FCC-ee was described and its general advantages for flavour physics were explained. The remainder

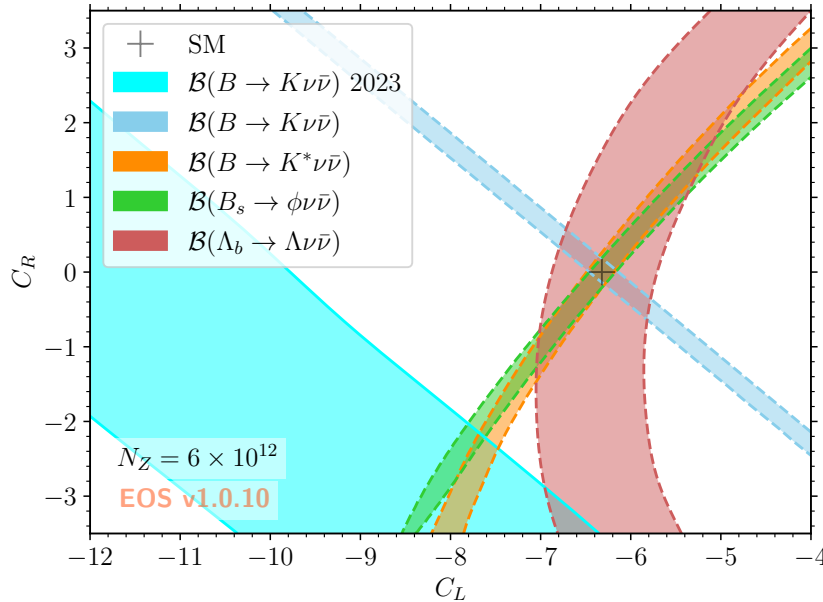


Figure 10.12: Comparison between the current constraint due to  $\mathcal{B}(B \rightarrow K\nu\bar{\nu})$  measurements [113] (cyan band) and the sensitivities predicted at FCC-ee in this study (blue, orange, green and red bands). The experimental uncertainties are those determined in Section 10.3 and the form factors uncertainties are again assumed to have improved by a factor of ten by the time of the FCC-ee measurements.

of the chapter was devoted to a feasibility study for the measurement of  $b \rightarrow s\nu\bar{\nu}$  decays at the FCC-ee that shows that this new collider will allow for measurements that significantly improve upon those from current experiments as well as measurements that are currently impossible. Basic studies were presented to determine required PID and vertexing performance followed by the impact of the measurements on SM and NP interpretations. This forms a foundation from which future studies can be performed to understand the potential of other measurements and inform the design of future detectors. Ref. [27] will serve as an input to the upcoming update to the European Strategy for Particle Physics via the FCC reports and ECFA notes such as Ref. [140].





# 11 Conclusions

“What?”

---

Philomena Cunk

This thesis has presented the results of two studies. The first double Dalitz plane analysis of  $B^0 \rightarrow DK^+\pi^-$  decays at LHCb has successfully been used to extract a value for the CKM angle  $\gamma$ , this result is currently blinded. Although it is not yet finished the majority of the analysis is complete and only a determination of the systematic uncertainties remains. This is the first such analysis of its kind to ever be performed. The feasibility study of  $b \rightarrow s\nu\bar{\nu}$  decay measurements at the FCC-ee is the first study to determine the sensitivity with which the BFs of a variety  $b \rightarrow s\nu\bar{\nu}$  decays could be measured at the FCC-ee and the required detector performance with respect to PID and vertexing.

## 11.1 Double Dalitz

As the first analysis of its kind it is a great success to have successfully extracted  $\gamma$  from LHCb data using this method. Once the systematic uncertainties have been completely determined this analysis will be ready for publication. As the first analysis utilising this novel method it will form a foundation from which LHCb can optimise the method for future runs of the LHC. In particular, now that the background Dalitz distributions are known for the major background decays it will be possible to optimise the  $B$  Dalitz binning with their presence taken into account using the method described in Ref. [62].

In addition to a fully optimised  $B^0 \rightarrow DK^+\pi^-$  analysis one could also consider other multi-body decays of beauty hadrons from which  $\gamma$  could be extracted using this method. The method of optimising the binning and extracting  $\gamma$  could be developed in a general manner such that it can be applied to study other decays such as  $B^+ \rightarrow DK^+\pi^0$  and  $B^+ \rightarrow D\pi^+K_S^0$ . Furthermore one could perform the first double Dalitz analysis of a 4-body  $B$  decay,  $B^+ \rightarrow DK^+\pi^-\pi^+$ , and the first double Dalitz plane analysis of a baryon decay,  $\Lambda_b^0 \rightarrow DpK^-$ . Alternatively it can be used to perform a time-dependent measurement of

the CKM angle  $\beta$  [141].

This work is just the beginning of the utilisation of this novel analysis method which, given proper development, has the potential to become one of the single most sensitive methods for measuring  $\gamma$  which will help LHCb achieve sub-degree sensitivity to  $\gamma$ .

## 11.2 The FCC-ee

### 11.2.1 $b \rightarrow s\nu\bar{\nu}$ at the FCC-ee

Table [11.1] shows the estimated relative uncertainty on certain  $b \rightarrow s\nu\bar{\nu}$  decay BF's if they were to be measured at the FCC-ee. These will be world leading measurements and the first, depending on the exact timelines of the FCC-ee and the Circular Electron-Positron Collider proposed for construction in China [142], for decays from  $B_s^0$  mesons and  $\Lambda_b^0$  baryons. As explained in Section [10.4], they will enable highly sensitive extractions of SM parameters and searches for new physics. As Fig. [10.12] illustrates the variety of decays possible at the FCC-ee will allow for combinations of measurements to achieve incredibly precise extractions of WEFT parameters. Given the number of  $Z$  bosons expected to be produced at the FCC-ee, analyses beyond simple BF measurements will also be possible, for example novel measurements of  $CP$  violation could be performed as noted in Ref. [143].

Decay	Relative BF Uncertainty (%)
$B^0 \rightarrow K^{*0}\nu\bar{\nu}$	0.76
$B_s^0 \rightarrow \phi\nu\bar{\nu}$	1.20
$B^0 \rightarrow K_S^0\nu\bar{\nu}$	3.37
$\Lambda_b^0 \rightarrow \Lambda\nu\bar{\nu}$	9.86

Table 11.1: Estimated relative BF uncertainty for measurements of  $b \rightarrow s\nu\bar{\nu}$  decays at the FCC-ee under nominal experimental conditions and assuming SM physics.

The naive PID and vertexing requirement studies presented in Section [10.3.2] show that the nominal design of the IDEA detector concept is sufficient for highly sensitive measurements of  $b \rightarrow s\nu\bar{\nu}$  decays. Given that the FCC-ee will have four interaction points it is likely that the design of the detectors at each point could be optimised for different kinds of physics analyses. Therefore it will be beneficial to determine the dependence of the detector design on flavour physics measurements in a more detailed manner to guide the designs.

### 11.2.2 FCC-ee flavour physics

The decays studied in Section [10.3] are not the only ones for which the FCC-ee will provide new or vastly improved opportunities.

Other  $b \rightarrow s\nu\bar{\nu}$  decays such as  $B^+ \rightarrow K^+\nu\bar{\nu}$  and  $B_c^+ \rightarrow D_s^+\nu\bar{\nu}$  are obvious candidates. Furthermore, the charged-lepton counterparts of the  $b \rightarrow s\nu\bar{\nu}$  decays will provide complementary probes of new physics. Studies of  $b \rightarrow s\tau^+\tau^-$  will be of particular interest as outlined in Ref. [140]. It is expected that LHCb and Belle II measurements will only be able to set limits on the BFs at two orders of magnitude greater than the SM predictions. Observations of these decays at the FCC-ee will provide probes of NP complementary to existing  $b \rightarrow sl^+l^-$  measurements and the  $b \rightarrow s\nu\bar{\nu}$  measurements. In particular the combination of  $b \rightarrow s\nu\bar{\nu}$  and  $b \rightarrow s\tau^+\tau^-$  measurements will enable searches for NP exhibited by the third generation of leptons [144].

In addition to studies of rare decays the FCC-ee will allow for improved measurements of the CKM sector. During the  $Z$  pole run BF measurements of  $B_{(c)}^+ \rightarrow \tau^+\nu_\tau$  decays will allow for extractions of  $|V_{ub}|$  and  $|V_{cb}|$  significantly more sensitive than possible with current experiments [112, 145]. Additionally, during the  $WW$  run of the FCC-ee the large number of on-shell  $W$  bosons,  $\mathcal{O}(10^8)$ , will allow for sub-percent relative uncertainty measurements of the magnitudes of the up and charm CKM elements [140].

This is not an exhaustive discussion of the potential of the FCC-ee with respect to flavour physics, there is of course plenty of potential for Higgs flavour physics, tests of CKM unitarity,  $\tau$  lepton property measurements and more to be explored in the future. The construction of the FCC-ee is undoubtedly an exciting prospect with significant potential to advance the field of flavour physics.



# A Double Dalitz BDT

The distributions of the training variables for the signal and background samples for the KsHH\_DD topology are shown in the main text in Sec. [5.2.2](#). The distributions for the other topologies are shown here.

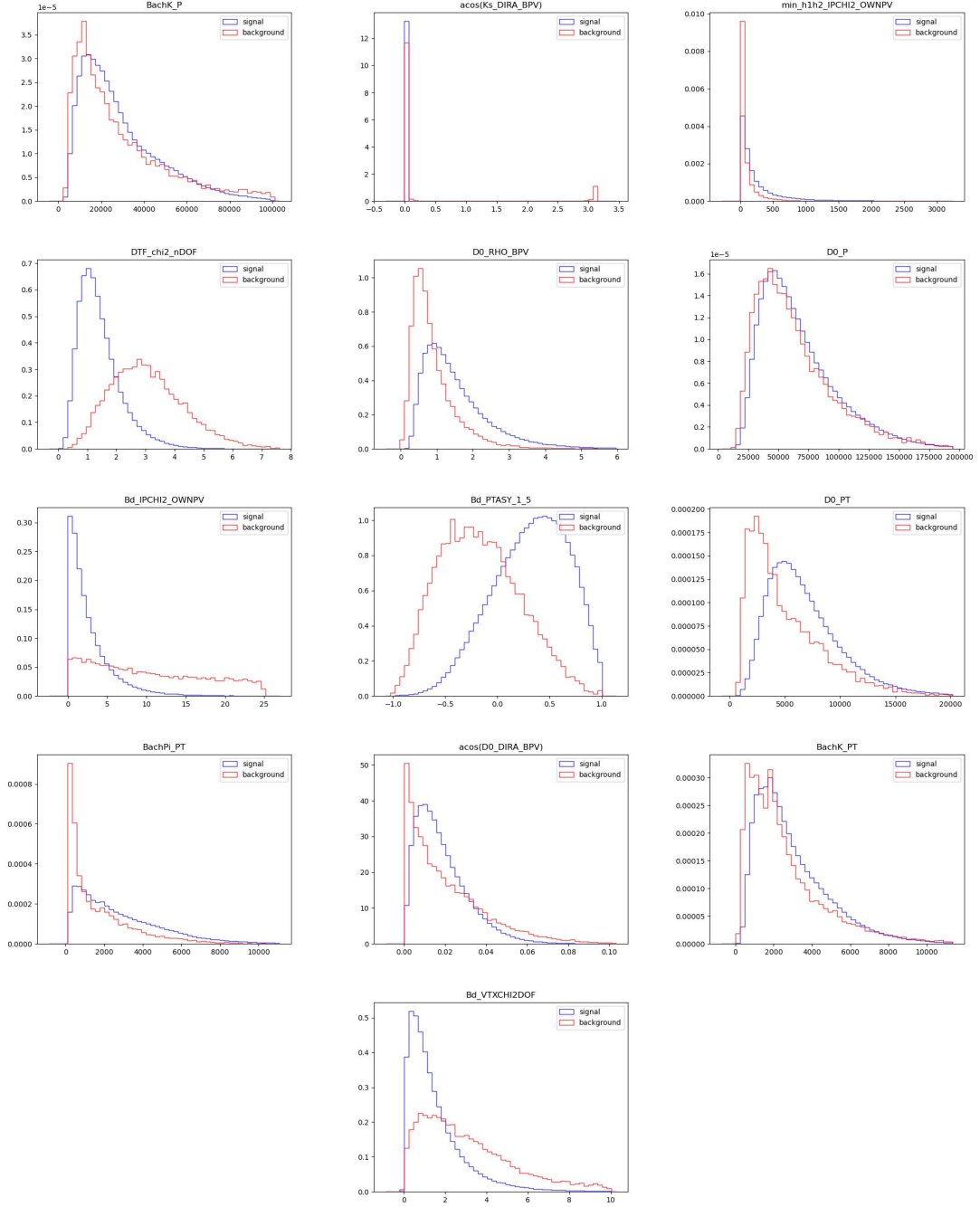


Figure A.1: Comparison between the signal (blue) and background (red) distributions for the BDT input variables used in the  $D \rightarrow K_S^0 \pi^+ \pi^-$  DD topology for Run 1.

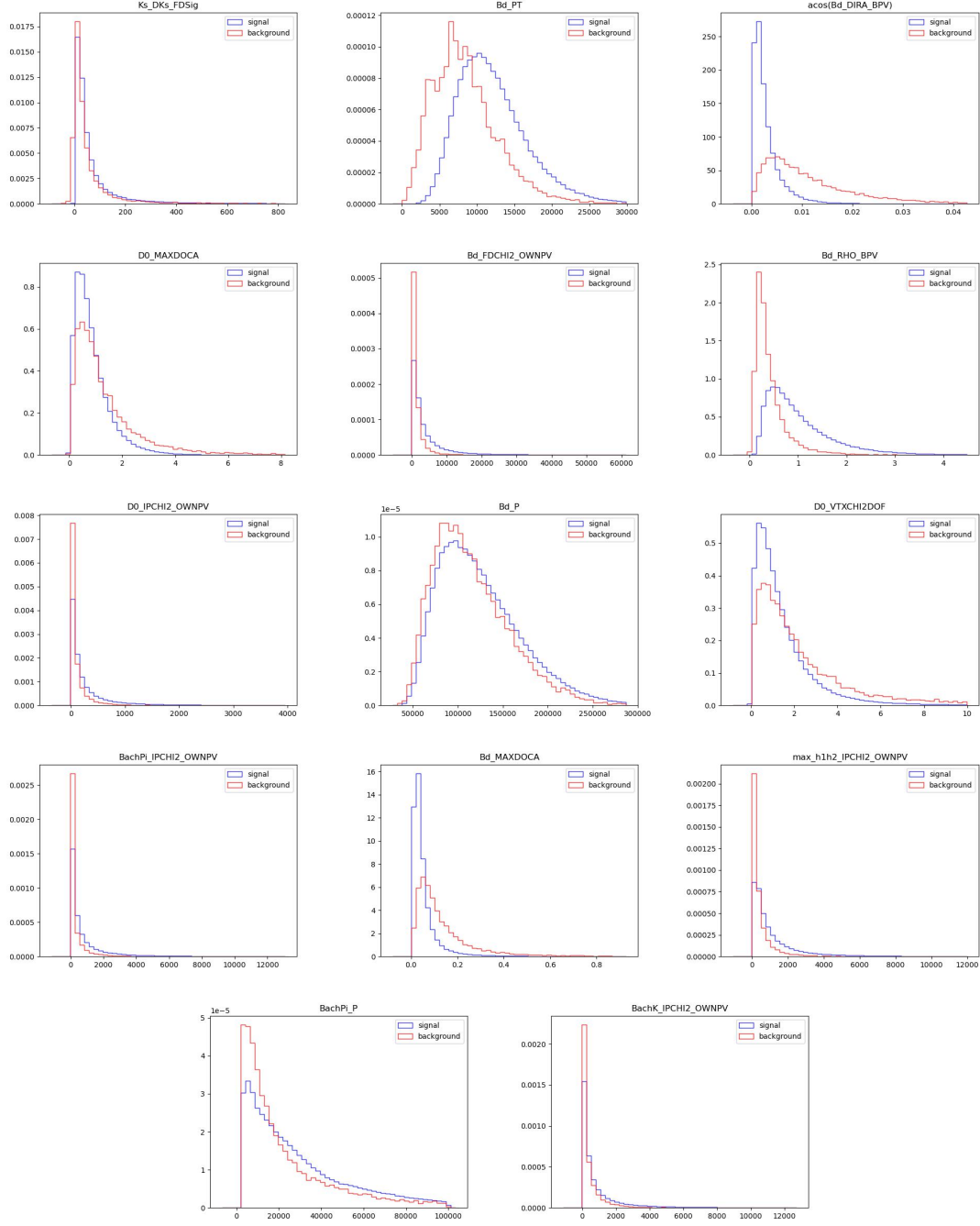


Figure A.2: Comparison between the signal (blue) and background (red) distributions for the BDT input variables used in the  $D \rightarrow K_S^0 \pi^+ \pi^-$  DD topology for Run 1.



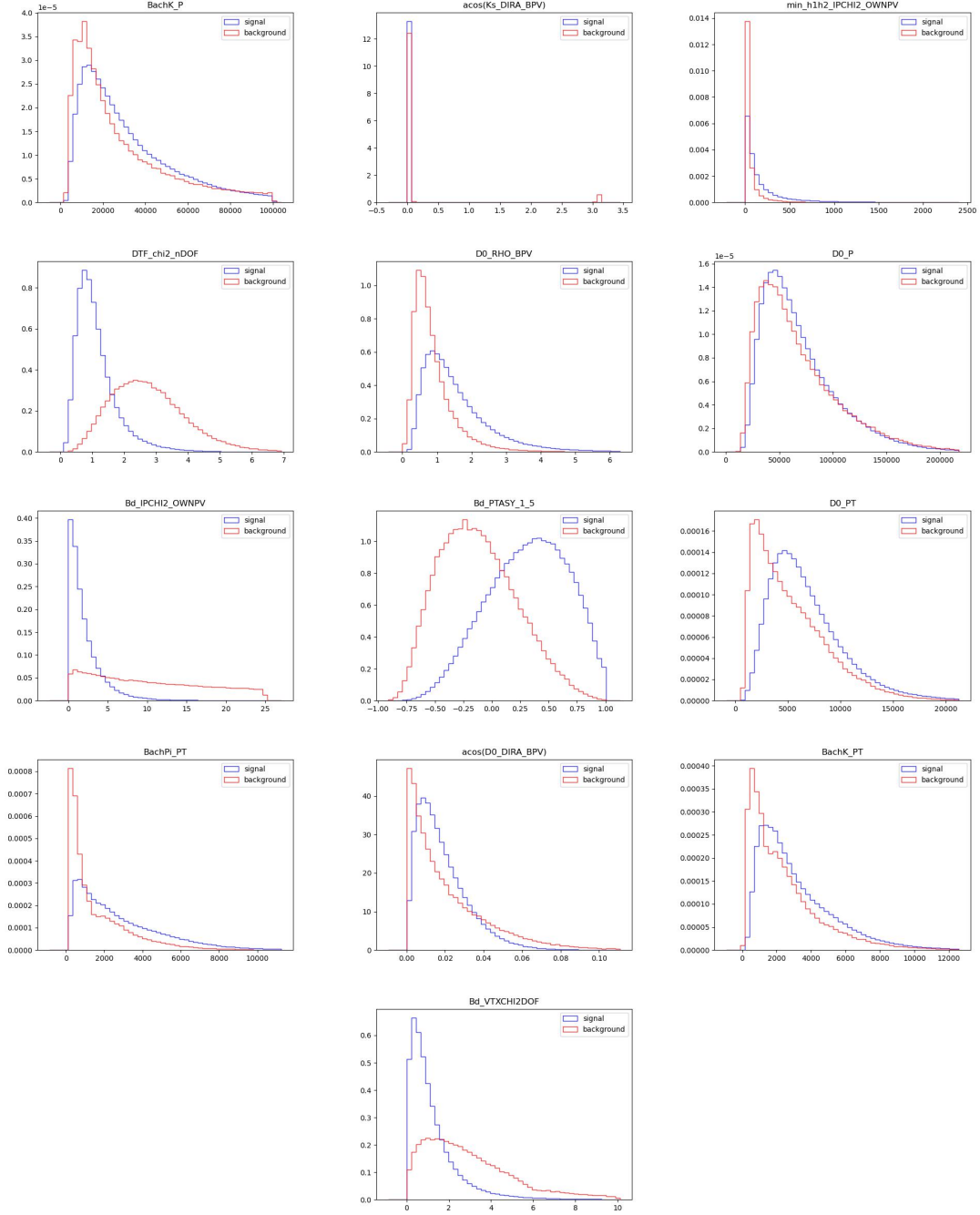


Figure A.3: Comparison between the signal (blue) and background (red) distributions for the BDT input variables used in the  $D \rightarrow K_S^0 \pi^+ \pi^-$  DD topology for Run 2.

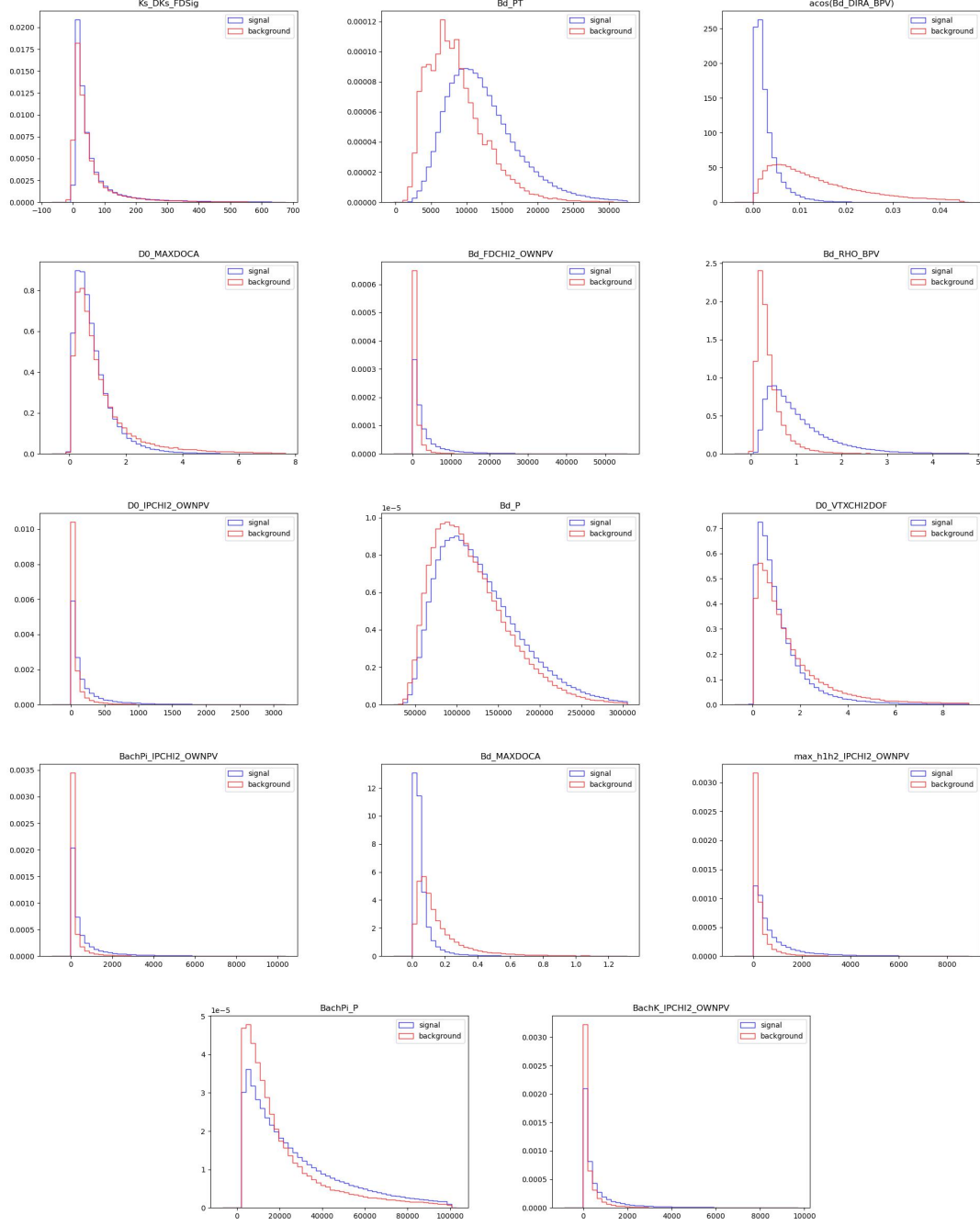


Figure A.4: Comparison between the signal (blue) and background (red) distributions for the BDT input variables used in the  $D \rightarrow K_S^0 \pi^+ \pi^-$  DD topology for Run 2.

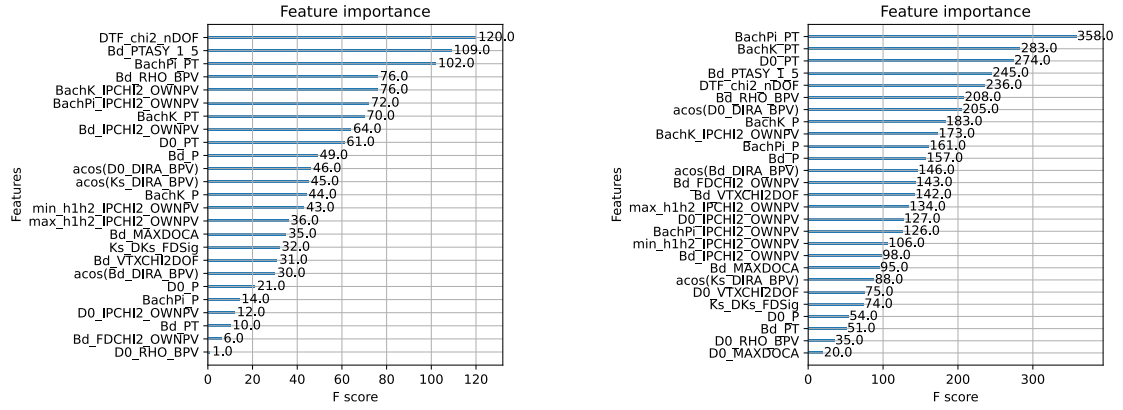


Figure A.5: Feature importance for the input variables to the BDT for the  $D \rightarrow K_S^0 \pi^+ \pi^-$  DD decay.

## B $CP$ fit correlations

The statistical correlation matrix from the data fit is shown in Table B.1. Table B.2 shows the correlations for just the  $x_{\alpha}^{\pm}$ ,  $y_{\alpha}^{\pm}$  and  $(\overline{\kappa})_{\alpha}$  parameters for ease of reading.

[illegible]

Table B.1: Statistical correlation matrix for the  $CP$  fit to data.

	$x_1^+$	$y_1^+$	$x_1^-$	$y_1^-$	$x_2^+$	$y_2^+$	$x_2^-$	$y_2^-$	$x_3^+$	$y_3^+$	$x_3^-$	$y_3^-$	$x_4^+$	$y_4^+$	$x_4^-$	$y_4^-$	$\kappa_1$	$\bar{\kappa}_1$	$\kappa_2$	$\bar{\kappa}_2$	$\kappa_3$	$\bar{\kappa}_3$	$\kappa_4$	$\bar{\kappa}_4$
$x_1^+$	1.00	0.03	0.35	-0.02	0.23	-0.02	0.23	-0.02	0.28	-0.00	0.24	-0.01	0.28	0.00	0.27	0.01	0.02	-0.02	-0.02	0.00	0.02	0.00	0.03	-0.01
$x_1^-$	0.03	1.00	0.01	0.01	-0.02	0.02	-0.02	0.01	-0.00	0.01	0.00	-0.00	0.01	0.00	0.01	0.01	0.09	-0.08	0.08	-0.07	0.07	-0.07	0.07	-0.08
$y_1^+$	0.35	0.01	1.00	-0.05	0.24	-0.02	0.24	-0.02	0.28	-0.00	0.25	-0.01	0.28	0.00	0.28	0.01	-0.00	-0.08	-0.04	0.02	0.00	0.02	0.01	0.01
$y_1^-$	-0.02	0.01	-0.05	1.00	-0.02	0.01	-0.02	0.01	-0.02	0.00	-0.01	0.00	-0.01	0.00	-0.01	0.00	0.01	-0.01	0.02	-0.02	0.01	-0.02	0.01	-0.02
$x_2^+$	0.23	-0.02	0.24	-0.02	1.00	-0.06	1.00	-0.06	0.21	-0.02	0.17	0.02	0.18	-0.00	0.17	0.00	-0.23	0.23	-0.27	0.22	-0.20	0.21	-0.18	0.22
$x_2^-$	-0.02	0.02	-0.02	0.01	-0.06	1.00	-0.04	0.01	-0.02	0.01	-0.01	0.01	-0.01	0.00	-0.00	0.01	0.10	-0.11	0.11	-0.08	0.09	-0.10	0.08	-0.10
$y_2^+$	0.23	-0.02	0.24	-0.02	0.22	-0.04	1.00	-0.00	0.21	-0.02	0.17	0.02	0.18	-0.00	0.18	0.00	-0.21	0.21	-0.24	0.20	-0.17	0.19	-0.16	0.20
$y_2^-$	0.00	0.01	0.00	0.01	-0.00	0.01	-0.00	0.00	-0.00	0.00	0.00	0.00	0.00	0.00	0.00	0.00	0.02	-0.02	0.02	-0.01	0.02	-0.02	0.01	-0.02
$x_3^+$	0.28	-0.00	0.28	-0.02	0.21	-0.02	0.21	-0.00	1.00	-0.02	0.19	0.01	0.22	-0.00	0.21	0.01	-0.08	0.09	-0.11	0.09	-0.11	0.07	-0.05	0.09
$x_3^-$	-0.00	0.01	-0.00	0.00	-0.02	0.01	-0.02	0.00	-0.02	1.00	-0.00	-0.01	0.00	0.00	0.00	0.00	0.07	-0.08	0.07	-0.07	0.09	-0.06	0.06	-0.07
$y_3^+$	0.24	0.00	0.25	-0.01	0.17	-0.01	0.17	0.00	0.19	-0.00	1.00	-0.04	0.19	0.00	0.19	0.01	-0.00	0.01	-0.03	0.01	0.02	-0.01	0.01	0.00
$y_3^-$	-0.01	-0.00	-0.01	0.00	0.02	-0.01	0.02	0.00	0.01	-0.01	-0.04	1.00	-0.01	0.00	-0.01	-0.00	-0.08	0.09	-0.08	0.08	-0.13	0.09	-0.07	0.09
$x_4^+$	0.28	0.01	0.28	-0.01	0.18	-0.01	0.18	0.00	0.22	0.00	0.19	-0.01	1.00	-0.01	0.22	0.01	0.04	-0.03	0.02	-0.02	0.05	-0.02	0.02	-0.03
$x_4^-$	0.00	0.00	0.00	0.00	-0.00	0.00	-0.00	0.00	-0.00	0.00	0.00	0.00	-0.01	1.00	0.00	0.00	0.01	-0.01	0.01	-0.01	0.01	-0.01	0.01	-0.01
$y_4^+$	0.27	0.01	0.28	-0.01	0.17	-0.00	0.18	0.00	0.21	0.00	0.19	-0.01	0.22	0.00	1.00	0.01	0.06	-0.05	0.04	-0.04	0.06	-0.04	0.04	-0.05
$y_4^-$	0.01	0.01	0.01	0.00	0.00	0.01	0.00	0.00	0.01	0.00	0.01	-0.00	0.01	0.00	0.01	1.00	0.02	-0.03	0.02	-0.02	0.02	-0.02	0.03	-0.01
$\kappa_1$	0.02	0.09	-0.00	0.01	-0.23	0.10	-0.21	0.02	-0.08	0.07	-0.00	-0.08	0.04	0.01	0.06	0.02	1.00	-0.88	0.88	-0.78	0.75	-0.78	0.70	-0.87
$\bar{\kappa}_1$	-0.02	-0.08	0.00	-0.01	0.23	-0.11	0.21	-0.02	0.09	-0.08	0.01	0.09	-0.03	-0.01	-0.05	-0.03	-0.88	1.00	-0.88	0.73	-0.77	0.73	-0.79	0.80
$\kappa_2$	-0.02	0.08	-0.04	0.02	-0.27	0.11	-0.24	0.02	-0.11	0.07	-0.03	-0.08	0.02	0.01	0.04	0.02	0.88	-0.88	1.00	-0.81	0.76	-0.79	0.70	-0.88
$\bar{\kappa}_2$	0.00	-0.07	0.02	-0.02	0.22	-0.08	0.20	-0.01	0.09	-0.07	0.01	0.08	-0.02	-0.01	-0.04	-0.02	-0.78	0.73	-0.81	1.00	-0.69	0.65	-0.70	0.72
$\kappa_3$	0.02	0.07	0.00	0.01	-0.20	0.09	-0.17	0.02	-0.11	0.09	0.02	-0.13	0.05	0.01	0.06	0.02	0.75	-0.77	0.76	-0.69	1.00	-0.72	0.61	-0.77
$\bar{\kappa}_3$	0.00	-0.07	0.02	-0.02	0.21	-0.10	0.19	-0.02	0.07	-0.06	-0.01	0.09	-0.02	-0.01	-0.04	-0.02	-0.78	0.73	-0.79	0.65	-0.72	1.00	-0.71	0.71
$\kappa_4$	0.03	0.07	0.01	0.01	-0.18	0.08	-0.16	0.01	-0.05	0.06	0.01	-0.07	0.02	0.01	0.04	0.03	0.70	-0.79	0.70	-0.70	0.61	-0.71	1.00	-0.81
$\bar{\kappa}_4$	-0.01	-0.08	0.01	-0.02	0.22	-0.10	0.20	-0.02	0.09	-0.07	0.00	0.09	-0.03	-0.01	-0.05	-0.01	-0.87	0.80	-0.88	0.72	-0.77	0.71	-0.81	1.00

Table B.2: Statistical correlation matrix for the nominal CP fit.

## C FCC-ee BDT inputs

To illustrate how each BDT input contributes to the BDT discrimination their feature importance and distribution in signal and inclusive background simulated data are shown in Tables C.1 and C.2 and Figs. C.1 to C.6. The background distribution is obtained from a sum of the three background categories weighted according to their production fraction. Similar performance is exhibited in the training for the other decays studied.

Variable	Feature importance
Total energy in the minimum energy hemisphere	0.587132
Total neutral energy in the minimum energy hemisphere	0.166852
Number of reconstructed vertices in the minimum energy hemisphere	0.061202
Total energy in the maximum energy hemisphere	0.052493
Number of neutral particles in the minimum energy hemisphere	0.035719
Maximum radial distance between each vertex and the primary vertex	0.015352
Number of charged particles in the minimum energy hemisphere	0.013361
Minimum radial distance between each vertex and the primary vertex	0.010174
Vertex multiplicity	0.009899
Candidate multiplicity	0.009096
Number of tracks associated to the primary vertex	0.008849
Number of charged particles in the maximum energy hemisphere	0.006313
Number of reconstructed vertices in the maximum energy hemisphere	0.005186
Total neutral energy in the maximum energy hemisphere	0.005098
Total charged energy in the minimum energy hemisphere	0.004624
Average radial distance between each vertex and the primary vertex	0.003763
Number of neutral particles in the maximum energy hemisphere	0.002828
Total charged energy in the maximum energy hemisphere	0.002059

Table C.1: Feature importance for the input variables in the stage 1 BDT for the  $B^0 \rightarrow K^{*0} \nu \bar{\nu}$  decay.

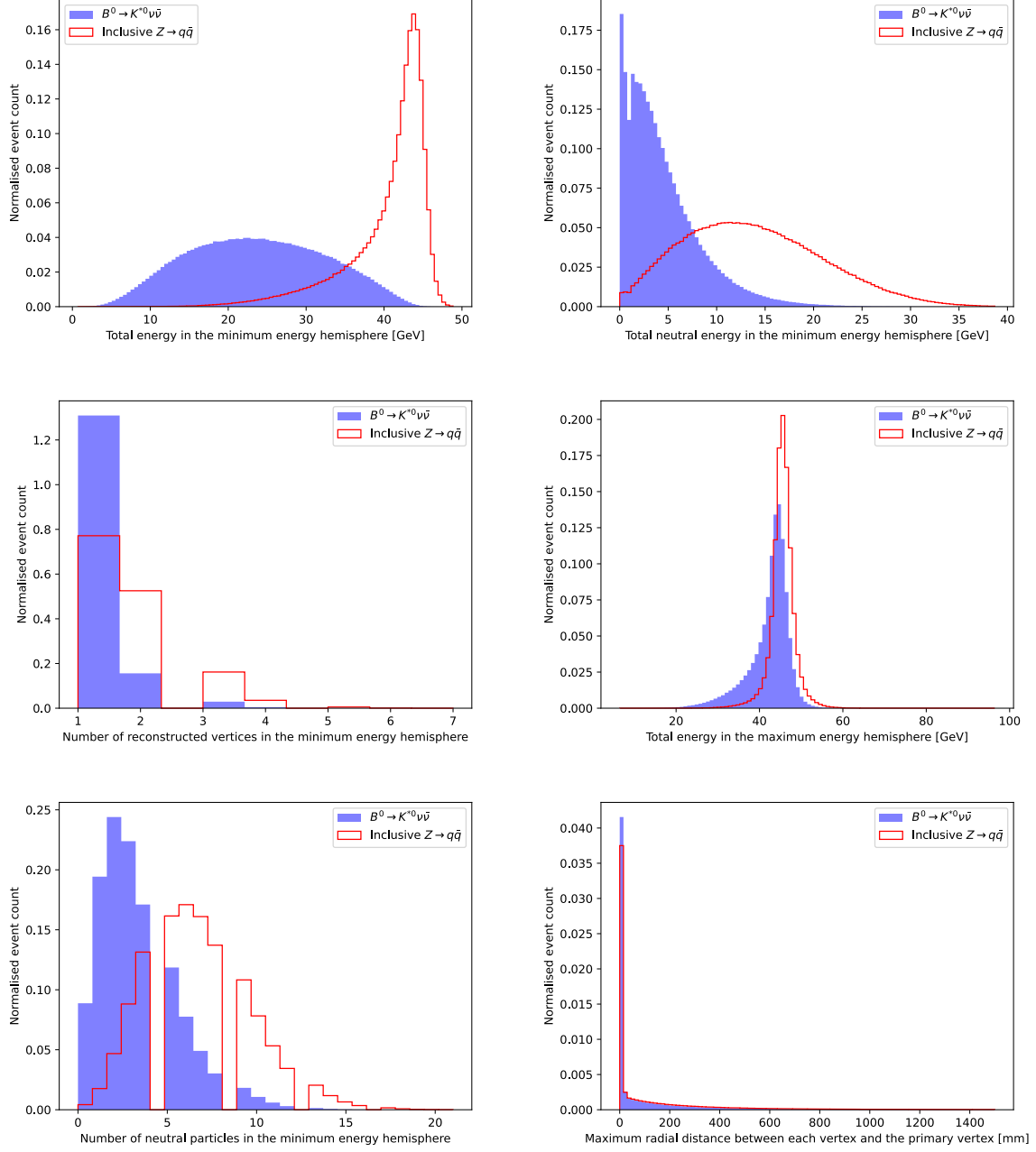


Figure C.1: Distributions of the input variables for the stage 1 BDT in signal and inclusive background simulated data for the  $B^0 \rightarrow K^{*0} \nu \bar{\nu}$  decay, in order of feature importance. Figure one of three.

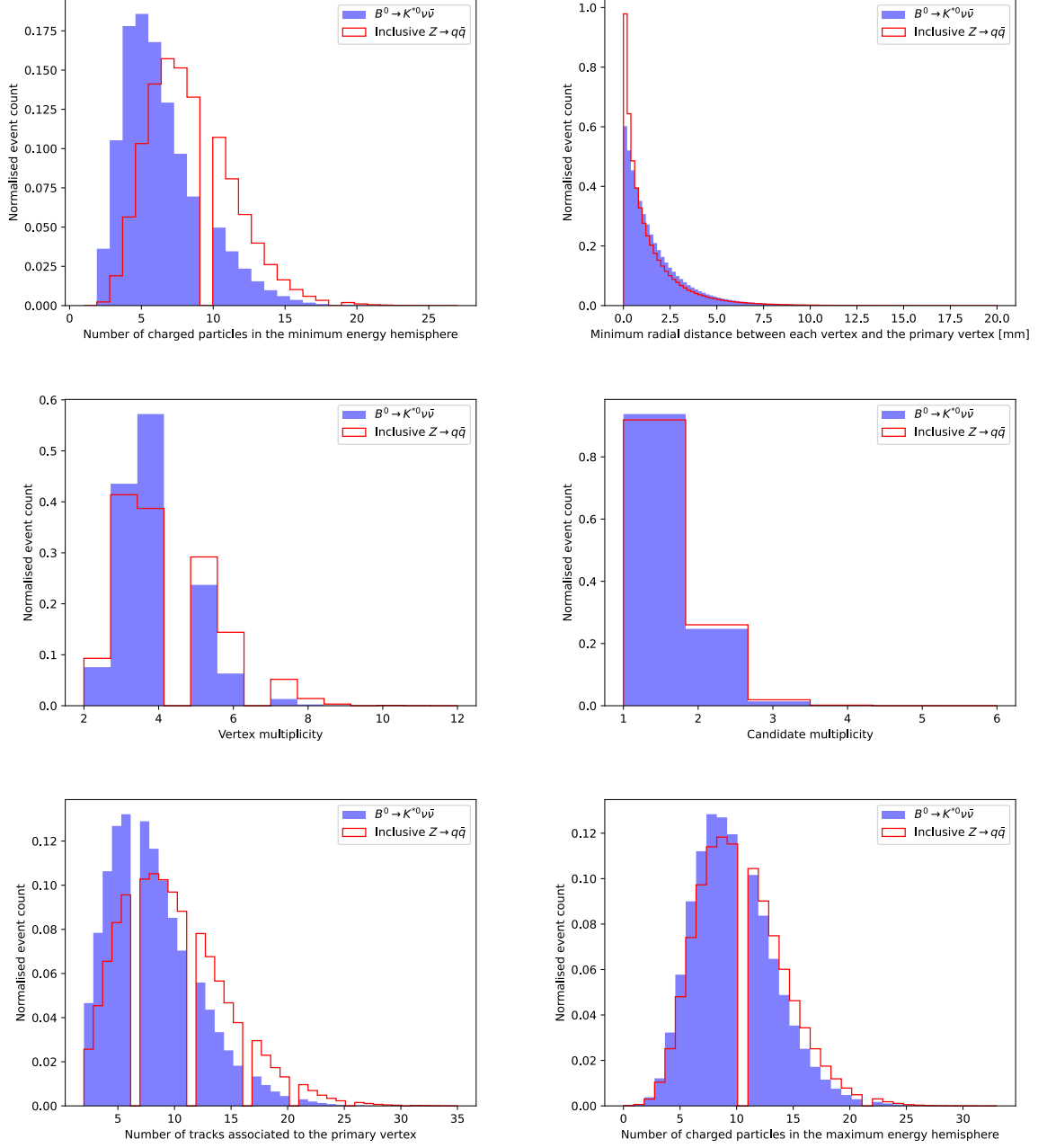


Figure C.2: Distributions of the input variables for the stage 1 BDT in signal and inclusive background simulated data for the  $B^0 \rightarrow K^{*0} \nu \bar{\nu}$  decay, in order of feature importance. Figure two of three.



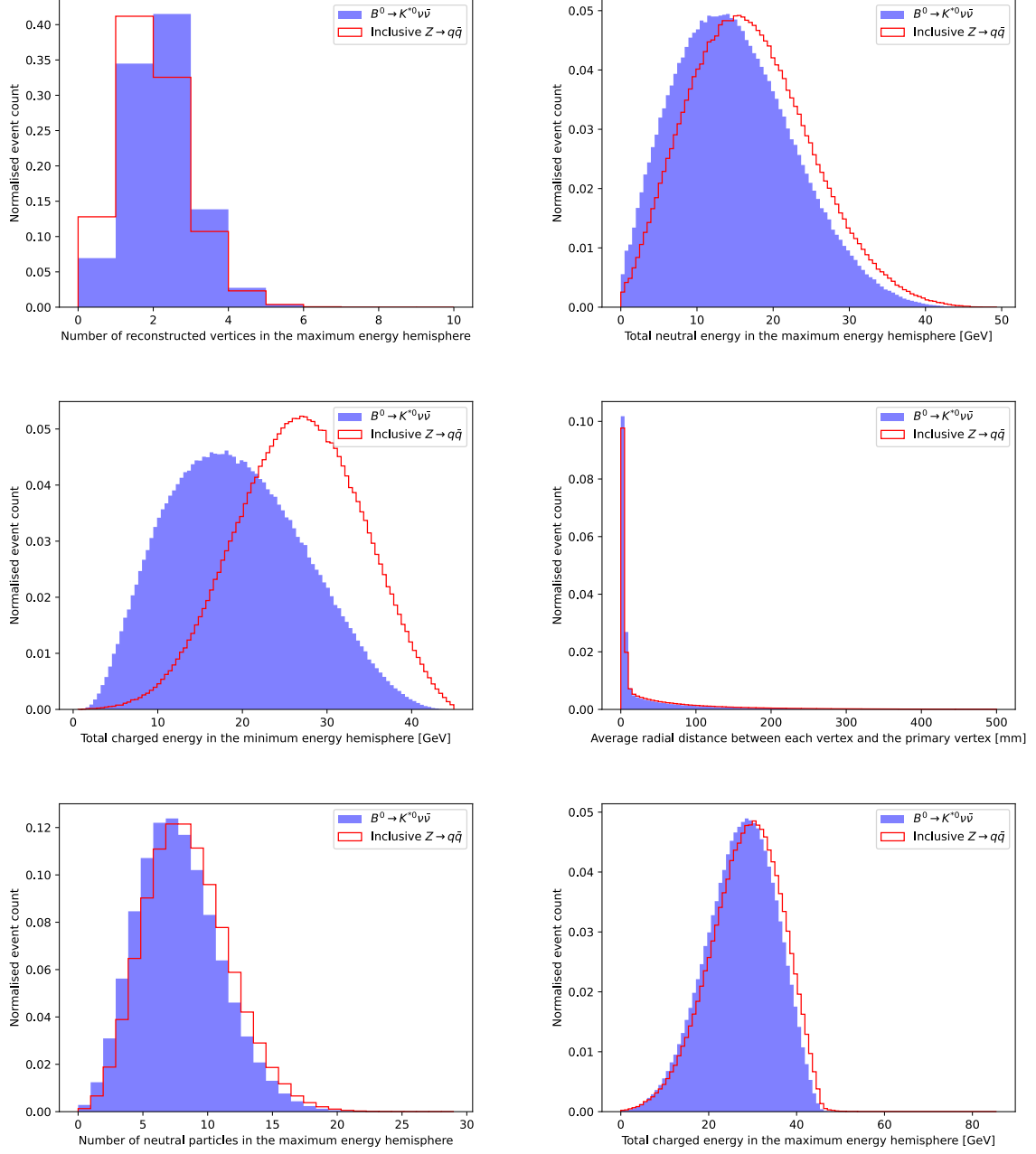


Figure C.3: Distributions of the input variables for the stage 1 BDT in signal and inclusive background simulated data for the  $B^0 \rightarrow K^{*0} \nu \bar{\nu}$  decay, in order of feature importance. Figure three of three.

---

Variable	Feature importance
Nominal energy of the B hadron	0.389404
Candidate mass	0.216474
Candidate angle with respect to the thrust axis	0.065637
Minimum transverse impact parameter of the reconstructed vertices	0.060161
Maximum transverse impact parameter of the reconstructed vertices	0.052633
Candidate transverse impact parameter	0.034654
Primary vertex mass	0.029098
Maximum longitudinal impact parameter of the reconstructed vertices	0.028863
Candidate flight distance	0.022973
Candidate momentum	0.021480
Average longitudinal impact parameter of the reconstructed vertices	0.016834
Candidate $p_x$	0.012371
Minimum longitudinal impact parameter of the reconstructed vertices	0.012317
Candidate $p_y$	0.011666
Candidate longitudinal impact parameter	0.008898
Candidate multiplicity	0.007141
Candidate $p_z$	0.005312
Average transverse impact parameter of the reconstructed vertices	0.003719
Candidate vertex $\chi^2$	0.000365

Table C.2: Feature importance for the input variables in the stage 2 BDT for the  $B^0 \rightarrow K^{*0} \nu \bar{\nu}$  decay.

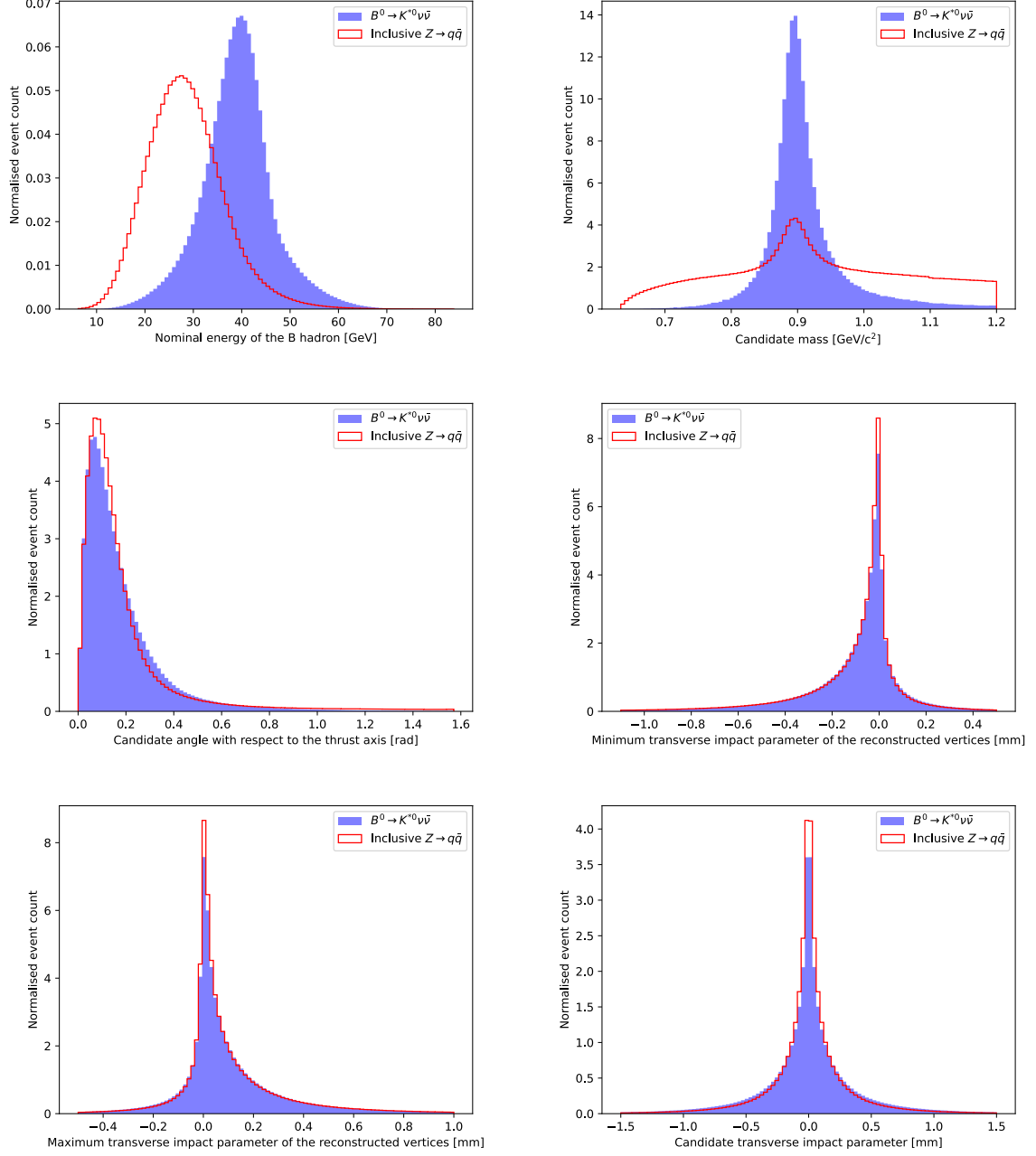


Figure C.4: Distributions of the input variables for the stage 2 BDT in signal and inclusive background simulated data for the  $B^0 \rightarrow K^{*0} \nu \bar{\nu}$  decay, in order of feature importance. Figure three of three.

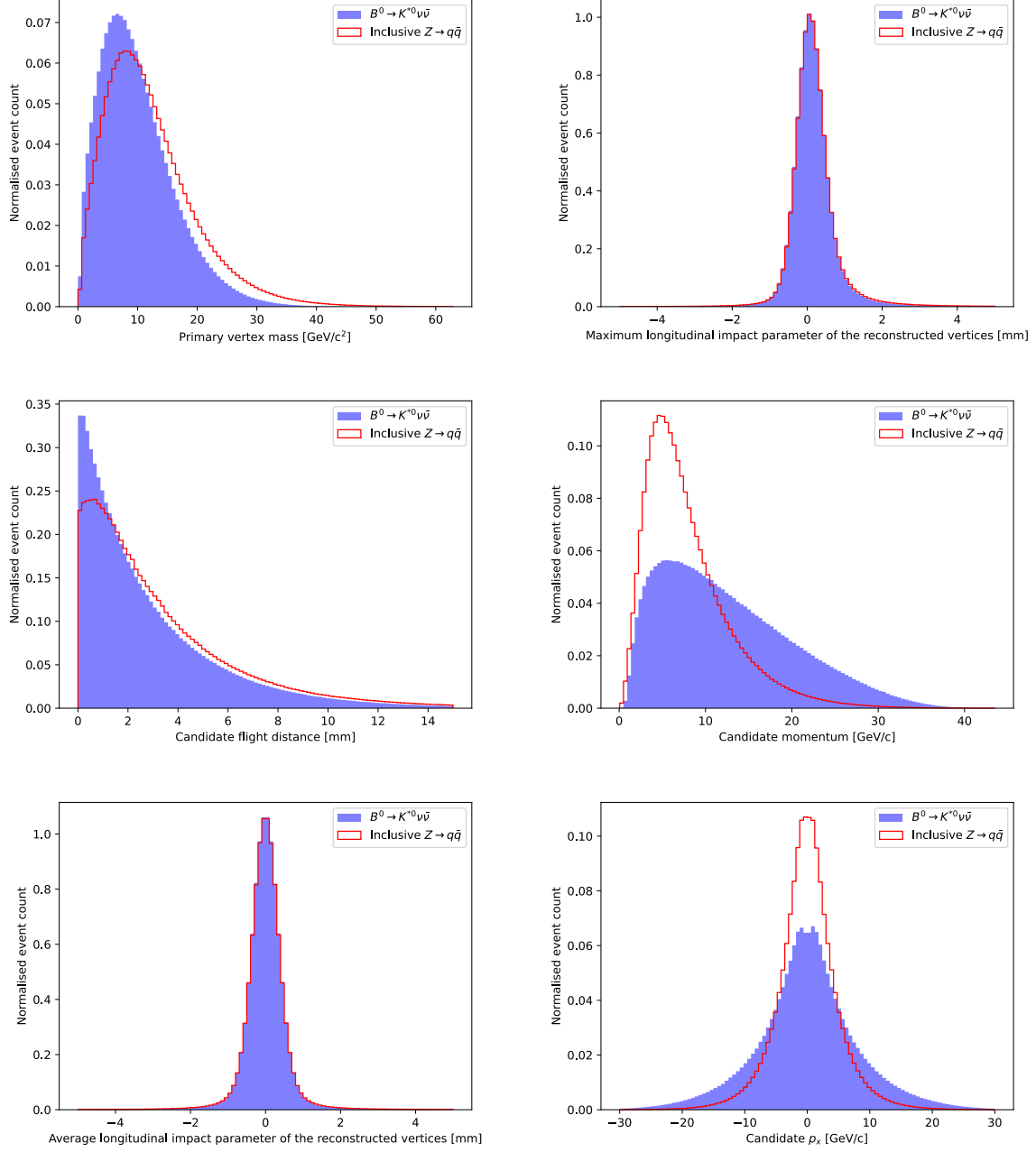


Figure C.5: Distributions of the input variables for the stage 2 BDT in signal and inclusive background simulated data for the  $B^0 \rightarrow K^{*0} \nu \bar{\nu}$  decay, in order of feature importance. Figure three of three.

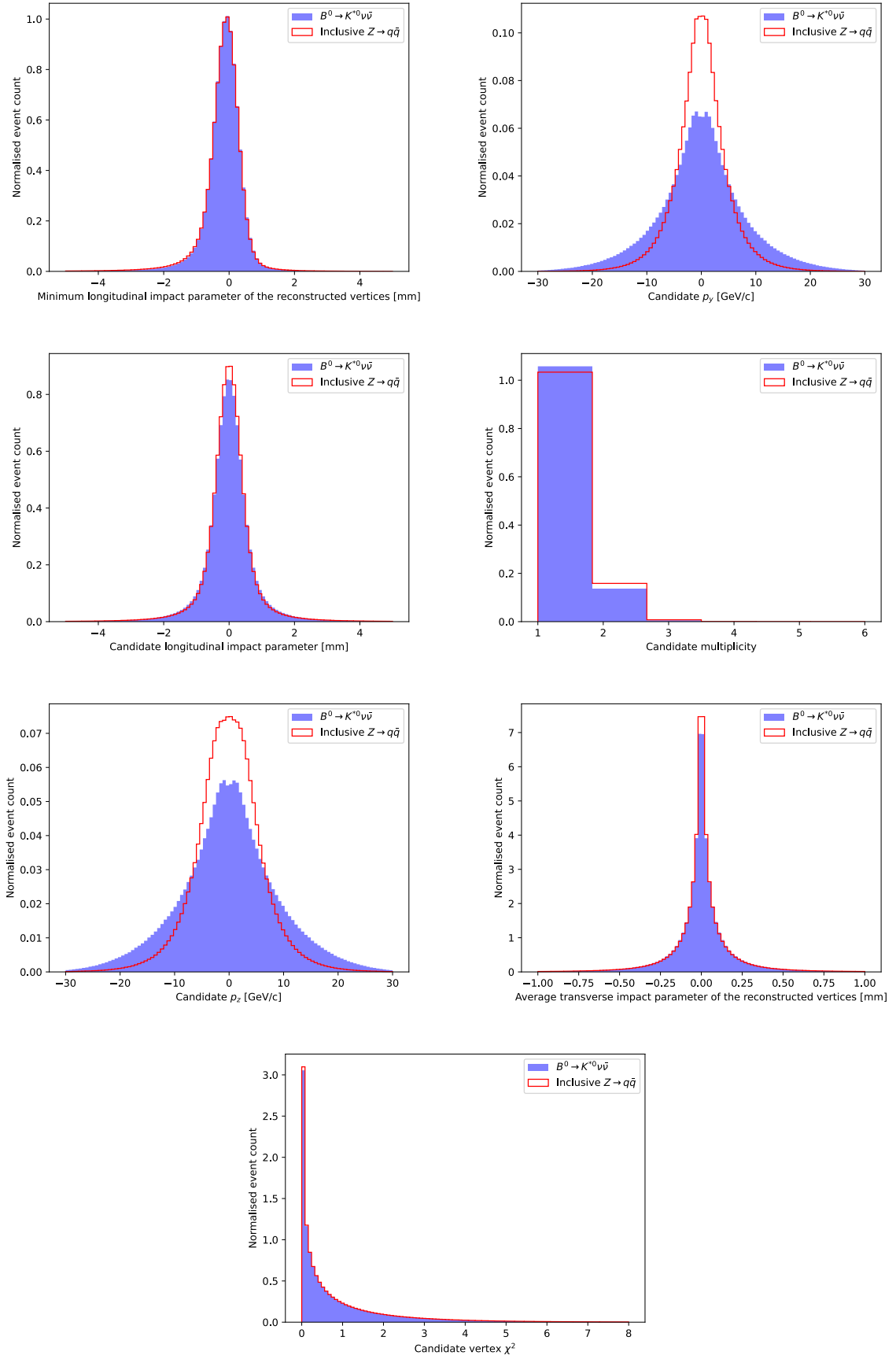


Figure C.6: Distributions of the input variables for the stage 2 BDT in signal and inclusive background simulated data for the  $B^0 \rightarrow K^{*0} \nu \bar{\nu}$  decay, in order of feature importance. Figure three of three.

# References

- [1] ATLAS, G. Aad *et al.*, *Observation of a new particle in the search for the Standard Model Higgs boson with the ATLAS detector at the LHC*, [Phys. Lett. B \*\*716\*\* \(2012\) 1](#), [arXiv:1207.7214](#).
- [2] CMS, S. Chatrchyan *et al.*, *Observation of a New Boson at a Mass of 125 GeV with the CMS Experiment at the LHC*, [Phys. Lett. B \*\*716\*\* \(2012\) 30](#), [arXiv:1207.7235](#).
- [3] A. Riotto, *Theories of baryogenesis*, in *ICTP Summer School in High-Energy Physics and Cosmology*, 1998, [arXiv:hep-ph/9807454](#).
- [4] L. Evans and P. Bryant, *LHC Machine*, [JINST \*\*3\*\* \(2008\) S08001](#).
- [5] FCC, A. Abada *et al.*, *FCC-ee: The Lepton Collider: Future Circular Collider Conceptual Design Report Volume 2*, [Eur. Phys. J. ST \*\*228\*\* \(2019\) 261](#).
- [6] E. Noether, *Invariante Variationsprobleme*, Nachrichten von der Gesellschaft der Wissenschaften zu Göttingen, Mathematisch-Physikalische Klasse **1918** (1918) 235.
- [7] Particle Data Group, R. L. Workman *et al.*, [Review of particle physics](#), [Prog. Theor. Exp. Phys. \*\*2022\*\* \(2022\) 083C01](#).
- [8] G. Luders, *Proof of the TCP theorem*, [Annals Phys. \*\*2\*\* \(1957\) 1](#).
- [9] J. H. Christenson, J. W. Cronin, V. L. Fitch, and R. Turlay, *Evidence for the  $2\pi$  Decay of the  $K_2^0$  Meson*, [Phys. Rev. Lett. \*\*13\*\* \(1964\) 138](#).
- [10] N. Cabibbo, *Unitary symmetry and leptonic decays*, [Phys. Rev. Lett. \*\*10\*\* \(1963\) 531](#).
- [11] M. Kobayashi and T. Maskawa, *CP-violation in the renormalizable theory of weak interaction*, [Prog. Theor. Phys. \*\*49\*\* \(1973\) 652](#).
- [12] L.-L. Chau and W.-Y. Keung, *Comments on the Parametrization of the Kobayashi-Maskawa Matrix*, [Phys. Rev. Lett. \*\*53\*\* \(1984\) 1802](#).
- [13] L. Wolfenstein, *Parametrization of the Kobayashi-Maskawa Matrix*, [Phys. Rev. Lett. \*\*51\*\* \(1983\) 1945](#).

- 
- [14] CKMfitter group, J. Charles *et al.*, *Current status of the standard model CKM fit and constraints on  $\Delta F = 2$  new physics*, [Phys. Rev. \*\*D91\*\* \(2015\) 073007](#), [arXiv:1501.05013](#), updated results and plots available at <http://ckmfitter.in2p3.fr/>.
  - [15] C. Jarlskog, *Commutator of the Quark Mass Matrices in the Standard Electroweak Model and a Measure of Maximal CP Violation*, [Phys. Rev. Lett. \*\*55\*\* \(1985\) 1039](#).
  - [16] J. Brod, A. Lenz, G. Tetlalmatzi-Xolocotzi, and M. Wiebusch, *New physics effects in tree-level decays and the precision in the determination of the quark mixing angle  $\gamma$* , [Phys. Rev. D \*\*92\*\* \(2015\) 033002](#), [arXiv:1412.1446](#).
  - [17] LHCb collaboration, *Simultaneous determination of the CKM angle  $\gamma$  and parameters related to mixing and CP violation in the charm sector*, [LHCb-CONF-2022-003](#), 2022.
  - [18] LHCb collaboration, R. Aaij *et al.*, *Measurement of the CKM angle  $\gamma$  in the  $B^0 \rightarrow D^0 K^{*0}$  channel using self-conjugate  $D^0 \rightarrow K_S^0 h^+ h^-$  decays*, [Eur. Phys. J \*\*C84\*\* \(2024\) 206](#), [arXiv:2309.05514](#).
  - [19] LHCb collaboration, R. Aaij *et al.*, *Study of CP violation in  $B_{(s)}^0 \rightarrow DK^*(892)^0$  decays with  $D \rightarrow K\pi(\pi\pi)$ ,  $\pi\pi(\pi\pi)$ , and  $KK$  final states*, [JHEP \*\*05\*\* \(2024\) 025](#), [arXiv:2401.17934](#).
  - [20] R. H. Dalitz, *On the analysis of  $\tau$ -meson data and the nature of the  $\tau$ -meson*, [Phil Mag. Ser. 7 \*\*44\*\* \(1953\) 1068](#).
  - [21] J. Back *et al.*, LAURA<sup>++</sup>: A Dalitz plot fitter, [Comput. Phys. Commun. \*\*231\*\* \(2018\) 198](#), [arXiv:1711.09854](#).
  - [22] G. N. Fleming, *Recoupling Effects in the Isobar Model. I. General Formalism for Three-Pion Scattering*, [Phys. Rev. \*\*135\*\* \(1964\) B551](#).
  - [23] D. Morgan, *Phenomenological Analysis of  $I = \frac{1}{2}$  Single-Pion Production Processes in the Energy Range 500 to 700 MeV*, [Phys. Rev. \*\*166\*\* \(1968\) 1731](#).
  - [24] D. J. Herndon, P. Söding, and R. J. Cashmore, *Generalized isobar model formalism*, [Phys. Rev. D \*\*11\*\* \(1975\) 3165](#).
  - [25] U. Egede, S. Nishida, M. Patel, and M.-H. Schune, *Electroweak Penguin Decays of  $b$ -Flavored Hadrons*, [Ann. Rev. Nucl. Part. Sci. \*\*72\*\* \(2022\) 283](#), [arXiv:2205.05222](#).
  - [26] S. L. Glashow, J. Iliopoulos, and L. Maiani, *Weak Interactions with Lepton-Hadron Symmetry*, [Phys. Rev. D \*\*2\*\* \(1970\) 1285](#).

- 
- [27] Y. Amhis, M. Kenzie, M. Reboud, and A. R. Wiederhold, *Prospects for searches of  $b \rightarrow s\nu\bar{\nu}$  decays at FCC-ee*, [JHEP \*\*01\*\* \(2024\) 144](#), [arXiv:2309.11353](#).
  - [28] A. J. Buras, J. Girrbach-Noe, C. Niehoff, and D. M. Straub,  *$B \rightarrow K^{(*)}\nu\bar{\nu}$  decays in the Standard Model and beyond*, [JHEP \*\*02\*\* \(2015\) 184](#), [arXiv:1409.4557](#).
  - [29] C.-H. Chen and C. Q. Geng, *Study of  $\Lambda_b \rightarrow \Lambda\nu\bar{\nu}$  with polarized baryons*, [Phys. Rev. D \*\*63\*\* \(2001\) 054005](#), [arXiv:hep-ph/0012003](#).
  - [30] N. Gubernari, M. Reboud, D. van Dyk, and J. Virto, *Dispersive Analysis of  $B \rightarrow K^{(*)}$  and  $B_s \rightarrow \phi$  Form Factors*, [arXiv:2305.06301](#).
  - [31] D. Bećirević, G. Piazza, and O. Sumensari, *Revisiting  $B \rightarrow K^{(*)}\nu\bar{\nu}$  decays in the Standard Model and beyond*, [Eur. Phys. J. C \*\*83\*\* \(2023\) 252](#), [arXiv:2301.06990](#).
  - [32] T. Blake, S. Meinel, M. Rahimi, and D. van Dyk, *Dispersive bounds for local form factors in  $\Lambda_b \rightarrow \Lambda$  transitions*, [arXiv:2205.06041](#).
  - [33] LHCb collaboration, A. A. Alves Jr. *et al.*, *The LHCb detector at the LHC*, [JINST \*\*3\*\* \(2008\) S08005](#).
  - [34] LHCb collaboration, C. Elsasser,  *$\bar{b}b$  production angle plots*, [https://lhcb.web.cern.ch/lhcb/speakersbureau/html/bb\\_ProductionAngles.html](https://lhcb.web.cern.ch/lhcb/speakersbureau/html/bb_ProductionAngles.html). Accessed: 10-May-2024.
  - [35] LHCb collaboration, *LHCb VELO (VERTex LOcator): Technical Design Report*, [CERN-LHCC-2001-011](#), 2001.
  - [36] LHCb collaboration, *LHCb outer tracker: Technical Design Report*, [CERN-LHCC-2001-024](#), 2001.
  - [37] LHCb collaboration, *LHCb inner tracker: Technical Design Report*, [CERN-LHCC-2002-029](#), 2002.
  - [38] LHCb collaboration, R. Aaij *et al.*, *Measurement of the track reconstruction efficiency at LHCb*, [JINST \*\*10\*\* \(2015\) P02007](#), [arXiv:1408.1251](#).
  - [39] R. Arink *et al.*, *Performance of the LHCb Outer Tracker*, [JINST \*\*9\*\* \(2014\) P01002](#), [arXiv:1311.3893](#).
  - [40] LHCb collaboration, *LHCb magnet: Technical Design Report*, [CERN-LHCC-2000-007](#), 2000.
  - [41] LHCb collaboration, *LHCb RICH: Technical Design Report*, [CERN-LHCC-2000-037](#), 2000.



- 
- [42] LHCb RICH Group, M. Adinolfi *et al.*, *Performance of the LHCb RICH detector at the LHC*, [Eur. Phys. J. C \*\*73\*\* \(2013\) 2431](#), [arXiv:1211.6759](#).
- [43] LHCb collaboration, *LHCb calorimeters: Technical Design Report*, [CERN-LHCC-2000-036](#), 2000.
- [44] LHCb collaboration, *LHCb muon system: Technical Design Report*, [CERN-LHCC-2001-010](#), 2001.
- [45] LHCb collaboration, *LHCb muon system: second addendum to the Technical Design Report*, Technical design report. LHCb, CERN, Geneva, 2005. Submitted on 9 Apr 2005.
- [46] LHCb collaboration, R. Aaij *et al.*, *LHCb detector performance*, [Int. J. Mod. Phys. \*\*A30\*\* \(2015\) 1530022](#), [arXiv:1412.6352](#).
- [47] LHCb collaboration, *LHCb performance*, <https://lhcb.web.cern.ch/speakersbureau/html/PerformanceNumbers.html>. Accessed: 06-Nov-2024.
- [48] LHCb, S. Borghi, *Novel real-time alignment and calibration of the LHCb detector and its performance*, [Nucl. Instrum. Meth. A \*\*845\*\* \(2017\) 560](#).
- [49] LHCb collaboration, C. Marin Benito, *PID strategy and performance at LHCb in Run 2*, [PoS ICHEP2018 \(2019\) 687](#).
- [50] R. Aaij *et al.*, *Design and performance of the LHCb trigger and full real-time reconstruction in Run 2 of the LHC*, [JINST \*\*14\*\* \(2019\) P04013](#), [arXiv:1812.10790](#).
- [51] LHCb collaboration, *LHCb trigger system: Technical Design Report*, [CERN-LHCC-2003-031](#), 2003.
- [52] LHCb, R. Quagliani, *Novel real-time alignment and calibration of LHCb detector for Run II and tracking for the upgrade.*, [J. Phys. Conf. Ser. \*\*762\*\* \(2016\) 012046](#).
- [53] LHCb collaboration, R. Aaij *et al.*, *DaVinci*, <https://gitlab.cern.ch/lhcb/DaVinci/>. Accessed: 10-May-2024.
- [54] LHCb collaboration, R. Aaij *et al.*, *Analysis Productions*, <https://lhcb-ap.docs.cern.ch/index.html>. Accessed: 10-May-2024.
- [55] A. Tsaregorodtsev *et al.*, *DIRAC3: The new generation of the LHCb grid software*, [J. Phys. Conf. Ser. \*\*219\*\* \(2010\) 062029](#).

- 
- [56] LHCb collaboration, R. Aaij *et al.*, *Measurement of the CKM angle  $\gamma$  in  $B^\pm \rightarrow DK^\pm$  and  $B^\pm \rightarrow D\pi^\pm$  decays with  $D \rightarrow K_S^0 h^+ h^-$* , [JHEP \*\*02\*\* \(2021\) 0169](#), [arXiv:2010.08483](#).
  - [57] A. Bondar. *Proceedings of BINP special analysis meeting on Dalitz analysis*, 24–26 Sep. 2002.
  - [58] A. Giri *et al.*, *Determining  $\gamma$  using  $B^\pm \rightarrow DK^\pm$  with multibody  $D$  decays*, [Phys. Rev. D \*\*68\*\* \(2003\) 054018](#), [arXiv:hep-ph/0303187](#).
  - [59] A. Bondar and A. Poluektov, *Feasibility study of model-independent approach to  $\phi_3$  measurement using Dalitz plot analysis*, [Eur. Phys. J. C \*\*47\*\* \(2006\) 347](#), [arXiv:hep-ph/0510246](#).
  - [60] A. Bondar and A. Poluektov, *The Use of quantum-correlated  $D^0$  decays for  $\phi_3$  measurement*, [Eur. Phys. J. C \*\*55\*\* \(2008\) 51](#), [arXiv:0801.0840](#).
  - [61] A. Ceccucci *et al.*, *Origins of the method to determine the CKM angle  $\gamma$  using  $B^\pm \rightarrow DK^\pm$ ,  $D \rightarrow K_S^0 \pi^+ \pi^-$  decays*, [arXiv:2006.12404](#).
  - [62] CLEO collaboration, J. Libby *et al.*, *Model-independent determination of the strong-phase difference between  $D^0$  and  $\bar{D}^0 \rightarrow K_{S,L}^0 h^+ h^-$  ( $h = \pi, K$ ) and its impact on the measurement of the CKM angle  $\gamma/\phi_3$* , [Phys. Rev. D \*\*82\*\* \(2010\) 112006](#), [arXiv:1010.2817](#).
  - [63] M. Bjørn and S. Malde, *CP violation and material interaction of neutral kaons in measurements of the CKM angle  $\gamma$  using  $B^\pm \rightarrow DK^\pm$  decays where  $D \rightarrow K_S^0 \pi^+ \pi^-$* , [JHEP \*\*07\*\* \(2019\) 106](#), [arXiv:1904.01129](#).
  - [64] J. Garra Tico, *A strategy for a simultaneous measurement of CP violation parameters related to the CKM angle  $\gamma$  in multiple  $B$  meson decay channels*, [arXiv:1804.05597](#).
  - [65] BESIII collaboration, M. Ablikim *et al.*, *Model-independent determination of the relative strong-phase difference between  $D^0$  and  $\bar{D}^0 \rightarrow K_{S,L}^0 \pi^+ \pi^-$  and its impact on the measurement of the CKM angle  $\gamma/\phi_3$* , [Phys. Rev. D \*\*101\*\* \(2020\) 112002](#), [arXiv:2003.00091](#).
  - [66] BESIII collaboration, M. Ablikim *et al.*, *Improved model-independent determination of the strong-phase difference between  $D^0$  and  $\bar{D}^0 \rightarrow K_{S,L}^0 K^+ K^-$  decays*, [Phys. Rev. D \*\*102\*\* \(2020\) 052008](#), [arXiv:2007.07959](#).
  - [67] I. Mackay, S. Malde, H. Pullen, and G. Wilkinson, *A measurement of the CKM angle  $\gamma$  using  $B^0 \rightarrow DK^{*0}$  decays in the  $D \rightarrow K_S^0 \pi^+ \pi^-$ ,  $K_S^0 K^+ K^-$  final states using the Run 1 and Run 2 data set*, [LHCb-ANA-2020-032](#), 2023.

- 
- [68] LHCb collaboration, R. Aaij *et al.*, *A model-independent Dalitz plot analysis of  $B^\pm \rightarrow DK^\pm$  with  $D \rightarrow K_S^0 h^+ h^-$  ( $h = \pi, K$ ) decays and constraints on the CKM angle  $\gamma$* , [Phys. Lett. \*\*B718\*\* \(2012\) 43](#), [arXiv:1209.5869](#).
  - [69] LHCb collaboration, R. Aaij *et al.*, *Measurement of the CKM angle  $\gamma$  using  $B^\pm \rightarrow DK^\pm$  with  $D \rightarrow K_S^0 \pi^+ \pi^-$ ,  $K_S^0 K^+ K^-$  decays*, [JHEP \*\*10\*\* \(2014\) 097](#), [arXiv:1408.2748](#).
  - [70] LHCb collaboration, R. Aaij *et al.*, *Measurement of the CKM angle  $\gamma$  using  $B^\pm \rightarrow DK^\pm$  with  $D \rightarrow K_S^0 \pi^+ \pi^-$ ,  $K_S^0 K^+ K^-$  decays*, [JHEP \*\*08\*\* \(2018\) 176](#), Erratum [ibid. \*\*10\*\* \(2018\) 107](#), [arXiv:1806.01202](#).
  - [71] T. Gershon and A. Poluektov, *Double Dalitz Plot Analysis of the Decay  $B^0 \rightarrow DK^+ \pi^-$ ,  $D \rightarrow K_S^0 \pi^+ \pi^-$* , [Phys. Rev. D \*\*81\*\* \(2010\) 014025](#), [arXiv:0910.5437](#).
  - [72] LHCb collaboration, R. Aaij *et al.*, *Constraints on the unitarity triangle angle  $\gamma$  from Dalitz plot analysis of  $B^0 \rightarrow DK^+ \pi^-$  decays*, [Phys. Rev. \*\*D93\*\* \(2016\) 112018](#), Erratum [ibid. \*\*D94\*\* \(2016\) 079902](#), [arXiv:1602.03455](#).
  - [73] D. Craik, T. Gershon, and A. Poluektov, *Optimising sensitivity to  $\gamma$  with  $B^0 \rightarrow DK^+ \pi^-$ ,  $D \rightarrow K_S^0 \pi^+ \pi^-$  double Dalitz plot analysis*, [Phys. Rev. D \*\*97\*\* \(2018\) 056002](#), [arXiv:1712.07853](#).
  - [74] Belle collaboration, *Study of  $B^0 \rightarrow \pi^+ \pi^-$  decays*, [arXiv:hep-ex/0412072](#).
  - [75] Belle, A. Poluektov *et al.*, *Measurement of  $\phi(3)$  with Dalitz plot analysis of  $B+ \rightarrow D(*)K(*)+$  decay*, [Phys. Rev. D \*\*73\*\* \(2006\) 112009](#), [arXiv:hep-ex/0604054](#).
  - [76] M. Gronau, *Improving bounds on  $\gamma$  in  $B^\pm \rightarrow DK^\pm$  and  $B^{\pm,0} \rightarrow DX_s^{\pm,0}$* , [Phys. Lett. \*\*B 557\*\* \(2003\) 198](#), [arXiv:hep-ph/0211282](#).
  - [77] BESIII collaboration, M. Ablikim *et al.*, *Measurement of the  $D \rightarrow K^- \pi^+ \pi^+ \pi^-$  and  $D \rightarrow K^- \pi^+ \pi^0$  coherence factors and average strong-phase differences in quantum-correlated  $D\bar{D}$  decays*, [JHEP \*\*05\*\* \(2021\) 164](#), [arXiv:2103.05988](#).
  - [78] M. Gronau and D. Wyler, *On determining a weak phase from charged  $B$  decay asymmetries*, [Physics Letters B \*\*265\*\* \(1991\) 172](#).
  - [79] M. Gronau and D. London, *How to determine all the angles of the unitarity triangle from  $B^0 \rightarrow DK_s^0$  and  $B_s^0 \rightarrow D\varphi$* , [Physics Letters B \*\*253\*\* \(1991\) 483](#).
  - [80] M. Bjorn and S. Malde, *Measurement of the CKM angle  $\gamma$  in  $B^\pm \rightarrow [K_S^0 h^+ h^-]_D h^\pm$  decays using the full Run 1 and 2 dataset*, [LHCb-ANA-2020-001](#), 2020.

- 
- [81] BESIII collaboration, M. Ablikim *et al.*, *Measurement of the CP-even fraction of  $D^0 \rightarrow \pi^+\pi^-\pi^+\pi^-$* , [arXiv:2208.10098](#).
  - [82] BESIII collaboration, M. Ablikim *et al.*, *Improved measurement of the strong-phase difference  $\delta_D^{K\pi}$  in quantum-correlated  $D\bar{D}$  decays*, [Eur. Phys. J. C \*\*82\*\* \(2022\) 1009](#), [arXiv:2208.09402](#).
  - [83] M. Battaglieri *et al.*, *Analysis Tools for Next-Generation Hadron Spectroscopy Experiments*, [Acta Phys. Polon. B \*\*46\*\* \(2015\) 257](#), [arXiv:1412.6393](#).
  - [84] Hans Dembinski and Piti Ongmongkolkul *et al.*, *scikit-hep/iminuit*, .
  - [85] F. James and M. Roos, *Minuit: A System for Function Minimization and Analysis of the Parameter Errors and Correlations*, [Comput. Phys. Commun. \*\*10\*\* \(1975\) 343](#).
  - [86] W. D. Hulsbergen, *Decay chain fitting with a Kalman filter*, [Nucl. Instrum. Meth \*\*A552\*\* \(2005\) 566](#), [arXiv:physics/0503191](#).
  - [87] T. Head, *The LHCb trigger system*, [JINST \*\*9\*\* \(2014\) C09015](#).
  - [88] V. V. Gligorov and M. Williams, *Efficient, reliable and fast high-level triggering using a bonsai boosted decision tree*, [JINST \*\*8\*\* \(2013\) P02013](#), [arXiv:1210.6861](#).
  - [89] Particle Data Group, P. A. Zyla *et al.*, *Review of particle physics*, [Prog. Theor. Exp. Phys. \*\*2020\*\* \(2020\) 083C01](#).
  - [90] A. Poluektov, *Correction of simulated PID response with variable transformation*, <https://indico.cern.ch/event/572934/contributions/2318786/attachments/1357558/2052812/pidcorr.pdf>. Accessed: 31-May-2020.
  - [91] T. Chen and C. Guestrin, *XGBoost: A Scalable Tree Boosting System*, [KDD '16: Proceedings of the 22nd ACM SIGKDD International Conference on Knowledge Discovery and Data Mining \(2016\) 785](#), [arXiv:1603.02754](#).
  - [92] D. Craik, T. Gershon, T. Latham, and M. Whitehead, *Measurement of  $\gamma$  with an amplitude analysis of  $B^0 \rightarrow DK^+\pi^-$  decays*, [LHCb-ANA-2015-024](#), 2015.
  - [93] Anjos, J. C. *et al.*, *Dalitz plot analysis of  $D \rightarrow K\pi\pi$  decays*, [Phys. Rev. D \*\*48\*\* \(1993\) 56](#).
  - [94] BaBar collaboration, B. Aubert *et al.*, *Dalitz plot analysis of  $D^0$  hadronic decays  $D^0 \rightarrow K^0K^-\pi^+$ ,  $D^0 \rightarrow \bar{K}^0K^+\pi^-$  and  $D^0 \rightarrow \bar{K}^0K^+K^-$* , in *31st International Conference on High Energy Physics*, 2002, [arXiv:hep-ex/0207089](#).

- 
- [95] LHCb collaboration, R. Aaij *et al.*, *Dalitz plot analysis of  $B_s^0 \rightarrow \bar{D}^0 K^- \pi^+$  decays*, [Phys. Rev. \*\*D90\*\* \(2014\) 072003](#), [arXiv:1407.7712](#).
  - [96] T. Gershon *et al.*, *Time-dependent CP asymmetries in  $B^0 \rightarrow D \pi^+ \pi^-$* , [LHCb-ANA-2022-016](#), 2022.
  - [97] A. Brossa Gonzalo, T. Gershon, M. W. Kenzie, and T. E. Latham, *Observations of the  $B_s^0 \rightarrow \bar{D}^{*0} K^- \pi^+$  and  $B^0 \rightarrow \bar{D}^{*0} K^+ \pi^-$  decays*, [LHCb-ANA-2020-014](#), 2020.
  - [98] LHCb collaboration, R. Aaij *et al.*, *Study of beauty baryon decays to  $D^0 p h^-$  and  $\Lambda_c^+ h^-$  final states*, [Phys. Rev. \*\*D89\*\* \(2014\) 032001](#), [arXiv:1311.4823](#).
  - [99] LHCb collaboration, R. Aaij *et al.*, *Observation of the suppressed  $\Lambda_b^0 \rightarrow D p K^-$  decay with  $D \rightarrow K^+ \pi^-$  and measurement of its CP asymmetry*, [Phys. Rev. \*\*D104\*\* \(2021\) 112008](#), [arXiv:2109.02621](#).
  - [100] LHCb collaboration, R. Aaij *et al.*, *Observation of the  $B^0 \rightarrow \bar{D}^{*0} K^+ \pi^-$  and  $B_s^0 \rightarrow \bar{D}^{*0} K^- \pi^+$  decays*, [Phys. Rev. \*\*D105\*\* \(2022\) 072005](#), [arXiv:2112.11428](#).
  - [101] G. A. Cowan, D. C. Craik, and M. D. Needham, *RapidSim: an application for the fast simulation of heavy-quark hadron decays*, [Comput. Phys. Commun. \*\*214\*\* \(2017\) 239](#), [arXiv:1612.07489](#).
  - [102] D. J. Lange, *The EvtGen particle decay simulation package*, [Nucl. Instrum. Meth \*\*A462\*\* \(2001\) 152](#).
  - [103] A. Mathad, D. O’Hanlon, A. Poluektov, and R. Rabadan, *Efficient description of experimental effects in amplitude analyses*, [JINST \*\*16\*\* \(2021\) P06016](#), [arXiv:1902.01452](#).
  - [104] D. Ao *et al.*, *Observation of the decays  $B_{(s)}^0 \rightarrow D_{s1}(2536)^\mp K^\pm$* , [LHCb-ANA-2021-026](#), 2021.
  - [105] T. Skwarnicki, *A study of the radiative cascade transitions between the Upsilon-prime and Upsilon resonances*, PhD thesis, Institute of Nuclear Physics, Krakow, 1986, [DESY-F31-86-02](#).
  - [106] D. Hill and P. Gandini, *Probability density functions for describing partially reconstructed B-hadron decays*, [LHCb-INT-2020-017](#), 2020.
  - [107] H. Pullen, G. Wilkinson, N. Jurik, and M. John, *Analysis of  $B_{(s)}^0 \rightarrow D K^{*0}$  with  $D \rightarrow K \pi, K K, \pi \pi, K \pi \pi \pi$  final states*, [LHCb-ANA-2018-044](#), 2018.

- 
- [108] LHCb collaboration, R. Aaij *et al.*, *Precise measurement of the  $f_s/f_d$  ratio of fragmentation fractions and of  $B_s^0$  decay branching fractions*, [Phys. Rev. \*\*D104\*\* \(2021\) 032005](#), [arXiv:2103.06810](#).
  - [109] T. M. Karbach and M. Schlupp, *Constraints on yield parameters in extended maximum likelihood fits*, [arXiv:1210.7141](#).
  - [110] M. Kenzie, *LHCb Gamma Combination 2015 update*, [LHCb-ANA-2015-046](#), 2015.
  - [111] S. Bodhisattva, M. Walker, and M. Woodroffe, *On the unified method with nuisance parameters*, *Statist. Sinica* **19** (2009) 301.
  - [112] Y. Amhis *et al.*, *Prospects for  $B_c^+ \rightarrow \tau^+ \nu_\tau$  at FCC-ee*, [JHEP \*\*12\*\* \(2021\) 133](#), [arXiv:2105.13330](#).
  - [113] Belle-II, I. Adachi *et al.*, *Evidence for  $B^+ \rightarrow K^+ \nu \bar{\nu}$  Decays*, [arXiv:2311.14647](#).
  - [114] Belle, J. Grygier *et al.*, *Search for  $B \rightarrow h \nu \bar{\nu}$  decays with semileptonic tagging at Belle*, [Phys. Rev. D \*\*96\*\* \(2017\) 091101](#), [arXiv:1702.03224](#), [Addendum: *Phys. Rev. D* **97**, 099902 (2018)].
  - [115] Belle, O. Lutz *et al.*, *Search for  $B \rightarrow h^{(*)} \nu \bar{\nu}$  with the full Belle  $\Upsilon(4S)$  data sample*, [Phys. Rev. D \*\*87\*\* \(2013\) 111103](#), [arXiv:1303.3719](#).
  - [116] DELPHI, W. Adam *et al.*, *Study of rare  $b$  decays with the DELPHI detector at LEP*, [Z. Phys. C \*\*72\*\* \(1996\) 207](#).
  - [117] Belle II, W. Altmannshofer *et al.*, *The Belle II Physics Book*, [PTEP \*\*2019\*\* \(2019\) 123C01](#), [arXiv:1808.10567](#), [Erratum: *PTEP* **2020**, 029201 (2020)].
  - [118] FCC collaboration, *Future Circular Collider (FCC) Feasibility Study Midterm Report*, .
  - [119] FCC PED Flavour Group, A. R. Wiederhold, *Flavour prospects at the FCC-ee*, [PoS \*\*HQL2023\*\* \(2024\) 057](#).
  - [120] LHCb collaboration, R. Aaij *et al.*, *Measurement of the  $b$ -quark production cross-section in 7 and 13 TeV  $pp$  collisions*, [Phys. Rev. Lett. \*\*118\*\* \(2017\) 052002](#), Erratum [ibid. \*\*119\*\* \(2017\) 169901](#), [arXiv:1612.05140](#).
  - [121] LHCb collaboration, *Physics case for an LHCb Upgrade II — Opportunities in flavour physics, and beyond, in the HL-LHC era*, [arXiv:1808.08865](#).
  - [122] S. Monteil and G. Wilkinson, *Heavy-quark opportunities and challenges at FCC-ee*, [Eur. Phys. J. Plus \*\*136\*\* \(2021\) 837](#), [arXiv:2106.01259](#).



- 
- [123] L. Li, M. Ruan, Y. Wang, and Y. Wang, *Analysis of  $B_s^0 \rightarrow \phi \nu \bar{\nu}$  at CEPC*, [Phys. Rev. D \*\*105\*\* \(2022\) 114036](#), [arXiv:2201.07374](#).
  - [124] M. Adinolfi *et al.*, *The tracking detector of the KLOE experiment*, [Nucl. Instrum. Meth. A \*\*488\*\* \(2002\) 51](#).
  - [125] A. M. Baldini *et al.*, *MEG Upgrade Proposal*, [arXiv:1301.7225](#).
  - [126] G. Chiarello *et al.*, *A new construction technique of high granularity and high transparency drift chambers for modern high energy physics experiments*, [Nucl. Instrum. Meth. A \*\*824\*\* \(2016\) 512](#).
  - [127] DREAM, R. Wigmans, *The DREAM project: Towards the ultimate in calorimetry*, [Nucl. Instrum. Meth. A \*\*617\*\* \(2010\) 129](#).
  - [128] DELPHES 3, J. de Favereau *et al.*, *DELPHES 3, A modular framework for fast simulation of a generic collider experiment*, [JHEP \*\*02\*\* \(2014\) 057](#), [arXiv:1307.6346](#).
  - [129] C. Helsens, E. Perez, and D. Hill, *Hep-fcc/fcc-config: spring2021\_bc2taunu*, 2021. doi: [10.5281/zenodo.4817845](#).
  - [130] V. Volkl *et al.*, *key4hep/k4SimDelphes: v00-01-06: More Evtgen / Test Fixes*, 2021. doi: [10.5281/zenodo.4748578](#).
  - [131] V. Volkl *et al.*, *key4hep/edm4hep: v00-03-02*, 2021. doi: [10.5281/zenodo.4785063](#).
  - [132] P. Z. Skands, *The Perugia Tunes*, in *1st International Workshop on Multiple Partonic Interactions at the LHC*, 284–297, 2009, [arXiv:0905.3418](#).
  - [133] N. Davidson, T. Przedzinski, and Z. Was, *PHOTOS interface in C++: Technical and physics documentation*, [Comp. Phys. Comm. \*\*199\*\* \(2016\) 86](#), [arXiv:1011.0937](#).
  - [134] T. Chen and C. Guestrin, *XGBoost: A Scalable Tree Boosting System*, in *Proceedings of the 22nd ACM SIGKDD International Conference on Knowledge Discovery and Data Mining*, [KDD '16](#), (New York, NY, USA), 785–794, ACM, 2016.
  - [135] Heavy Flavor Averaging Group, Y. Amhis *et al.*, *Averages of  $b$ -hadron,  $c$ -hadron, and  $\tau$ -lepton properties as of 2018*, [Eur. Phys. J. \*\*C81\*\* \(2021\) 226](#), [arXiv:1909.12524](#), updated results and plots available at <https://hflav.web.cern.ch>.
  - [136] R. Aleksan, L. Oliver, and E. Perez, *Study of CP violation in  $B^\pm$  decays to  $\bar{D}^0(D^0)K^\pm$  at FCCee*, [arXiv:2107.05311](#).
  - [137] Flavour Lattice Averaging Group (FLAG), Y. Aoki *et al.*, *FLAG Review 2021*, [Eur. Phys. J. C \*\*82\*\* \(2022\) 869](#), [arXiv:2111.09849](#).

- 
- [138] M. Ciuchini *et al.*, *Constraints on lepton universality violation from rare  $B$  decays*, [Phys. Rev. D \*\*107\*\* \(2023\) 055036](#), [arXiv:2212.10516](#).
- [139] N. Gubernari, M. Reboud, D. van Dyk, and J. Virto, *Improved theory predictions and global analysis of exclusive  $b \rightarrow s\mu^+\mu^-$  processes*, [JHEP \*\*09\*\* \(2022\) 133](#), [arXiv:2206.03797](#).
- [140] J. de Blas *et al.*, *Focus topics for the ECFA study on Higgs / Top / EW factories*, [arXiv:2401.07564](#).
- [141] A. Bondar, A. Kuzmin, and V. Vorobyev, *A method for model-independent measurement of the CKM angle  $\beta$  via time-dependent analysis of the  $B^0 \rightarrow D\pi^+\pi^-$ ,  $D \rightarrow K_S^0\pi^+\pi^-$  decays*, [JHEP \*\*03\*\* \(2018\) 195](#), [arXiv:1802.00200](#).
- [142] CEPC Study Group, M. Dong *et al.*, *CEPC Conceptual Design Report: Volume 2 - Physics & Detector*, [arXiv:1811.10545](#).
- [143] S. Descotes-Genon, S. Fajfer, J. F. Kamenik, and M. Novoa-Brunet, *Probing CP violation in exclusive  $b \rightarrow s\nu\nu^-$  transitions*, [Phys. Rev. D \*\*107\*\* \(2023\) 013005](#), [arXiv:2208.10880](#).
- [144] L. Allwicher, C. Cornella, G. Isidori, and B. A. Stefanek, *New physics in the third generation. A comprehensive SMEFT analysis and future prospects*, [JHEP \*\*03\*\* \(2024\) 049](#), [arXiv:2311.00020](#).
- [145] X. Zuo *et al.*, *Prospects for  $B_c^+$  and  $B^+ \rightarrow \tau^+\nu_\tau$  at FCC-ee*, [Eur. Phys. J. C \*\*84\*\* \(2024\) 87](#), [arXiv:2305.02998](#).